University of Southampton

Faculty of Environmental and Life Sciences

School of Ocean and Earth Science

Development Of An Autonomous Dissolved Inorganic Carbon Sensor For Oceanic Measurements

by

Samuel Andrew Monk

ORCID ID 0000-0003-1631-4154

Thesis for the degree of Doctor of Philosophy

January 2020

University of Southampton

Abstract

Faculty of Environmental and Life Sciences

School of Ocean and Earth Science

Thesis for the degree of Doctor of Philosophy

Development Of An Autonomous Dissolved Inorganic Carbon Sensor For Oceanic Measurements

by

Samuel Andrew Monk

Since the industrial revolution the CO_2 concentrations in the atmosphere have increased from 280 ppm to over 400 ppm, and each year the oceans take up approximately 25% of the annually emitted anthropogenic CO_2. This increase in CO_2 in the oceans has had a measureable impact on the marine carbonate system, and the resultant increase in the acidity of the ocean is a potential stressor for a range of ecosystems. In order to fully quantify the marine carbonate system there are four variables that can be measured, these are dissolved inorganic carbon (DIC), pH, total alkalinity and partial pressure of CO_2. By measuring two of the four variables the others can be determined. Of these variables DIC is the only one without either an underway or *in situ* sensor, despite being one half of the preferred pairs for observing the carbonate system. To address this technological gap and increase the measurement coverage there is a clear need for an autonomous sensor capable of making quality measurements while having a robust, small physical size, and low power requirements. Presented here are the results of developmental work that has led to a full ocean depth rated autonomous DIC sensor, based on a microfluidic "Lab On Chip" (LOC) design. The final version of the DIC LOC sensor operates by acidifying < 1 ml of seawater, converting the DIC to CO_2, which is diffused across a gas permeable membrane into an acceptor solution. The CO_2 reacts with the acceptor resulting in a conductivity drop that is measured using a Capacitively Coupled Contactless Conductivity Detector (C4D). Each measurement takes ~15 minutes and the sensor can be set up to perform calibrations *in situ*. Laboratory testing demonstrated this system has a precision of < 1 µmol kg^{-1}. The sensor was deployed as part of a large EU project aiming to detect a simulated sub-seabed leak of CO_2. Over multiple deployments in the North Sea the sensor collected data used to locate the leak. A number of field tests have established the sensor has a precision of < 10 µmol kg^{-1}. This work has demonstrated that this sensor offers potential to fill the current technological gap and collect data that will enhance understanding of the marine carbonate system.

Table of Contents

Table of Tables

Table of Tables

Table of Figures

Table of Figures

Table of Figures

Research Thesis: Declaration of Authorship

Print name:

Title of thesis: Development Of An Autonomous Dissolved Inorganic Carbon Sensor For Oceanic Measurements

I declare that this thesis and the work presented in it are my own and has been generated by me as the result of my own original research.

I confirm that:

1. This work was done wholly or mainly while in candidature for a research degree at this University;
2. Where any part of this thesis has previously been submitted for a degree or any other qualification at this University or any other institution, this has been clearly stated;
3. Where I have consulted the published work of others, this is always clearly attributed;
4. Where I have quoted from the work of others, the source is always given. With the exception of such quotations, this thesis is entirely my own work;
5. I have acknowledged all main sources of help;
6. Where the thesis is based on work done by myself jointly with others, I have made clear exactly what was done by others and what I have contributed myself;
7. None of this work has been published before submission

Signature: Date:

Acknowledgements

I would like to begin by thanking my supervisory panel for all their assistance, in particular Dr Socratis Loucaides for all the guidance and encouragement he has provided throughout this process. I would also like to thank my unofficial supervisors Dr Martin Arundell and Dr Stathys Papadimitriou. Thanks to Martin for all his help devising various experiments and assistance fabricating electrodes. Thanks also to Stathys for sharing his carbonate knowledge and all his assistance with editing this thesis. I would also like to thank Prof. Matthew Mowlem for his feedback throughout the development of the sensor.

I would like to express my gratitude to all members of the Ocean Technology and Engineering Group, both past and present. It would have been impossible to complete this work without the group and all the previous work that has gone into the development of the Lab On Chip platform.

I wish to thank all those involved in the STEMM-CCS project. A special thanks to all the crew and participants on the cruise JC180, for making it both a success and a joy. In particular, to Allison Schaap and Rudi Hanz for their roles in the LOC Sensor Squad.

To process the bottled samples I was assisted by numerous VINDTA wranglers. I would like to thank Dr Cynthia Dumousseaud for her guidance and assistance with the VINDTA in the University of Southampton Carbon Laboratory. Thanks also to both Becky Garley, for running samples in Bermuda, and also to Dr Anita Flohr, for running the ROV bottled samples.

I also wish to thank Matt Wilson for his fluid dynamics assistance. Thanks to all those whose names grace the back of door 251/28, it has been a fantastically supportive group that have passed through, and I am happy that we have all shared an office and plenty of coffee.

I would also like to thank Carolyn Drake, not least for making the time to proof read this, and many other documents over the course of the last few years, but also for her unending support over the course of this project.

I would like to finish by thanking my friends and family for their boundless support throughout this process, and for demonstrating that support by not always asking how the thesis was going.

"Most of the time spent wrestling with technologies that don't quite work yet is just not worth it for end users, however much fun it is for nerds."
Douglas Adams

Definitions and Abbreviations

AUV	Autonomous Underwater Vehicle
C4D	Contactless Capacitively Coupled Conductivity Detector
CCS	Carbon Capture and Storage
CRM	Certified Reference Material
DIC	Dissolved Inorganic Carbon
GEU	Gas Exchange Unit
GOA-ON	Global Ocean Acidification Observing Network
ID	Internal Diameter
JGOFS	Joint Global Ocean Flux Study
LB	Large Barrel
LOC	Lab On Chip
OD	Outer Diameter
OTEG	Ocean Technology and Engineering Group, National Oceanography Centre
PDMS	Polydimethylsiloxane
PMMA	Poly(methyl methacrylate)
ROV	Remotely Operated Vehicle
SB	Small Barrel
SOCAT	Surface Ocean CO_2 Atlas
SOP	Standard Operating Procedures
STEMM-CCS	Strategies for Environmental Monitoring of Marine Carbon Capture and Storage
TA	Total Alkalinity
TIAT	Tube In A Tube
TRL	Technology Readiness Level
VOS	Volunteer Observing Ship
WOCE	World Ocean Circulation Experiment

Chapter 1 Introduction

Global protests brought climate change, and the importance of carbon to its emergence and advancement over the last two centuries, to mainstream attention over 2019 (Horton, 2019). The industrial revolution led to an increase in both life expectancy and global population, dramatically increasing the human impact on global biogeochemical systems. The 'Anthropocene' has been proposed as the name for this recent period of geological time (Crutzen, 2006). One proposed metric for defining this epoch is the anthropogenic alteration of the atmospheric composition (Steffen, Crutzen and McNeill, 2007). Discussion about the start date and what may be the most appropriate metric to define this new epoch continues (Smith and Zeder, 2013), but the general scientific consensus is that the anthropogenic alteration of the atmospheric composition is very likely to have resulted in changes to the climate system (IPCC, 2014). This is especially true of gases which impact on the thermal mass balance of the atmosphere, or greenhouse gases. Carbon dioxide (CO_2) is one of the main greenhouse gases, the others including water vapour, methane and nitrous dioxide (Millero, 2007). Although CO_2 does not have the highest capacity to store heat, it is seen as the key contributor to global warming due to its high atmospheric levels, relatively long atmospheric residence time and the amount emitted through various human activities (Ciais *et al.*, 2013).

1.1 Global Carbon Cycle

The global carbon cycle has been described as a system of reservoirs of carbon linked by various exchanges or fluxes (IPCC, 2014). These reservoirs and their annual fluxes are quantified in Figure 1.1, which demonstrates that the carbon in the Earth System is in constant flux, moving between the various reservoirs at different rates. The arrows in Figure 1.1 illustrate the anthropogenic fluxes of carbon averaged between 2009 and 2018 and the size of the reservoirs is illustrated in the relative magnitude of the circles (Friedlingstein *et al.*, 2019). When considering the oceanic and atmospheric reservoirs, it has been shown that more than 98% of the carbon is stored as dissolved inorganic carbon (DIC) in the oceans, as illustrated by the large circle on the right of Figure 1.1 (Zeebe and Wolf-Gladrow, 2001).

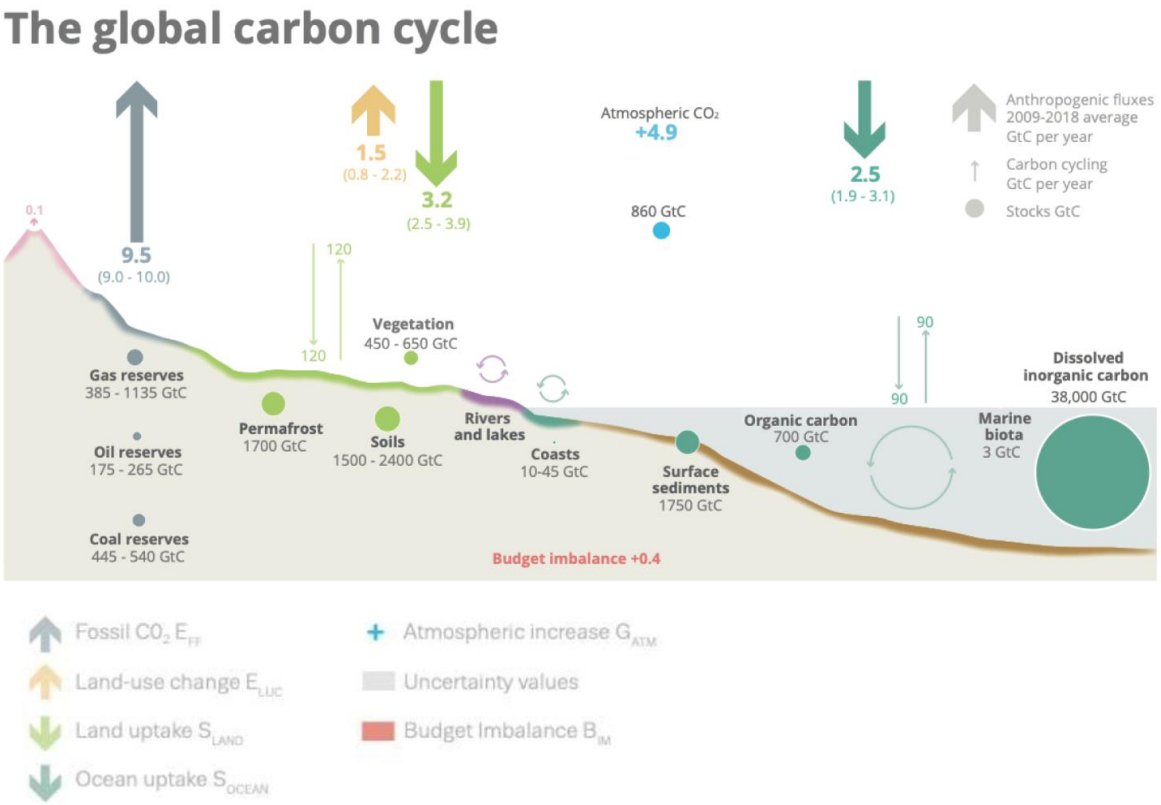

Figure 1.1 Schematic showing the fluxes and reservoirs of the global carbon cycle. The circles illustrate the reservoirs of carbon and the arrows show the annual fluxes between them, based on the global carbon budget for the decade from 2009 to 2018. Schematic from Friedlingstein *et al.* (2019).

1.1.1 Atmospheric Trends

Before the industrial revolution the global carbon cycle was in an approximately steady state (Pongratz *et al.*, 2009). Since the late 1950s, when Keeling initiated regular atmospheric CO_2 measurements at Mount Mauna Loa, Hawaii (Keeling, Bacastow and Bainbridge, 1976), it has been shown that the annual average CO_2 concentrations in the atmosphere have increased from 317 parts per million (ppm) to over 400 ppm (Betts *et al.*, 2016). The atmospheric data presented in Figure 1.2 show a clear saw tooth pattern revealing annual trends due to the uneven distribution of land across the globe (Tans and Keeling, 2020). The northern hemisphere contains more land than the southern hemisphere; during the northern hemisphere spring and summer more CO_2 is taken up by the biosphere. This results in a drop in the atmospheric CO_2, leading to the saw tooth pattern in the data (Ciais *et al.*, 2019). Despite the annual dip, the atmospheric concentration has not dropped below 400 ppm since 2015, as shown in Figure 1.2.

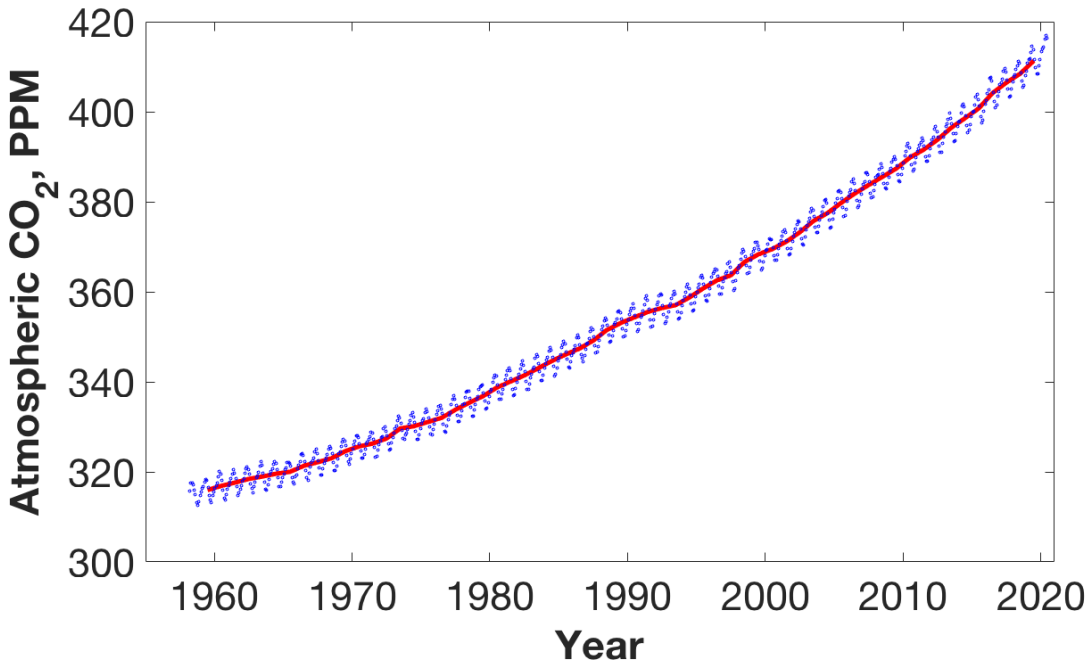

Figure 1.2 Atmospheric CO_2 concentration recorded in Hawaii, known as The Keeling Curve. The data is from the Global Monitoring Laboratory, Tans and Keeling (2020).

It is estimated that a total of 555 ± 85 PgC of carbon has been added to the atmosphere since the industrial revolution (Ciais *et al.*, 2013) and the ocean has absorbed approximately a third of the total anthropogenic CO_2 (Sabine *et al.*, 2004). Between 2009 and 2018, of the 9.5 ± 0.5 GtC yr^{-1} emitted CO_2, 2.5 ± 0.6 GtC yr^{-1} was absorbed by the ocean, 3.2 ± 0.7 GtC yr^{-1} was taken up by terrestrial reservoirs with 4.9 GtC yr^{-1} remaining in the atmosphere; in 2018 it was the first year over 10 GtC were emitted to the atmosphere (Friedlingstein *et al.*, 2019). It has been estimated that the ocean may be responsible for up to 40% of the observed decadal variability in the volume of CO_2 which remains in the atmosphere (DeVries *et al.*, 2019).

The Paris Agreement committed countries to limit average global temperature rise to less than 2 °C by 2100 (UNFCCC. Conference of the Parties (COP), 2015; Rogelj *et al.*, 2016), and aimed to achieve this by reducing net greenhouse gas emissions. One proposed strategy to help achieve this goal is carbon capture and storage (Turley *et al.*, 2009; Szulczewski *et al.*, 2012), which aims to remove carbon from the atmosphere and store it so that it can no longer influence the climate. Several projects have investigated offshore aquifers as potential CO_2 storage sites and such projects require active monitoring to ensure there would be no adverse effects to the water around the storage sites (Blackford *et al.*, 2014, 2015; Wallmann *et al.*, 2015). Given the size of the oceanic DIC pool, the role of the ocean in modulating the anthropogenic CO_2 in the

atmosphere, and in offering a potential site for sequestration, the oceanic carbon cycle has been actively investigated over the last several decades.

1.1.2 Oceanic Carbon Cycle

The solubility of CO_2 is greater than that of the other atmospheric gases, which is an important factor in driving the large fluxes of carbon between the ocean and atmosphere. Gaseous CO_2 ($CO_{2(g)}$) dissolves into seawater to form aqueous dissolved CO_2 ($CO_{2(aq)}$), which reacts with water molecules to form carbonic acid (H_2CO_3) which dissociates to hydrogen (H^+), bicarbonate (HCO_3^-) and carbonate (CO_3^{2-}) ions (Equation 1.1).

$$CO_{2(aq)} + H_2O \leftrightharpoons H_2CO_3 \leftrightharpoons HCO_3^- + H^+ \leftrightharpoons CO_3^{2-} + 2H^+ \quad (1.1)$$

As a result of the dynamic $CO_{2(g)}$ dissolution-disassociation equilibrium in water the absorption of excess anthropogenic CO_2 by oceanic water has caused an increase in H^+ and the associated decrease in the pH of the ocean, which has been termed "The Other CO_2 Problem" (Doney *et al.*, 2009) or more commonly Ocean Acidification .

The oceanic DIC reservoir is not homogenous throughout the oceans, but varies with depth and latitude as shown in Figure 1.3. There are three mechanisms that influence the DIC concentration at depth (Volk and Hoffert, 1985; Williams and Follows, 2011). The solubility pump is the physical mixing of the cold carbon-rich surface waters from high latitudes as they undergo subduction. The biological soft tissue pump is when biologically formed material sinks from the ocean surface and is respired at depth. The carbonate pump is the sinking of marine organisms that have precipitated carbonate shells at the surface. These processes work together to give the distributions seen in Figure 1.3.

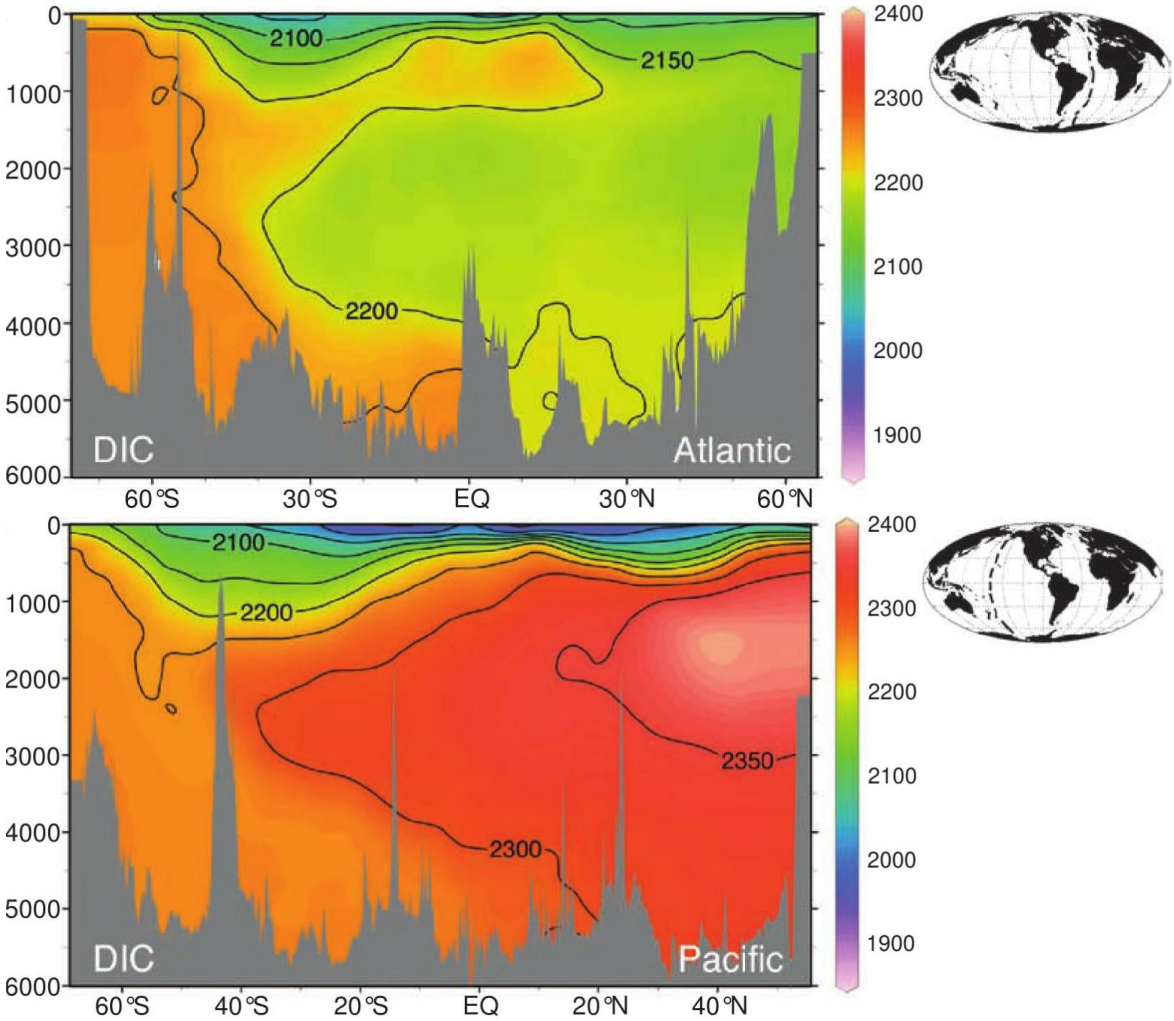

Figure 1.3 Meridional sections of DIC from the Atlantic and Pacific Basins, units are µmol kg^{-1}. Modified from Williams and Follows (2011).

1.1.3 Oceanic Trends

It was recognised in the 1980s that it would be important to quantify the role of the oceans in the global carbon cycle and this recognition was one of the driving forces that led to the Joint Global Ocean Flux Study (JGOFS) establishing two open ocean long term time-series sites. In the North Atlantic the Bermuda Atlantic Time-series Study (BATS) was established while in the Pacific the Hawaii Ocean Time-series (HOT), began monthly cruises in 1988, with both programmes sharing the aim of monitoring long term trends in the physics, chemistry and biology of the ocean. It has been shown that the surface pH at the BATS and HOT sites has decreased by 0.0017 ± 0.0001 $year^{-1}$ and 0.0016 ± 0.0001 $year^{-1}$, respectively (Bates *et al.*, 2014). The change in DIC, normalised to remove salinity influences, at BATS has been found to be 1.12 ± 0.07 µmol kg^{-1} $year^{-1}$, shown in Figure 1.4. The normalisation of the DIC data removes the impact of variations of the freshwater fluxes on the signal. The freshwater fluxes are the result of the net change between precipitation and evaporation at the site.

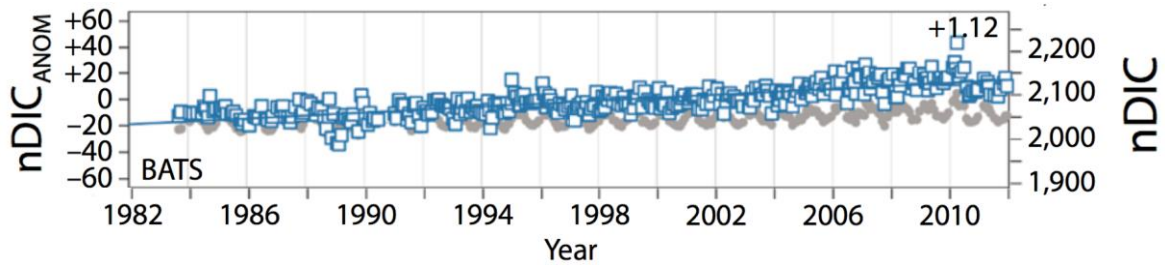

Figure 1.4 Long term trends in DIC concentrations measured at BATS, normalised to remove salinity influences. The grey symbols are the observations and the blue symbols are the anomalies from the observations and the climatological means. Modified from Bates, R. N., Astor, Y. M. (2014).

The planning for the World Ocean Circulation Experiment (WOCE) also began in the 1980s, with the goal of improving global measurement coverage (Wallace, 2001). Over the 1990s a large-scale international effort meant multiple transect lines were measured, giving the first global snapshot of the ocean. These transect lines have since been reoccupied, allowing temporal variations to be investigated. One such comparative study has revealed that the uptake of DIC, between 1994 and 2007, was not uniform throughout the ocean (Gruber *et al.*, 2019). On average the surface waters were found to have increased by 14 µmol kg^{-1}, and the largest increases were in the southern Atlantic, shown in Figure 1.5.

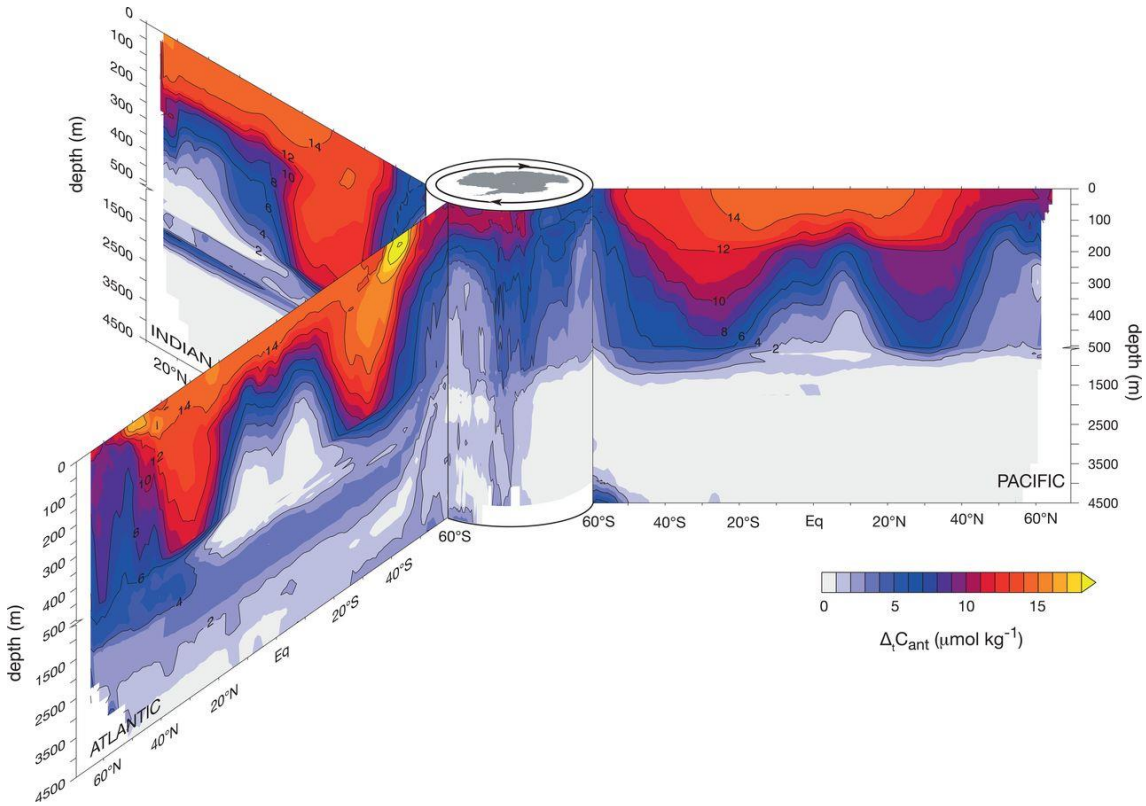

Figure 1.5 Spatial variations in DIC uptake between 1994 and 2007, over the three main ocean basins. Figure from Gruber *et al.* (2019). Reprinted with the permission of AAAS.

While the ocean is currently absorbing a quarter of the anthropogenic CO_2, this rate is unlikely to be sustained into the future because the ability of the ocean to store CO_2 will decrease as acidification continues (Zeebe and Wolf-Gladrow, 2001; Sabine *et al.*, 2004). Quantifying the marine carbonate cycle is therefore essential to the understanding of the carbon system and quantifying the anthropogenic CO_2 reservoir in the atmosphere in the future.

1.1.4 Impact of Ocean Acidification

The reduction in the pH of the ocean, via anthropogenic acidification, is likely to impact the functioning of many ecosystems, including those supporting fisheries, through altering several biologically important processes such as ion transport, and enzyme and protein functionality (Turley and Gattuso, 2012). In 2014 fisheries provided 3.1 billion people with a fifth of their intake of animal protein (FAO, 2016) and provided an estimated 260 million people with employment (McClanahan, Allison and Cinner, 2015). A review of the impacts of ocean acidification on fish has found that many physiological systems may be stressed and the early life stages of many fish are likely to be affected (Heuer and Grosell, 2014).

Ocean acidification decreases the availability of carbonate ion (CO_3^{2-}) that results in an increase in the dissolution of calcium carbonate ($CaCO_3$), which is an important component of the shells of many marine organisms (Kleypas et al., 2006). Coral reefs, in tropical zones and those in deep cooler water, are sensitive to this decrease in $CaCO_3$ (Tracey et al., 2013). Ocean acidification is not the only stressor on ecosystems and fisheries, with many under stress from other sources of pollution and environmental change (Breitburg et al., 2015). While it is currently hard to attribute changes in a reef ecosystem to any one cause it has been suggested that changes in reef calcification rates can be attributed to ocean acidification in some places (Albright et al., 2016). Quantifying changes to the carbonate system is key to understanding how these systems will be affected if meaningful predictions about their future socio-economic impacts are to be made.

1.1.5 Measuring Carbonate Chemistry

There are four parameters of the oceanic carbonate system which, when combined with measurements of the water's physical properties (temperature, salinity and pressure) can be used to describe the system fully:

- Dissolved Inorganic Carbon (DIC) which is defined as the sum of the concentrations of the dissolved species formed via the dissolution of CO_2 in water:

$$[DIC] = [CO_2] + [HCO_3^-] + [CO_3^{2-}]$$

- pH is the negative logarithm of the hydrogen ion (proton) concentration in a solution with different proton scales used, most often the total proton scale that includes free protons and bisulphate ions
- Fugacity of CO_2 (fCO_2) is defined as the partial pressure of CO_2 that is in equilibrium with sea water
- Total Alkalinity (TA) is defined as the number of moles of hydrogen ion equivalent to the excess of proton acceptors over proton donors in solution

It is sufficient to measure two of the above four parameters and derive the others (Millero, 2007; Wolf-Gladrow *et al.*, 2007; Williams and Follows, 2011). Historically the DIC and TA pair has been preferred, due to the availability of instruments capable of making these measurements with high precision and accuracy (Hoppe *et al.*, 2012; Martz *et al.*, 2015). However, to reduce the propagated errors in the derived values, the preferred pair is either DIC and pH, which gives the lowest probable error for the derived TA and fCO_2, or DIC and fCO_2 which gives the lowest probable error of pH calculations, as highlighted in Table 1.1 (Millero, 2007). Overdetermination of the oceanic carbonate system, i.e. measuring more than two parameters, is a useful practise often used to assess the quality of measurements (Byrne, 2014; Sastri *et al.*, 2019).

Table 1.1 Estimated error in the derived carbonate parameters based on the initial pair, from Millero (2007).

Pairing	pH	TA ($\mu mol\ kg^{-1}$)	DIC ($\mu mol\ kg^{-1}$)	fCO_2 (μatm)
DIC & pH		± 2.7		±1.8
DIC & fCO_2	± 0.0025	± 3.4		
DIC & TA	±0.0062			± 5.7
pH & TA			± 3.8	± 2.1
pH & fCO_2		± 21	± 18	
fCO_2 & TA	± 0.0026		± 3.2	

The pairing of the pH and TA measurement relies on various assumptions which may not hold true in all areas where carbonate chemistry is being studied, such as waters with high freshwater fluxes, such as coastal areas, estuarine environments and areas close to ice melt (Fassbender *et al.*, 2015). In regions with high freshwater inputs the assumptions about the seawater composition, which the pH and TA measurements are based on, may not be valid (Dickson, Sabine and Christian, 2007). In these areas the DIC and pH forms the optimal pair for a reliable full characterisation of the carbonate system. DIC is highly desirable to measure as it is more sensitive to changes in photosynthesis and respiration than other parameters, and by measuring DIC it is possible to investigate changes in biological systems which pairs such as pH and TA have been demonstrated as not being capable of resolving (Fassbender *et al.*, 2015).

As biologists seek to understand how the changing carbonate chemistry might impact various ecosystems there has been increasing interest in microcosm studies. In these studies various techniques are used to alter the carbonate chemistry and the biological response is monitored. It is widely recognised that for these studies to be relevant correct monitoring of the carbonate chemistry is essential (Gattuso *et al.*, 2010). A sensor capable of making highly precise and accurate measurements at an appropriate frequency for the temporal dynamics of the system, and at a viable cost, would enhance these studies.

1.1.6 Carbonate Data Availability

The preceding sections have presented some limited DIC data however the global spatiotemporal coverage of the carbonate system remains low, despite recent improvements. This is clearly exemplified by the Surface Ocean CO_2 Atlas (SOCAT). SOCAT is an annually updated database for

surface fCO_2 measurements. The most recent version has 25.7 million discrete points covering the time period 1957 to 2019, Version 2019:(Bakker *et al.*, 2016). When all these data points are plotted they show good coverage of the North Atlantic but large gaps in the South Pacific and the Southern Ocean (Figure 1.6 Panel A). Investigating data available for 2018, the last full year of the database, reveals even lower spatial coverage (Figure 1.6 Panel B). The SOCAT database is only for surface fCO_2 measurements and a decent number of commercially available instruments exist, which are capable of making underway fCO_2 measurements (Martz *et al.*, 2015). These instruments can be installed on cargo ships giving good coverage of regular trade routes. Measurements of DIC are even sparser, in part due to the fact there are no commercially available underway DIC instruments (Martz *et al.*, 2015).

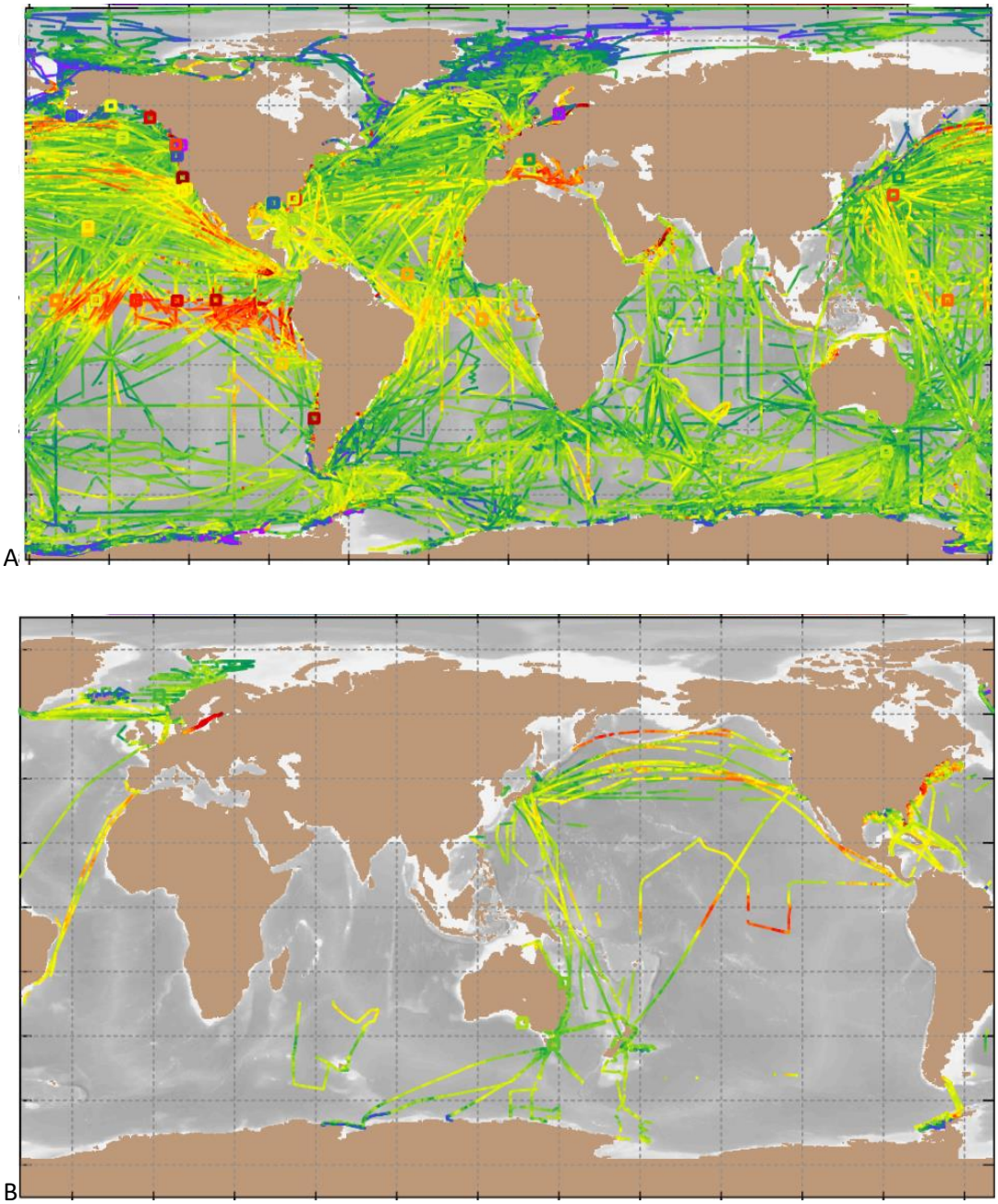

Figure 1.6 Spatial coverage of surface fCO_2 measurements. Panel A shows the global coverage in SOCAT from 1957 to 2019. Panel B shows the global coverage for 2018, the last full year in SOCAT Version 2019: Bakker *et al.* (2016).

Many regions of interest for investigating the carbonate system, such as coastal zones, the Southern Ocean and areas of ice cap melting, are highly dynamic areas with a high degree of spatiotemporal heterogeneity (Butterworth and Miller, 2016). These areas are also traditionally under sampled due to the practicalities of ship-based measurements. However a sensor mounted on an automated platform would be able to provide valuable data in an economically efficient and practical manner.

1.2 Current State of the Art for DIC Measurements

1.2.1 Standard Operating Procedures

The current technique for making DIC measurements requires bottled samples to be collected and then analysed in a specialist laboratory. It was in the early 1990s that a series of Standard Operating Procedures (SOP) were established to standardise the way in which samples were collected, stored and analysed, by the oceanographic community (Dickson and Goyet, 1994). These have been continually updated since and provide a high level of detail into how samples should be handled to give confidence that data are comparable between laboratories (Dickson, Sabine and Christian, 2007). For DIC the two most relevant SOP methods are:

- SOP 01; which details how discrete bottle samples should be collected
- SOP 02; which details how the samples should be analysed

The currently accepted standard method for measuring DIC, as described by the SOP handbook is to acidify a known volume of a seawater sample in a stripping chamber, then purge the generated CO_2 from sample with an inert gas, and use colourimetry to measure the amount of CO_2 produced. Specifically, the CO_2 gas purged from the sample is reacted with an absorbent containing ethanolomine, and the hydroxyetheylcarbamic acid formed is titrated coulometrically. The original instrument based on this technique was named the Single Operator Multi-parameter Metabolic Analyser (SOMMA) and was produced commercially in the early 1990s. Currently Marianda produce the commercially available Versatile INstrument for the Determination of Total inorganic carbon and titration Alkalinity, VINDTA 3C, (Marianda, Germany). The VINTDA 3C is comparable to the SOMMA system but also records TA. Marianda also produces the Automated Infra Red Inorganic Carbon Analyzer, or AIRICA, which is based on the IR-detection of CO_2. Another available instrument is the AS-C3 DIC Analyser Apollo (SciTech, USA), which measures the CO_2 gas using a non-dispersive infrared (NDIR) sensor. The efficiency of these systems is calibrated using known amounts of CO_2 gas or standard solutions. These instruments are capable of achieving DIC measurements with an accuracy of ± 1.0 µmol kg^{-1} (Bockmon and Dickson, 2015).

1.2.2 Certified Reference Material

By the late 1980s it was clear that for laboratories to generate comparable DIC measurements a Certified Reference Material (CRM) would be needed (Dickson, 2010). The Dickson group at Scripps Institution of Oceanography, USA, developed a CRM for DIC and TA analyses and by 2010 had produced 56,000 bottles (Dickson, 2010); this CRM is the standard recommended in the SOP.

The CRM is not measured and certified for DIC concentration using the method detailed in SOP 02, but it is determined manometrically following acidification and CO_2 extraction by vacuum distillation in a vacuum manifold (Guenther, Keeling and Emanuele, 1994). This technique is highly precise, with a precision of ~0.5 µmol kg^{-1}, one quarter of that of the colourimetric method, however it is not suited to processing large numbers of samples.

1.2.3 Required Measurement Performance

The Global Ocean Acidification Observing Network (GOA-ON) has set two quality levels for the reporting of DIC data; these are "weather" and "climate" quality (Newton *et al.*, 2014). The "weather" quality data should provide resolution of relative spatial patterns and short-term variation. To achieve this the measurement should achieve a precision of ~10%, and for DIC this would be ± 10 µmol kg^{-1}. The "climate" quality data provide resolution of long term trends in the ocean acidification signal; this requires a precision of 1%, which for DIC is defined as ±2 µmol kg^{-1}. The only current technique to achieve the climate quality measurements is to collect water samples and analyse them in a laboratory, following SOP 01 and SOP 02 detailed in the previous section.

Results of an inter-laboratory comparison found that most were capable of measuring DIC to the "weather" target but were short of the 2 µmol kg^{-1} window required for data to be used for the "climate" standard (Bockmon and Dickson, 2015). This comparison highlighted the requirement of most instruments to have highly trained operators to make consistently high quality measurements.

1.2.4 Performance Assessment Metrics

To assess the performance of a sensor the two most commonly used metrics are accuracy and precision. Accuracy is defined as the difference between the sensor recorded value and the true value, as measured using conventional techniques (Okazaki *et al.*, 2017). Precision is defined as the reproducibility of the measurement of a sample (Schuster *et al.*, 2009). For a DIC sensor these metrics can be calculated by replicate measurements of a CRM (section 1.2.2). The repeatability of a measurement is a short term precision estimate (Okazaki *et al.*, 2017; Birchill *et al.*, 2019) which can neglect systematic errors leading to an overestimation of the sensor's performance, potentially resulting in over interpretation of the data collected (Worsfold *et al.*, 2019). Increasingly more robust techniques have been used to quantify sensor uncertainty. The Nordtest™ (Magnusson *et al.*, 2012) combines the random and systematic effects on measurements over a longer time period to make an uncertainty estimate. This uncertainty is

typically larger than the estimate of precision but is more representative of the sensor performance and therefore less likely to lead to over interpretation of data.

1.2.5 Definitions of Benchtop, Underway and Sensor Instruments

For the purpose of this study the definitions of benchtop, underway and sensor instruments will follow the convention used in a recent review of commercially available technology (Martz *et al.*, 2015). Benchtop instruments make measurements on discrete bottle samples, and while the measurements are autonomous a technician is required to operate the instrument. The instruments described in section 1.2 would be classed as benchtop systems. Underway instruments make automated measurements on a flow-through sample stream. These systems are routinely mounted on ships to make surface water measurements and are externally powered but require minimal user interaction to operate. A sensor would be capable of making autonomous *in situ* measurements and be internally powered. The following section provides a review of the platforms which these automated instruments can be mounted on to collect spatial data.

1.3 Review of Platforms for Automated Measurements

Poor spatiotemporal coverage of measurements has been a long-standing challenge for oceanography, as highlighted in section 1.1.6. In 1989 Stommel published a science fiction article in which he envisioned a future 25 years on from then when fleets of autonomous vehicles would patrol the ocean, collecting data similar to the large transects set up by the WOCE (Stommel, 1989). The vision was for a fleet of vehicles to make continuous measurements, whilst calibrating themselves against each other. For such vehicles to contribute to our knowledge of the carbonate system they would require autonomous sensors. While such a large fleet of propelled vehicles has not been realised yet, the Argo program has managed to significantly improve the data coverage in all ocean basins, and emerging technologies are getting close to making Stommel's vision a reality. This section will provide an overview of the various platforms available for making oceanographic measurements, with Table 1.2 providing a summary of the platforms discussed and highlighting the requirements these platforms would have for autonomous sensors.

Table 1.2 Review of the different oceanographic sensor platforms.

	Sensor size limited	Sensor Power limited	Spatial Coverage	Temporal Coverage	Limitation	Availability
Argo Float	High	High	High (no directional control)	Months to decades	Not recovered	High
Autonomous Underwater Vehicles	High	High	High	Days to years	Low power and miniature sensor needed	High
Remotely Operated Vehicles	High	No	Limited Extent	Hours to weeks	Requires specialist ship and crew	Low
Mooring	No	High	Low	Hours to decades	Requires specialist ship and crew	Low
Cabled Observatory	No	No	Low	Hours to decades	High Cost	Low
Volunteer Observing Ship	No	No	Repeat Transect	Months to decades	Limited Depth	Low

A recent review of platform technologies presented a visual representation of the different spatiotemporal scales over which these platforms can provide observations, Figure 1.7 (Bushinsky, Takeshita and Williams, 2019). This figure provides a useful comparison of the length scales of various processes relevant to the carbonate system and the platforms suitable for observing them.

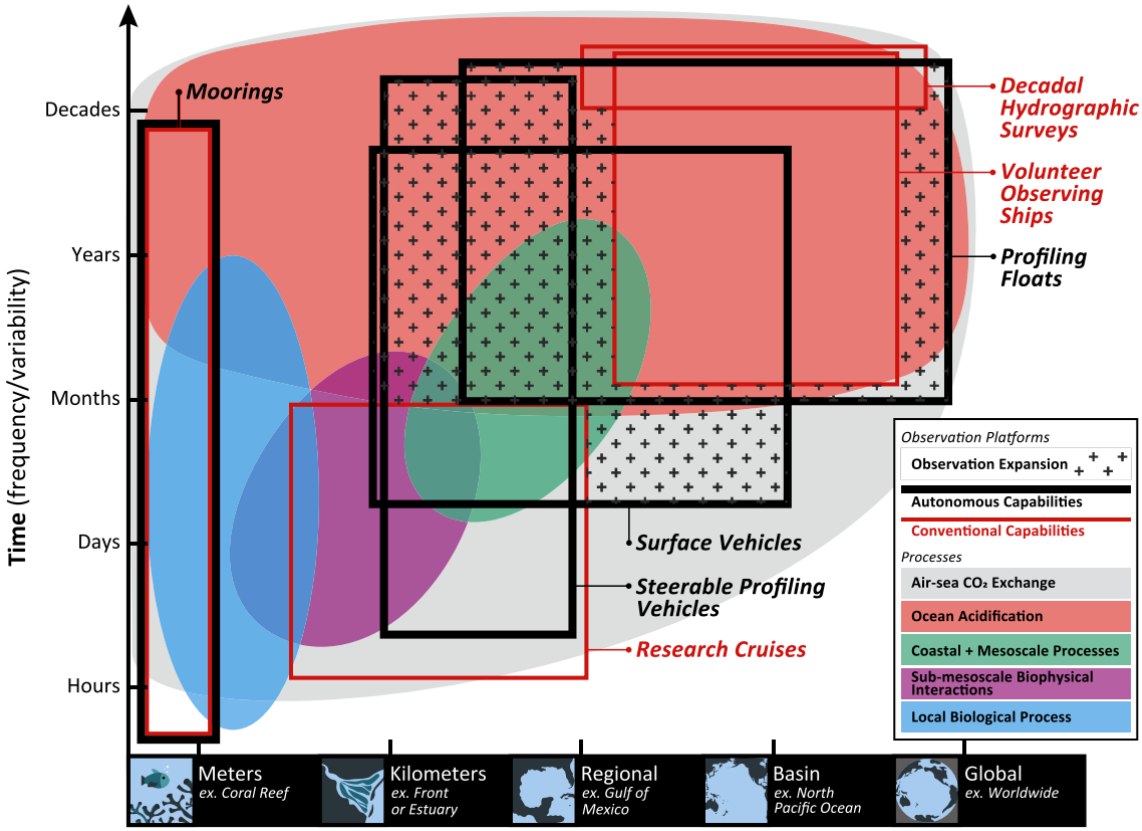

Figure 1.7 A visual representation of the spatiotemporal scales over which different instrument platforms can provide observations relevant to the carbonate system. Figure from Bushinsky, Takeshita and Williams (2019).

1.3.1 Argo Floats

The Argo program utilises a large array of lagrangian profiling floats. The floats collect one profile from 2000 m depth to the ocean surface every 10 days and transmit the collected data back to the user via satellite (Riser *et al.*, 2016). The floats can make observations over large spatial and temporal ranges, providing insight into a range of medium to large-scale processes, as shown in Figure 1.7. There are currently close to 4000 Argo floats collecting data around the world (Figure 1.8 Panel A), allowing studies to be conducted without the costly need for a ship (or fleet of ships) and in regions and seasons too dangerous for ships to be operational.

While the data yielded by the Argo program has resulted in over 2000 publications since 1998 these floats are still limited in terms of which sensors they can carry. All floats carry the basic conductivity temperature depth (CTD) sensor, which allows basic hydrography to be measured (Riser *et al.*, 2016). To collect biogeochemical data Argo floats have been equipped with sensors capable of measuring parameters such as oxygen, nitrate and pH however currently there are

only 367 biogeochemical Argo units. Of these only 150 are capable of measuring pH, which is not enough information to fully quantify the carbonate system (Figure 1.8 Panel B).

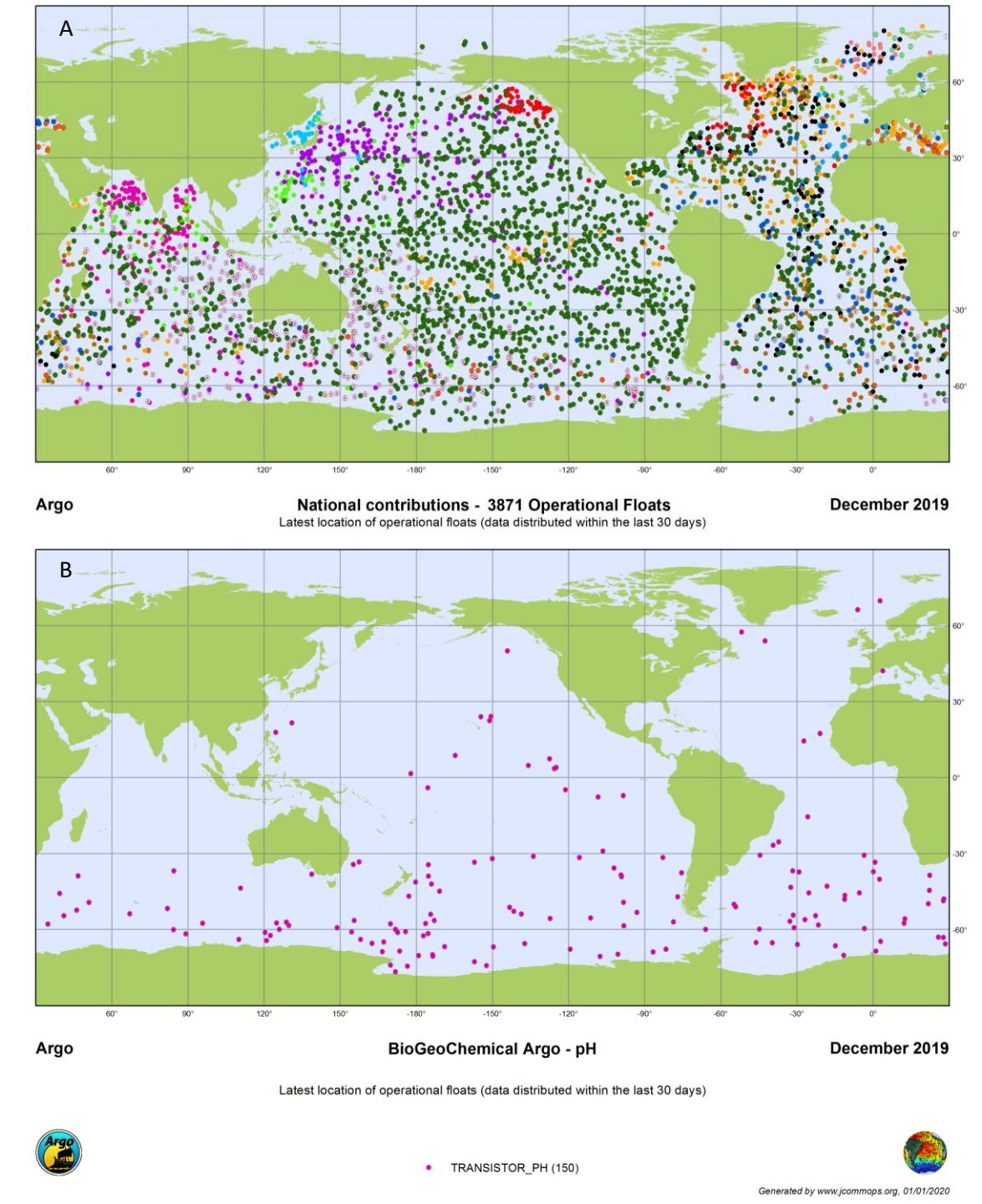

Figure 1.8 Argo float global distribution. Panel A shows the locations of the 3871 operational Argo floats. Panel B shows the locations of the 150 biogeochemical Argo floats equipped with pH sensors. Both figures are from www.jcommops.org, (accessed January 2020).

To improve this biogeochemical coverage floats require small sensors with low power demands, which are capable of taking measurements at a frequency that matches that of their velocity

through the water column. These platforms are normally deployed and remain at sea until no longer operational, which means that sensors need to be capable of self-calibrating and use stable reagents.

1.3.2 Autonomous Underwater Vehicles

Autonomous Underwater Vehicles (AUV) differ from lagrangian floats as they are capable of controlling their direction (Alam, Ray and Anavatti, 2014) and are increasingly common as platforms for research (Wynn *et al.*, 2014). There are a number of different designs for AUVs, including submarine style vehicles which control their propulsion using propellers (e.g. Autosub, Sentry) and glider type AUVs which control their propulsion by altering their buoyancy and pitch (e.g. Deep Glider, Slocum Glider). Like Argo floats, AUVs typically send data back to servers via a satellite or radio link, allowing data to be quality controlled during the deployment. These platforms can collect data over large spatial areas and as this technology matures longer deployments have become possible. Figure 1.7 highlights that these platforms overlap considerably with Argo floats.

Currently AUVs have been used extensively for mapping (Wynn *et al.*, 2014) and to be able to answer more biogeochemical questions they will require new sensors which will have similar requirements as the sensors on Argo floats which require miniature, low power sensors. The advantage AUVs have over floats is that they can be piloted to visit sites of interest without the need for a ship to travel to their ultimate deployment location. The ability to pilot AUVs also allows them to be recovered easily with the potential for batteries and sensor reagents to be replaced over the course of a mission.

1.3.3 Remotely Operated Vehicles

Another tool available for oceanographic research as a sensor platform is the Remotely Operated Vehicles (ROV), such as *Jason* and *ROPOS*. These differ from AUVs in that they are tethered to a ship by a cable and usually require constant piloting. They often have robotic manipulators capable of carrying out complex sampling (Yoerger *et al.*, 2007). The tether allows for data and power to be transferred between the ship and vehicle. The benefit of this is that sensors on these platforms can be larger, more power intensive units. The drawback of these systems is that they require a specialist crew and ship capable of deploying these typically large units, which limits their spatial coverage.

1.3.4 Moorings and Landers

Since the 1960s moorings have been deployed around the world's oceans to collect a variety of long term data, which have been used across all oceanographic research areas (Weller *et al.*, 2000). Mooring technology has greatly improved over time. Initially moorings were deployed and then collected after recording data for a set period, with the possibility that the mooring and data could be lost before recovery. A variety of systems have been used to mitigate this risk, such as adding satellite telemetry to surface moorings. Landers can be viewed as a subset of moorings, which can take a variety of physical forms. They differ from moorings in that they only record measurements on the seabed and have no surface expression, which limits their ability to transmit data back while *in situ*. In both cases the data collected can be over long temporal scales, but limited spatial scales, as shown in Figure 1.7.

A benefit of mounting sensors on these systems is that measurements can be taken at a selected site, with minimal spatial drift. Sensors on moorings need to have low power requirements, with stable reagents but can be larger than the sensors on mobile platforms. Depending on the temporal variation to be measured, these sensors can also have a lower sample frequency. Limitations of this platform are the requirement of specialist ships and crews for installation and service of the moorings, and their low spatial coverage.

1.3.5 Cabled Observatories

In the last decade two large projects have been completed with moorings and landers connected, via fibre optic cables to land, allowing data and power to be transferred in real time. Ocean Network Canada has been recording data for a decade and the Ocean Observing Initiative data are soon to go on line (Kelley, Delaney and Juniper, 2014). Sensors mounted on these platforms can be large and power intensive, as power is provided to the sensor via the cable connected to land. This feature and the high rate of data transmission provides sensors with the option to carry out high frequency measurements. As with more traditional moorings, sensors mounted on these platforms would require stable reagents and the ability to self-calibrate. A limitation would be poor spatial coverage and the high cost.

1.3.6 Volunteer Observing Ship

A Volunteer Observing Ship (VOS) typically makes regular and repeated journeys along the same track. The Ferry Box sensor scheme is an example of a VOS where sensors are mounted on a ferry to collect repeat measurements (Schneider *et al.*, 2014). The Oleander line is another example where a transect of long term data have been collected by mounting sensors on a shipping

container that regularly travels between New Jersey, USA, and Bermuda, crossing the Gulf Stream weekly (Rossby *et al.*, 2014).

Advantages of mounting sensors on a VOS is that they are not limited by size or power requirements and can be regularly serviced while collecting repeat data along a transect. This platform has potential for both large spatial and temporal coverage, as shown in Figure 1.7. A potential limitation for sensors mounted on such platforms is that they lack depth coverage.

1.4 Techniques Currently in Development

There are a variety of different approaches being developed by groups globally to create sensors capable of autonomously measuring DIC (Schuster *et al.*, 2009; Byrne, 2014). Table 1.3 provides details of each of the techniques that this section will detail. For each technique there will be a brief overview of each method, a summary of the results achieved and their advantages and disadvantages with respect to the technique being used for a deep rated, autonomous DIC sensor.

Table 1.3 A review of published techniques used in developmental DIC sensors.

Technique	**Field Deployed?**	**Precision** µmol kg^{-1}	**Sample Frequency** samples $hour^{-1}$	**Reference**
Coulometry	Underway system	± 1.0	4	Amornthammarong *et al.* (2014)
Spectrophotometry	Dock deployment (3 weeks)	± 2.0	7	Wang *et al.* (2015)
Conductometry	Dock deployment (8 week)	± 2.7	1	Sayles and Eck (2009)
Non-Dispersive Infrared Absorption	Surface mooring (7 months)	± 5.0	5 (maximum, 0.33 mooring deployment)	Fassbender *et al.* (2015)
Dual Isotope Dilution and Cavity Ring-down Spectroscopy	Underway system	± 0.4	15	Huang *et al.* (2015)
Membrane Introduction Mass Spectrometry	-	-	-	Bell, Short and Byrne, (2011)

All of the following methods, except for the Dual Isotope Dilution and Cavity Ring-Down Spectroscopy, are based on acidifying the sample to convert the DIC to CO_2. Reducing the pH of the sample to less than 2 converts all the HCO_3^- and CO_3^{2-} to CO_2, as shown in Figure 1.9, taken from (Emerson and Hedges J, 2008). The methods differ in whether a carrier gas or gas permeable membrane is used to extract the CO_2 from the sample, and the method for detecting that CO_2.

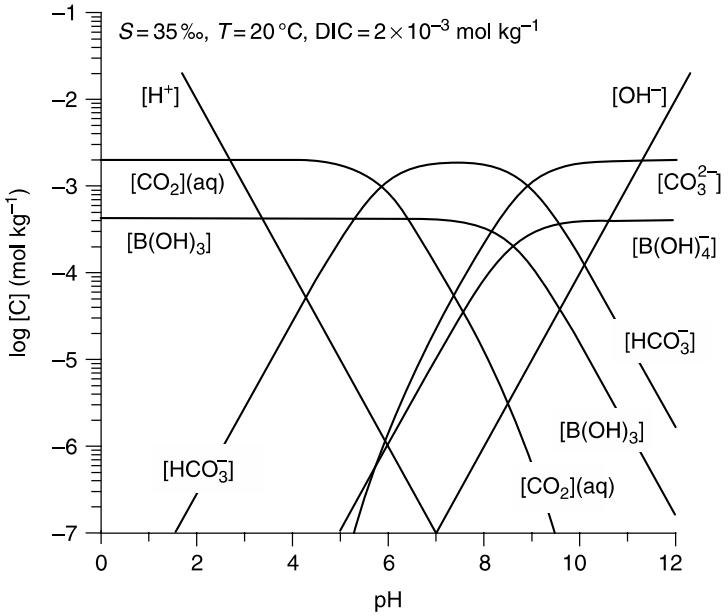

Figure 1.9 Plot showing the different concentrations of the carbonate species as a function of pH, from Emerson and Hedges (2008).

1.4.1 Coulometry

This technique is described fully in section 1.2.1. Recent work to automate a coulometric sensor has been reported, with a prototype instrument capable of measuring 8 samples without operator interaction, with accuracy and precision of ±1.2 µmol kg^{-1} and 0.022% respectively, and a sample frequency of 4 samples per hour (Amornthammarong *et al.*, 2014). The performance of this system is close to that of commercially available instruments. In this technique a sample is acidified, and the released CO_2 is stripped from the acidified sample by an inert CO_2 free carrier gas where the amount of CO_2 is titrated coulomterically. Then the CO_2 reacts quantitatively with ethanolamine to form hydroxyethyl carbonic acid, which is titrated with OH^- ions generated by the reduction of H_2O at a cathode. The endpoint of the titration is measured photometrically, with thymolphthalein used as the colour-changing indicator.

This technique is suited to measurements of surface waters but in its current form is an underway instrument not capable of making *in situ* measurements. This method also uses hazardous chemicals, which could cause challenges for some platforms where the waste storage of reagents may present an issue. The relatively large sample volume of 25 mL required would also generate significant waste fluid over the course of a long term deployment, an issue for platforms limited on space for sensors. The long measurement time of 15 minutes per sample would also prevent this system from being deployed on a fast moving platform and high power requirements could also prove problematic for several platforms (see section 1.3).

1.4.2 Spectrophotometry

In spectrophotometric methods the seawater sample is acidified and CO_2 is driven across a gas permeable membrane into an acceptor solution containing a pH indicator dye. As the CO_2 decreases the pH of the acceptor solution, the dye changes colour which can be measured by monitoring different wavelengths of light passing through the solution.

This technique is used in several prototype systems under development (Byrne *et al.*, 2002; Tue-Ngeun *et al.*, 2005; Wang *et al.*, 2007, 2015; Wang, Chu and Hoering, 2013; X. Liu *et al.*, 2013; DeGrandpre *et al.*, 2014). Various indicator dyes, such as m-cresol purple and Bromocresol purple, can be used and require measurement at different wavelengths which allows for optimisation. In short-term testing, over 3 weeks, the most accurate *in situ* system using this technique had an accuracy of ± 2 µmol kg^{-1} and had a response time of ~22 seconds (Wang *et al.*, 2015). This system used Bromocresol purple as the indicator dye, and the TA of the indicator was optimised to ensure that the pH of the acceptor solution after the sample CO_2 addition would fall between ~5.6 − 6.4, where the colour change is the greatest, to enhance the sensitivity of the sensor.

To achieve the highest possible accuracies the indicator solutions need to be purified (Ma *et al.*, 2019) and the temperature of the measurement cell needs to be monitored precisely (DeGrandpre *et al.*, 2014).

1.4.3 Conductometry

For the conductometric method a known volume of sample is acidified, and the DIC within the sample is converted to gaseous CO_2, which then diffuses across a gas permeable membrane into an acceptor solution. In the literature both sodium hydroxide (NaOH) and Milli-Q ™ water (Merck Sigma, USA) have been trialled as acceptor solutions, with NaOH being most commonly used. The conductivity of the acceptor solution is monitored and as the CO_2 reacts with the solution its conductivity drops proportionally to the concentration of DIC in the sample. The conductivity drop is the result of the CO_2 reacting with hydroxide:

$$CO_{2(aq)} + 2OH^- \Rightarrow CO_3^{2-} + H_2O \quad (1.2)$$

$$CO_{2(aq)} + OH^- \Rightarrow HCO_3^- \quad (1.3)$$

This technique was originally described in the early 1990s (Hall and Aller, 1992) and various systems have been built and tested since (Kubáň and Dasgupta, 1993; Monser, Adhoum and Sadok, 2004; Hoherčáková and Opekar, 2005; Sayles and Eck, 2009; Pencharee *et al.*, 2012). Originally this technique was used to reduce the required sample volume, from several mL to less than 100 µL and produced no toxic by-products while using a flow-through system to achieve a high sample rate. This technique has been improved over time by changing electrode designs and

sample to acceptor solution volumetric ratios to improve accuracy and sensitivity. Recent laboratory and coastal water deployments of a sensor based on this technique achieved precision of 2.7 µmol kg^{-1} and 3.6 µmol kg^{-1}, respectively (Sayles and Eck, 2009).

A potential limitation of this technique is that the measurements would be sensitive to changes in the conductivity cell volume, which could be avoided by mounting electrodes in a glass channel to limit their expansion. Bio-fouling could also change the cell volume and would need to be minimised over long deployments. Conductivity measurements are also sensitive to temperature changes and this needs to be accounted for in sensor designs. This technique may not be suitable for use in areas of elevated hydrogen sulphide concentrations, such as anoxic waters, as this could interfere with the conductivity measurements (Hall and Aller, 1992).

A benefit of using this technique is that very small sample volumes are required, on the order of a few hundred µL, to enable gas exchange across the membrane and achieve rapid sample rates. The acceptor solution can also be chosen to maximise the concentration gradient of CO_2 between the sample and acceptor, which can also reduce the time taken for each sample to increase throughput. Another advantage of the conductometric method is the simplicity of the detection, which doesn't rely on purified dyes.

1.4.4 Non-Dispersive Infrared Absorption

In this technique a known volume of sample is acidified and the generated CO_2 gas is purged with a carrier gas, passing through a desiccator, and into an infrared detector, which measures the mole fraction of CO_2. The Ideal Gas Law is used to determine the moles of CO_2 in the gas phase, while Henry's Law is used to calculate the concentration of CO_2 in the sample at equilibrium with the carrier gas (Hales, Chipman and Takahashi, 2004; Kaltin, Haraldsson and Anderson, 2005; Fassbender *et al.*, 2015).

A system based on this technique was deployed in two field tests (Fassbender *et al.*, 2015). This system used two calibration points for each sample, this was because the infrared detectors response is temperature dependant and to save power its temperature stabilisation mechanism was disabled. To calculate the sample DIC concentration the number of moles of CO_2 in the gas and liquid phases at equilibrium were summed and then divided by the mass of the sample. The first test was a month-long deployment in an aquarium in Seattle and the second test was a 7−month deployment on a mooring in a bay in Hawaii. Laboratory testing determined this sensor's precision to be ± 5 µmol kg^{-1}.

The use of the Ideal Gas Law requires accurate measurements of temperature and salinity to yield accurate results. This measurement currently takes ~12 minutes and to complete the 7 month mooring deployment sampling was reduced to once every three hours.

1.4.5 Dual Isotope Dilution and Cavity Ring-down Spectroscopy

In this method the ratio of $^{13}C/^{12}C$ is measured by a mixture of a seawater sample and a ^{13}C labelled spike, DIC is then calculated based on the mixing ratio of the sample and spike (Huang *et al.*, 2015). This system has been tested both in the laboratory and at sea, and gave a precision of 0.2 µmol kg^{-1} and 0.3 µmol kg^{-1} in each test respectively, while comparing within the error of samples measured coulometrically (Huang *et al.*, 2015). This sensor had a sample time of 4 minutes, which would provide good temporal resolution.

1.4.6 Membrane Introduction Mass Spectrometry

In this method, a sample is acidified and the CO_2 diffuses across a gas permeable membrane before being measured by a mass spectrometer (Bell *et al.*, 2007; Bell, Short and Byrne, 2011). This work appears to be in the experimental phase, as no precision for DIC measurements have been reported but the system may have potential as it can measure a wide range of analytes such as fCO_2, CH_4, N_2, O_2, H_2S.

1.5 Overarching Thesis Aims and Sensor Design Overview

The focus of this study is on techniques developed for measuring DIC, with the aim to design and build an automated, full ocean depth, DIC sensor. As outlined in the previous sections, DIC is one of the key parameters to measure when investigating the oceanic carbonate system and a recent review of commercial technology available for ocean acidification research highlighted the lack of a DIC sensor, capable of making either underway or autonomous *in situ* measurements (Martz *et al.*, 2015), and other work has stated the need for a DIC sensor (Schuster *et al.*, 2009; Byrne, 2014; Bushinsky, Takeshita and Williams, 2019). By designing a DIC sensor that can be mounted on a range of platforms it will improve the coverage of DIC measurements and facilitate more experiments to increase our understanding of the carbonate system.

1.5.1 Sensor Requirements

The preceding sections have demonstrated a clear need for a DIC sensor, section 1.3 provided a review of sensor platforms and section 1.4 reviewed the current methods in development. The ideal DIC sensor should be designed to:

- Make precise and accurate measurements equivalent to "climatic" observations
- Be easily miniaturised
- Have low power demands
- Require low reagent volumes and create little waste
- Be suitable for deployment at depth
- Have a high sampling frequency
- Be capable of self-calibration, against certified reference materials

1.5.2 Lab On Chip

To meet these criteria, the design of the sensor in this work was based on a microfluidic "Lab On Chip" (LOC) design (Nightingale, Beaton and Mowlem, 2015). LOC systems have grown in popularity as rapid prototyping and replication of polymers has improved (Ohno, Tachikawa and Manz, 2008; Temiz *et al.*, 2015). Microfluidic systems allow samples in order of µL to be manipulated, and so, means small reagent volumes are required and chemical reactions can occur rapidly, thus reducing the power requirement of the sensor. The term microfluidics generally refers to systems operating on channels of width/height scales of order 100 nm to 100 µm and sample volumes measured in µL (Convery and Gadegaard, 2019). By utilising narrow channels, fluids move in laminar flow, which is more easily modelled than turbulent flow, allowing systems to be modelled before fabrication.

The LOC v3 hardware developed by the Ocean Technology and Engineering Group, National Oceanography Centre Southampton, has been altered and configured for a range of biogeochemical parameters (Beaton *et al.*, 2012; Clinton-Bailey *et al.*, 2017; Grand *et al.*, 2017). The development of the DIC sensor using this platform exploits the ~15 years of development that has resulted in robust LOC sensors capable of full ocean depth deployments. A Nitrate sensor based on this LOC design has recently been integrated into gliders (Vincent *et al.*, 2018) demonstrating the versatility of this system.

1.5.3 System Overview

The DIC LOC sensor was designed to operate in a similar manner to the sensors previously described (section 1.4). Specifically, the DIC in the sample is converted to CO_2 by acidification, the

degassed CO_2 then diffuses across a gas permeable membrane into an acceptor solution and the CO_2 reacts with the acceptor solution to produce a measureable electrochemical change, whose magnitude is related to the sample concentration of DIC, as shown in Figure 1.10.

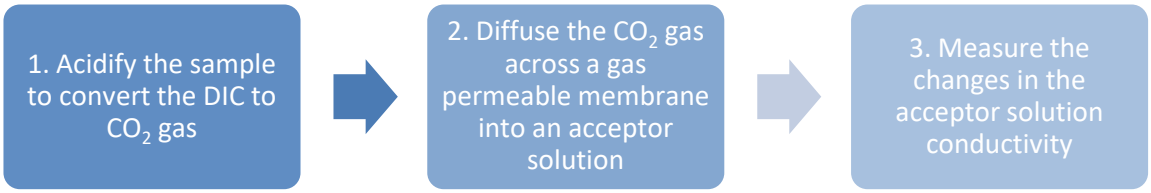

Figure 1.10 Flow diagram showing an overview of the sensor operation.

This system can be seen as thee modules, each of which was optimised individually, whilst ensuring they are easily integrated to make a compact sensor. The first module controls the acidification of the sample. The second module facilitates the CO_2 diffusion, and for this study is referred to as the Gas Exchange Unit (GEU). The third module is the detector that monitors changes in the acceptor solution.

In the GEU the acidified sample (referred to as the donor fluid) is separated from the acceptor solution by a gas permeable membrane. Diffusion across a membrane is a function of the membrane thickness, the surface area to volume ratio, concentration gradient and the membrane material property known as the diffusion coefficient (de Jong, Lammertink and Wessling, 2006) and by varying these properties the GEU can be optimised. The work carried out to design and optimise the GEU is detailed in Chapter 2.

The two most common methods of detection in development for DIC sensors use photometric detection (detailed in section 1.4.2) or conductometric detection (detailed in section 1.4.3). For this study, the conductometric method was chosen because it allows for sub-mL sample volumes to be measured, which facilitates rapid gas diffusion. Low sample volumes minimise the volumes of reagents required and waste created which results in low power requirements. Conductometric detection also relies on more readily available reagents, which unlike spectrophotometric indicators, do not need purifying. There is also a range of designs for conductometric detectors that can be used to optimise the measurement system. The theory, development and optimisation of the conductometric detector used in this study are detailed in Chapter 3.

Chapter 4 describes the integration of the modules to produce a benchtop instrument. Chapter 5 then details the miniaturisation of this benchtop instrument and presents field testing data collected using the DIC LOC sensor.

1.5.4 Engineering Concept

The Technology Readiness Level (TRL) framework was used in this work to assess the development of the DIC sensor. This framework provided the means to assess the maturity of the technology and also provided a roadmap for development. The framework was originally developed by NASA to allow comparisons of different technologies but has been adopted widely, including in the field of oceanic sensors (Waldmann *et al.*, 2010). The levels range from TRL 1 to TRL 9, which describe the transition from the initial idea phase to the final version proven by collecting data in deployments, detailed in Table 1.4. As such the levels provide a developmental roadmap that can be summarised more fully as: idea, to proof of concept, to benchtop instrument, to deployable prototype, to final product. This is the roadmap used for the development of the DIC sensor, with Chapters 2 and 3 focusing on development work up to TRL 3, Chapter 4 focusing on work to bring the sensor to TRL 4 and Chapter 5 detailing developments and deployments to reach TRL 6 and 7.

Table 1.4 The Technology Readiness Level roadmap adapted from Waldmann *et al.* (2010).

TRL	Detailed Description	Broad Roadmap Description
1	Basic principles observed and reported	Idea
2	Technology concept and/or application formulated	Proof of concept
3	Analytical and experimental critical function and/or characteristic proof of concept	
4	Component and/or breadboard validation in laboratory condition	Benchtop instrument
5	Component and/or breadboard validation in relevant environment	Deployable prototype
6	System/subsystem model or prototype demonstration in relevant environment	
7	System prototype demonstrated in ocean environment	
8	Actual system completed and “ocean mission qualified” through test and demonstration	
9	Actual system proven through successful deployment	Final product

Chapter 2 Design and Optimisation of the Gas Exchange Unit

2.1 Introduction

As described in section 1.5.3, the DIC LOC sensor developed in this work operates by acidifying a seawater sample, converting the DIC to CO_2 which then crosses a membrane into a NaOH solution where the CO_2 reacts with OH^- resulting in a measurable conductivity drop, the magnitude of which is related to the DIC concentration in the sample. The CO_2 exchange takes part in a module referred to as the Gas Exchange Unit (GEU). The GEU is an essential component of the sensor and this chapter details the optimisation work carried out to ensure efficient and rapid gas exchange. Initially various membranes were tested to determine their gas exchange properties. These results were then applied through modelling to estimate how long the gas exchange would take. Following this techniques for fabricating a GEU were evaluated before the final design was selected.

Membranes function as a semipermeable barrier separating two fluids whilst facilitating the exchange of selected solutes between them (Baker, 2012; Yampolskii and Finkelshtein, 2017), and as such they are used in a wide variety of systems (Abdelrasoul *et al.*, 2015). In this application the membrane separates the acidified seawater sample, referred to as the donor solution, from a NaOH solution, referred to as the acceptor solution, and CO_2 gas molecules are the species transported from the donor to the acceptor.

Membranes can be broadly categorised by their physical morphology, and described as either porous or dense (de Jong, Lammertink and Wessling, 2006). Porous membranes are characterised by many openings, or pores, that allow the transport of molecules that are smaller than the pore diameter to pass through the barrier. Due to concerns about whether these pores would deform (either rupturing to fully open or collapsing into a closed position) at the pressures of the deep ocean this work has mainly focused on non-porous dense membranes. Dense membranes rely on the transported species dissolving into the membrane to cross the barrier, in a process known as the solution-diffusion model, described in further detail in section 0.

2.1.1 Design Requirements and Considerations

When designing the GEU the objective was to have minimal gas exchange time, to maximise the potential measurement frequency. This is influenced by both physical and chemical properties of

the membrane, such as the membrane thickness and diffusion coefficients respectively. Reducing the sample volume can also be used as a method to reduce the gas exchange time, however this needs to be balanced by ensuring enough of the associated acceptor fluid, is used to match the volume of the detector. A lower volume also reduces the time required to fully flush the system, again increasing measurement frequency.

Another design consideration was the geometry of the GEU. There are two main geometries that have been previously applied in the development of DIC sensors (Byrne *et al.*, 2002; Pencharee *et al.*, 2012; Wang, Chu and Hoering, 2013; X. Liu *et al.*, 2013; Bresnahan and Martz, 2018). These can be broadly classified as planar GEU, where either a flat membrane is bonded or clamped between two fluid channels, or as Tube In A Tube (TIAT), where a tubular membrane is held within an impermeable tube, as illustrated in Figure 2.1.

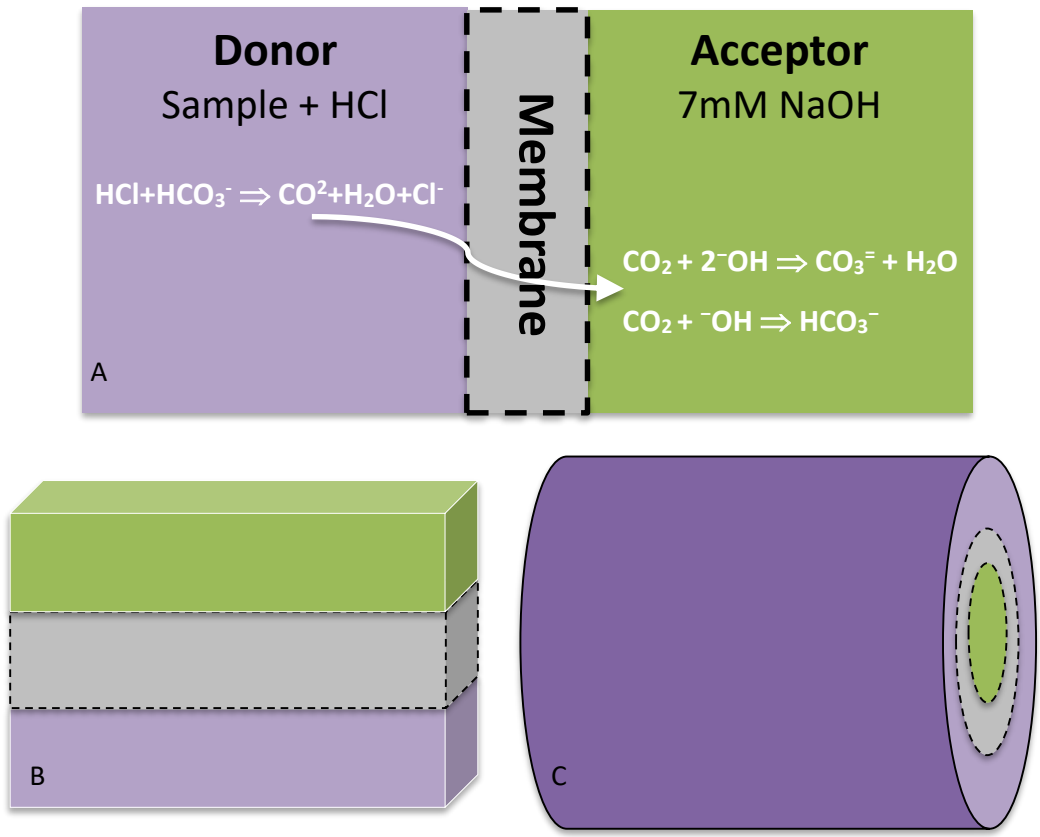

Figure 2.1 Schematic illustrating the different GEU geometries. Panel A depicts the reactions involved. Panel B shows a planar membrane with the membrane (grey) sandwiched between the acceptor (green) and the donor (purple). In Panel C a tube in a tube GEU is shown with the donor inside a tubular membrane, surrounded by the acceptor.

It is possible to build a TIAT system with multiple inner tubes in the core, known as a membrane contractor (Marzouk *et al.*, 2010; Singh R, 2015). A useful metric to consider when comparing different GEU systems is the surface area to volume ratio because enhancing this ratio can

facilitate a faster exchange of gas. TIAT systems have been suggested as having a geometry which enhances the surface area to volume ratio (Bresnahan and Martz, 2018) however similar ratios can be achieved in planar systems using shallow and wide channels.

2.1.2 Gas Transport Across Membranes: The Solution-Diffusion Model

Transport across a dense membrane is driven by molecular diffusion and has been described by the solution-diffusion model (Wijmans and Baker, 1995; Baker, 2012). In this model the transported species dissolve into the membrane to cross from high concentration in the donor solution to the low concentration in the acceptor solution. The transported molecules dissolve into the free space between the polymer chains in order to traverse membrane. The free spaces are < 5 – 10 Å, in membranes with larger pores the flow is dominated by pore-flow transport (Baker, 2012). The differences in the solubility of the transported species in the membrane give the membrane its semi-permeable property. This is a material specific property known as the diffusion coefficient.

The diffusion coefficient varies between the transported species, and membrane materials, a property which can be used to separate species (Baker, 2012). Fick's Law describes this diffusion system:

$$J_i = -D_i \frac{dc_i}{dx}, \tag{2.1}$$

where J_i is the flux density of transport of the species *i* (moles cm^{-2} s^{-1}), D_i is the diffusion coefficient (cm^2 s^{-1}), dc_i is the concentration gradient (moles cm^{-3} cm^{-1}) and *dx* is the membrane thickness (cm).

The diffusion coefficient is specific to the species and the membrane material. If the membrane area, thickness and flux density are known then D_i can be determined experimentally by rearranging Fick's Law to:

$$D_i = \frac{J_i \times dx}{dc_i} \tag{2.2}$$

Four different membrane materials were studied to determine their physical characteristics, as described in section 2.2. The physical characteristics were then used to model the design of a GEU, described in section 2.3.1.

2.2 Determination of Diffusion Coefficient

Experimental determination of the gas diffusion coefficient for CO_2, D, was conducted to facilitate modelling of the GEU that was then used to estimate the time scales for the gas exchange to occur. This initial testing was also utilised to establish which membrane geometries could be readily incorporated into a LOC sensor. This was achieved by comparing TIAT and planar GEU geometries. Details of the four membranes investigated are listed in Table 2.1. Polydimethylsiloxane (PDMS) is widely used in the development of microfluidic "Lab On Chip" (LOC) systems as it is easy to manufacture, low cost, bonds readily to itself and glass, is biocompatible and is gas permeable. Its gas permeability properties mean that it has been widely used as a membrane (Yeom, Lee and Lee, 2000; Cardenas-Valencia *et al.*, 2013; Nguyen, Leho and Esser-Kahn, 2013; Mäki *et al.*, 2015).

Table 2.1 Physical characteristics of the four membranes initially trialled.

	Wall Thickness µm	**Porous**	**Geometry**	**Supplier**
Accurel® PP Q3/2	200	Yes	Tube in a tube	Membrana GmbH, Germany
Teflon™ AF2400	300	No	Tube in a tube	BioGeneral, USA
Asos™ Zeus ePTFE	350	Yes	Clamped Planar Membrane	Zeus Inc., USA
PermSelect® Tinymodule (PDMS)	55	No	Multi-core tube in a tube (commercially available)	PermSelect, USA

To calculate the diffusion coefficient, using equation 2.2, a sodium bicarbonate sample solution was acidified in various GEUs, and the CO_2 gas crossed membranes of known thicknesses into an acceptor stream whose conductivity was recorded. As the membrane thickness and CO_2 concentrations were known, and the CO_2 flux density was determined from a calibration, D_i could be estimated.

The measurement was achieved by acidifying a 3 mL sample loop of solution, which was re-circulated through the GEU, where the CO_2 gas was diffused into the acceptor solution, as shown in Figure 2.2.

A

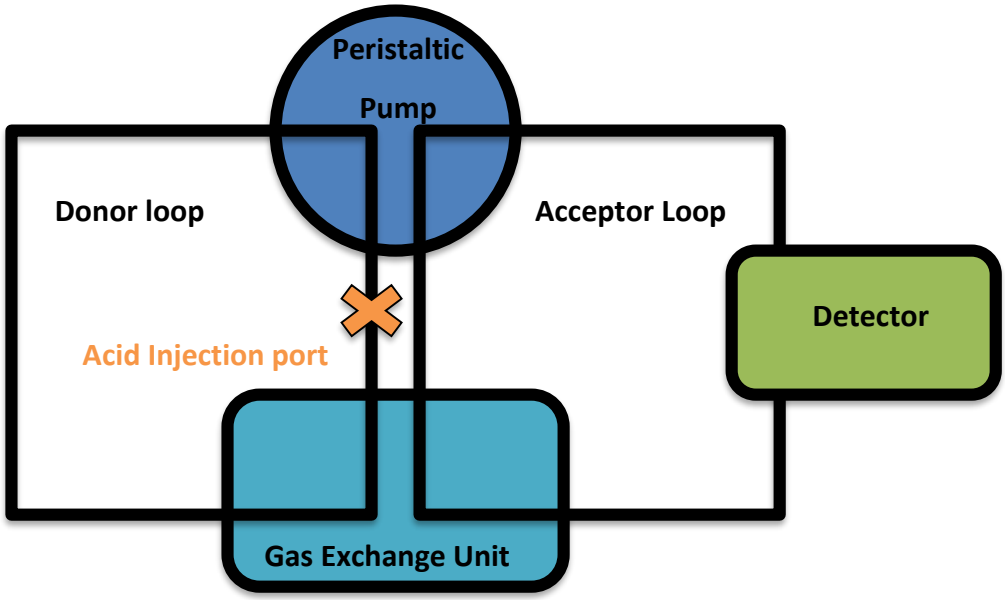

B

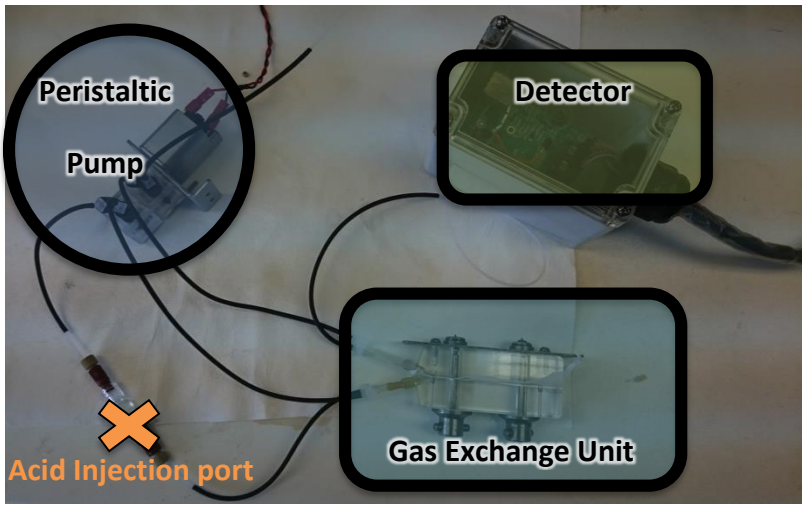

Figure 2.2 Setup for membrane characterisation rig. Panel A is a schematic of the set up. Panel B shows a photo of the system. All the components apart from the pumps were submerged in a water bath (not shown for clarity). The GEU shown is the planar system, though the TIAT system was also tested using this rig.

A stock solution of 2500 µmol kg^{-1} sodium bicarbonate (Fisher Scientific, UK) was used as the sample. The 50 µL 3 M HCl was used to acidify the sample and this was made by a volumetric dilution of 12 M reagent grade HCl (Sigma Aldrich, UK). The acceptor solution was made by volumetric dilution of a 0.1 M NaOH (Sigma Aldrich, UK) working solution to reach a 7 mM concentration. The acid was injected into the sample loop using a syringe pump (Nanomite, Harvard Apparatus UK) via an inline septum (Thistle Scientific, Glasgow). Both the acceptor and donor solutions were re-circulated for 15 minutes at ~1 mL min^{-1} by a peristaltic pump (100 series, 35 rpm, 12v DC, with Viton® tubing, Williamson Manufacturing Company UK). The tubing material

used for the donor and acceptor loops was Viton® tubing with 1/16" (1600 µm) ID and 1/8" (3175 µm) OD (Cole-Palmer, UK) which was chosen due to its low permeability for CO_2. The CO_2 permeability for Viton® was 77 barrer compared to 360 barrer for Tygon® tubing, or 20,000 barrer for PDMS, from their respective manufactures datasheets (1 barrer = 1 $\frac{\text{g cm}}{\text{s cm}^2 \text{ bar}}$).

The conductivity of the acceptor solution was recorded by a custom conductivity detector produced by eDAQ Pty Ltd, Australia, which logged voltage proportional to the conductivity of the acceptor solution for the duration of each run, this system is fully described in Chapter 3. The experiment was conducted in a constant temperature water bath (Grant TX150, UK) held at 25 °C, to prevent temperature fluctuations influencing the conductivity measurements, as detailed in section 3.1.1. Before and after each run the membrane was checked for leaks by acidifying a sample of Milli-Q® water (Merck Sigma, USA) and ensuring the acceptor conductivity and pH did not change. The pH of the acceptor solution was checked after the addition of acid using simple pH test strips (Sigma Aldrich, UK).

Over the course of the measurement the conductivity of the acceptor solution dropped as the CO_2 reacted with the NaOH solution. The CO_2 flux density was estimated by comparing the recorded conductivity changes to a calibration of the detector. The flux density was estimated when the diffusion was not limited by concentration gradients, which was when the change in conductivity was linear as seen in Figure 2.3. This prevents the calculated diffusion coefficient being limited by a reduction in the concentration gradient. The diffusion coefficients are summarised in Table 2.2.

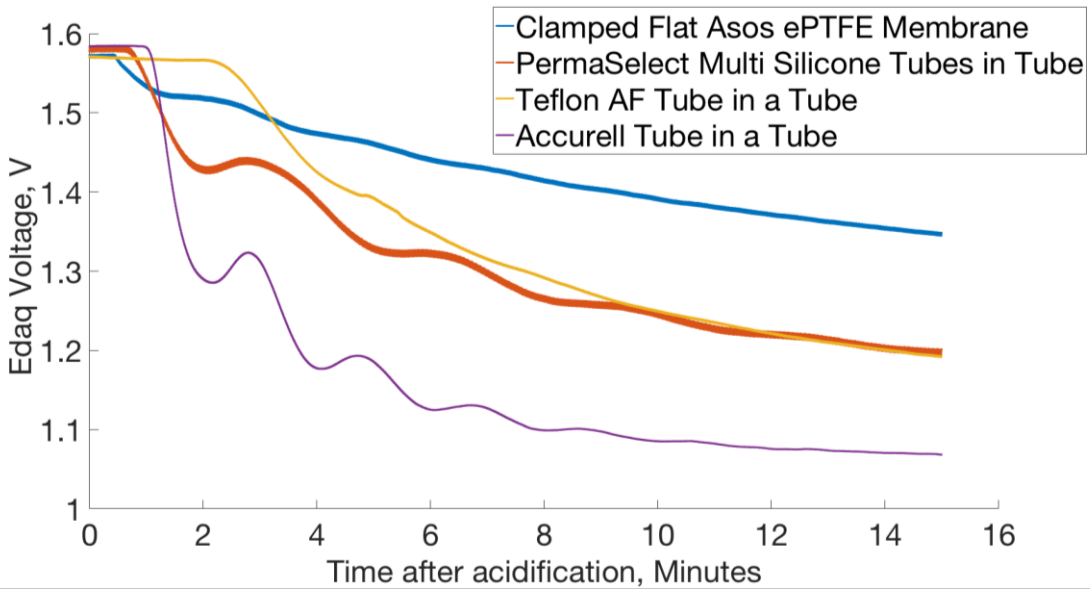

Figure 2.3 Conductivity voltage data from the eDAQ detector for the four membranes tested. The time where diffusion was not limited by the concentration gradient is the initial drop in voltages between 0.5 and 4 minutes after acidification, where the conductivity drop is approximately linear.

Table 2.2: Summary of results from diffusion coefficient testing combined with physical membrane properties.

	Diffusion Coefficient ($cm^2\ s^{-1}$)	**Porous**	**Geometry**	**Surface Area to Volume Ratio** ($\mu L\ mm^{-1}$)
Accurel® PP Q3/2	4.7E-05	Yes	Tube in a tube	2.9
Teflon™ AF2400	9.1E-06	No	Tube in a tube	10.8
Asos™ Zeus ePTFE	9.8E-07	Yes	Clamped Planar Membrane	0.8
PermSelect® Tinymodule (PDMS)	5.8E-06	No	Multi-core tube in a tube (commercially available)	3.6

Table 2.2 shows the diffusion coefficients calculated for the membranes tested. The membrane with the optimal diffusion coefficient, facilitating the most rapid gas exchange, was the porous membrane Accurel® PP Q3/2. Despite this performance the material was not considered further in the GEU design process due to uncertainties about how the pores would perform at high pressure, such as in the deep ocean. There was a concern that the pores could either rupture or collapse. If the pores ruptured it would result in mixing of the donor and acceptor solutions, leading to a failure of the sensor. If the pores collapsed the gas exchange would be less efficient, or halted completely, resulting in failed measurements. This membrane could be considered if the system was for surface oceanic measurements only, however as the goal for this sensor was to be rated for full ocean deployment both porous membranes were removed from consideration. Future testing could be carried out to determine if the pores do deform and then used to define a depth limit for membrane style.

The experimentally determined value of the diffusion coefficient for PermSelect® Tinymodule (PDMS) was within one order of magnitude of the results from the literature for other PDMS membranes, detailed in Table 2.3 (Merkel *et al.*, 2000; Kanehashi *et al.*, 2014; Mäki *et al.*, 2015). The value for Teflon™ AF2400 was close to that of PDMS and both were incorporated in to modelling as described in section 2.3.1. This result is interesting as the gas permeability data for PDMS and Teflon™ AF2400 from the literature and the manufactures specifications show that

Teflon™ AF2400 has a higher gas permeability, with a value of 2800 barrer, according to the manufactures datasheet, compared to 200 − 1800 barrer depending on PDMS composition (Lamberti, Marasso and Cocuzza, 2014) .

Table 2.3 Diffusion coefficients for PDMS from the literature.

Diffusion Coefficient $cm^2\ s^{-1}$	**Reference**
4.2×10^{-5}	Mäki *et al.* (2015)
2.0×10^{-5}	Kanehashi *et al.* (2014)
2.2×10^{-5}	Merkel *et al.* (2000)

The Asos™ ePTFE had the lowest calculated gas diffusion coefficient and also took the longest time to reach equilibrium. This planar membrane was clamped between two blocks, one with a channel for the donor and the opposite channel for the acceptor. These channels were relatively deep, ~3 mm, which may have limited cross channel mixing. This combined with the low surface area to volume ratio may have impacted the efficiency of this unit. For these reasons this calculated diffusion coefficient may be an underestimation. Altering the channel design, to reduce the channel volumes and encourage mixing, could improve the efficiency of the design and would be testable in the future. The clamped membrane rig experienced more leaks than the TIAT systems, which once assembled were robust enough to stand up to multiple months of testing. This finding highlighted an advantage of using a TIAT GEU.

Previous research (Bresnahan and Martz, 2018) has suggested that TIAT systems can be used to increase the surface area to volume ratio (or “aspect ratio”) however the surface area to volume ratio can also be enhanced by designing shallow, wide microfluidic channels which can be manufactured reproducibly using micro-milling. Section 2.3.2 provides details of a bonding technique that was developed with the aim of using wide shallow channels to create a planar membrane with the same surface area to volume ratio as the TIAT.

2.3 Planar Membrane Investigation

Section 2.2 details experimentally determined diffusion coefficients for PDMS and Teflon™ AF2400. Both of these materials are available in thin sheets, so could potentially be used as a membrane in a planar GEU. This section details work that investigated whether planar membranes had the potential to be integrated in to the DIC LOC sensor.

2.3.1 Planar Membrane Modelling

Modelling of a planar membrane system was carried out to confirm that the gas exchange times for a PDMS or Teflon™ AF2400 planar membrane were of an appropriate order of magnitude before a GEU was designed and fabricated. To maximise the sensor's measurement frequency the gas exchange needs to be of the order of seconds to minutes.

COMSOL Multiphysics® 5.2 Software was used to model gas exchange across a planar membrane, the system's geometry is shown in Figure 2.4. The system was modelled as two 'U' shaped channels separated by a 100 µm thick membrane. The channel dimensions were based on the channel size that could be milled by the Datron Neo (Datron, Germany) micro-milling machine used for LOC fabrication. The surface area to volume ratio for this system was 4 mm^{-1}, comparable to the 2.8 mm^{-1} for one of the TIAT systems tested and five times greater than that of the first planar system tested in section 2.2. One channel contained the donor fluid with the concentration set to 1 arbitrary unit at the inflow, and the other contained the acceptor whose concentration was set to 0. The concentration measured at the outlet of the acceptor after 15 seconds was used to assess the gas exchange.

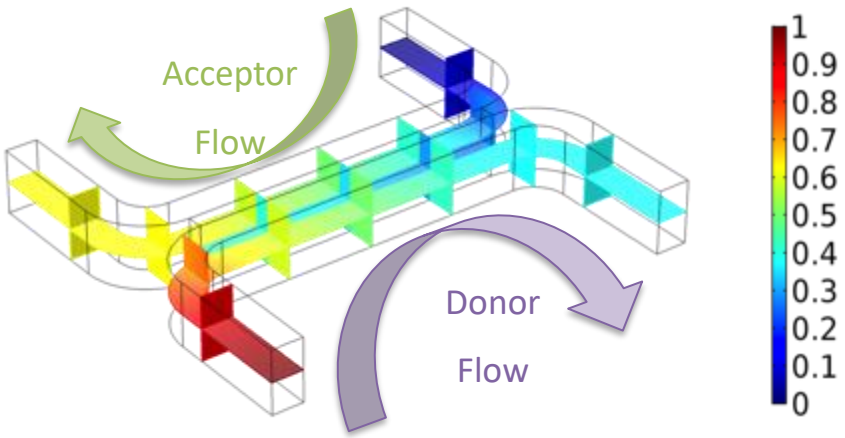

Figure 2.4 Overview of the COMSOL Multiphysics® model. Warm colours show high concentrations and cool colours show low concentrations. The arrows indicate the fluid flow directions and illustrate the counter circulating flow.

The COMSOL model used the laminar flow module to describe the fluid flow in the channels and the transport of diluted species module to describe the diffusion across the membrane. As described in section 1.5.2 the flow within microfluidic channels is laminar, which reduces the modelling complexity. Previous studies have found that relative direction of the acceptor and donor flow impacted the time taken for gas exchange, finding that flowing the fluids in opposite

directions maintained a maximum concentration gradient so encouraged rapid gas exchange (Wang, Chu and Hoering, 2013). For this reason the model was setup to drive the fluids' flow in opposite directions to give a counter circulation.

Two values for the diffusion coefficient (D) of the membrane were used in the modelling. The lower D was the lowest from the membrane characterisation experiment for Teflon™ AF2400 (Table 2.2) and the higher D for PDMS was taken from the literature (Table 2.3). This covered the range of options that were identified as potential materials in section 2.2. The model estimated that using the value of D for PDMS from the literature this GEU would achieve 99.5% gas exchange in less than 15 seconds. Using the value of D for the Teflon™ AF2400 gave 97.8% exchange in less than 15 seconds. This result compared well to 2D modelling carried out within OTEG, which predicted ~15 seconds for gas exchange in a similar set up.

A limitation of this basic model was that the CO_2 was not consumed on the acceptor side. In the real system the CO_2 rapidly reacts with the NaOH, maintaining the maximum concentration gradient possible, provided there is an excess of NaOH. This means the model may have reached a state where the exchange rate was reduced as the concentration gradient was reduced; the result of this limitation is that the model may estimate a longer gas exchange time or lower efficiency.

The rapid gas exchange predicted by this modelling confirmed that a planar membrane had the potential to provide the fast gas exchange required by this sensor. Following on from this result work was carried out to investigate suitable bonding methods for sealing a PDMS sheet into a planar GEU.

2.3.2 Planar Membrane Bonding

A planar GEU can be visualised as a sandwich with a membrane as the filling between two layers that contain the fluid channels, as shown in the diagram in Figure 2.5. For a planar membrane to be readily incorporated into a GEU it needs to be bonded to seal the unit and prevent leaks (Temiz *et al.*, 2015). The initial modelling results demonstrated that a planar sheet of PDMS could be a viable membrane, capable of facilitating a rapid gas exchange. Poly(methyl methacrylate) (PMMA) is a popular material for LOC systems as it is easily machined and forms good seals when layers are bonded together (Ogilvie *et al.*, 2010; Temiz *et al.*, 2015).

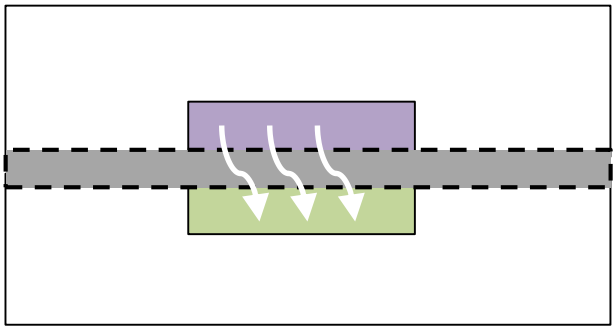

Figure 2.5 Cross section of a planar membrane with channels. The clear area represents the PMMA chip; the grey layer with a dashed outline is the PDMS; the coloured rectangles show the fluid channels, and the gas exchange is represented by the white arrows.

PMMA and PDMS do not readily bond, which presents a challenge for integrating a PDMS membrane into a PMMA LOC, however several studies have developed techniques for altering the surface chemistry of both PDMS and PMMA to achieve robust bonding (Kim, Park and Yang, 2010; Tang and Lee, 2010; Johnston *et al.*, 2014).

These methods all followed similar steps to alter the surface chemistry of the PMMA and PDMS in order to chemically bond the two materials. The first step is to activate the PMMA to generate hydroxyl groups on the PMMA surface. These are then exposed to, and react with, the amine groups of either aminopropyltriethoxysilane (ATPES) or 3-Glycidoxypropyltriethoxysilane (GPTES) to form amide bonds. Before the PDMS is mated with the PMMA, the surface of the PMMA is also activated to generate hydroxyl groups on its surface. The activation of the PMMA was achieved by exposure to oxygen plasma or to UV-Ozone.

Initial work was conducted to compare three published bonding methods by bonding PDMS to laser cut squares of PMMA. After an initial method was selected, more complex proto-chips were manufactured by cutting channels into 6 × 10 cm PMMA chips using a laser cutter. These proto-chips were bonded by modifying the initial technique and their surfaces were analysed with a profilometer.

2.3.2.1 Initial Bonding Technique Comparison

The methods for bonding PDMS to PMMA described in three papers were tested and summarised in Table 2.4. To test each method a 50 mm square of PDMS was bonded to a 30 mm square of PMMA. To test whether bonding was achieved a peel test was used. The peel test involved using the overhanging PDMS tab to attempt to peel the PDMS off the PMMA (Figure 2.6, Panel B). If the

tab ripped without removing the membrane the bond was demonstrated to be stronger than the tear strength of the PDMS.

Thin sheets of PDMS were purchased (SILEX Silicones Ltd, UK) and bonding was tested using 50 µm, 100 µm and 250 µm thick sheets. The thickest sheets were tested initially and the thinner sheets were used for further testing. The APTES and GPTES reagents listed in Table 2.4 were from Sigma Aldrich, UK.

Table 2.4 Summary of the PDMS – PMMA bonding methods trialled from the literature.

Author and Year	Method Steps
Tang and Lee (2010)	1. Oxygen plasma treat the PDMS and PMMA (1 min, 50-60 W) to generate hydroxyls on both surfaces 2. Apply 1%(v/v) aqueous APTES to PDMS and GPTES to PMMA for 20 min to generate surface amine and epoxy functions 3. MQ rinse and dry both the PDMS and PMMA 4. Bond by bringing surfaces together for one hour at room temperature to form an amine-epoxy bond
Kim, Park and Yang (2010)	1. PMMA cleaned with IPA 2. Oxygen plasma treat the PMMA (1 min, 200 W) 3. PMMA submerged into 5% 3-APTES (heated to 85 ^{o}C for 1 min, and dried with N_2 gas) 4. Hold PMMA at 65 ^{o}C for 10 min in atmosphere to stabilise the self-assembled layer 5. PMMA and PDMS surface treated by oxygen plasma treatment 6. Surfaces mated and held together in oven at 65 ^{o}C for 2 hours
Johnston et al. (2014)	1. IPA to clean the PMMA 2. Dry the PMMA with N_2 gas 3. UV-Ozone treat the PMMA for 30 minutes, using a PSD-UVT system (Novoscan, USA) 4. Expose the PMMA to APTES vapour at 60 ^{o}C for 1.5 hours (Figure 2.6, Panel A) 5. Rinse the PMMA with MQ and N_2 dry 6. Ozone treat the PDMS for 15 minutes 7. Mate the PDMS and PMMA and clamp at 60 ^{o}C for 12 hours minimum

Of the three tested methods only the method described by Johnston *et al.* (2014) achieved a bond that passed the peel test for the 250 µm membrane. After passing the peel test a PMMA – PDMS – PMMA sandwich was fabricated using the same method to ensure that the bonding method would be stackable and verify that repeating the process did not cause the initial bond to fail. This also passed the peel test. Following this the thinner PDMS sheets (50 µm and 100 µm thick) were successfully bonded using the same method.

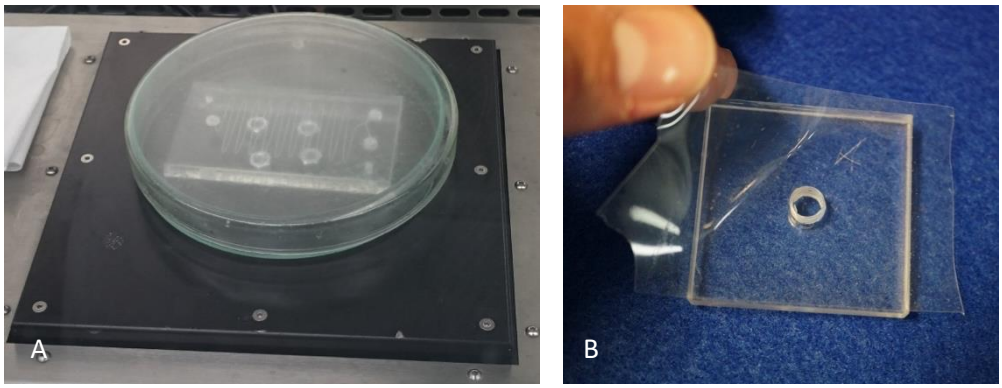

Figure 2.6 Photos highlighting two steps in the bonding process. Panel A shows a test chip being exposed to APTES vapour on a hot plate at 60 °C. Panel B shows a partially bonded test square. Approximately 75% of the square achieved bonding, this was classified as a failure to bond.

The PMMA – PDMS – PMMA sandwich test confirmed that the 50 µm sheets of the PDMS material were a potentially viable membrane material. During the testing it was observed that some of the attempts failed at the edges of the PMMA but were more successfully bonded in the centre. This failure suggested that the PMMA squares potentially had imperfections along the edges that prevented a proper bond from forming. Upon visual inspection it appeared that the top surfaces of the laser cut chips had ridges, or burrs, which impeded the bonding. The burrs, and how to limit them, was further investigated and discussed in the following section.

2.3.2.2 Optimising Laser Cutting of Test Chips for Bonding

After the initial bonding technique was selected further tests were carried out on larger PMMA chips to ensure that the technique was scalable. Some of the initial failures appeared to be the result of burrs that were formed as an artefact of the laser cutting preventing the clamped PDMS from being held flush against the PMMA. Several different laser-cutting powers were trialled to minimise the formation of these burrs, which were measured using a profilometer.

To optimise the bonding technique laser cut test chips were cut and bonded. These were used in place of micro-milled chips as these could be rapidly produced. One laser cut chip could be produced in a minute, faster than a chip produced by the precision mill. While the milled chips are more accurate and repeatedly manufactured, the laser cut chips provided a quick test material. A laser cutter (Speedy 400, Trotec Laser, UK) was used to engrave channels on 60 × 100 mm clear PMMA chips. Clear PMMA was chosen to allow visual inspection of the bond. Various power and speed combinations were tested to cut chips and engrave channels. The channels were investigated using a Zeta-20 profilometer (KLA-Tencor, USA) to ensure that the chosen settings

would create channels deep and wide enough to be analogous to the channels created using the micro-milling machine, while also ensuring that the edges of the cuts were smooth (without ridges that could interfere with bonding). The profilometer was also utilised to assess the chip surface before and after bonding, an example of the data collected is shown in Figure 2.7.

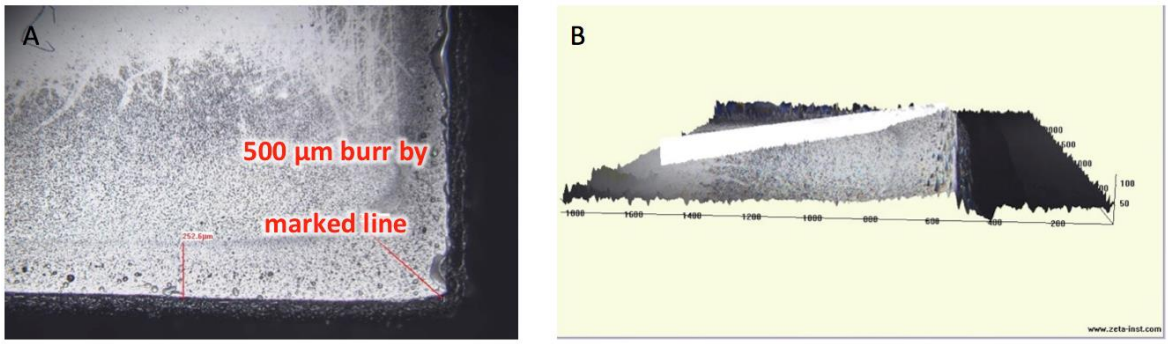

Figure 2.7 Example images from the profilometer showing an example of a burr on the corner of a laser cut chip. Panel A shows a plan view of the chip corner, with burr along the chip edge. Panel B shows the same corner viewed at an angle, with the burr raising up to the corner.

In order to minimise the burrs caused by laser cutting 13 different power and frequency settings were used to make straight and circular cuts in PMMA. These cuts were then viewed using a profilometer to assess the height of any burrs formed. Burrs were measured at two corners and averaged to assess the laser settings and the burr around the circular cut was also measured. The results of these measurements are presented in Table 2.5.

Table 2.5 Laser cutter settings tested to reduce burr formation.

	Laser Settings				Result		
	Power %	**Speed**	**Passes**	**Frequency** kHz	**Cut Success**	**Straight Cut Edge Burr Notes**	**Hole Cut Burr Height**
1	100	0.35	2	1	Yes	600 µm wide 50 µm height	Circular hole – up to 100 µm burr
2	100	0.6	3	10	Yes	600 µm wide 50 µm height	35 µm
3	50	0.6	3	10	Partially	600 µm wide 50 µm height	80 µm
4	40	0.8	4	10	No	-	-
5	30	0.6	4	10	No	-	-
6	100	0.35	2	10	Yes	500 µm wide 40 µm height	Elliptical cut
7	50	0.5	3	10	Yes	560 µm wide 35 µm height	90 µm
8	40	0.5	3	10	No	-	-
9	40	0.5	4	10	Yes	540 µm wide 45 µm height	95 µm
10	40	0.45	4	10	Yes	540 µm wide 35 µm height	110 µm
11	50	0.65	4	10	Yes	540 µm wide 630 µm height	110 µm
12	80	0.6	4	10	Yes	580 µm wide 35 µm height	50 µm
13	40	0.4	4	10	Yes	580 µm wide 40 µm height	60 µm ridge, elliptical hole

Each of the settings tested to cut the chips produced a burr to some extent; however setting group 2 (power 100%, speed 0.6, passes 3, frequency 10 kHz) produced the smallest ridge around the hole and low corner burrs so this setting was used for future testing. To test whether a deburring tool could remove the burr and improve the bonding a chip was cut, and its burrs

measured on the profilometer, shown in Figure 2.8 Panels A and B. Then the burrs were removed using a Noga 1003 deburring tool (RS Components, UK) and the surface was measured again. The deburring tool removed the 40 µm burr and an extra 200 µm of material, shown in Figure 2.8 Panels C and D. This deburred chip was then successfully bonded to a thin PDMS membrane, using the method from section 2.3.2.1.

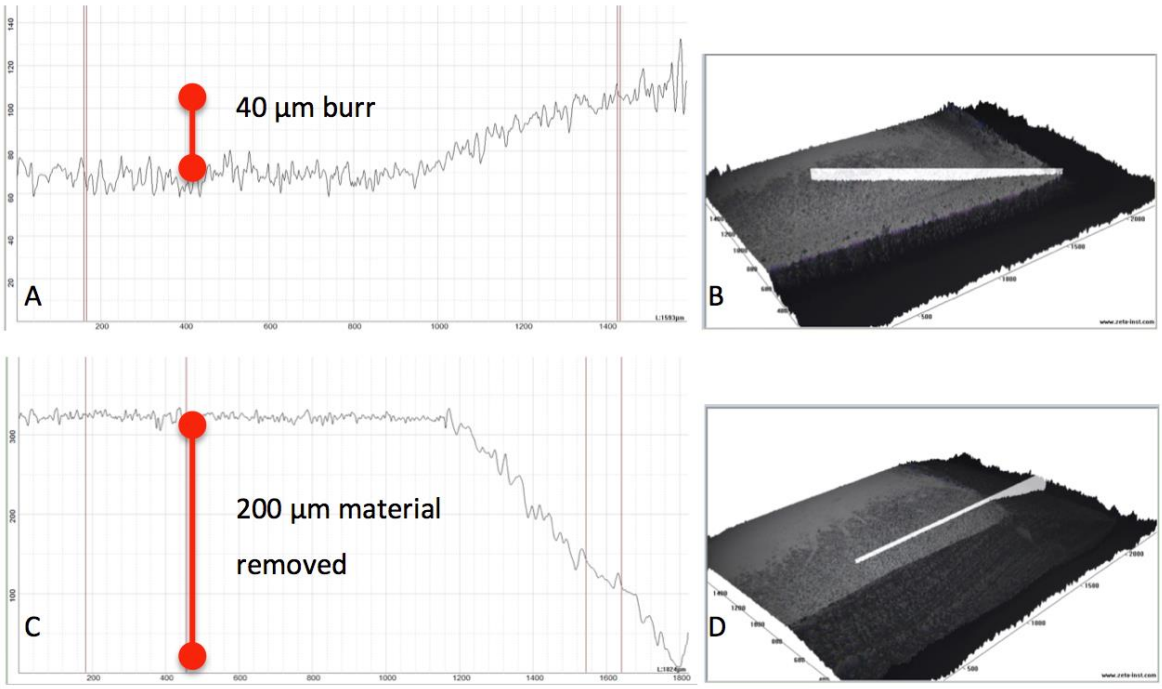

Figure 2.8 Profilometer images from before and after deburring. Panel A shows the profile of a laser cut PMMA chip. Panel B shows an image of the corner with the burr rising to the right. Panel C shows the profile after deburring. Panel D shows an angle image taken after the burr was removed.

To study the effect the laser settings had on the laser engraved channels five different power settings were tested. Each setting produced a channel, with an example shown in Figure 2.9. The settings tested are detailed in Table 2.6, along with the results of the measurements taken with the profilometer.

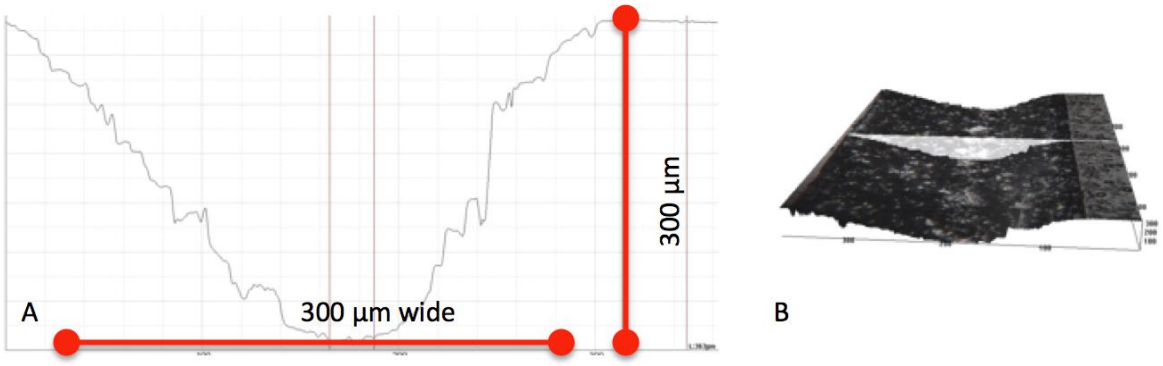

Figure 2.9 Laser cut channel profile example. Panel A shows the cross section of a channel. Panel B shows a view of the channel, with the white line marking the position the cross section is taken from.

Table 2.6 Laser cutter settings and measured channel dimensions.

	Laser Settings					Results		
	Power	**Speed**	**DPI or Frequency**	**Passes**	**Engrave or Cut**	**Channel Depth**	**Channel Height**	**Notes**
1	55%	1000	500 PPI	1	Engrave	63 µm	190 µm	Slightly Stepped Channel
2	10%	0.9	10 kHz	1	Cut	324 µm	300 µm	Smooth Symmetric Channel
3	5%	0.9	10 kHz	1	Cut	28 µm	165 µm	Rougher Channel
4	10%	2	10 kHz	1	Cut	150 µm	270 µm	Asymmetric Channel
5	10%	0.9	1 kHz	1	Cut	510 µm	340 µm	Rough Channel and Burr on Edge

The laser settings that gave the smoothest channels, and with dimensions close to those achieved with the micro-mill, were group 2 (power 10, speed 0.9, 1 pass, frequency 10 kHz). These settings were used to cut multiple test chips that were then bonded while the method was modified.

2.3.2.3 Optimising the Bonding Technique

Multiple pairs of PMMA chips were cut using the optimal settings found in section 2.3.2.2. These were bonded using variations on the Johnston *et al.* (2014) method. The optimisation focused on the way the PMMA was exposed to the APTES. In initial tests the chips were submerged into

diluted APTES. This technique failed to bond consistently, and it was suspected that submerging the PMMA was not resulting in an even coating. In the next tests the APTES was applied to the PMMA using a cotton bud. This application technique also produced a high failure rate, potentially due to contamination from particles shed from the cotton bud. For the next application technique the PMMA chip was exposed to APTES vapour. In the initial test the PMMA chip was placed in a glass dish and 200 µl of APTES was pipetted around the dish, which was then sealed and placed on a 60 ^{o}C hotplate (Electronic Micro Systems Ltd, UK) for 90 minutes. This method produced more successful bonds than the previous methods. A further modification to the method was to raise the PMMA chip off the glass dish by placing it on six stainless steel M6 nuts. Raising the chip prevented any of the APTES from being drawn under the chip, in a capillary action. This application method produced the most repeatable bonding so was used to bond six pairs of micro-milled GEU chips (Figure 2.10). These had a bonding success rate of 50%. The typical failure was that one side would fail to bond fully. The chips that bonded successfully were used for multiple months before the bonds failed. One of the successfully bonded planar GEUs was utilised in a benchtop instrument. This benchtop instrument is described further in sections 3.5.2 and 4.2.

Further work is being undertaken to improve the bonding success rate. One area under investigation is whether improved clamping during the bond formation stage might aid the formation of a uniform bond. Another area being investigated is whether a more thorough cleaning of the PMMA before the APTES application impacts the strength of the bond.

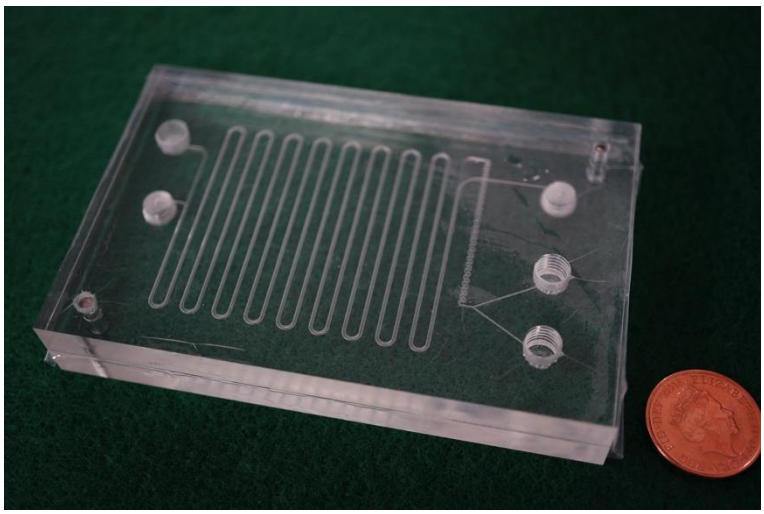

Figure 2.10 A successfully bonded milled chip. One pence coin for scale.

2.4 Tube in a Tube Gas Exchange Unit

Many of the previously developed DIC sensors in the literature utilised a TIAT design for a GEU (Byrne *et al.*, 2002; Wang *et al.*, 2007, 2015; Pencharee *et al.*, 2012; Wang, Chu and Hoering, 2013; Bresnahan and Martz, 2018). There are many advantages to using a TIAT, which is most likely why the design has been widely used. As described in the introduction it is possible to achieve high surface area to volume ratios using TIATs. Over the course of the initial testing described in section 2.2 the TIAT was found to be more robust than the planar membranes. The initial testing also demonstrated that a TIAT system can be constructed more simply and rapidly than a planar bonded system. A TIAT can be fabricated in less than 30 minutes, without the complex bonding steps which leads to the fabrication of a planar system taking over two days (section 2.3.2). Over the course of the testing TIATs suffered far fewer failures than the bonded GEU. Depending on the failure method the TIAT could also be repaired, which was a clear advantage over the bonded GEU system, which could not be repaired. A further advantage of a TIAT is that simply varying its length can alter its volume, allowing the volume of the TIAT to be matched to the volume of the detector. Altering the diameter of the inner tube also allows the volume ratio of acceptor to donor to be easily modified. Due to these many benefits, a TIAT was selected as the GEU for the final version of the DIC LOC sensor, described fully in Chapter 5.

A cross section of the TIAT is shown in Figure 2.11. For the outer tubing and fittings Polyether ether ketone (PEEK) was selected as it has a low CO_2 diffusion coefficient, 1.3×10^{-8} cm^2s^{-1} as listed in the material datasheet. For the initial characterisation work the Teflon™ AF2400 had a membrane thickness of ~300 µm, with tube dimensions of 810 µm Outer Diameter (OD), 200 µm Inner Diameter (ID). The PEEK outer tubing had dimensions of ~1600 µm OD and ~1400 µm ID, this gave a volume ratio of the outer to inner tube of 9 : 1. This ratio alters the relative flow rates of the acceptor and donor, which could have been a potential way to increase the time for gas exchange, however this PEEK was found to kink if too great a bend was applied to it, so a more robust PEEK with thicker walls was selected for the final version.

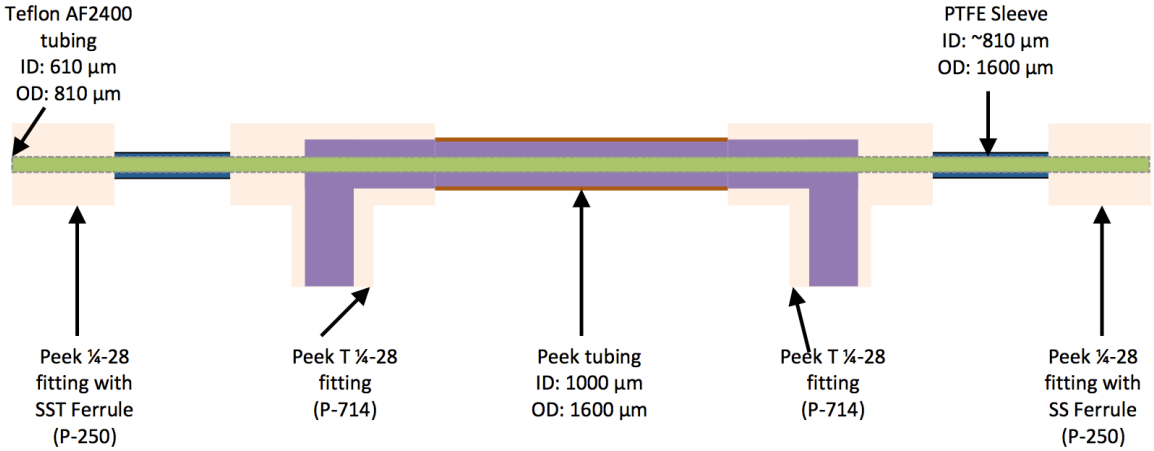

Figure 2.11 Cross sectional schematic of a TIAT. The purple line represents the acidified sample donor solution. The green line represents the NaOH acceptor solution, inside the Teflon™ AF2400. The pale orange areas represent the PEEK fittings and the brown section shows the outer PEEK tubing, not to scale.

Reducing the thickness of the membrane would reduce the time taken for gas exchange to occur so two thinner Teflon™ AF2400 membranes were investigated. The thinnest tested had a wall thickness of ~70 µm, with dimensions of 740 µm OD and 610 µm ID. As noted in the modelling work in section 2.3.1, previous studies had stated that flowing the acceptor and donor in opposite directions reduced the time taken for gas exchange (Wang, Chu and Hoering, 2013). For this reason a quick investigation was conducted into the impact of the relative flow direction of the acceptor and donor using this membrane. A 1500 mm long TIAT was constructed with a PEEK outer tubing with an ~1600 µm OD and ~1400 ID µm, this gave a volume ratio of 4 : 1 for the outer to inner tubes. For this test a 2000 µmol kg^{-1} sodium bicarbonate solution was used as a sample, which was acidified using 1 M HCl in the inner tube. The acceptor solution was 7 mM NaOH and flowed in the outer tube. The conductivity of the acceptor solution was measured an early version of the detector, described in section 3.2. The length of time between the beginning of the acidification and the time of the minimum conductivity recorded by the detector was used to assess the rate of the gas exchange. Four replicate measurements were taken for both fluids flowing in the same direction (parallel flow) and in the opposite direction (counter flow), and the results are presented in Table 2.7. This found that counter circulation of the acceptor and donor fluids reduced the time for gas exchange by one third. For this reason, counter circulation of the acceptor and donor was used in all of the work described in this work.

Table 2.7 Results from investigation into impact of relative flow direction on gas exchange time.

	Time from sample acidification to minimum conductivity recorded, minutes				
	1	**2**	**3**	**4**	**Average**
Parallel Circulation	20.0	21.5	23.6	20.3	**21.4**
Counter Circulation	14.8	12.5	15.6	13.0	**14**

The 70 µm thin walled Teflon™ AF2400 was found to be much less robust, and would easily bend and buckle, so was not used in the final sensor. This thin membrane could be used in a future design, provided a more resilient holding system for the TIAT was used. For the final sensor more robust Teflon™ AF2400 was selected which has a thickness of 100 µm (810 µm OD, 610 µm ID). The outer PEEK tubing selected for the final version has dimensions of ~1600 µm OD and ~1000 µm ID. This PEEK was more robust and also gave the TIAT a volume ratio of 1:1 for the outer and inner tubes. The length of the TIAT used for the final version of the DIC LOC sensor was 300 mm, which gave the acceptor and donor volume inside the TIAT of ~100 µL. Whether the acceptor or the donor was on the inside had little impact as both inner and outer tubes had the same volume; ultimately the acceptor was chosen as the inner tube because it made assembling the three modules of the sensor simpler. The final TIAT is shown in Figure 2.12.

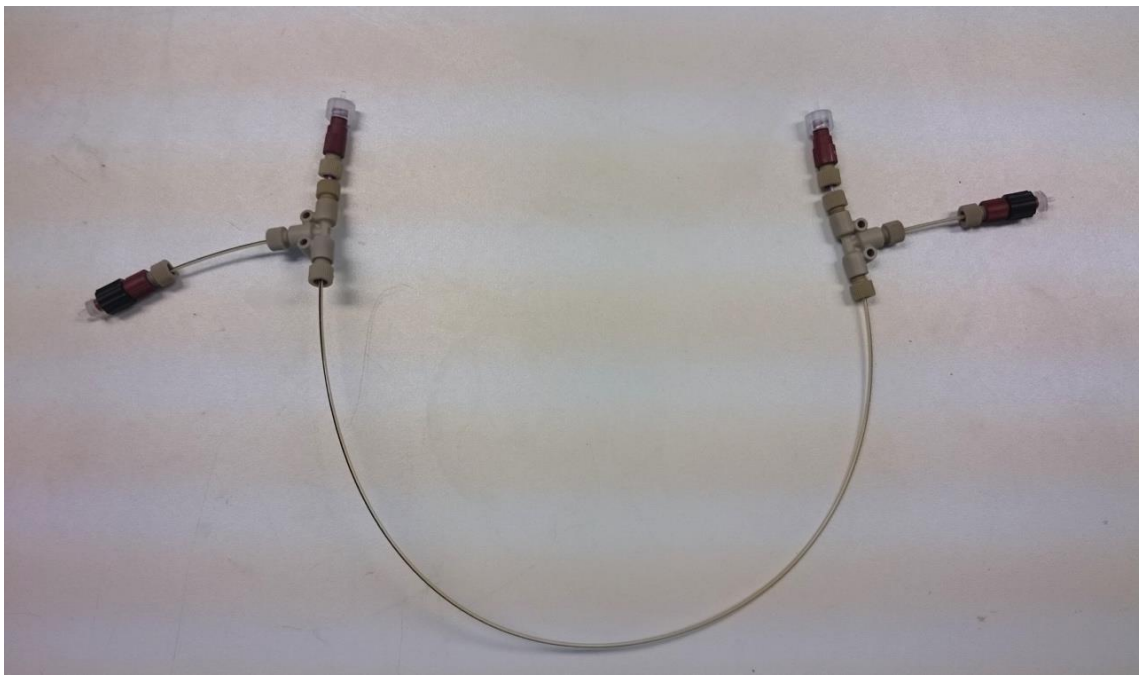

Figure 2.12 Photograph of the final version of the TIAT.

The time taken for a full gas exchange to occur was tested using the final version of the TIAT and the first prototype DIC LOC sensor, detailed in Chapter 5. For this test a 2500 µmol kg^{-1} sodium

bicarbonate solution was used as a sample, which was acidified using 1 M HCl. The acceptor solution was 7 mM NaOH. The conductivity of the acceptor solution was measured using the final version of the detector, described in section 3.3. The pumping and mixing of the solutions was controlled by the DIC LOC sensor, which is fully described in section 5.2.1. Two methods were used to alter the residence times of the solutions in the GEU. For the first method the acidified sample was stopped in the TIAT for between 1 second and 15 minutes. After the period of stopped flow the pumping was resumed and the detector recorded the conductivity drop. The data plotted in Figure 2.13 shows that for the stopped flow method the magnitude of the measured signal reached its maximum after a residence time in the TIAT of 60 seconds. In the second test the flow rate of the solutions was varied to alter the residence time from 15 seconds to 6 minutes. This method produced similar results as the first, with the maximum signal reached when the flow rate was 100 µL min^{-1}, with a residence time of 60 seconds. Further increases to the residence time produced no further increase in the signal, demonstrating that full exchange had occurred.

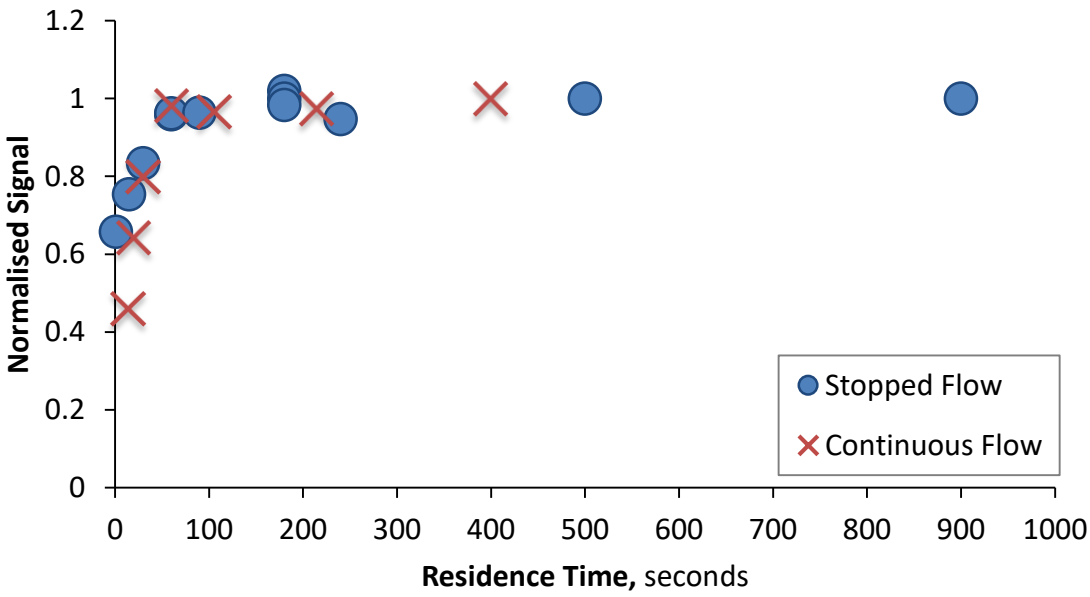

Figure 2.13 Plot showing influence of residence time in the TIAT on the relative conductivity signal recorded by the detector.

Both tests demonstrated that full exchange was reached with a residence time of 60 seconds so for the final version of the sensor described in chapter 5 the flow rate of the donor was selected to ensure that a residence time of 60 seconds was reached in the TIAT.

2.5 Conclusions

This chapter described the work to design and optimise a GEU. Both planar and TIAT geometries were tested, with both demonstrating potential, facilitating rapid gas exchange. While the bonded planar GEU was not selected for the final sensor it was used in a benchtop instrument where it performed well, this is described in sections 3.5.2 and 4.2. Due to the longer fabrication process and the high failure rate a bonded planar GEU was not selected for the final version of this sensor.

2.5.1 GEU Selected for the DIC LOC Sensor

For the final version of the DIC LOC sensor a TIAT was selected as the GEU, as there were many benefits to using this system over the bonded planar unit. The TIAT system was found to have a lower failure rate than the bonded planar system and could also be easily repaired. Another advantage was that the donor and acceptor volumes could be modified simply, adding flexibility to the system. The TIAT performed well and gave a complete gas exchange within 60 seconds; this finding was used to determine the flow rate for the final sensor.

2.5.2 Future GEU Developments

The vision for future versions of the DIC LOC sensor is to have the membrane bonded into the main PMMA chip, and a longer-term goal is to integrate the detecting electrodes directly into the PMMA so that the GEU and detector are fully integrated, as described in section 6.1.4. Combining the detector and the membrane in this way would reduce the required sample volume, which in turn would also reduce the waste produced. This would mean a lower total volume for the sensor, which would improve the flushing of the sensor.

Chapter 3 Detector Design and Optimisation

3.1 Introduction

The two most commonly applied detection techniques that have been used to develop experimental oceanic DIC sensors are spectrophotometry and conductometry, as described in section 1.4. In both techniques a sample is acidified, and the DIC in this acidified donor solution is converted to CO_2, which then diffuses across a gas permeable membrane into an acceptor solution where a signal is monitored. In the spectrophotometric method the monitored signal is a colour change, resulting from the CO_2 lowering the pH of the acceptor solution. This is detected optically by measuring a colour change in a pH sensitive dye, at a constant salinity and total alkalinity. In order to make high quality repeatable measurements of the pH change spectrophotometrically, a purified dye is required but currently there are no commercial sources of purified dye (Ma *et al.*, 2019). Spectrophotometric measurements are sensitive to staining or fouling on the optical windows of the light source and detector, as well as misalignment of the light source and detector. The signal measured using the conductimetric method is the conductivity change caused as the CO_2 reacts with the acceptor solution, altering the ionic composition of the acceptor. Conductimetric measurements are not affected by the issue of optical staining but are sensitive to changes in the cell detector volume and temperature, as detailed in the following sections. Conductimetric detection was chosen for this sensor as previous studies have shown that there is a wide range of designs for electrodes that can enhance the measured signal, and more readily available acceptor reagents can be used. The electrodes can also be fabricated and modified simply, allowing potential for rapid optimisation.

This chapter will first describe the theory behind conductivity measurements using both contacting and contactless electrodes, and then outline work done to optimise two different electrode configurations.

3.1.1 Acceptor Reagent Selection

Previous work developing DIC instruments and sensors based on the conductimetric technique have utilised either NaOH or ultra pure water as the acceptor fluid (Hall and Aller, 1992; Kubáň and Dasgupta, 1993; Sayles and Eck, 2009; Martinotti, Balordi and Ciceri, 2012). One study comparing ultra pure water and NaOH as acceptor solutions found that the NaOH solution improved sensitivity of the system by a third, by reducing the limit of detection, and also improved the relative standard deviation a replicate measurement by 20% (Pencharee *et al.*,

2012). A benefit of using NaOH as the acceptor solution is that the CO_2 reacts with the OH^- and is consumed; this maintains the maximum concentration gradient across the membrane, ensuring the maximum diffusive flux of CO_2 across the membrane. Sayles and Eck (2009) demonstrated there are three potential reactions that the addition of CO_2 to OH^- can take:

$$CO_2 + 2OH^- \Rightarrow CO_3^= + H_2O \quad (3.1)$$

$$CO_2 + OH^- \Rightarrow HCO_3^- \quad (3.2)$$

$$CO_2 + CO_3^= + H_2O \Rightarrow 2HCO_3^- \quad (3.3)$$

Each of these chemical reactions result in a drop in conductivity in the acceptor, but when the reaction shown in equation 3.1 dominates the largest conductivity drop occurs, as the specific conductance of the OH^- is greater than that of the $CO_3^=$. This is because the individual ionic molar conductivity (at 25 °C) of OH^- is 197 mS kg cm^{-1} mol^{-1}, HCO_3^- is 44 mS kg cm^{-1} mol^{-1} and $CO_3^=$ is 139 mS kg cm^{-1} mol^{-1} (McCleskey et al., 2012). Sayles and Eck (2009) went on to determine that 7 mM NaOH was the optimal concentration of NaOH to ensure that the reaction shown in equation 3.1 dominated for typical seawater DIC concentrations. For this reason 7 mM NaOH was selected as the acceptor solution in this work.

To determine what range of conductivities the detector should be optimised for the change in molar conductivity of 7mM NaOH was calculated over a range of temperatures. This was repeated for the 7 mM NaOH after the equivalent addition of 2500 µmol kg^{-1} DIC. These calculations were based on a method developed for calculating the conductivity of natural waters (McCleskey *et al.*, 2012). The results show that the detector should be focused on the range of 0.5 – 2 mS cm^{-1}, as shown in Figure 3.1. The conductivity of a solution is dependant on the concentration of ions and their average velocity which is a function of temperature (Gray, 2005). Previous studies have found conductivity of NaOH is altered by ~1.5 - 2% per °C (McKee, 2009).

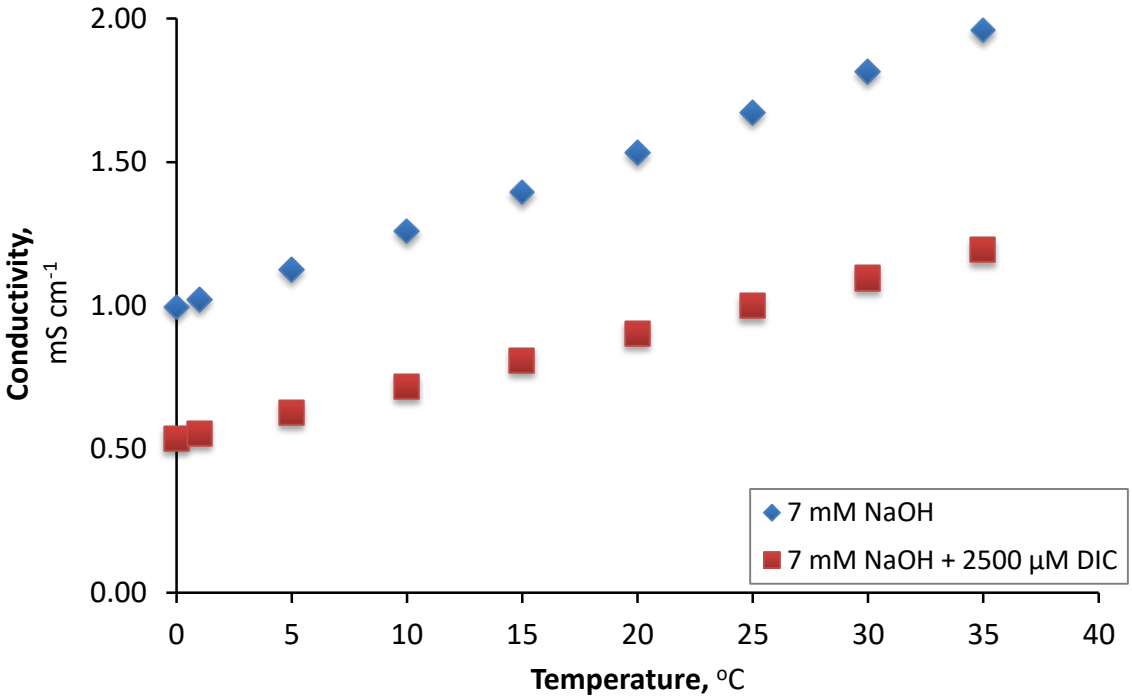

Figure 3.1 Theoretical conductivity calculated for 7 mM NaOH before and after the addition of 2500 µmol kg^{-1} DIC, over a range of temperatures.

3.1.2 Design Considerations

The rate-limiting factor in determining the measurement frequency is the gas exchange step. Chapter 2 focused on optimising the gas exchange unit. Reducing the sample volume is one way to reduce the gas exchange time but ultimately the volume of the detector determines the volume of sample required. Minimising the detector volume can result in a smaller sample volume that can increase the sampling frequency. By combining microfluidics and small electrodes the sensor developed in this work aimed to minimise the sample volume while maintaining high quality conductivity measurements.

3.1.3 Conductivity Measurement Theory

Electrical conductance is a measure of how easily an electric current can pass through a material and is equivalent to the inverse of its resistance. The relationship between conductance (G in Siemens, S) and resistance of a solution (R in ohms, Ω) can be expressed as:

$$G = \frac{1}{R} \qquad (3.4)$$

Resistance, and therefore conductance, are extensive properties, i.e. they depend on the dimensions of the materials being measured. The conductivity of a solution (σ in Siemens per

meter, S m^{-1}) is a material property of a solution, independent of the material dimensions, and can be expressed as:

$$\sigma = K_c \frac{1}{R} = K_c . G \quad (3.5)$$

In this equation K_c is the cell constant, which is the ratio of the area to length of the conductivity cell, which is discussed further in the following section. K_c can be calculated but experimental determination provides a more accurate value (Ciobotaru *et al.*, 2016).

There are two main electrode array designs that can be used to measure the conductivity of a solution. These can be divided into contacting and contactless electrodes; both have been investigated over the course of this study. Both contacting and contactless electrodes allow rapid measurements of conductivity to be made, and by altering their design high quality conductivity measurements can be achieved. The following sections briefly describe the theory of operation for each design, then summarises their benefits and limitations.

3.1.3.1 Contacting Electrodes

In a conductivity detector system based on contacting electrodes the electrodes are in direct contact with the measured solution; the simplest of these systems consist of two electrodes, as shown in Figure 3.2. In these systems the resistance of the fluid between the two electrodes is measured and the conductivity is derived using equation 3.5 (Brom-Verheijden, Goedbloed and Zevenbergen, 2018). The cell constant (K_c) in this equation depends on the electrode geometry such that:

$$K_c = \frac{d}{A} \quad (3.6)$$

In this equation d is distance between the electrodes and A is the effective electrode area. Adjusting the cell geometry, by altering the electrode area and separation, is a method for optimising the electrodes to measure the target conductivity (Gong *et al.*, 2008; Ramos *et al.*, 2008; Fouletier and Fabry, 2013). Benefits of this system are that it is simple to manufacture and easy to modify.

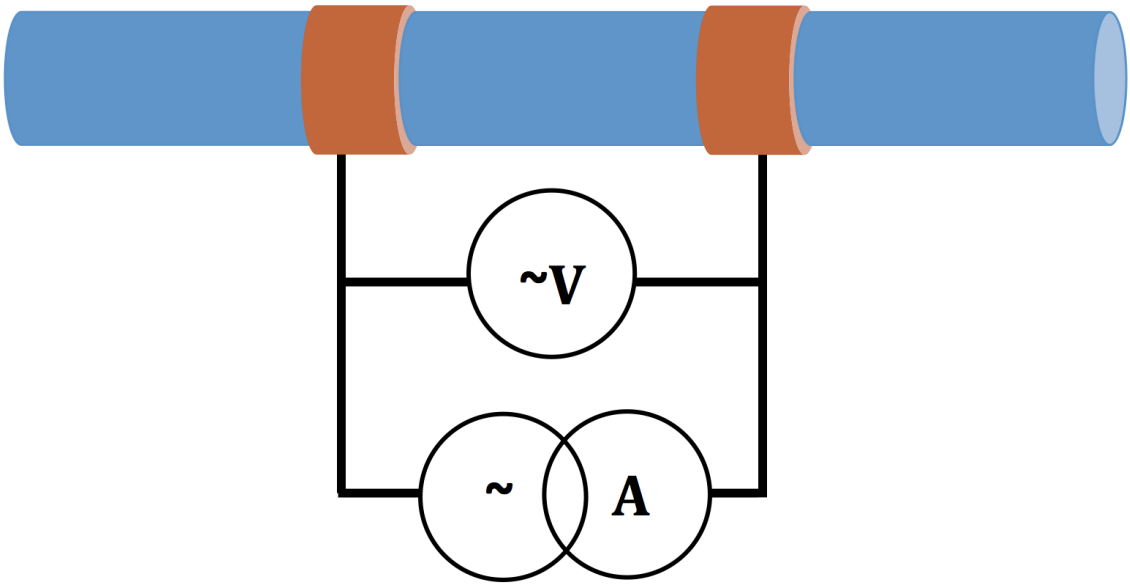

Figure 3.2 Diagram of contacting two-electrode array.

Previous studies have found the optimal cell constants for different conductivity ranges, shown in Table 3.1. These values were considered to determine approximate electrode design dimensions for the testing and development described in section 3.5.

Table 3.1 Cell constants and optimal conductivity ranges, modified from Fouletier and Fabry (2013).

Cell Constant cm^{-1}	**Optimum Conductivity Range** $mS\ cm^{-1}$
0.1	4×10^{-4} to 0.4
1	0.01 to 2
10	1 to 200

Two-electrode systems have several limitations. Applying a current to the electrodes can lead to polarisation effects which result in an accumulation of ionic species near the electrodes causing chemical reactions to occur at the electrode surfaces, which impact on the conductivity measurements (Jones, 2002; Gong *et al.*, 2008; Brom-Verheijden, Goedbloed and Zevenbergen, 2018). This can lead to errors in measurements taken at conductivities lower than 10 mS cm^{-1} (Gong *et al.*, 2008). Polarisation effects can be removed by using a four-electrode system (Ramos *et al.*, 2008; Huang *et al.*, 2011). A second limitation of contacting two-electrode systems is that measured resistance also includes the electrode impedance, which reduces sensitivity and accuracy of the system. Previous studies have found that this is exacerbated when miniaturised cell configurations are used (Laugere *et al.*, 2003).

In a four-electrode system an extra pair of electrodes, located between the input electrodes, measures the voltage output, effectively function as a voltmeter, as shown in Figure 3.3. No current flows through this inner electrode pair because of the high impedance of the voltmeter circuitry, this prevents the build up of ions at the electrode. The benefit of this is that the polarisation effects can be eliminated, allowing a greater range of conductivities to be measured. It also allows the system to compensate for any fouling or scale build-up on the electrodes (Gong *et al.*, 2008).

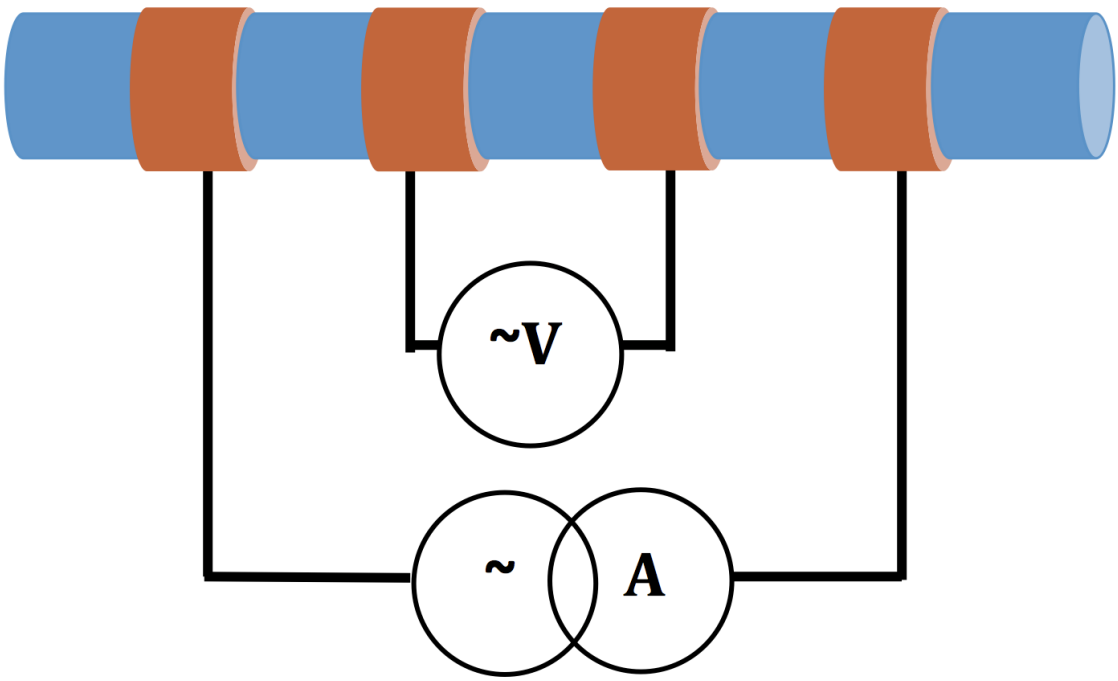

Figure 3.3 Diagram of contacting four-electrode array.

3.1.3.2 Contactless Electrodes

In a contactless electrode system the electrodes are insulated, so they are not in direct contact with the measured solution. This prevents the polarisation effects described in the preceding section and also reduces the potential for the electrodes to become fouled over time. The insulating layer thickness can vary from 10's of µm to mm scale thick depending on the insulation type and application.

Capacitively Coupled Contactless Conductivity Detection (C4D) was initially developed in the 1980s by groups interested in electrophoresis (Gaš, Demjanenko and Vacík, 1980). The initial interest was driven by the aim to minimise the interference of the AC detection voltage with the electrophoretic DC voltage. More recently C4D has been used in a wide range of applications, as detailed in various review papers (Kubáň and Hauser, 2004, 2008, 2013; Pumera, 2007; Coltro *et*

al., 2012) and has also been commercialised by eDAQ Pty Ltd, Australia, in collaboration with Hauser.

C4D detectors operate by applying an AC current to an input electrode and then detecting the induced current in a second pick up electrode (J. Liu *et al.*, 2013). Both electrodes are isolated from the fluid and the insulating layer behaves as a capacitor (Laugere *et al.*, 2003). As the insulation layer has lower capacitance than the double layer capacitance of contacting electrodes, higher working frequencies are required by C4D systems (Kubáň and Hauser, 2008). In order to prevent cross talk, or stray capacitance, between the two electrodes a faradaic shield can separate the electrodes (as shown in Figure 3.4).

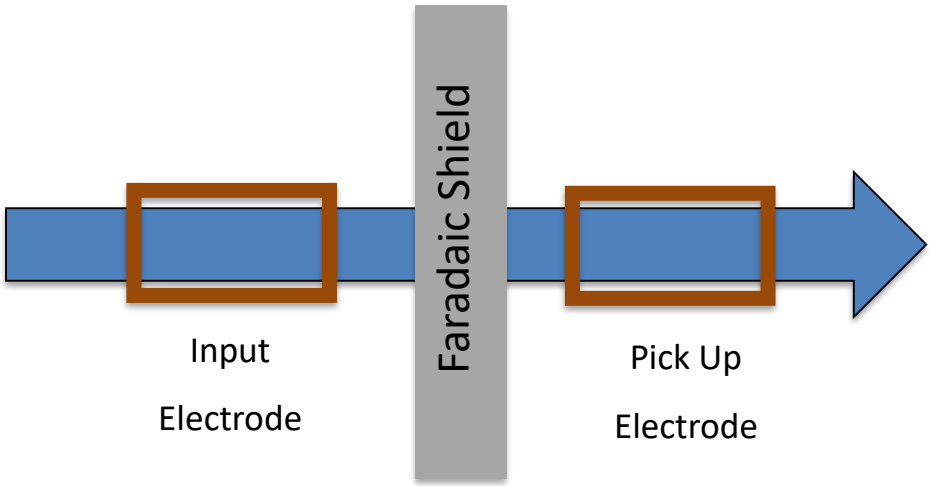

Figure 3.4 C4D schematic, where the blue represents the fluid flowing through a tube, the brown rectangles show the electrodes, and the grey rectangle represents the shield to limit cross talk between the electrodes.

Various studies using C4D have demonstrated the flexibility of the system and the degree to which sensitivity can be increased. Using thin-walled tubing to isolate the measured solution from tubular electrodes has been shown to improve measurement sensitivity at low concentrations (Hoherčáková, Opekar and Štulík, 2005; Míka *et al.*, 2009; Tůma, Samcová and Štulík, 2009). Varying the distance between the electrodes alters the volume of fluid, which alters the resistance between the electrodes and is one way to improve the sensitivity of the detector (Tůma, Opekar and Štulik, 2002; Pencharee *et al.*, 2012). The input frequency can also be optimised to ensure the maximum signal is recorded (Baltussen *et al.*, 2002; Kubáň and Hauser, 2004; Novotný, Opekar and Štulík, 2005).

The theory behind these optimisations can be understood if the system is visualised as an equivalent electrical circuit as shown in Figure 3.5. In this model, R is the resistance of the solution, and the capacitance between the electrode and the solution is represented by C. The

value of this capacitance is dependant on the insulator thickness in addition to the area of the electrodes (Laugere *et al.*, 2003; Kubáň and Hauser, 2004). The stray capacitance (C_{stray}) or cross talk between electrodes can be removed using a faradaic shield. The presence of the capacitances can result in nonlinear output, but by optimising the insulation thickness and input frequency the output can be approximated to a linear response over the conductivity range of interest (Coltro *et al.*, 2012).

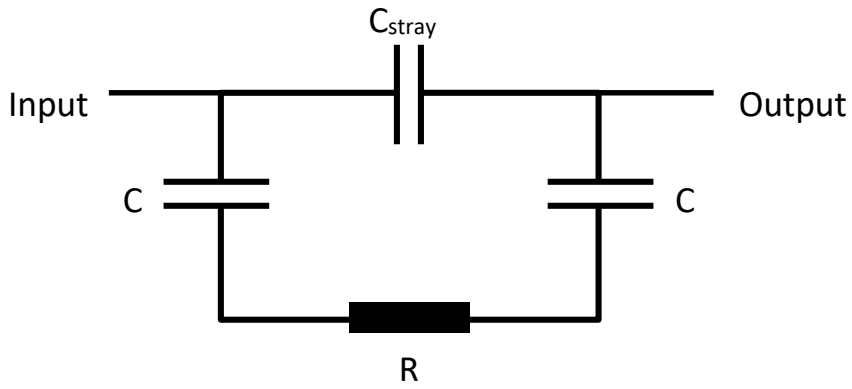

Figure 3.5 Equivalent circuit diagram of a C4D detector.

In this circuit model, the resistance is related to the conductivity (G) being measured, the area of the insulating tube (A), and the length separating the electrodes (L). This is detailed in the following equation:

$$\mathrm{R} = \frac{L}{GA} \tag{3.7}$$

The coupling capacity is given by:

$$\mathrm{C} = \frac{2\pi\varepsilon_0\varepsilon_r l}{\ln(\frac{OD}{ID})}, \tag{3.8}$$

where OD and ID are the outer and inner diameter of the insulating tubing respectively, l is the electrode length, ε_0 is the permittivity of the vacuum, and ε_r is the relative permittivity of the tubing. To achieve the most linear results, the coupling capacity should be as high as possible with the total impedance for the circuit lower than the value of the measured R.

For the initial work optimising a detector for the DIC LOC sensor a contactless C4D system was selected as it isolated the electrodes from the acceptor solution and was predicted to give the system improved stability over long deployments.

3.2 Initial C4D Optimisation: Insulation Thickness and Input Signal Frequency

The objective of initial testing was to optimise the C4D conductivity measurement over the range 0.5 −2 mS cm^{-1}, calculated to be of interest based on initial estimates in section 3.1.1. Altering the thickness of the insulation and the input signal frequency are two parameters that can be used to optimise a C4D detector to ensure a linear output. For the initial testing and optimisation a customised C4D board was manufactured by eDAQ Pty Ltd, Australia.

The eDAQ C4D-SPL unit consists of a circuit board with two tubular brass electrodes, through which a fluidic tube runs so the acceptor fluid can flow through the electrodes, insulated by the tubing wall, shown in Figure 3.6. The electrodes and insulating tubing are on the right of the board. The input electrode is visible in the lower right corner and the pick up electrode is in the top right corner inside a small metal cage, which acts as a faradaic shield. The eDAQ C4D-SPL was designed so that both the fluidic tubing (which governs the insulating wall thickness) and input signal frequency could be manipulated so that the optimal combination could be found for measuring the conductivity range of interest. The circuitry to the left of the image has jumper pins that can be used to set the input frequency to one of four values (200 kHz, 400 kHz, 870 kHz, and 1070 kHz).

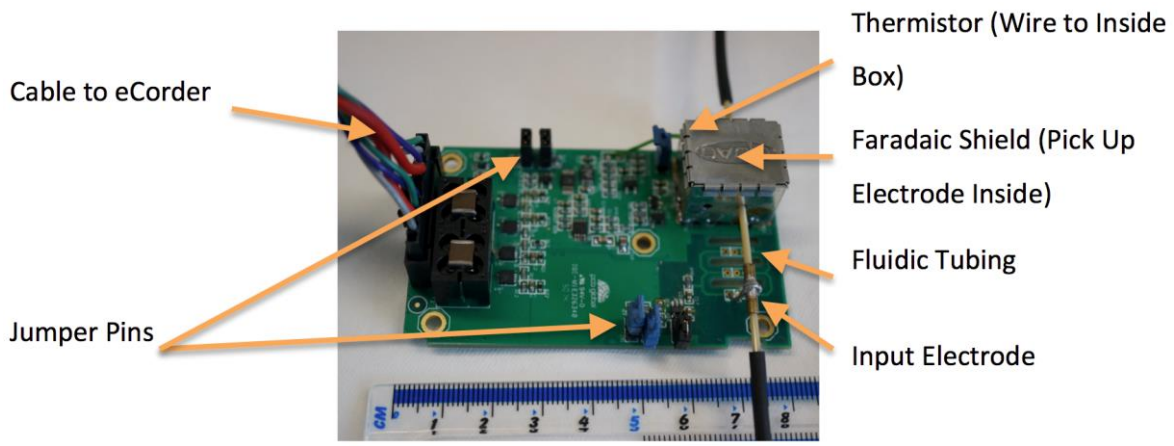

Figure 3.6 Annotated photograph of the custom eDAQ C4D-SPL board. Ruler for scale.

The electrodes are made of brass tubes 10 mm long with an internal diameter (ID) of 1600 µm (1/16”), which allows for the use of an insulating tube of equivalent outer diameter (OD). By varying the ID of the fluidic tubing the insulation thickness was varied. The input electrode applies an AC current to the fluid and the induced current is detected by the shielded pick up electrode. This current is converted to a voltage by a current to voltage converter and the voltage recorded is proportional to the conductivity of the fluid between the electrodes. The data logging was

achieved using a PC running the Chart Software (eDAQ Pty Ltd, Australia) interfaced with the C4D−SPL by an eCorder 410 (eDAQ Pty Ltd, Australia).

To determine the optimum input frequency and insulation thickness for measuring the conductivity target range of 0.5 – 2 mS cm^{-1} three PTFE tubes (OD 1600 µm) were tested. These had an ID of 300 µm, 500 µm and 800 µm, which gave the insulation thicknesses of 650 µm, 550 µm, and 400 µm respectively.

A working stock of NaOH was diluted to give seven solutions with conductivities of 0.4 − 2.5 mS cm^{-1}. The conductivity of each solution was measured using a HI-8733 conductivity probe (HANNA Instruments, UK) before taking measurements with the eDAQ C4D-SPL. For each NaOH solution, replicate measurements were taken for each input frequency and PTFE tube ID. The optimal combination of input frequency and PTFE tube ID would maximise the sensitivity of the detector by providing a linear response over the range of target conductivities.

To dampen the impact of laboratory temperature fluctuation on the conductivity measurements, detailed in section 3.1.1, the C4D-SPL unit was submerged in mineral oil while the measurements were made. The temperature of the oil was monitored using a precision thermometer (RT1-PS503J2, US Sensor Corporation, USA) built into the C4D-SPL board. This thermometer had a precision of 0.1 ^{o}C.

The results of comparing the three insulation thicknesses, over four different input frequencies, are presented in Figure 3.7. The thickest insulating layer, of 650 µm, shows the lowest response over the range of conductivities, in Panel A. The 550 µm thick insulation showed an increased signal response, in Panel B, but the thinnest insulation of 400 µm had the greatest response over the range of target conductivities, shown in Panel C. For the 400 µm thick insulation both the 200 kHz and 400 kHz input frequency had nonlinear responses over the range of conductivities. The nonlinear response is likely the result of the capacitances (Coltro *et al.*, 2012). The 870 kHz and 1070 kHz input signals were both linear but the 870 kHz had the largest signal range so was selected as the optimum setup for the C4D-SPL.

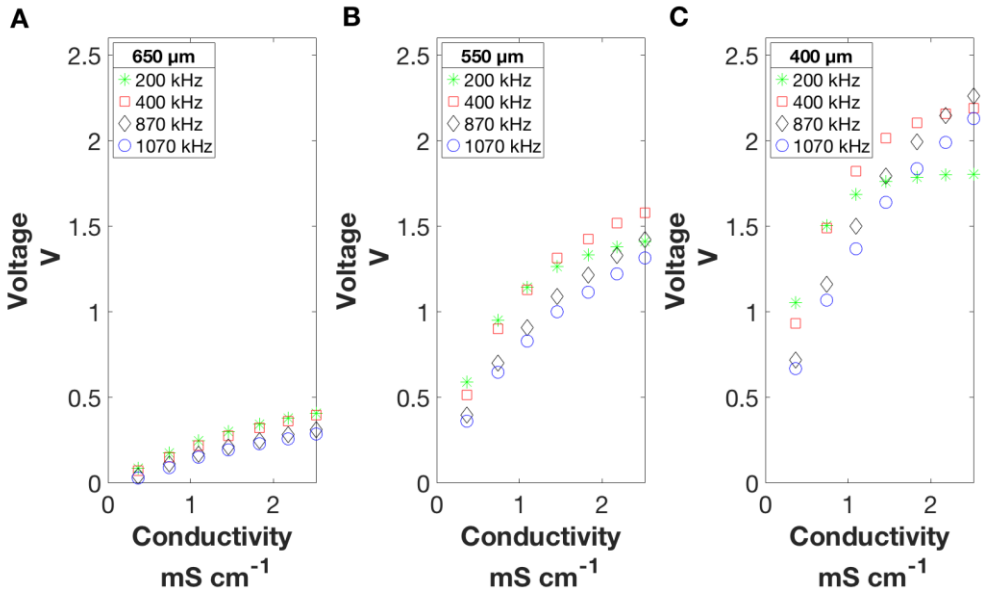

Figure 3.7 Comparison of signal response for different insulation thicknesses and input signal frequencies. Panel A shows the thickest insulation of 650 µm, Panel B 550 µm thick insulation and Panel C 400 µm thick insulation.

This investigation demonstrated that the optimum insulation thickness and input signal frequency combination to determine conductivity in the range of interest using the eDAQ C4D-SPL system was 400 µm and 870 kHz respectively. This setup gave a linear response over the largest range of conductivities. These settings were then used for the initial work carried out to develop a benchtop DIC instrument, described in Chapter 4. This C4D-SPL unit functioned adequately for a benchtop instrument, reaching TRL 4 as defined in section 1.5.4, with data logged on a PC. To reach higher TRL levels an autonomous sensor required a detector that can run independently of a PC. This stand-alone unit was developed and is described in the following section.

3.3 Development of a Stand-alone C4D

To operate as an autonomous DIC sensor, a conductivity detector that runs as a stand-alone unit is a key requirement. For the development of the DIC LOC sensor eDAQ Pty Ltd, Australia, developed the C4D-EPU359 from the earlier C4D-SPL version. The C4D-EPU359 runs without the need for an eCorder unit or PC, and was optimised for the conductivity range of 0.5 - 2 mS cm^{-1}, with improved precision compared to the C4D-SPL unit described in section 3.2. This stand-alone detector board, shown in Figure 3.8, requires a 5 V supply (<500 mA) to run and can communicate via a serial line to the processing board used in the DIC LOC sensor, further described in section 5.2.1.

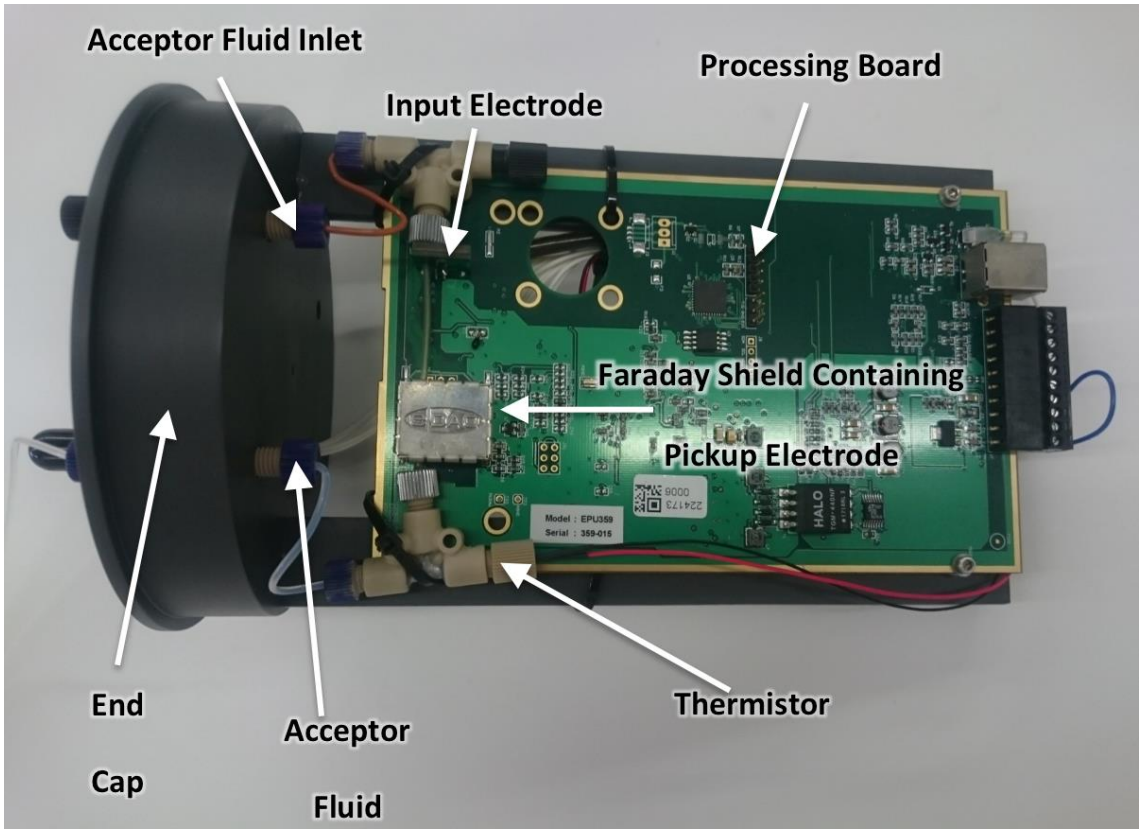

Figure 3.8 Annotated photograph of EPU-359 detector.

In this version of the C4D detector PEEK tubing was selected as the insulating tube as it has a lower diffusion coefficient for CO_2 (1.4×10^{-7} $cm^2\,s^{-1}$) than the PTFE (7×10^{-7} $cm^2\,s^{-1}$) used in the C4D-SPL work. The initial testing with the C4D-SPL had confirmed the theory that thinner insulation improved the detector performance. Therefore for the EPU359 the PEEK tubing selected had an ID of 1400 µm, giving an insulation thickness of 100 µm.

The performance of the EPU359 was assessed by measuring different NaOH concentrations with a range of conductivities of 0.5 – 3.0 mS cm^{-1}. Each concentration was measured for one minute and was compared to the data recorded by the C4D-SPL.

The initial testing of the EPU359 board demonstrated that this unit had an improved sensitivity over the previous C4D-SPL. The new board had a greater signal range, and achieved improved precision. The result of these improvements was the new board achieved an improved relative standard deviation, shown in Table 3.2. The improved relative standard deviation was a result of an increased signal over the range and reduced noise, resulting in better precision.

Table 3.2 Comparison of the EPU359 and C4D-SPL detectors over the target conductivity measurement range.

	Signal Range Over Conductivity Range 0.5 – 2mS cm^{-1} V	**Standard Deviation Over One Minute Measurement of 7 mM NaOH** V	**Relative Standard Deviation**
C4D-SPL	1.3	0.0005	3.8×10^{-4}
EPU359	1.7	0.0003	1.8×10^{-4}

Following the initial testing phase, the board was tested at a pressure of 200 dbar and continued to perform well. These assessments confirmed that the EPU359 was suitable for the development of the deployable LOC DIC sensor so this board was used in the final sensor, described fully in Chapter 5.

3.4 Testing a Novel Application of a Brass Lacquer as an Insulator for C4D Electrodes

The findings of section 3.2, and previous studies of C4D electrodes, have shown that decreasing the thickness of the insulation between the electrode and the fluid resulted in an increased sensitivity of the electrodes at lower conductivities (Tůma, Opekar and Štulik, 2002). Thinly insulated wires have been successfully used as C4D electrodes (Hoherčáková, Opekar and Štulík, 2005). Building on this background, a brass lacquer was trialled as a possible insulator coating, less than 100 µm thick. Incralac (Rylard, UK) has been used by the Navy to limit corrosion to brass shell cases and has also been used to prevent corrosion on bronze monuments (McNamara *et al.*, 2004). An initial comparison between a coated and an uncoated brass rod, which were exposed to seawater over a period of several months, visibly demonstrated the potential for the coating to reduce corrosion, Figure 3.9.

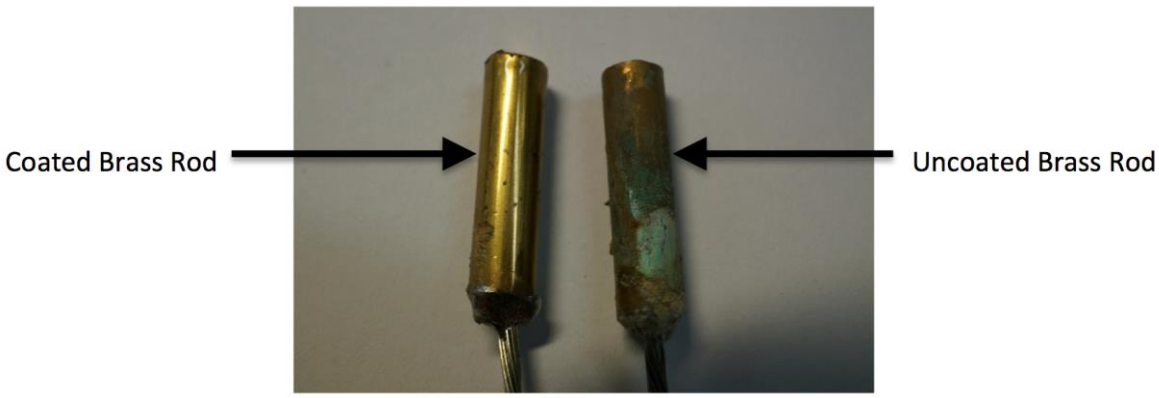

Figure 3.9 Incralac-coated (left) and non-coated (right) brass rods following exposure to seawater over a period of several months.

A prototype coated electrode C4D system was fabricated from 20 mm lengths of brass rod, bored out with a 1 mm through hole and then dip coated in Incralac. The coated electrodes were connected using PEEK tubing (1400 µm ID, 1600 µm OD). The PEEK tubing passed through an earthed metal plate, which functioned as a Faradaic Shield removing stray capacitance between the two electrodes. These components were all mounted to PMMA for structural integrity, shown in Figure 3.10.

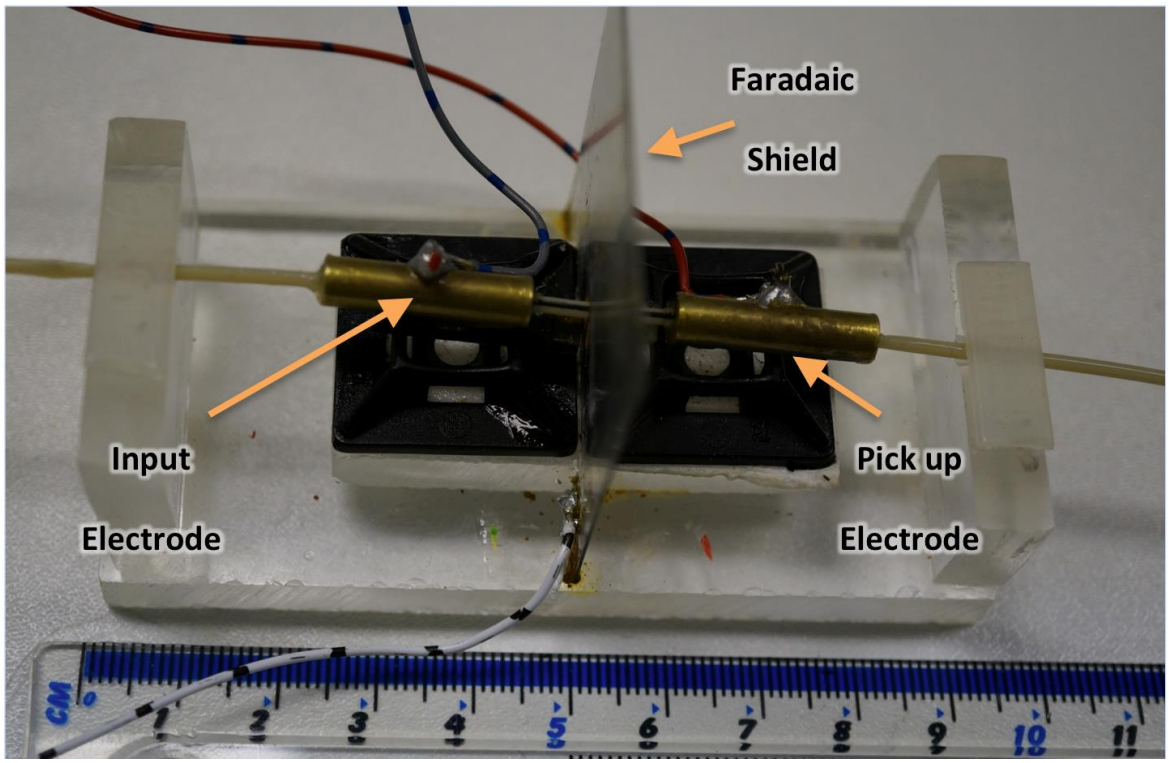

Figure 3.10 In-house built prototype C4D electrodes consisting of Incralac coated brass rods. Ruler for scale.

A comparison of the prototype coated C4D electrodes built in-house and a SBE 4 conductivity sensor (Sea-Bird Scientific, USA) was carried out by measuring the conductivity of different

concentrations of potassium chloride (KCl) solutions to give a conductivity range of 0.5 − 2.0 mS cm^{-1}. This initial test demonstrated that the coated electrodes were capable of resolving conductivity changes down to sub 0.01 mS cm^{-1}. To determine whether this coating was stable over months of exposure to NaOH a long term stability test was conducted.

3.4.1 Long Term Stability Test of the Novel Coating

A long term stability test was conducted to verify whether the coating was stable over extended periods when in contact with the chosen acceptor solution. To carry out the stability test six pairs of identical electrodes, each with an ID of 0.3 mm, were fabricated from brass rod. Three pairs were dip coated with Incralac to achieve an insulating layer estimated to be ~20 µm thick and the remaining three pairs were left uncoated, shown in Figure 3.11. The uncoated electrodes functioned as a contacting two-electrode conductivity detector (as described in section 3.1.3.1) while the coated electrodes functioned as a contactless detector (as described in section 3.1.3.2). Each pair of the coated and uncoated electrodes were stored containing a 7 mM NaOH solution for 60 days to investigate the stability of the electrodes after long term immersion and exposure to the acceptor solution. Conductivity measurements on 7 mM NaOH were made 11 times over the 60 days.

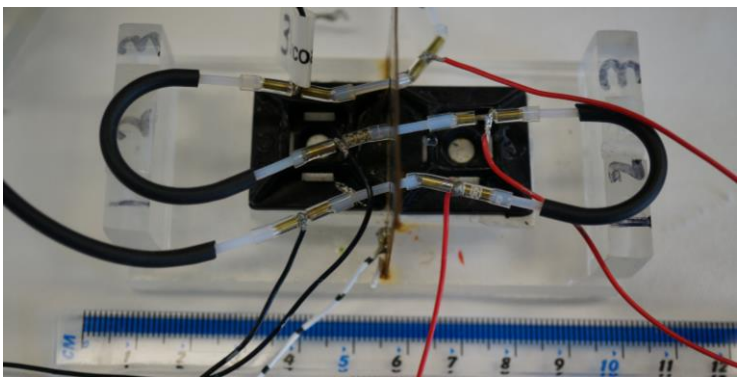

Figure 3.11 Photograph of the coated electrode test rig used for the long term stability test.

An Ivium CompactStat (Ivium Technologies, Netherlands) was used to provide the current injection and data recording. The CompactStat was used in scanning mode, providing a constant current input of 10 µA, over the input frequency range of 1 Hz to 1.5 kHz. The CompactStat recorded the resistivity of the solution, which is the inverse of its conductivity, at each frequency. Monitoring the change in the resistivity data over the input frequencies would show whether the contacting or contactless electrodes were more stable. The pairs with the lowest variance over the test would be demonstrated to be the most stable. To reduce the thermal impact on the measurements, readings were conducted on a constant temperature of 7 mM NaOH, pumped

from a 25 °C water bath (Grant TX150, Cambridge, UK) by a peristaltic pump (100 series, Williamson Manufacturing Company, UK).

The gradient of the resistivity divided by the input frequency is plotted over the 60 days in Figure 3.12. This data show that the three pairs of uncoated electrodes, in blue lines, had two orders of magnitude less variation than the coated electrodes.

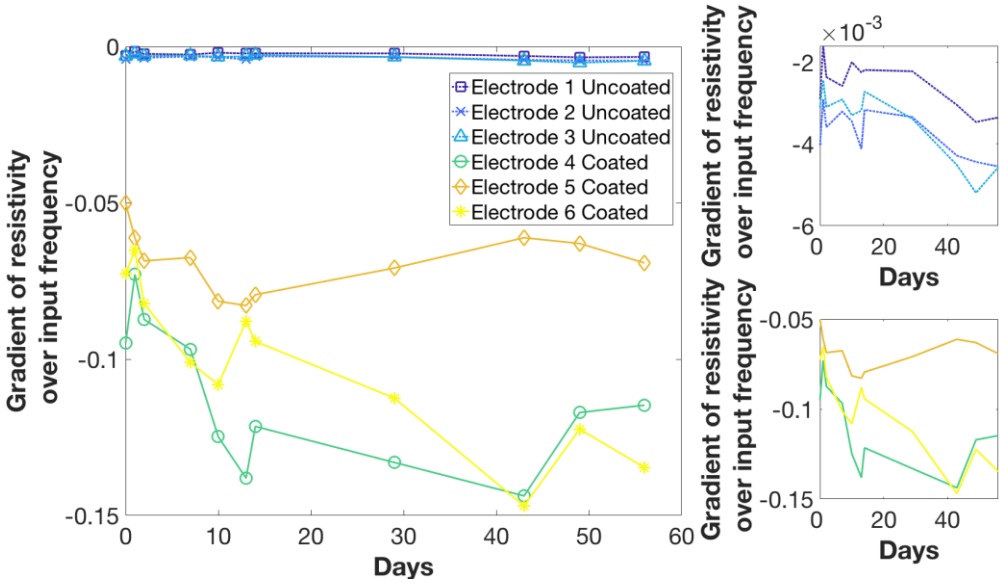

Figure 3.12 Gradient of resistivity against the frequency over the course of the 60 days the electrodes were stored in 7mM NaOH.

The change in the response of the coated electrodes over time suggested the coating was not stable. Following from this experiment nine brass blocks 10 mm × 20 mm × 5 mm were coated in Incralac. Three of the blocks were stored in air, three were stored in Milli-Q ™ water (Merck Sigma, USA), and the final three were stored in 7mM NaOH. The blocks were stored in their medium for a month and were visually inspected before and after storage. After one month the blocks stored in Milli-Q ™ and NaOH had both developed a white precipitate not seen on the coating stored in air, Figure 3.13.

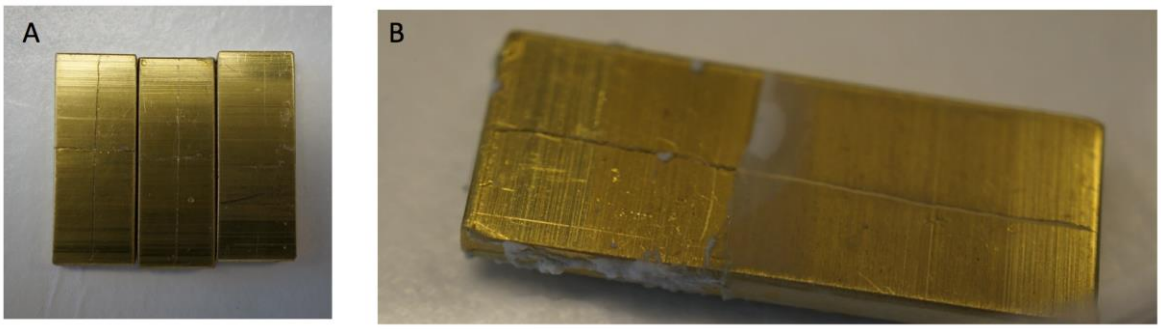

Figure 3.13 Brass block coated in Incralac and stored in 7mM NaOH for one month. Panel A shows three blocks stored in air, with no physical change. Panel B shows a block stored in 7 mM NaOH, with visible fluid ingress beneath the coating.

This demonstrated that the Incralac coating used to insulate the electrodes was not stable when stored in either pure water or a strong electrolyte solution. This suggested that fluid had ingressed into the space between the brass and coating. For this reason, despite the good sensitivity achieved in initial testing and its performance after exposure to seawater, the novel coating was no longer investigated as a potential coating for the electrodes in this system. This also demonstrated that the uncoated contacting electrodes had good stability, so these were further investigated through the development of contacting electrode arrays, described in the following section.

3.5 Contacting Electrode Array Development

The stability tests of the brass electrodes described in the preceding section demonstrated that, despite being adversely affected by the seawater, uncoated contacting electrodes did not display signs of corrosion when exposed to 7 mM NaOH over the long term test. This demonstrated the potential of contacting electrodes to be used in the conductivity detector for the DIC LOC sensor. Following this, further work was carried out to optimise the contacting electrode design. To determine experimentally whether a contacting two-electrode or four-electrode array would provide more accurate conductivity measurements over the relevant conductivity range, arrays of both electrode configurations were fabricated and tested.

3.5.1 Comparison of Contacting Two and Four-Electrode Arrays

Both the two and four electrode arrays were constructed using brass tubes with an ID of 0.3 mm, connected by PTFE tubing with an 0.7 mm ID and 1.6 mm OD, shown in Figure 3.14. The electrodes were separated by ~1 mm, giving a cell constant of ~50 cm^{-1}. To minimise the impact of temperature fluctuations on the measurements these electrodes were housed in a box containing

mineral oil and then submerged in a water bath at 25 °C (Grant TX150, Cambridge). An Ivium Compact Stat (Ivium Technologies, Netherlands) was used to provide the input current of 1 μA at 1.6 kHz and record resistivity data. The input frequency was selected after running the CompactStat in scanning mode to determine the input frequency with an angular phase of zero.

A stock solution of 0.1 M NaOH (Sigma Alridch, UK) was diluted to give a range of solutions with concentrations of 1 − 8 mM. The conductivity of these solutions was determined at 25 °C using a HI-8733 conductivity probe (HANNA, UK).

Figure 3.14 Prototype contacting four-electrode array. The separation between the electrodes is visible. One pound coin for scale.

The Ivium CompactStat and eDAQ C4D-SPL record conductivity data in different ways. The Ivium system, used to record data for the contacting electrodes array, records the fluids resistivity whereas the eDAQ Pty Ltd system, used for the contactless C4D, records a voltage which is proportional conductivity. To enable direct comparison, for both systems their responses were normalised to their response to a 1.5 mS cm^{-1} solution. Over the target range of conductivities the contacting four-electrode array had the best performance of the three systems, shown in Figure 3.15.

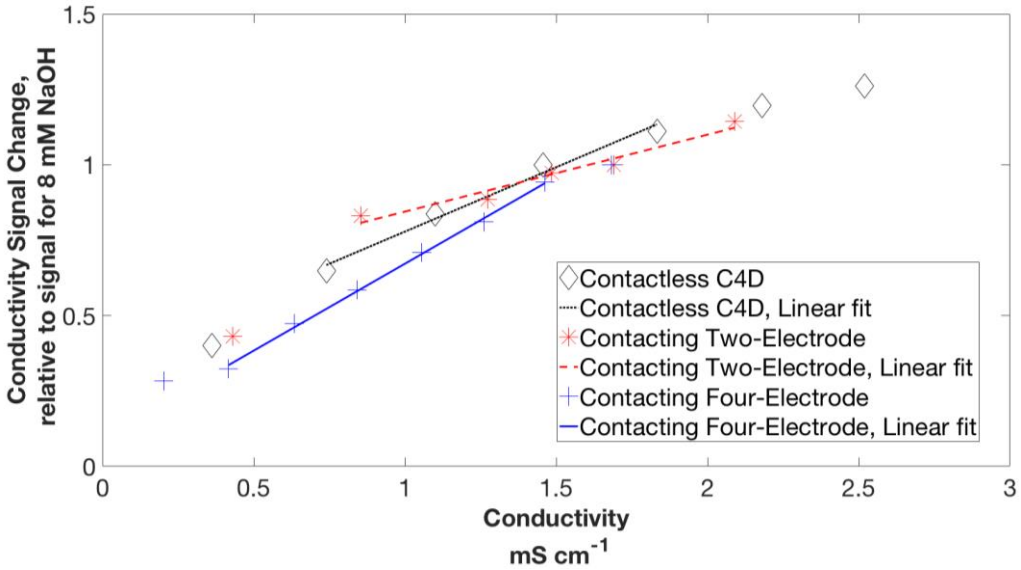

Figure 3.15 Comparison of the contactless C4D and the contacting two and four-electrode arrays.

A linear regression of the normalised conductivity signal against the conductivity of the solution as measured by the HI-8733 conductivity probe (HANNA, UK) was carried out for each of the electrode arrays, and the results of these are presented in Table 3.3. The four-electrode array had a linear response over the widest range of conductivities, and also had the best R^2. The four-electrode system also had the steepest gradient, showing it had the potential to improve the detector's performance by increasing the signal range.

Table 3.3 Comparison of the contactless and contacting electrodes.

	Linear Fit	R^2	P Value	n	Standard Error
Contactless C4D	Signal = 0.43 × $Conductivity_{Probe}$ + 0.351	0.985	0.007	4	0.03
Contacting Two-Electrode	Signal = 0.26 × $Conductivity_{Probe}$ + 0.255	0.959	0.004	5	0.03
Contacting Four-Electrode	Signal = 0.54 × $Conductivity_{Probe}$ + 0.121	0.992	<0.001	7	0.02

The improved performance of the contacting four-electrode system over the two-electrode array would be expected from the theory described in section 3.1.3.1, as the four-electrode array would gain increased sensitivity at low conductivities and show reduced polarisation effects. Based on

this result a benchtop DIC instrument was assembled to carry out a direct comparison of the contacting four-electrode and the C4D-SPL from section 3.2.

3.5.2 Comparison of Contacting Four-Electrode Detector and C4D Detector in a Benchtop DIC Instrument

The preceding section demonstrated that the contacting four-electrode array out performed both the contacting two-electrode system and the eDAQ C4D-SPL; following this an improved four-electrode array was constructed and sealed by potting in Polyurethane (Soudal, Belgium). The four electrodes were fabricated from brass tubes (6 mm length, 0.5 mm ID, 0.7 mm OD) and were connected by PEEK tubing (bored out to 0.7 mm ID, 1.6mm OD). A prototype unit was fabricated to optimise the construction and potting technique. The potting used in the prototype was confirmed not to leak so a second unit was constructed. The second version had electrodes with sub mm separation, which gave an approximate cell constant of 5 cm^{-1}. The aim of reducing the cell constant from ~50 cm^{-1} in the initial version was to enhance the performance of the system, following the theory described in section 3.1.3.1 and Table 3.1. The final potted version of the four-electrode system, shown in Figure 3.16, was demonstrated not to leak over several months of testing in a water bath at 25 ^{o}C.

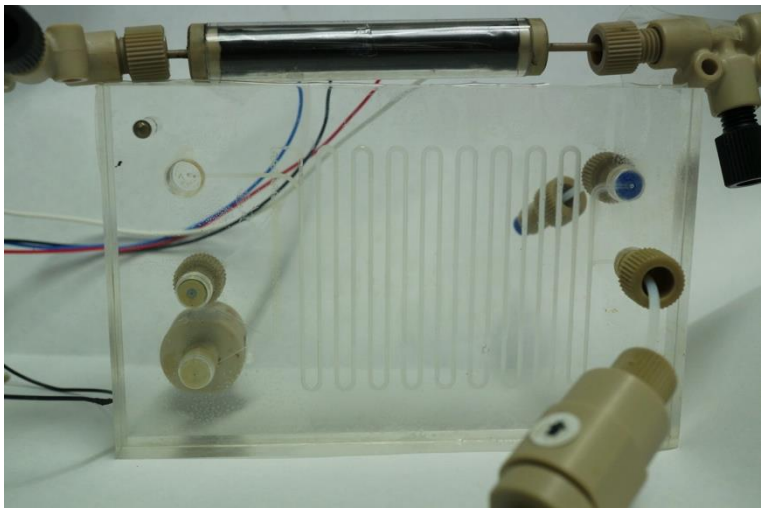

Figure 3.16 Photograph showing a potted four-electrode array at the top of the image, the separation of electrodes was approximately 100 µm, but this is not visible through the PU potting. Below that is the bonded GEU used in this benchtop instrument fabricated from clear PMMA.

A benchtop instrument, similar to that described fully in section 4.2, was constructed with two detectors. This enabled direct comparison of the same sample signal detected using both the contacting four-electrode array and the contactless eDAQ C4D-SPL. For this benchtop instrument the Gas Exchange Unit (GEU) was a bonded 100 µm thick PDMS planar GEU (as described in

section 2.3.2). Acidifying different concentrations of $NaHCO_3$ with 1M HCl in the GEU and measuring the conductivity drop in the NaOH acceptor generated the measured signal. The $NaHCO_3$ concentrations used were 1000 µM to 2500 µM in 500 µM steps. The wide range of DIC equivalent samples was used to establish how the detectors would perform over the target range of potential oceanic DIC concentrations.

Both the acceptor and acidified donor solutions were pumped at 20 µL min^{-1} with a PHD ULTRA™ (Harvard Apparatus, USA) syringe pump. The flow rate was chosen to give the sample a residence time in the GEU of 4 minutes, more than triple the residence time modelling predicted to ensure full gas exchange occurred. Each sample measurement was made on 200 µL of sample pumped at 50 µL min^{-1} with a syringe pump (New Era, USA). The mixing of the acid and sample was enhanced with an inertial microfluidic mixer on the GEU chip, further described in section 5.2.1. Each bicarbonate sample was measured in duplicate.

To reduce the impact of laboratory temperature fluctuations on the conductivity measurements both detectors were submerged in mineral oil. This dampened the temperature changes, and as both detectors were recording the conductivity of the acceptor at the same time, both systems recorded the same thermally induced conductivity variation.

The Ivium CompactStat (Ivium, Netherlands) used to drive the contacting four-electrode array recorded a voltage proportional to the resistivity of the acceptor fluid, which is the inverse of the conductivity. The C4D-SPL system recorded a voltage proportional to the conductivity. To calculate the measured signal step each sample had an associated blank measurement. The blank voltage was recorded over 30 seconds when only acid in the donor and NaOH in the acceptor were pumped through the GEU. Following the blank, a sample was injected into the GEU. The sample was acidified and the CO_2 diffused across the membrane, which resulted in the signal in the recorded data. For the contacting four-electrode detector the recorded data were a voltage proportional to resistivity, so the signal was a peak. The C4D-SPL recorded a voltage proportional to the conductivity, so the signal was a trough. The measured signal for each sample was the step between the blank voltage and the peak or trough. To enable comparison of the two, the absolute step was used.

The contacting four-electrode array recorded the wider range of step voltages, with a range of 334 mV compared to 156 mV for the eDAQ C4D-SPL, shown in Figure 3.17. This is equivalent to 4.5 µM DIC mV^{-1} for the four-electrode system and 9.6 µM DIC mV^{-1} for the eDAQ C4D-SPL. For the eDAQ C4D-SPL the linear regression of the signal step ($Step_{eDAQ}$) against the range of sample concentrations ($Sample_{concentration}$) is described by $Step_{eDAQ} = 0.107 \times Sample_{concentration} - 50.35$, ($R^2 = 0.98$, $p < 0.01$, $n = 4$, $SE_{regression} = 11.84$ mV). For the contacting four-electrode the linear

regression of the step ($Step_{Contacting4}$) against the range of sample concentrations ($Sample_{concentration}$) is described by $Step_{Contacting4} = 0.286 \times Sample_{concentration} - 90.55$, ($R^2 = 0.99$, $p < 0.005$, $n = 4$, $SE_{regression} = 13.82$ mV).

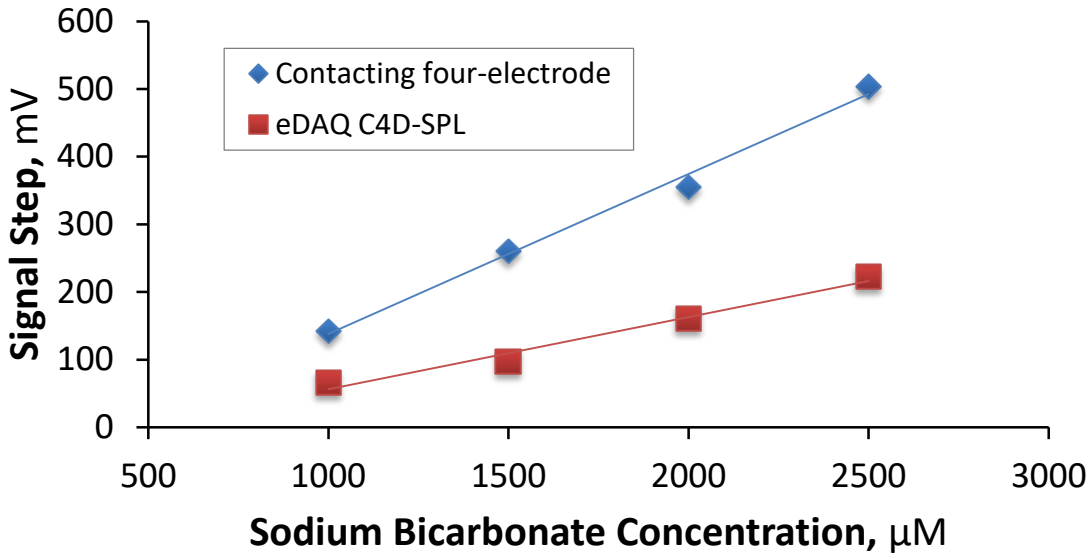

Figure 3.17 Comparison of measurement step signal as recorded by the contacting four-electrodes and the C4D-SPL.

The four-electrode detector recorded the largest range of step voltages over the measured DIC concentration range. This resulted in the contacting four-electrode array having a finer resolution of 4 µmol kg^{-1} mV^{-1} compared to 10 µmol kg^{-1} mV^{-1} achieved with the eDAQ C4D-SPL. By having a larger signal range the contacting four-electrode array has potential to enhance the signal to noise ratio to improve the accuracy of the sensor.

This section found that the contacting-four electrode system has demonstrated it has the potential to be the conductivity detector in this application. To become a deployable system this detector requires further development work, as currently the electrodes are controlled by a potentiostat connected to a PC. This would need to be miniaturised before the system could be deployed as part of an autonomous sensor.

3.6 Detector Conclusions

This chapter has described the work carried out to optimise a conductivity detector. Both contacting and contactless electrodes were assessed and shown to be capable of measuring the range of conductivities determined to be relevant in section 3.1.1.

Work carried out to optimise a C4D system was described in section 3.2, this configuration was then used to construct a benchtop DIC instrument and this is detailed in section 4.2. Following

from this a standalone C4D EPU-359 unit was developed by eDAQ Pty Ltd, Australia. The initial work using the C4D-SPL confirmed the theory that thin insulation between the electrode and fluid enhanced the signals, which led to a novel lacquer coating being tested as a potential electrode insulator. Long term stability testing of the coating demonstrated that the coating was stable in seawater but not in 7 mM NaOH. However the uncoated contacting electrodes were stable in the 7 mM NaOH acceptor solution. Despite the contacting electrodes achieving a larger signal over the relevant conductivity range, this system was not chosen as the detector in the deployable sensor due to time constraints, which prevented the extra work needed to miniaturise the control electronics.

3.6.1 Detector Selected for the DIC LOC Sensor

For the deployable DIC LOC sensor eDAQ Pty Ltd developed the contactless C4D EPU359 detector. This system was shown to work well during the testing described in section 3.3 and was found to be stable when tested at pressures of 200 dbar, equivalent to double the depth of the initial field deployments of the DIC LOC sensor, the results of which are described further in Chapter 5.

3.6.2 Future Detector Developments

Based on the success of the contacting tubular four-electrode system it is being further developed into a planar four-electrode system. Initial modelling has shown that planar electrodes require a lower sample volume, an advantage for increasing the measurement frequency. A reduced sample volume would also aid the flushing of the device, requiring a lower volume to flush the system. Planar electrodes have been used previously in microfluidics (Denuault, 2009; Temiz *et al.*, 2015) and may also prove to be easier to integrate into the LOC platform. The planar electrodes could have the potential to reduce the power requirements of the detector, which would increase the endurance of the sensor.

Chapter 4 Optimisation of a Benchtop Analyser for Seawater DIC Measurements

4.1 Introduction

The Technology Readiness Level (TRL) framework, introduced in section 1.5.4, provides both a metric for assessing the maturity of a technology in development and highlights developmental milestones. As such it provides an approximate roadmap for the development of new technology. In order to progress from the conceptual stage (TRL 1) to a final deployable sensor (TRL 8/9), the technology needs to be validated in a laboratory environment (TRL 4). For the DIC sensor to reach TRL 4, the gas exchange unit (Chapter 2) and the conductivity detector (Chapter 3) were integrated and tested as a benchtop instrument. This chapter presents an initial integration and then details optimisation experiments conducted using a similar benchtop instrument using the simplex optimisation technique.

4.2 Benchtop Instrument

4.2.1 System Description

The integrated benchtop instrument operated following the same general principle as detailed in section 1.5.3. First a discrete seawater sample was acidified, converting the DIC to CO_2. The CO_2 from the donor solution then diffused across a membrane into a NaOH acceptor solution, which was then pumped to the detector that measured the resultant decrease in conductivity due to the reaction of NaOH and CO_2, as described in 3.1.1.

For the initial benchtop instrument, shown in Figure 4.1, a TIAT was used as the Gas Exchange Unit (GEU), as described in section 2.4. This was selected because the TIAT GEU was shown to offer flexibility for easily changing the acceptor and donor solution volumes, and was also mechanically robust and facilitated rapid gas exchange. The membrane tube material was Teflon AF2400 (Biogeneral, USA). The membrane had a wall thickness of ~270 µm, from the tubing dimensions of 890 µm Outer Diameter (OD), 350 µm Inner Diameter (ID). The TIAT was 2 m long, the length selected to yield an acceptor volume in the TIAT double that of the tubing connected to the detector. The outer tube of the TIAT was PEEK tubing (1600 µm OD, 1400 µm ID). This yielded an acceptor solution volume of ~1800 µL and donor solution volume of ~200 µL. This TIAT, therefore, had an acceptor to donor volume ratio of 9 : 1, ensuring there would be an excess of

NaOH. The excess of NaOH ensured that the rate of diffusion would not be limited by a drop in the concentration gradient across the membrane.

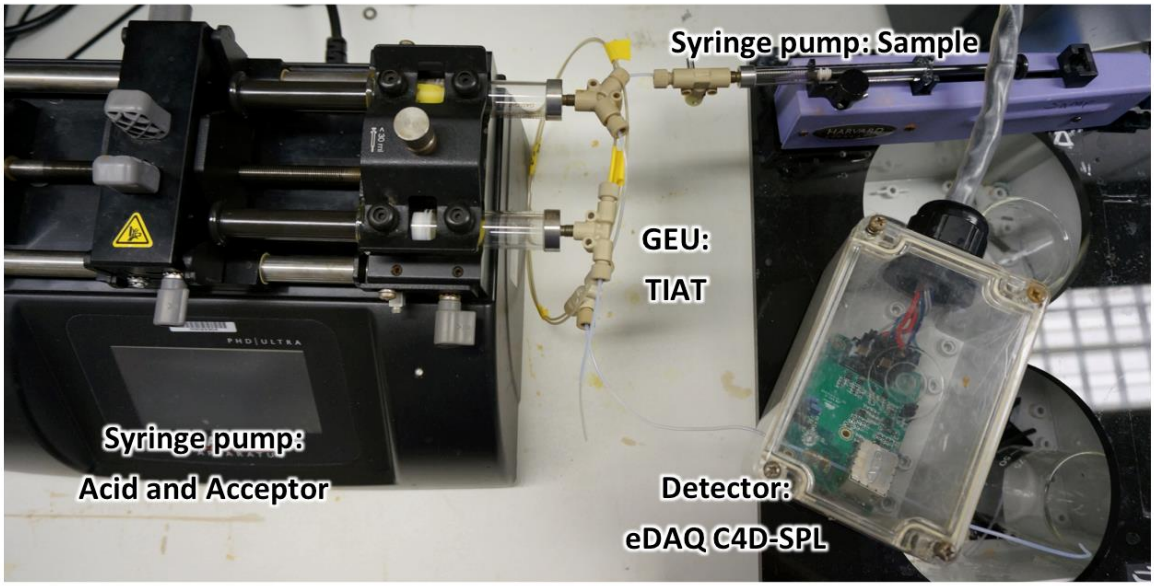

Figure 4.1 Annotated photograph of the initial benchtop instrument.

The conductivity of the acceptor solution was measured using the eDAQ C4D-SPL connected to an eDAQ eCorder and PC. Section 3.2 described fully the initial optimisation work conducted to determine the optimal input frequency and insulation thickness of this unit. The settings established in the initial work were used for the benchtop instrument. Specifically, the input frequency used was 870 kHz and the wall thickness for the C4D insulation was 400 µm, using a PTFE tube with 1600 µm OD and 800 µm ID. The selected insulating tubing gave the conductivity cell a volume of 5 µL and the total volume of tubing connecting the Tube In A Tube (TIAT) to the detector was ~100 µL.

For the initial trials, described in section 2.2, a peristaltic pump was used to drive the fluid flow and as part of the integration work three different types of pump were investigated. To select the optimum pump, comparison conductivity measurements were made on a 7 mM NaOH solution pumped through the eDAQ C4D-SPL detector at 1 mL min^{-1}. The pumps tested were a peristaltic pump, a High Precision Liquid Chromatography (HPLC) pump and a syringe pump. Peristaltic pumps operate by compressing a flexible tube using rotating rollers; the rollers pinch the tube and as they turn the rollers displace fluid to drive flow. This mechanism gives the flow a surging action, or pulsing flow (Klespitz and Kovács, 2014). The peristaltic pump tested used Viton® tubing for the flexible tubing, selected for its low CO_2 permeability (100 series, Williamson Manufacturing Company, UK). The HPLC pump operates with a piston used to a fill a chamber that drives the flow. This can reduce the pulsing flow and can be designed to give a continuous flow. The HPLC pump tested was a Series 3 (Fox Scientific Inc., USA). In a syringe pump, a plunger

withdraws to load the fluid into the barrel, which then injects to drive the flow. This is a popular pump design in microfluidic applications as the pulse free flow can be readily controlled. The model tested was a PhD Ultra (Harvard Apparatus, UK).

The conductivity voltage recorded for ten seconds of pumping with each of the pumps is shown in Figure 4.2 for this plot the voltages were normalised so the initial reading was 1, then offset so the lines were not overlapping. The peristaltic pump had the largest standard deviation over the 10 seconds of 2.6 mV and the syringe pump had the lowest at 0.1 mV. The displacement of the tubing used by peristaltic pumps to generate flow results in the flow pulsing, which may be the cause of the noise seen here. The syringe pump had the lowest noise so it was selected for use in the benchtop instrument.

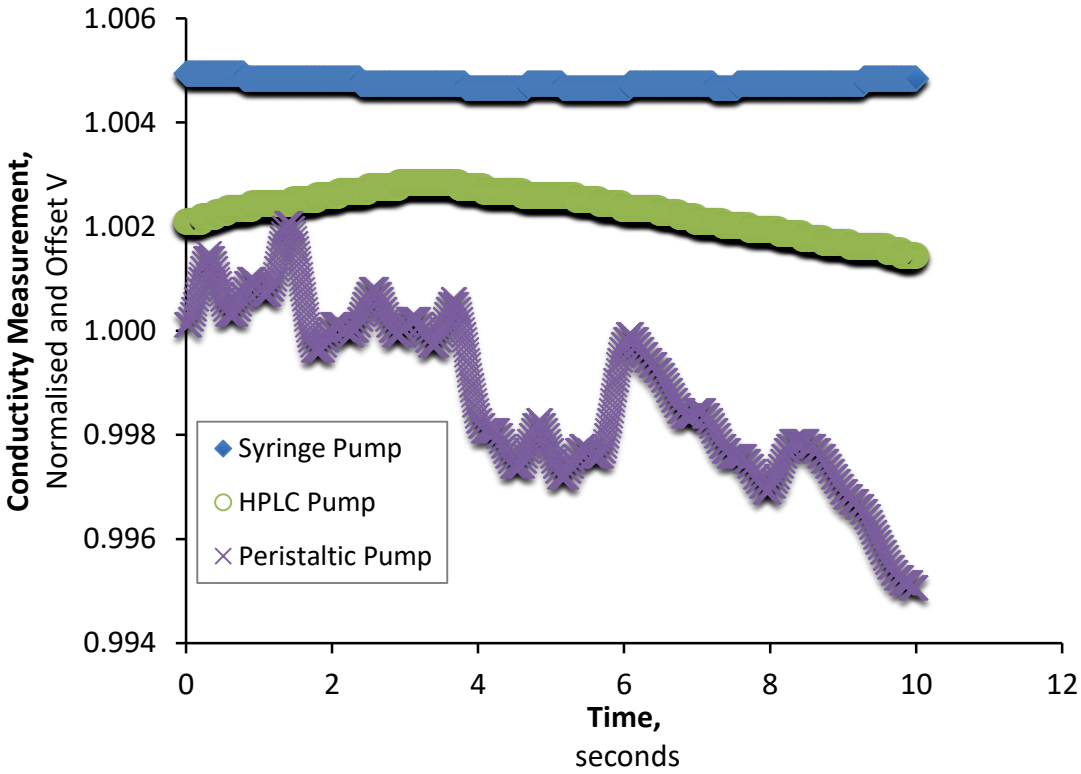

Figure 4.2 Comparison of pump-induced noise on conductivity measurements.

4.2.2 Benchtop Instrument Operation

The benchtop instrument measured discrete samples. A sample was loaded into the 1 mL syringe and the acid and NaOH acceptor solutions were loaded into two 10 mL syringes, as illustrated in Figure 4.3 Panel A. The acid and NaOH acceptor solutions were pumped by a PhD Ultra syringe pump (Harvard Apparatus, UK) with 10 mL gas-tight glass syringes (1000 series, Hamilton Company, USA), which were selected to prevent the solutions being affected by atmospheric CO_2. The sample addition was controlled by a Nanomite syringe pump (Harvard Apparatus, UK), with a

1 mL gas-tight glass syringe (1000 series Hamilton Company, USA). Initial modelling, described in section 2.3.1, predicted that the gas exchange would take less than 30 seconds, so the flow rates of the solutions was selected to give a residence time in the TIAT of ~1 minute to ensure complete diffusion of the CO_2.

The measurement cycle is shown in the flow diagram in Figure 4.3 Panel B. For each measurement the system was flushed with 4 mL of acid and NaOH at a flow rate of 1 mL min^{-1} which was then reduced to 200 µL min^{-1}. A blank measurement was taken before the sample addition, when only acid and NaOH were pumped through the GEU. To add the sample, the valve was opened and 1 mL of sample was injected while the acid flowed, to enhance the mixing of the sample and acid. The sample valve was then closed while the acid and NaOH solutions continued to flow.

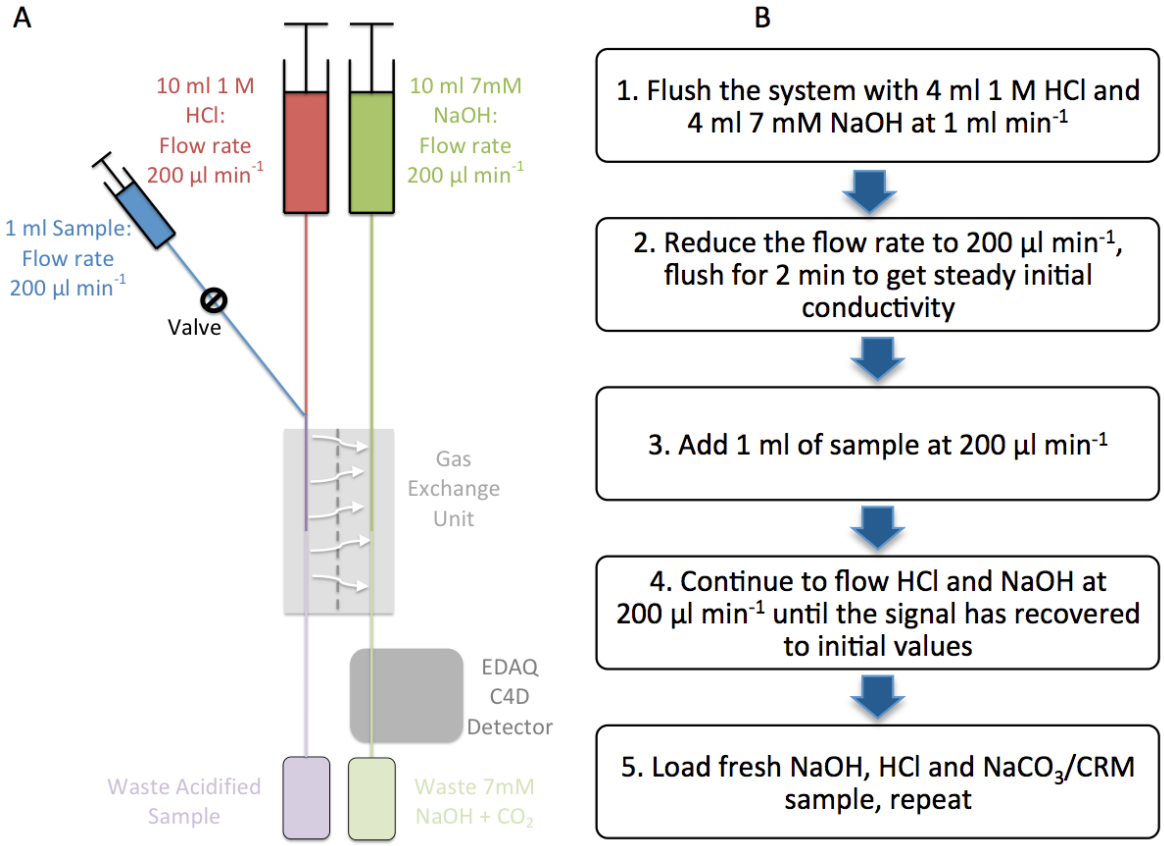

Figure 4.3 Overview of the benchtop instrument. Panel A shows a schematic of the benchtop instrument. Panel B illustrates the measurement cycle with a flow diagram.

Each measurement resulted in a conductivity drop, associated with the acidification of a sample or CRM. The magnitude of that conductivity drop was calculated by subtracting the minimum voltage from the blank voltage; this is referred to as the signal step.

4.2.3 Benchtop Instrument Calibration and Initial Results

For the initial calibration and testing, the system was run at a constant temperature of 25 °C in an environmental chamber (Discovery My, ACS, Italy). When the system was operated in the laboratory the temperature of the detector was found to vary by ~0.5 °C over the course of a run, which would cause a 0.75% change in the conductivity of the acceptor solution, as detailed in section 3.1.1. Initial trials in an environmental chamber reduced the temperature variation over the course of a sample measurement to 0.02 °C, reducing the variability between replicates.

For the calibration a stock solution of 0.5 M sodium bicarbonate (Fisher Scientific, UK) was volumetrically diluted using Milli-Q® water (Merck Sigma, USA) to give four calibration solutions with different DIC concentrations across the range of 1800 - 2400 µmol kg^{-1}. The DIC concentration of the four calibration solutions was determined using an Apollo DIC analyser (SciTech, USA). Each standard was measured in duplicate on the Apollo, and a description of the operation of Apollo is given in section 1.2.1. Each of the calibration solutions was measured in triplicate on the benchtop instrument to generate a calibration curve, shown in Figure 4.4**.**

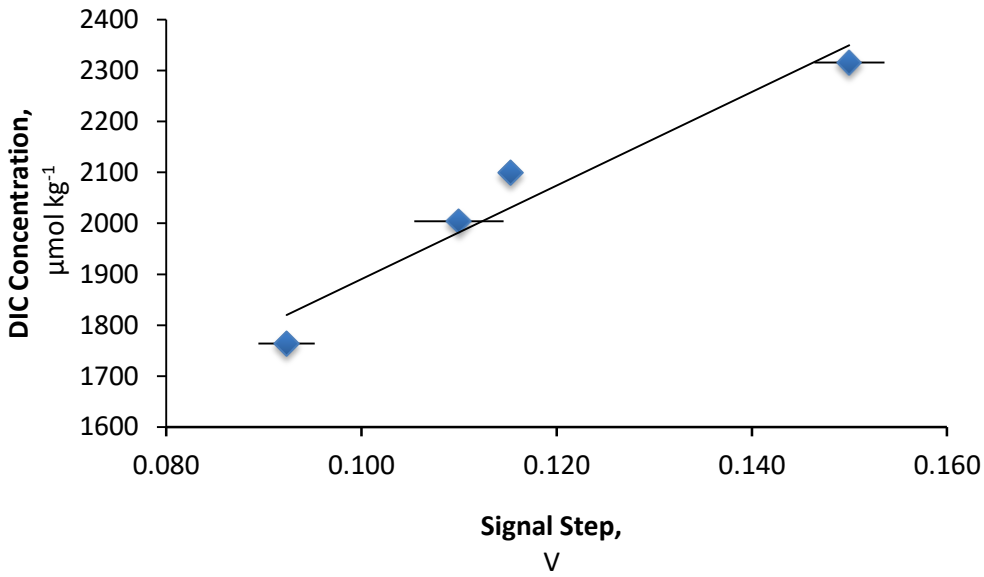

Figure 4.4 Calibration of the benchtop instrument, where the y axis is the signal response recorded by the C4D and is related to the DIC concentrations from standards measured using an Apollo DIC analyser such that [DIC] = 9037.6 × ΔV + 989.1, (R^2 = 0.93, p < 0.001, n = 12, Standard Error = 59.9 µmol kg^{-1}).

The accuracy and precision of the benchtop instrument was assessed by taking five replicate measurements of a Certified Reference Material (CRM, Scripps Institution of Oceanography, University of California, San Diego, USA). The CRM was Batch 151, [DIC] = 2033 µmol kg^{-1}. The results of the benchtop instrument measurements are shown in Table 4.1. The replicate

measurements show that the system ran repeatedly with a low standard deviation between runs, with an overall precision of ± 17 µmol kg^{-1} calculated from the standard deviation of the five replicates. The first replicate showed the largest estimated DIC concentration, which may have been effected by carry-over of the previous sample. If the final four replicates are used, the mean is 2067 µmol kg^{-1} and the precision is 9 µmol kg^{-1}, which is within the range of weather quality measurements as defined by the Global Ocean Acidification Observing Network (Newton *et al.*, 2014). The accuracy, defined as the difference between the mean concentration of the four replicates and the certified concentration value, was + 34 µmol kg^{-1}. This could have been caused by the length of time the CRM bottle was open during the measurements, as once exposed to the atmosphere the CRM can become compromised. However, to have more confidence in this conclusion the uncertainty associated with the measurement was calculated.

Table 4.1 Replicate measurements of CRM 151 with a benchtop DIC system.

Repeat	**Signal Step,** V	**DIC from Calibration,** µmol kg^{-1}
1	0.123	2101
2	0.120	2074
3	0.119	2065
4	0.118	2056
5	0.120	2074
Mean	0.120	2074
Standard Deviation (1σ)	0.002	17

As described in section 1.2.4 precision calculated from the standard deviation of a measurement alone can result in an overestimation of the sensor's performance, and calculating uncertainty is a more appropriate metric for assessing the performance of a measurement technique. To calculate the analytical uncertainty the approaches can be broadly categorised as either "bottom-up" or "top-down" (Worsfold *et al.*, 2019). In the bottom-up approach the measurement procedure is broken into steps and the error estimated for each step can be added together for a combined uncertainty. This method of error propagation can be used to highlight which steps in the analytical process are contributing the most uncertainty to the final measurement. A top-down approach, such as the Nordtest™, uses measured data to estimate the uncertainty in the system (Magnusson *et al.*, 2012). In this approach the data should be collected over several months to fully capture the range of possible errors (Birchill *et al.*, 2019). For the benchtop system there is

insufficient data for a top-down approach and the utilisation of a bottom-up approach allowed for the identification of the main sources of uncertainty in the measurement.

For the benchtop system running in the environmental chamber the three main identified sources of uncertainty are those stemming from the calibration, variations in the sample volume in the syringe, and the temperature influence on the conductivity measurement. The uncertainties are shown in Table 4.2. The uncertainty from the calibration ($u(c_0)$) can be estimated by:

$$u(c_0) = \frac{S}{B}\sqrt{\frac{1}{p}+\frac{1}{n}+\frac{(c_0-\bar{c})^2}{\sum_{j=1}^{n}\left(c_j-\bar{c}\right)^2}} \tag{4.1}$$

Where S is the standard error of the fit (in µmol kg^{-1}), B is the gradient of the linear fit, p is the number of measurements used to determine c_0, c_0 is the determined DIC concentration, $\bar{c}$ is the mean of the concentration of the calibration standards, n is the number of measurements made for the calibration, and j is the index for the number of measurements used in the calibration (Ellison and Williams, 2012). For the calibration this equates to:

$$u(c_0) = \frac{0.006318}{0.000102}\sqrt{\frac{1}{4}+\frac{1}{12}+\frac{(2067-2046)^2}{4700990.3}} \tag{4.2}$$
$$= 35.7\ \mu mol\ kg^{-1}$$

The uncertainty from the syringe volume ($u(V_L)$) consists of the calibration errors from the manufacturer and the errors when reading the syringe. For the 1 mL gas-tight glass syringe (1000 series Hamilton Company, USA) the calibration error provided by the manufacturer is 1 ml ± 1%. From the manufacturer stated calibration error the standard uncertainty is given using a triangular distribution. Assuming the reading error when filling the syringe is also ± 1% with triangular distribution (Csavina *et al.*, 2017) results in:

$$u(V_L) = \sqrt{\left(\frac{0.01}{\sqrt{6}}\right)^2+\left(\frac{0.01}{\sqrt{6}}\right)^2} = 0.006\ ml \tag{4.3}$$

The uncertainty from the temperature effect ($u(f_{temp})$) can be estimated using the relationship found in previous studies, which identified that the conductivity of NaOH is altered by ~1.5 – 2% per °C (McKee, 2009). The temperature recorded in the chamber was found to be 25 ± 0.02 °C, combining the 2% value with the temperature variations in the chamber, using a rectangular distribution (Csavina *et al.*, 2017) gives:

$$u(\mathrm{f}_{temp}) = \frac{0.02\times 0.02}{\sqrt{3}} = 0.0002 \tag{4.4}$$

Table 4.2 Uncertainty values for each step in the benchtop system measurements.

	Description	Value	Standard Uncertainty *u(x)*	Relative Uncertainty u(x)/x
c_0	Measured DIC mean concentration in CRM replicates	2067 µmol kg^{-1}	35.7 µmol kg^{-1}	0.0173
V_L	Sample syringe volume	1.0 ml	0.006 ml	0.0060
f_{temp}	Influence of temperature	1.0	0.0002	0.0002

To calculate the combined uncertainties the relative standard uncertainties are combined using:

$$\frac{u_c(DIC)}{[DIC]} = \sqrt{\left(\frac{u(c_0)}{c_0}\right)^2 + \left(\frac{u(V_L)}{V_L}\right)^2 + \left(\frac{u(f_{temp})}{f_{temp}}\right)^2}$$

$$\frac{u_c(DIC)}{[DIC]} = \sqrt{0.0173^2 + 0.0060^2 + 0.0002^2} \quad (4.5)$$

$$u_c(DIC) = [DIC] \times 0.0182 = 37.6\ \mu mol\ kg^{-1}$$

The calculated uncertainty shows that the calculated DIC concentration from the CRM (Batch 151, [DIC] = 2033 µmol kg^{-1}) replicate measurements of 2067 µmol kg^{-1} is within the uncertainty of this system. This also demonstrated that the largest contributor to the uncertainty was the uncertainty from the calibration. The following section details optimisation completed to increase the magnitude of the signal step, with the aim of improving the signal to noise ratio, ultimately with the goal of reducing the uncertainty from the calibration. This optimisation focused on the solution flow rates and volumes. The benchtop instrument that was optimised used a planar membrane rather than a TIAT as part of the evaluation of the planar system; this is described fully in section 4.3.2. This benchtop instrument demonstrated good initial potential, as shown in the weather quality precision. This system could provide useful information in areas of high daily CO_2 flux, such as areas with high respiration rates or areas with large DIC gradients.

4.3 Simplex Optimisation

In traditional analytical methods, optimising the response of a system requires several variables to be altered individually. This technique, known as univariate optimisation, is an iterative process and in complex systems is slow and labour intensive, relying on running experiments multiple times while changing one variable at a time. During the 1960s simplex optimisation was developed, which allows multiple variables to be altered in each optimisation experiment, while

the algorithm presents future test parameters based on the response of the system. The simplex method achieves this without the need for complex statistical tools, as described in section 4.3.1.

For the DIC sensor there are several factors that can be adjusted to increase the magnitude of the response signal step. In this system, the signal is the conductivity drop resulting from the CO_2 reacting with the OH^-, as described section 3.1.1. Once a detector and GEU have been selected, the two main ways to alter the signal are to vary the volume of sample that is acidified and to vary the length of time the acidified solution remains in the GEU where diffusion takes place.

This section will give a more detailed introduction to simplex optimisation and present results of the simplex optimisation carried out using the second version of the benchtop DIC sensor.

4.3.1 Simplex Optimisation Theory

The term simplex, from simplex optimisation, is a geometric figure that is used to represent the experimental variables as a surface (Walters *et al.*, 1991). The simplex has one more side than the number of variables (N + 1) used in the system. For example, a line would represent a single variable system; a two variable system would be represented by a triangle and a three variable system by a tetrahedron. To carry out a basic simplex optimisation this surface is displaced around the experimental region to find the optimal variables to maximise the signal. Early work detailed the initial version of simplex optimisation (Spendley, Hext and Himsworth, 1962).

In this version of simplex optimisation the simplex is reflected across the plain opposite to the lowest response, with no modification to the simplex form. This can be visualised in Figure 4.5 which shows the initial simplex, in this case a triangle, being reflected across the variable region multiple times to find the optimal variables. The initial experimental variables used are illustrated by the triangle in bold, with the vertices numbered 1, 2, 3 and the optimal response region denoted by the darkest ellipsoid. Of the initial variables tested vertex 1 showed the lowest response so the simplex was reflected across the plane formed between vertices 2 and 3. This was repeated until the optimal response was found.

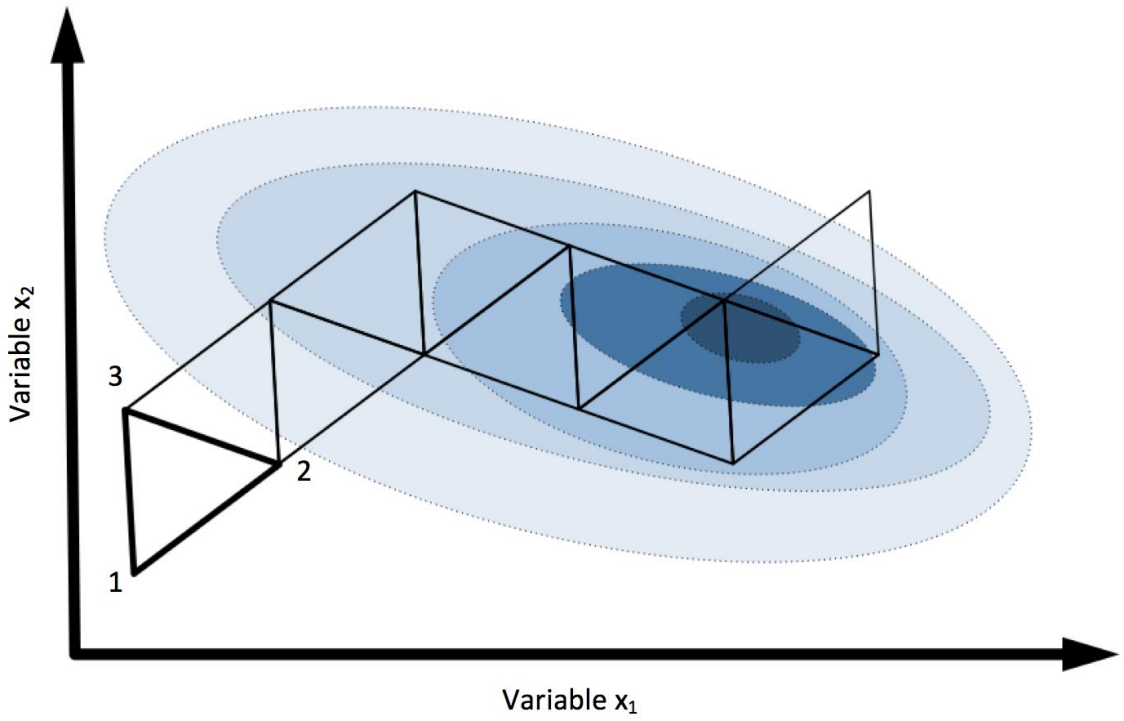

Figure 4.5 Schematic illustrating the basic simplex optimisation. The bold triangle represents the initial test conditions and the darkest ellipse represents the optimal response. Modified from Walters *et al.* (1991).

The basic simplex optimisation was further optimised with the algorithm developed to allow the shape of the simplex to be modified (Nelder and Mead, 1965). This change allowed the method to find the optimal solution more rapidly as the simplex was not only reflected but could also be contracted or expanded as illustrated by the comparative Figure 4.6.

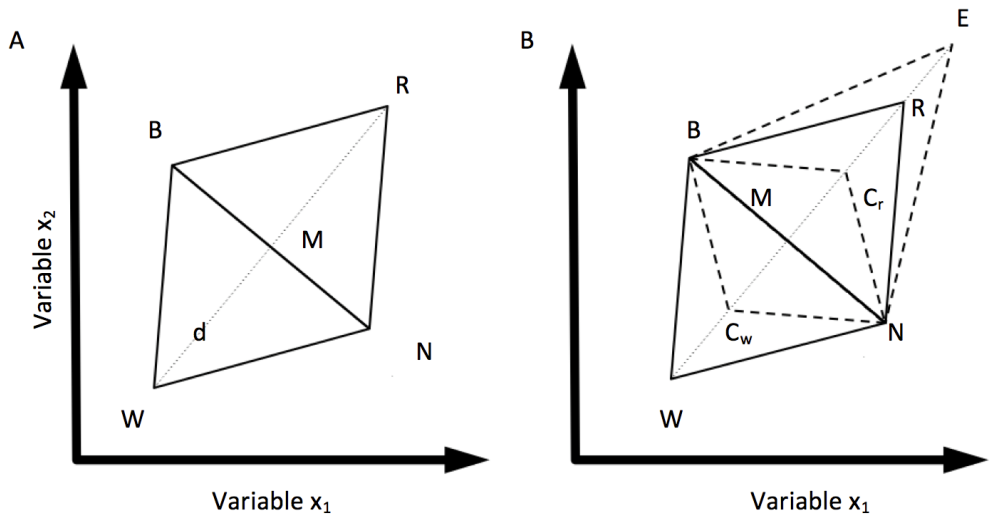

Figure 4.6 Comparison of basic simplex (Panel A) and modified simplex (Panel B). See Table 4.3 for explanation of abbreviations. Modified from Walters *et al.* (1991).

In the earlier version of simplex optimisation, shown in Figure 4.6 Panel A, the vertex B is the best response, N is the next best response and W is the worst value. The simplex optimisation equation, shown in Table 4.3, then predicts the reflected parameters denoted by R. R stands for the reflection and is effectively the point W reflected across the plane BN, which is equivilant to the mid point (M) of B and N, offset from BN by the distance to W, shown by the letter d. The new variable R is tested and then vertices are reassessed and the process repeated.

The modified simplex optimisation, demonstrated in Figure 4.6 Panel B shows the three extra vertices that may be generated, allowing the potential for the simplex to be altered. The simplex maybe expanded to point E, or contracted to point C_r. If the response of the predicted variable performs worse than W it indicates that it is necessary to carry out a contraction in the opposite direction, C_w.

Table 4.3 Definitions and formulas used in simplex optimisation.

Symbol	Definition	Basic Formula	Modified Formula
B	Best Response	-	-
N	Next Best Response	-	-
W	Worst Response	-	-
M	Mid-point on Plane BN	-	-
R	Reflected	R = M + d	R = 2M - W
d	Distance from W to Plane BN	d = M - W	-
E	Expansion	-	E = 3M – 2W
C_r	Contraction	-	Cr = 1.5M - 0.5W
C_w	Contraction and Direction Change	-	Cw = 0.5M + 0.5W

Simplex optimisation has been used to improve a wide range of analytical chemistry methods and more information on these applications can be found in various review papers (Deming, Jr and Denton, 2008; Bezerra *et al.*, 2016).

A potential limitation of simplex optimisation is that the system may only find local maxima, and has the potential to miss the optimal solution. To minimise this the initial variables should be selected after preliminary testing (Walters *et al.*, 1991).

4.3.2 Simplex Optimisation Implementation

Simplex optimisation was used to increase the signal step of the benchtop DIC instrument. The benchtop instrument that was optimised this way used the eDAQ SPL-C4D as the detector, set-up as described in section 4.2. The GEU was a bonded planar membrane, which consisted of a 100 µm Silex membrane bonded between two PMMA chips using the method described in section 2.3.2. This GEU was used as part of the assessment of the bonded GEU. This planar GEU had an acceptor and donor volume of 95 µL. The fluid flow was controlled using the same syringe pumps as described in section 4.2. A single concentration of 2000 µmol kg^{-1} $NaHCO_3$ was used as the sample, with its flow controlled by a Nanomite syringe pump (Harvard Apparatus, UK). The 7 mM NaOH and 1 M HCl flows were controlled by a PhD Ultra syringe pump (Harvard Apparatus, UK).

The response of the system has to be carefully defined for simplex optimisation to be utilised. For the DIC sensor the response for the optimisation work is not simply the conductivity step resulting from the reaction of CO_2 from the acidified sample with NaOH as recorded by the C4D, as used in section 4.2. The response required more careful definition than simply the signal step, as without a caveat to account for the length of time of the signal the simplex optimisation could offer solutions taking too long to be of practical use for the sensor, an issue known as peak band broadening. To account for this the response was taken as the area of the peak representing the conductivity drop, divided by the peak width at mean height (PWMH). This is illustrated in Figure 4.7. Using the metric of peak area divided by PWMH ensured that the simplex tended towards a maximised signal step, without the peak becoming too diffuse or taking too long to be useful in the final sensor.

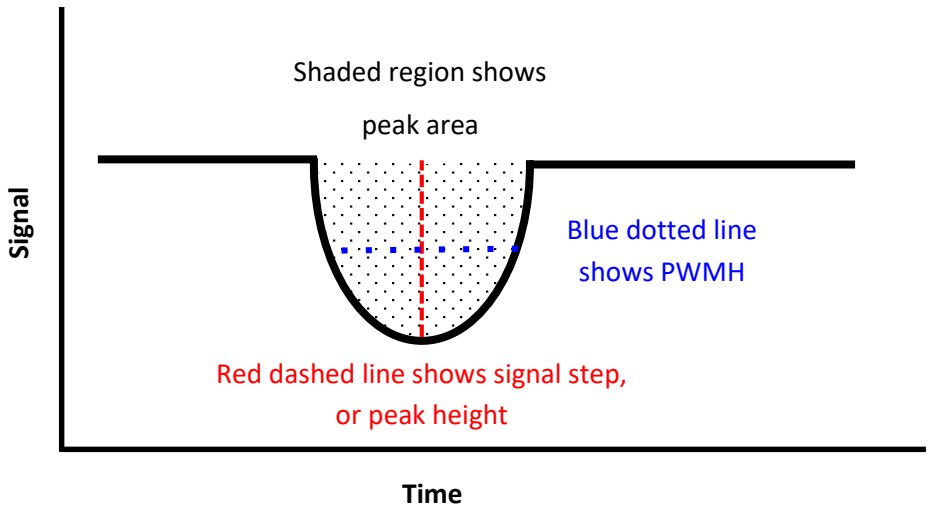

Figure 4.7 Schematic illustrating the response used as the assessment for the simplex optimisation.

The input variables identified to maximise the response were the volume of the $NaHCO_3$ solution added, the flow rate of the sample, and the flow rate of the acid and NaOH. The predication was that increasing the sample volume would increase both the peak height and the peak area as more CO_2 would be available to react with the acceptor. Altering the flow rates would adjust the residence time for the donor and acceptor solutions in the GEU, impacting the length of time available for gas exchange. It was predicted that decreasing the flow rates would increase the length of time available for gas exchange, which would increase the peak area but also increase the peak width, potentially broadening the peak.

The optimisation experiments were carried out at room temperature, so fluctuations in the laboratory temperature would have had an impact on the conductivity measurements, with each 1 ^{o}C change being equivalent to ~ 1.5% change in conductivity. An initial experiment was conducted to test the repeatability of this system, to verify that the results were stable at laboratory temperature. For this test a standard of 100 µL of 2000 µmol kg^{-1} $NaHCO_3$ was used at a flow rate of 35 µL min^{-1}, and both the 7 mM NaOH and 1 M HCl were at a flow rate of 50 µL min^{-1}. These flow rates were selected to give the standard a residence time in the GEU three times longer than the time required for gas exchange predicted by modelling from section 2.3.1. The results of these 3 replicate measurements are presented in Table 4.4. The signal step shows good repeatability and a low standard deviation, less than 10 mV, despite the laboratory temperature variations, however this was greater than the initial benchtop instrument achieved in the chamber (section 4.2) so for this reason the signal step was reported at 10 mV resolution for this work. The peak area also shows good repeatability, with a relative standard deviation of 3.7%. The PWMH had a standard deviation of 12 seconds. As a result of this test each vertex of the simplex optimisation was run twice and the average used to determine the response of the system.

Table 4.4 Reproducibility of benchtop instrument measurements using bonded GEU.

Replicate	**Step** V	**Peak Area**	**PWMH** minutes	**Area/PWMH**
1	0.107	0.480	4.2	0.113
2	0.103	0.503	4.5	0.112
3	0.095	0.468	4.6	0.102
Mean	0.102	0.484	4.4	0.109
Standard Deviation (1σ)	0.006	0.018	0.2	0.006

Before the simplex optimisation commenced, initial experiments were carried out to establish the first vertices; this tested a range of sample volumes from 35 to 200 µL and altered the flow rates such that the residence time in the GEU ranged from 1 minute to 20 minutes to ensure the simplex was carried out over a range likely to find the optimal solution. From these experiments the initial vertices were selected, as shown in the first five rows of Table 4.5.

4.3.3 Simplex Optimisation Results

A total of eleven runs were carried out as part of the simplex optimisation. The results of these are presented in Table 4.5. For vertices 6 and 9 the contracted and reflected (C_w) were tested as the reflected (R) vertices gave negative flow rates, which would be experimentally meaningless. For vertex 11 the C_w was also selected as the R was close to zero.

Table 4.5 Details of simplex optimisation experiments.

Vertex Number	**Sample Volume** µl	**NaOH and HCl Flow Rate** µl min^{-1}	**Sample Flow Rate** µl min^{-1}	**Signal Step** V	**Area / PWMH**	**Time to Minimum V** Minutes	**Initial Rank**	**Vertex Descriptor**
1	50	35	50	0.21	0.290	8	B	
2	35	35	35	0.14	0.184	8	…	
3	200	50	35	0.17	0.181	14	…	
4	100	50	35	0.16	0.177	9	N	
5	50	100	50	0.07	0.082	4	W	
6	70	70	44	0.09	0.091	7		C_w*
7	122	15	33	0.44	0.460	19		R
8	100	17	42	0.43	0.489	17		R
9	140	40	40	0.25	0.252	10		C_w*
10	170	20	50	0.50	0.519	16		R
11	125	40	30	0.37	0.387	11		C_w**
	*Reflected rejected as proposed flow rates were negative ** Reflected rejected as proposed flow rates were close to zero							

The results of the simplex optimisation are also presented visually in Figure 4.8. This shows that the biggest improvement in response was between the vertices 6 and 7. The drop in response on vertices 9 and 11, relative to the preceding vertices, indicates the simplex had moved in the wrong direction. Vertex 10 had the greatest response, increasing the step signal to 0.50 V from an initial low value of 0.14 V.

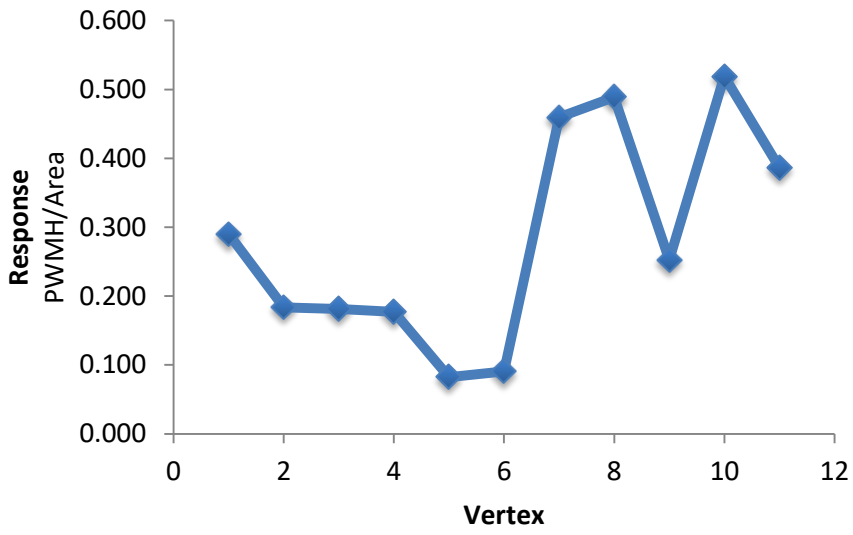

Figure 4.8 Simplex optimisation response for each of the vertices tested.

4.3.4 Discussion

The simplex optimisation demonstrated that within 11 iterations of testing the response of the sensor, defined as the peak area divided by the PWMH, the response was improved by 80%. This also resulted in a greater than doubling of the signal step, from 0.14 V to 0.5 V. This was achieved using a sample volume of 170 µL at a flow rate of 50 µL min^{-1} and a flow rate of 20 µL min^{-1} for the NaOH and acid. These settings resulted in a longer time to the peak minimum, from 8 minutes for the initial settings compared to 16 minutes for the optimised settings although this increase in time led to a significantly larger signal step. This increased time for each sample would still allow the sensor to function at a similar rate to the current benchtop instruments measuring DIC.

This optimisation found that to maximise the signal step the optimum ratio of the sample to acid flow rates was 1:2.5. However this ratio is currently unobtainable with the current LOC v3 hardware (Beaton *et al.*, 2012; Clinton-Bailey *et al.*, 2017; Grand *et al.*, 2017). In the current LOC v3 system a single stepper motor drives all three syringe pumps' barrels simultaneously, which is a potential limitation of the system. One method to vary the flow rate is to alter the barrel diameters on the pump. In the current hardware there are two barrel sizes which can be used to set a 1:9 flow ratio. To be able to adjust the flow rates to the desired ratio, independently

controlled pumps are required and are currently being developed for a new version of the LOC hardware. Once this improved pump has been tested, its application in the DIC sensor would allow the use of varying flow rates, which this optimisation work has demonstrated as a potential method to increase the signal step.

Chapter 5 Lab On Chip: Miniaturisation of Dissolved Inorganic Carbon Sensor

5.1 Introduction

Historically, all oceanographic data collection involved taking a water sample and either measuring it on a ship or returning it to a laboratory for measurement. Early temperature measurements, for example, involved collecting a bucket of seawater and measuring its temperature back on the ship (Carella *et al.*, 2017) while early salinity measurements involved making a titration of the collected sample (Pawlowicz *et al.*, 2015). Today, there are a wide range of sensors capable of making high quality, high frequency, measurements of physical water properties (temperature, salinity) but the technology to enable biogeochemical measurements to be taken *in situ* is still developing. Some biogeochemical sensors now exist, such as the SeaFET pH sensor (Sea-Bird Scientific, USA), which are capable of delivering high frequency measurements but often have issues with measurement stability or precision (Bresnahan *et al.*, 2014; Rérolle *et al.*, 2016; Miller *et al.*, 2018). To achieve the high precision measurements required to study the marine environment, many parameters still require samples to be collected and run in specialist facilities. One solution to this challenge has been to miniaturise laboratory techniques using microfluidics, which can then be deployed *in situ*. These miniaturised laboratory instruments became known as “Lab on Chip” (LOC) sensors.

5.1.1 Lab On Chip

Researchers have been using microfluidics to miniaturise laboratory systems since the 1980s. Initially those early systems were used for biomedical applications, allowing researchers to conduct trials on single cells, but their use has spread wider into chemistry (Convery and Gadegaard, 2019). The term microfluidics generally refers to systems operating on channels with width/height scales of the order of 100s nm to 100s µm and sample volumes measured in µL. By utilising small channels, fluids move in laminar flow, which is more easily modelled than turbulent flow, allowing systems to be accurately modelled before fabrication. There is no convective mixing in laminar flow, and so molecular diffusion dominates solute transport.

The requirements for a miniaturised DIC sensor were outlined in section 1.5.1. In summary, the sensor needs to make precise and accurate measurements, have small physical dimensions (or form factor), operate autonomously with low power requirements, have low reagent

consumption and be capable of measurement at depth. Utilising a microfluidic LOC platform for developing a DIC sensor can satisfy these requirements. Applying microfluidics inherently gives the LOC platform a small form factor and low reagent consumption. Pumping low volumes can also reduce the amount of power required to operate the sensor.

This chapter will detail the work carried out to design a microfluidic DIC LOC sensor. First an overview of the sensor is introduced. Then data from laboratory characterisation and field deployments of the sensor Version One are presented, along with details of the modifications made to the second version. The final section of the chapter details the characterisation and field deployments of the sensor Version Two.

5.1.2 STEMM-CCS

The development of the DIC LOC sensor was funded, in part, as a component of the European Union Horizon2020 project Strategies for Environmental Monitoring of Marine Carbon Capture and Storage (STEMM-CCS). The focus of the STEMM-CCS project was to increase understanding of Carbon Capture and Storage (CCS) in the marine environment. The aim of CCS is to mitigate anthropogenically emitted greenhouse gases in the atmosphere by trapping and storing them in geological systems (Turley *et al.*, 2009; Blackford *et al.*, 2014, 2015). For STEMM-CCS key goals were to establish a baseline for the environmental conditions around a potential site for CCS and then to test novel techniques to detect a simulated leak, induced by injecting $CO_{2(g)}$ into the surface sediment.

The development of the DIC sensor was a component of to two aspects of the project. The first was the aim to develop new tools and techniques to identify potential emissions of CO_2 in marine systems and the second was to establish geochemical baseline conditions. The project presented two opportunities for field deployments of the sensor in the North Sea. The first deployment was a cruise in 2018; its goal was to carry out an environmental baseline study. The second deployment in 2019 was during the gas release experiment phase of the project focused on the detection of the simulated leak.

5.2 Design of the DIC LOC Sensor

The DIC LOC sensor design was based on that of the benchtop instrument described in section 4.2, with each measurement consisting of three main steps: acidification of sample, gas diffusion into the acceptor solution, and finally the measurement of the conductivity drop, shown in Figure 5.1.

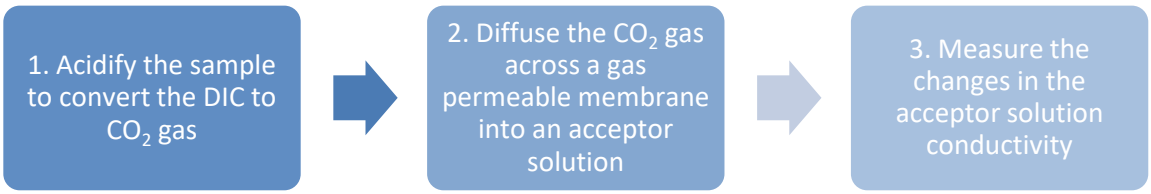

Figure 5.1 Flow diagram showing an overview of the DIC LOC sensor operation.

For the prototype DIC LOC sensor flexibility was a key objective to facilitate optimisation, so for this reason a modular design was utilised. This design consisted of three modules, each corresponding approximately to one of the three measurement steps as shown in Figure 5.1. The LOC Fluid Manipulation Module, described in section 5.2.1 and shown in Figure 5.2, controlled the fluid pumping and manipulation. The gas exchange module, selected following the work outlined in chapter 2, was a Tube In A Tube (TIAT) Gas Exchange Unit (GEU) as described below in section 5.2.2. The conductivity measurement was carried out using a Capacitively Coupled Contactless Conductivity Detector (C4D) module as described in section 5.2.3 and visible in Figure 5.2.

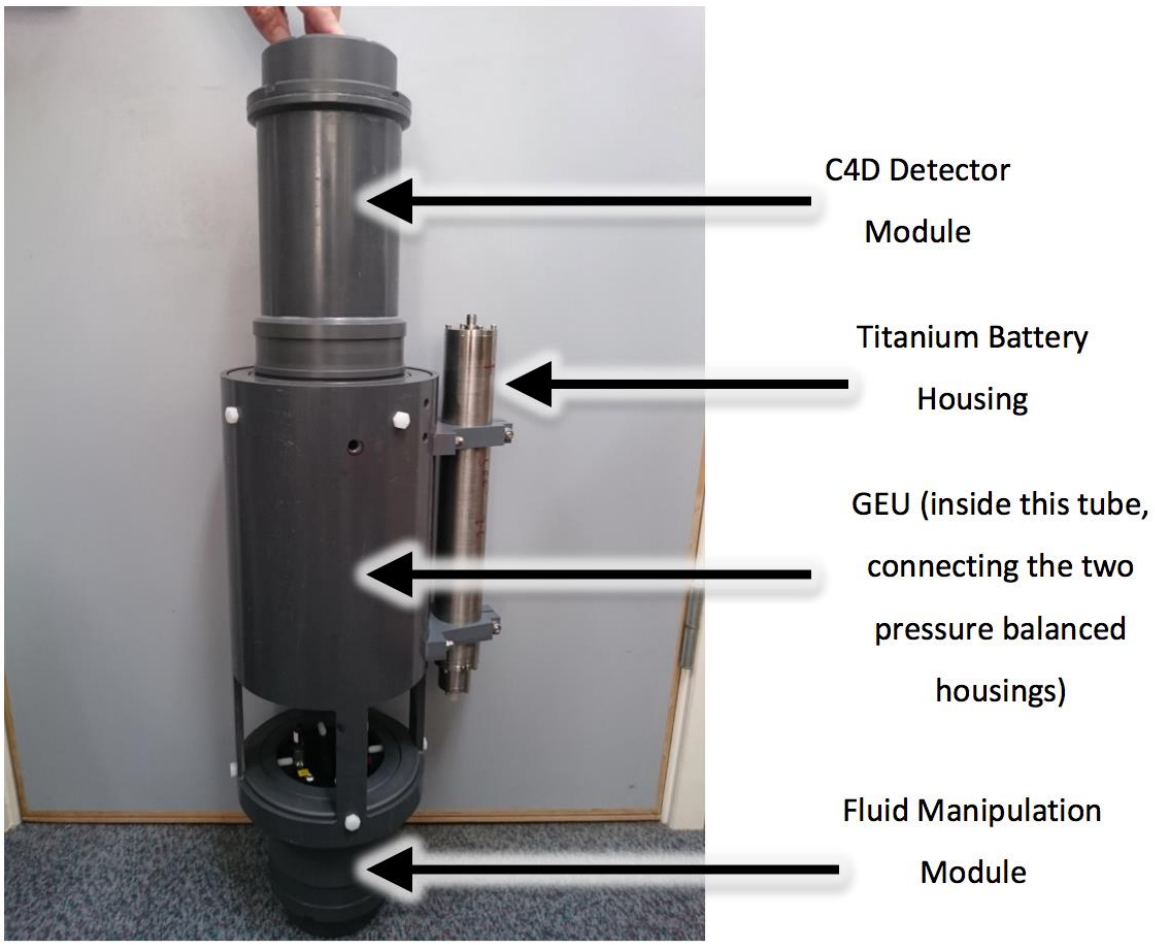

Figure 5.2 Photograph of DIC LOC sensor to illustrate the three modules.

5.2.1 DIC LOC Fluid Manipulation Module

The fluid manipulation module is based on the LOC v3 platform (Beaton *et al.*, 2012; Rérolle *et al.*, 2013; Clinton-Bailey *et al.*, 2017; Grand *et al.*, 2017), an example of which is shown in Figure 5.3. The LOC v3 sensors share a similar design and fabrication technique but they have different flow paths and external components. The function of the LOC fluid manipulation module in the DIC sensor is to control the manipulation of the sample and reagent fluids, and also to record data.

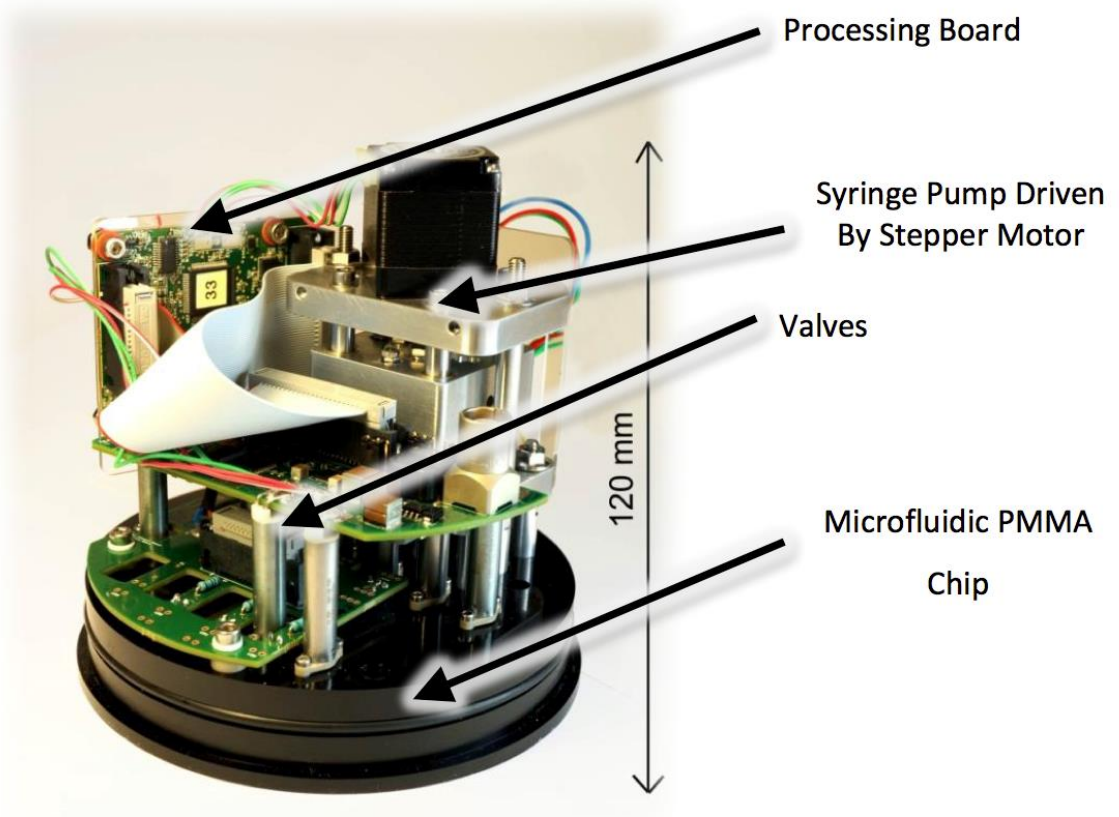

Figure 5.3 Annotated photograph of Generic LOC v3 hardware. Credit: OTEG Stock Image.

The microfluidic chip is fabricated from 3 layers of Poly(methyl methacrylate) (PMMA) with channels 150 µm wide and 300 µm deep micro-milled, using a Datron Neo (Datron, Germany) into one layer, before the layers are sealed by a solvent bonding process (Ogilvie *et al.*, 2010). The CAD design for the DIC sensor is shown in Figure 5.4. The chip forms one of the two end caps for the cylindrical pressure housing. The pressure housing is made from 125 mm diameter plastic tube and is filled with mineral oil (Sigma Aldrich, UK). The housing uses O-rings at either end to create a watertight seal with the chip at one end and a pressure-balancing cap at the other end. This pressure compensating design gives the housing its depth rating of at least 6000 m. The pressure tolerant electronic hardware, which provides the automation and control of the valves, pumps and data logging, is within the pressure housing. The firmware controlling the sensor is programmed using a bespoke application developed in-house to run on a PC.

When designing the layout for the microfluidic channels a key consideration was to build a system that maximised flexibility to allow various sample and acid pumping scenarios to be tested. A syringe pump, driven by a stepper motor, controls the fluid pumping on the LOC v3 platform. The stepper motor drives a plate with up to four syringe pump plungers attached to it, shown in Figure 5.3. There are two potential syringe barrel size options, a large one with 9.68 mm diameter and a small barrel with 3.29 mm diameter, giving syringe volumes 720 µL and 80 µL respectively. This pump design, therefore, has a fixed volume ratio of large to small barrels, and, hence, a fixed flow rate ratio of 9:1. The volume of the C4D detector dictated that the sensor required a large NaOH acceptor barrel. A second large barrel was added to the chip, which was designed with four potential fluid inlets. The first inlet is for the acid. The remaining three inlets were kept flexible. Depending on the deployment, the sensor could be configured with either one or two sample inlets, as for certain deployment scenarios it was a requirement that the sensor should be able to take measurements from two spatially distinct locations. To allow the sensor to carry out *in situ* calibrations, the remaining inlets can be used for DIC standards, which, throughout this study, were batches of CO_2 in Seawater Certified Reference Materials (CRMs; Scripps Institution of Oceanography, University of California, San Diego, USA). A small barrel was added to test whether the acid or sample could be added in a smaller volume.

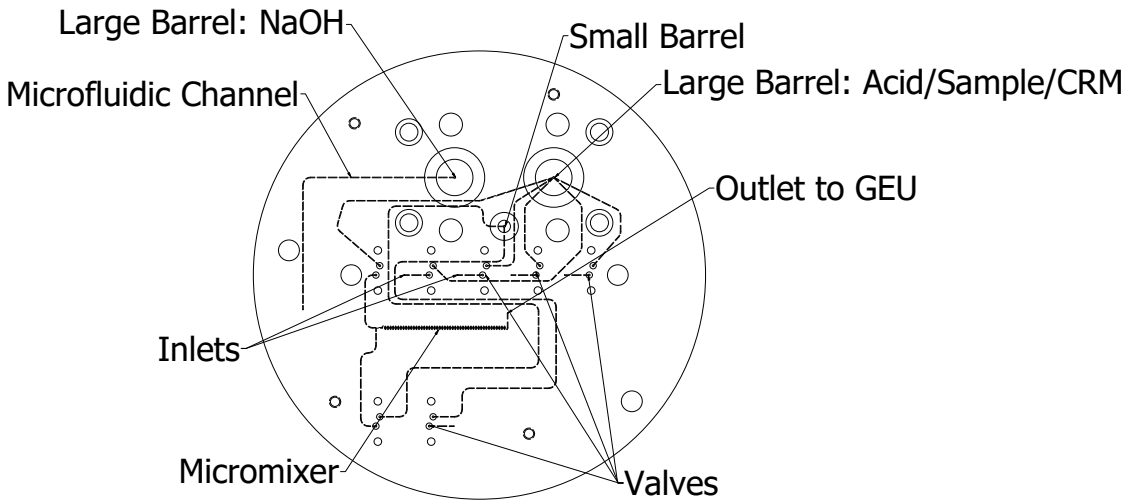

Figure 5.4 The CAD design used to mill the chip, created using Autodesk® Inventor® software.

To control the flow in the microfluidic channels two different types of valve were used; on chip solenoid valves and off chip check valves. The on chip vales were micro-inert solenoid vales (LFN125032H, The Lee Company, USA). The valves have been widely used in other LOC v3 sensors (Beaton *et al.*, 2012; Rérolle *et al.*, 2013; Clinton-Bailey *et al.*, 2017; Grand *et al.*, 2017) as they have low internal volume, zero dead volume, low power consumption, small form factor and are chemically compatible. On the schematic of the sensor presented in Figure 5.5 these are illustrated by red circles with red crosses inside. To control the acceptor NaOH fluid flow two

check valves were used, shown in Figure 5.5 as black circles with a green V (CI-5V, Bio-Chem Fluidics, New Jersey, USA,). These were not mounted on the chip but were connected to a PEEK Tee connector that links the reagent bag to the chip, and the chip to the GEU. One valve functioned as an inlet allowing the reagent to be pumped into the chip from the bag and the second as an outlet allowing the reagent to be pumped to the GEU. These check valves were selected as this channel did not require complex control and the check valves offer a low cost solution, no power requirement and low internal volume.

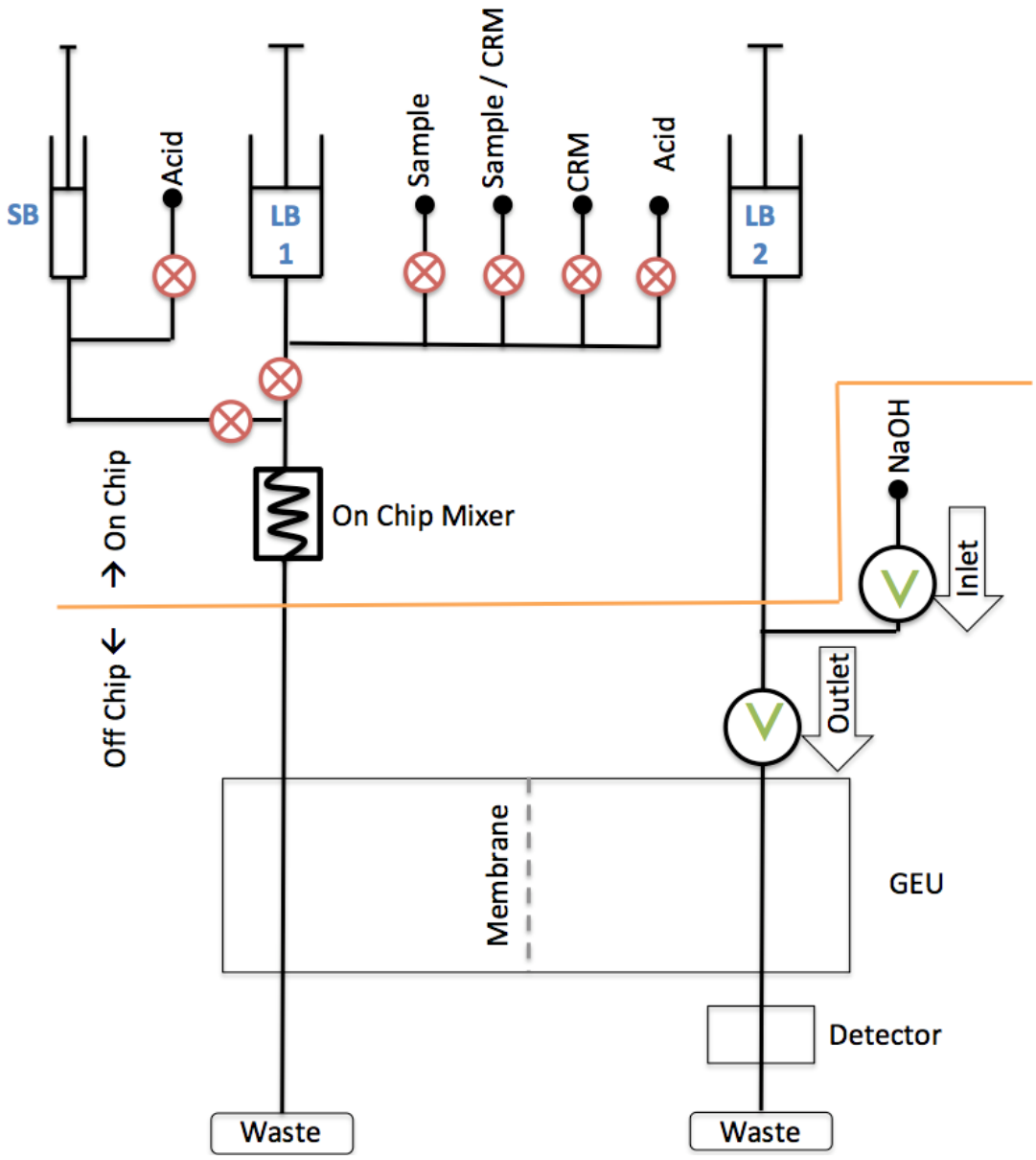

Figure 5.5 Line diagram of sensor showing the two Large Barrels (LB), Small Barrel (SB), valves (red circles with crosses), and check valves (black circles with green V denoting flow direction). Above the orange line are the components that make up the LOC fluid manipulation module, and below the orange line are the Off Chip components, including the GEU, detector and check valves.

An inertial microfluidic mixer was incorporated into the chip design to enhance mixing of the sample fluid and the acid. This was developed in-house and utilises the secondary flow of a fluid in a curved microfluidic channel to aid mixing (Di Carlo, 2009). The enhanced mixing of the acid and sample reduces the time taken for complete acidification to occur, increasing the potential sampling frequency.

The reagents were stored in either blood bags or gas sampling bags, depending on their sensitivity to CO_2. The 1 M HCl was made by volumetric dilution of 12 M reagent grade HCl (Sigma Aldrich, UK). As the acid is not sensitive to the effects of gas exchange with the atmosphere, it was stored in a 1 L Flexboy™ bag (ThermoFischer Scientific, USA). The 7 mM NaOH was diluted volumetrically from a stock solution of 0.1 M NaOH (Sigma Aldrich, UK). Because both the acceptor solution (7 mM NaOH) and the CRM are sensitive to exposure to the atmosphere, they were stored in 1 L Gas Tight Multilayer Foil Lined bags (Restek, USA). These bags were selected because their CO_2 permeability (0.0078 $cm^3\ m^{-1}\ day^{-1}$) was several orders of magnitude lower than the CO_2 permeability of the Flexboy™ bags (19.830 $cm^3\ m^{-1}\ day^{-1}$). The multilayer foil bags were filled by syphoning the fluid into the bags using Viton® tubing (Cole-Palmer, USA), to reduce the exposure of the fluids to the atmosphere. The reagent bags were connected to the chip and TIAT with PEEK tubing with 500 µm ID and 1600 µm OD. PEEK tubing was selected because it has a lower diffusion coefficient for CO_2 ($1.4\times10^{-7}\ cm^2\ s^{-1}$) compared to the diffusion coefficient of CO_2 for PTFE ($7\times10^{-7}\ cm^2\ s^{-1}$) tubing that is widely used for other LOC v3 sensors (Beaton *et al.*, 2012; Rérolle *et al.*, 2013; Clinton-Bailey *et al.*, 2017; Grand *et al.*, 2017). Waste was collected in two separate 5 L Flexboy™ bags (ThermoFischer Scientific, USA), allowing the waste containing the CRM with trace mercuric chloride levels to be disposed of safely.

To prevent suspended sediment, or biology, blocking the channels in the sample a disposable 13 mm 0.45 µm pore size Millex-HP filter (Sigma Aldrich, UK) was used on the sample inlet.

5.2.2 DIC LOC Gas Exchange Unit Module

A TIAT was selected for the GEU of the prototype DIC LOC, following the work described in Chapter 2. While several membrane materials were tested, Teflon™ AF2400 (Biogeneral, USA) was selected for the prototype and initial versions of the sensor. The Telfon™ AF2400 tubular membrane selected had a wall thickness of 100 µm (810 µm OD, 610 µm ID). The outer PEEK tubing selected for the final version had an ~1600 µm OD and ~1000 µm ID. This PEEK gave the TIAT a volume ratio of 1 : 1 for the outer and inner tubes. The length of the TIAT used for the final version of the DIC sensor was 300 mm, which gave the acceptor and donor volume inside the TIAT of ~100 µL.

By selecting a standalone TIAT instead of integrating the GEU directly into the fluid manipulation module the sensor gained flexibility, as the ratios of acceptor and donor volumes could be easily adjusted without having to refabricate an entire chip. Another benefit of the standalone TIAT is that it is physically accessible, allowing easy replacement and repair in the event of leaks during operation. The TIAT also acted as the fluidic link between the microfluidic chip module and the detector module, providing the connection between the pump in the LOC module and the detector module.

5.2.3 DIC LOC Conductivity Detector Module

As a result of the work described in Chapter 3, a custom-made conductivity detector was selected as the detector for the DIC LOC sensor. Specifically, eDAQ Pty Ltd, Australia, manufactured the C4D-EPU359 unit optimised for the relevant range of conductivities, determined to be $0.5 - 2$ mS cm^{-1} in section 3.1.1. This board was housed in a pressure-balanced oil filled housing, similar to the housing of the fluid manipulation module described in section 5.2.1. To make temperature corrections to the conductivity data accurate temperature measurements of the acceptor fluid are required, therefore a thermistor (Ampenol NTC P60BB203K, Pennsylvania, USA) was mounted directly in the acceptor fluid flow of each sensor. The thermistor was positioned immediately after the C4D electrodes, highlighted in Figure 5.6. These thermistors were selected due to their rapid response time, allowing accurate temperature measurements to be made of the NaOH acceptor fluid. The thermistors were calibrated against a precision thermometer (F250 mk2, Automatic Systems Laboratories, UK) which itself was calibrated against a SBE35 RT (Sea-Bird Scientific, USA), which is accurate to ± 1 mK. The thermistors were calibrated by taking reference readings over the range of 5 ^{o}C to 35 ^{o}C in a constant temperature water bath (7009 model Fluke, USA). A unique cubic relationship was established between the thermistor voltage and F250 mk2 temperature for each thermistor. Using the standard error of the regression fit of the voltage vs. temperature data as a metric, thermistor temperature uncertainty was better than 0.06 ^{o}C.

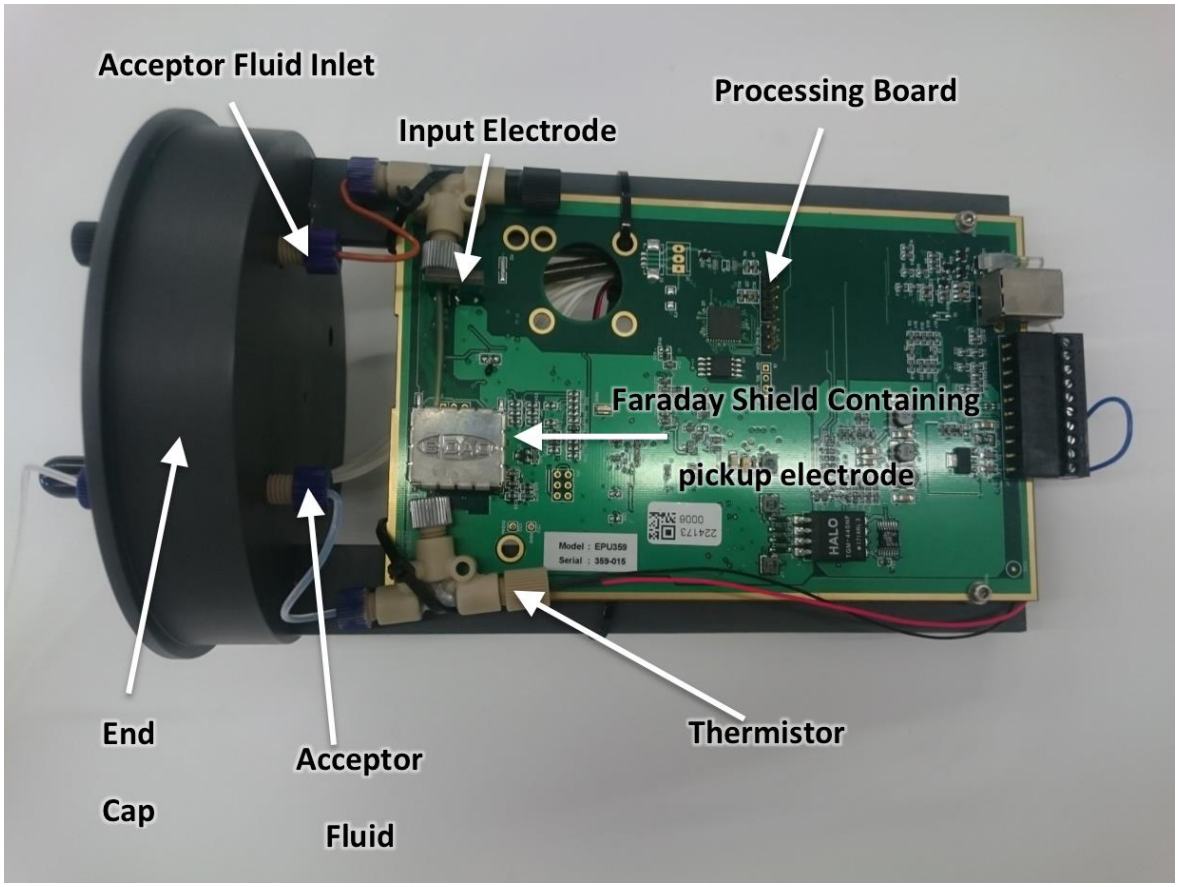

Figure 5.6 Annotated image of the C4D EPU359 board used in the LOC sensor.

The conductivity and thermistor temperature data were passed from the detector module to the processing board housed in the fluid manipulation module via an IE-55 cable, where the data were recorded to a micro SD card (SanDisk, USA). The C4D-EPU359 recorded a voltage proportional to the conductivity of the fluid between its electrodes; this voltage was used as the raw data. Each measurement resulted in a conductivity drop, associated with the acidification of a sample or CRM. The step of that conductivity drop was calculated by subtracting the minimum voltage from the blank voltage, where the blank voltage is measured when there is only acid and NaOH flowing in the GEU. This drop is referred to as the signal step and is illustrated in Figure 5.7. Various calibrations were trialled to convert the signal step (in V) to DIC concentration (in $\mu mol\ kg^{-1}$). These calibrations are described further in the following sections.

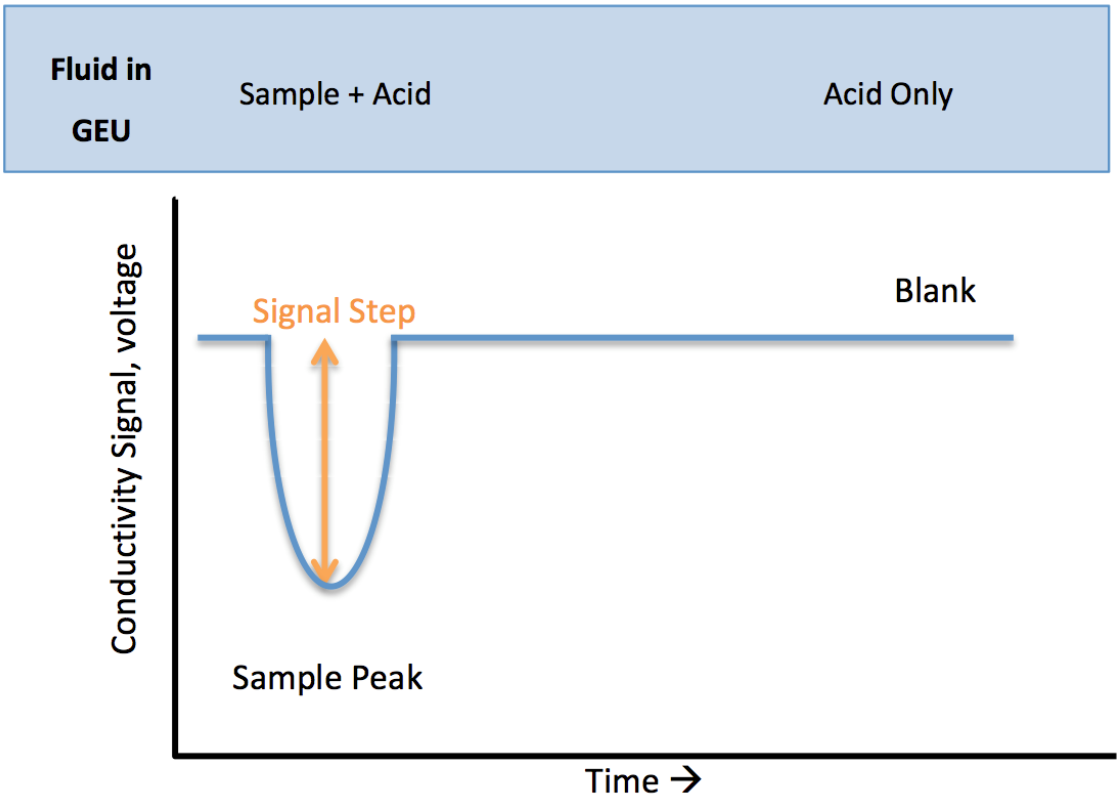

Figure 5.7 Illustration of the measured conductivity signal. The signal step is shown by the orange arrow and is calculated by subtracting the minimum voltage of the sample peak from the blank voltage. The text in the box above the graph illustrates which fluids are in the GEU.

The raw conductivity data were smoothed during processing to reduce noise. A Savitzky-Golay filter of 4th order and window length of 33 was selected as it preserves peaks with less rounding than a simple moving average filter (Press and Teukolsky, 1990). Following the filtering, the data were normalised to a reference temperature using a temperature correction factor. This is because the conductivity of a solution is dependent on both the concentration of ions and also their average velocity, which is a function of the temperature of the solution (Gray, 2005). Temperature correction of raw conductivity data is widely used in handheld conductivity instruments, so that readings taken at different temperatures can be directly compared (Mäntynen, 2001; Mettler Toledo, 2012). The temperature correction factor (α) can be expressed as follows (Mäntynen, 2001; Gray, 2005; Mettler Toledo, 2012):

$$\alpha = \frac{V_t - V_{ref}}{V_{ref} \times (T_t - T_{ref})}, \quad (5.1)$$

where V_t is the conductivity measurement at a temperature (T_t) and V_{ref} is the reference conductivity (V_{ref}) at a reference temperature (T_{ref}). Re-arranging equation 5.1 gives:

$$V_t = \alpha \times V_{ref} \times (T_t - T_{ref}) + V_{ref} \quad (5.2)$$

The α factor for each sensor was determined based on equation 5.2 by linear regression of the smoothed sensor conductivity measurements (V_t) in 7 mM NaOH against ($T_t - T_{ref}$) across a range of internal thermistor temperatures (T_t) with T_{ref} = 25 °C. Based on this, V_{ref} is equal to the regression intercept and α is found by dividing the slope of the fit by the intercept. The standard error (SE) of α was calculated by propagation of the standard error (SE) of the regression slope and intercept. The normalised conductivity measurement ($V_{normalised}$) can then be calculated from:

$$V_{normalised} = \frac{Vt}{1 + \alpha \times (T_t - T_{ref})} \quad (5.3)$$

To determine α, sensor conductivity measurements were taken in 7 mM NaOH in a constant temperature environmental chamber (Discovery My, ACS, Italy) set to temperatures from 5 to 25 °C. The temperature recorded by the internal thermistor in the detector module was ~4 °C warmer than the chamber temperature, so V_t was measured at T_t = 9 to 28 °C. The smoothed data from this experiment can be described by the linear regression fit, V_t = 1.506 + 0.03676 (T_t – 25), (R^2 = 0.99724, p < 0.001, n = 21, $SE_{regression}$ = 0.004 V), from this α was calculated to be 0.0244 ± 0.0032. This α was used to normalise the data, which are plotted in Figure 5.8. This has removed the temperature influence from the data as indicated by the non-statistically significant linear regression fit to the normalized data ($V_{normalised}$ = 1.508 + 0.00039 (T_t – 25), (R^2 = 0.01931, p = 0.548, n = 21, $SE_{regression}$ = 0.017 V).

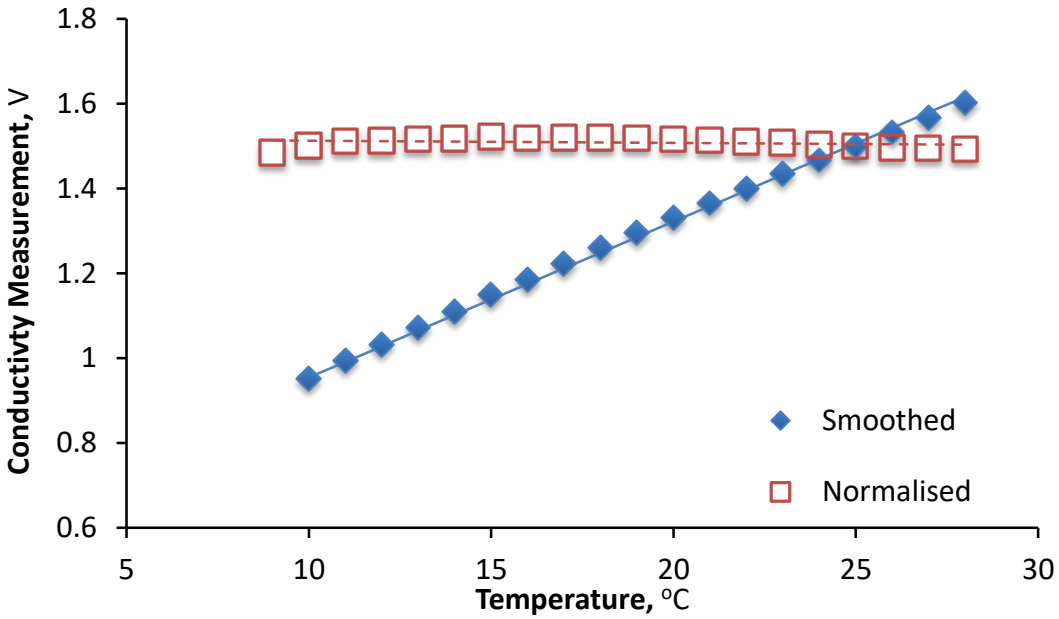

Figure 5.8 Chamber data used to calculate alpha. The solid blue and dashed red lines represent the linear fit to the data as described in the main text.

The change in conductivity due to the temperature change can be converted into an equivalent DIC change per °C, using the calibrations detailed in Table 5.6. For the smoothed data the voltage

step over the 19 °C is 0.65 V, converting this to a DIC concentration gives a value of 13.8 µmol kg^{-1} $°C^{-1}$. For the temperature normalised data the step is 0.008 V over 19 °C, which equates to 0.2 µmol kg^{-1} $°C^{-1}$.

This method of temperature normalisation relies on a linear relationship between temperature (T_t) and conductivity (V_t) across the expected operational temperature range of the sensor and should not be extrapolated outside the experimental temperature range.

5.3 DIC LOC Version One

Two units of DIC LOC Version One were fabricated for the target deployment during the 2018 STEMM-CCS cruise. The goal of this cruise was to establish the baseline conditions at the North Sea location before the gas release experiment in 2019 (Achterberg and Esposito, 2018). Prior to the cruise, the sensors were calibrated in the laboratory and then field-tested for two days with deployment in an estuarine environment. The objective of these tests and deployments was to assess sensor performance and calibration techniques, as well as to highlight potential design modifications for the second version of the DIC LOC sensor, which would be deployed on multiple platforms for the STEMM-CCS gas release experiment in 2019.

5.3.1 DIC LOC Version One Overview

One goal of the field test was to evaluate the measurement cycle protocol that had been developed in laboratory testing. In this protocol, first the blank measurement was recorded when only acid and NaOH flowed in the GEU. Then the system was flushed with the sample to be measured, before the sample was loaded and acidified using the small barrel, and the signal step in conductivity (Figure 5.7) was recorded. The system was then flushed before a CRM was measured in the same way as the sample. The measurement cycle took 48 minutes, giving a sampling frequency of 1 sample per hour, with details shown in Table 5.1. In the Version One deployments, a single CRM was used on the sensor, and the spare inlet channel was plugged with a ¼−28 blanking plug.

Table 5.1 The DIC LOC Version One sensor measurement cycle.

Step	Process	Action	Flow Rate (µL min^{-1})	Time (min)
1	Load acid for blank	Load Large Barrel 1 (LB1) with acid, Small Barrel (SB) with acid and Large Barrel 2 (LB2) with NaOH	850	1
2	Inject to measure blank	Inject LB1 acid to mixer, SB acid to mixer, LB2 to GEU	100	7
3	Load sample for flush	Load LB1 sample, SB acid and LB2 NaOH	850	1
4	Inject for sample flush	Inject LB1 sample to mixer, SB acid to bag, LB2 to GEU	100	7
5	Load sample for measurement	Load LB1 sample, SB acid and LB2 NaOH	850	1
6	Inject sample and acidify with small barrel	Inject LB1 sample to mixer, SB acid to mixer, LB2 to GEU	100	7
7	Load acid for flush	Load LB1 acid, SB acid and LB2 NaOH	850	1
8	Inject for acid flush	Inject LB1 acid to mixer, SB acid to mixer, LB2 to GEU	100	7
9	Load CRM for measurement	Load LB1 CRM, SB acid and LB2 NaOH	850	1
10	Inject CRM and acidify for measurement	Inject LB1 CRM to mixer, SB acid to mixer, LB2 to GEU	100	7
11	Load acid for flush	Load LB1 acid, SB acid and LB2 NaOH	850	1
12	Inject for acid flush	Inject LB1 acid to mixer, SB acid to mixer, LB2 to GEU	100	7
			Total	48
Repeat steps 1 to 12, starting so that each seawater sample is loaded on the hour.				

5.3.2 Calibration

For the DIC LOC Version One, three calibration methods were evaluated to determine the most reliable way to convert the smoothed, temperature-corrected voltage step to DIC concentration. The first calibration method was established by measuring three CRMs (batch 154 [DIC] = 2037.68 µmol kg^{-1}; batch 162 [DIC] = 2177.27 µmol kg^{-1}; batch 164 [DIC] = 2238.89 µmol kg^{-1}) in an environmental chamber (Discovery My, ACS, Italy) set to 15 °C. The range of the CRM certified values covered the likely range of DIC concentrations at the field

site in the North Sea. Five replicate measurements were made for each CRM and the voltage versus certified DIC concentration data were used to determine a calibration curve for the sensor, shown in Figure 5.9. The calibration in equation 5.4 was used as the initial calibration and is referred to from here as the chamber calibration.

$$Sample\ DIC\ Concentration\ (\mu mol\ kg^{-1}) = 4727\ \times\ Sample\ Signal\ Step\ (V) + 300.88 \quad (5.4)$$

(R^2 = 0.991, p < 0.0001, n = 3, $SE_{regression}$ = 0.003 µmol kg^{-1})

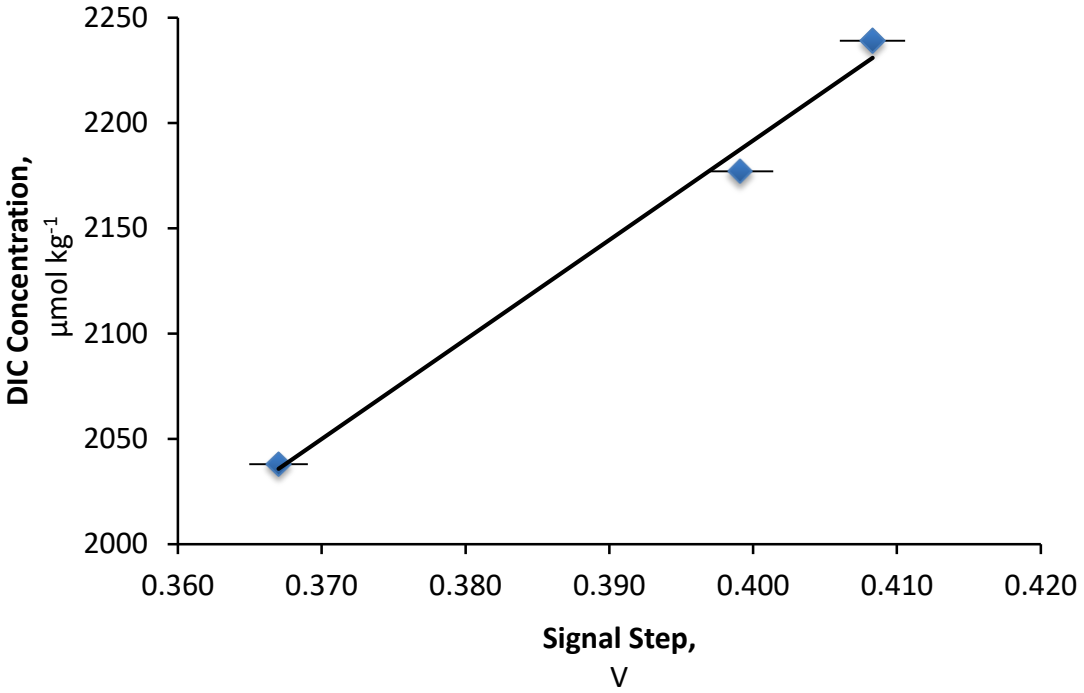

Figure 5.9 Chamber calibration using CRMs. Error bars represent one standard deviation of the 5 replicate measurements for each CRM.

Two further calibration methods were also carried out and evaluated based on the *in situ* measurements of the on-board CRMs measured during the field-testing. The first *in situ* calibration was a single point calibration based on the CRM measured following each sample (paired CRM), with the sample DIC concentration given by:

$$Sample\ DIC\ Concentration\ (\mu mol\ kg^{-1}) = Sample\ Signal\ Step\ (V)\frac{Paired\ CRM\ Value\ (\mu mol\ kg^{-1})}{Paired\ Onboard\ CRM\ Step\ (V)} \quad (5.5)$$

The second *in situ* calibration method was also a single point calibration, but based on the average of all on-board CRM measurements taken during each deployment, with the sample DIC concentration given by:

$$Sample\ DIC\ Concentration\ (\mu mol\ kg^{-1}) = Sample\ Signal\ Step\ (V)\frac{Average\ CRM\ Value\ (\mu mol\ kg^{-1})}{Average\ All\ Onboard\ CRM\ Step\ (V)} \quad (5.6)$$

To assess the accuracy and precision of the sensor performance, two metrics were used. The sensor accuracy was determined by finding the mean difference between the sensor-measured DIC concentration of the on-board CRMs and the certified CRM concentration, described by equation 5.7. One standard deviation of the mean of these differences was taken as the reproducibility of the measurement and used as a measure of the precision, as in equation 5.8.

$$Accuracy_{\ CRM}(\mu mol\ kg^{-1}) = Average_{measured} - Average_{certified} \quad (5.7)$$

$$Precision_{\ CRM}(\mu mol\ kg^{-1}) = Standard\ Deviation(Average_{measured} - Average_{certified}) \quad (5.8)$$

The *in situ* calibrations were based on the measurements of the on-board CRMs, and so, in order to assess the accuracy and precision of these calibrations independently, the same process was applied using bottled sample concentrations, such that:

$$Accuracy_{\ Bottled}(\mu mol\ kg^{-1}) = Average_{measured} - Average_{Bottled\ Conc.} \quad (5.9)$$

$$Precision_{Bottled}(\mu mol\ kg^{-1}) = Standard\ Deviation(Average_{measured} - Average_{Bottled\ Conc}) \quad (5.10)$$

The DIC concentrations in bottled samples were independently determined using either a VINDTA 3C (Marianda, Germany) or Apollo (SciTech, USA) following the method described in the SOP 02 (Dickson, Sabine and Christian, 2007). In this case, the precision given by equation 5.10 aggregates any potential errors from the bottle sampling and measurement process, as well as the sensor error so does not reflect the precision of the sensor alone.

5.3.3 Dock Deployment

The initial field-testing for the Version One sensor took place over two days in August 2018 in the estuarine environment of the docks in front of the National Oceanography Centre, Southampton. The sensor was deployed suspended from the dockside at 1 m depth. The sensor measurement cycle was timed so that the sensor would draw in the sample on the hour, which could then be easily matched to the corresponding bottled samples. The bottled samples were taken manually from the same depth as the sample inlet of the sensor using a Niskin bottle and were processed following the SOP 01 in (Dickson, Sabine and Christian, 2007). Following the SOP, 250 mL borosilicate glass bottles were used and the samples were preserved with 100 µL of saturated mercuric chloride solution. The bottled samples were stored for less than one month before being analysed in the Carbonate Laboratory, University of Southampton, on a VINDTA 3C (Marianda, Germany), as described in 1.2.1 and the SOP 02 in (Dickson, Sabine and Christian, 2007).

The aims of the field-testing were to evaluate the:

- sensor endurance
- filtering and temperature correction steps of the raw data processing protocol
- performance of the sensor in terms of accuracy and precision

Six D Cell lithium batteries (LSH20, Saft, France) housed in a titanium battery tube provided the sensor with power. The batteries were replaced after 18 hours, and then allowed to run until fully drained, taking ~24 hours.

The data processing steps of filtering and temperature correction applied to the raw conductivity data, described in 5.2.3, were investigated by examination of the 45 *in situ* measurements of the bagged on-board CRM. The standard deviation of the signal step for the CRMs calculated using the unsmoothed, uncorrected (raw) voltages was 5.5 mV, equivalent to a precision of 26 µmol kg^{-1} based on the chamber calibration. Smoothing the data using the Savitzky-Golay filter (4^{th} order and window length of 33) reduced the standard deviation to 5.4 mV, equivalent to 25 µmol kg^{-1}. The final step of temperature normalisation, using the α factor, improved the standard deviation further to 3.8 mV, equivalent to 16 µmol kg^{-1}. This provided confidence that the data processing routine developed during the laboratory characterisation stage of this study was appropriate for use in the field.

The chamber calibration and *in situ* calibrations were used to process the data recorded over the two days and are presented in Table 5.2. During the two days of deployment, the on-board CRMs were measured 45 times and there were 14 bottled samples with corresponding sensor measurements.

Table 5.2 Comparison of the accuracy and precision from the three calibration methods for the dock field test.

		On-board CRM Batch 161 2037 µmol kg^{-1} n = 45		**Bottled Samples** n = 14		**Range** µmol kg^{-1}
		Accuracy µmol kg^{-1}	**Precision** µmol kg^{-1}	**Accuracy** µmol kg^{-1}	**Precision** µmol kg^{-1}	
Laboratory Calibration	**Chamber Calibration**	280	± 17	38	± 42	52
***In situ* Calibrations**	**All CRM Measurements Averaged**	0	± 17	-249	± 33	56
	Paired CRM and Sample	-	-	-255	± 40	66

The chamber calibration overestimated the DIC concentration in the on-board CRMs by 280 ± 17 µmol kg^{-1} and in the bottled samples by 38 ± 42 µmol kg^{-1}. The *in situ* calibration based on the average of all the measured CRMs had a similar precision performance, with a precision from the CRMs of ± 17 µmol kg^{-1}; this calibration underestimated the DIC concentration in the bottled samples by 249 ± 33 µmol kg^{-1}. The *in situ* calibration based on the paired CRM measurements performed similarly, underestimating the DIC concentration in the bottled samples by 255 ± 40 µmol kg^{-1}.

This demonstrated that, for the dock field-test, the three calibration methods had similar precision performance. For the two calibrations where the precision could be calculated from the *in situ* CRM measurements (using equation 5.8), the precision was lower than that of the precision estimated from the bottled samples (equation 5.10). This is to be expected as the precision calculation based on the bottled samples also aggregates any sampling and laboratory instrument error.

Each of the calibrations have one accuracy value of approximately 250 µmol kg^{-1}. As the chamber calibration estimated sample concentrations close to the bottled sample data and it is likely that the bagged CRM had increased in DIC concentration. This would account for the underestimation of the bottled samples by the calibrations based on the *in situ* CRM measurements. Previous

studies have used different foil-lined bags and found that the CRM drifted during deployments, suggesting that the bags may have been damaged, exposing the aluminium foil, which could be reacting with the CRM (Wang *et al.*, 2015).

Plotting the sensor data from the deployment, using the *in situ* calibration based on the average value of all CRM measurements, showed no obvious sign of the sensor measured CRM concentration increasing steadily over the course of the deployment, Figure 5.10. However the CRMs were loaded shortly before the deployment, so were not exposed to the bags for any great length of time. This suggests that the change in the CRM may have occurred when the bag was filled.

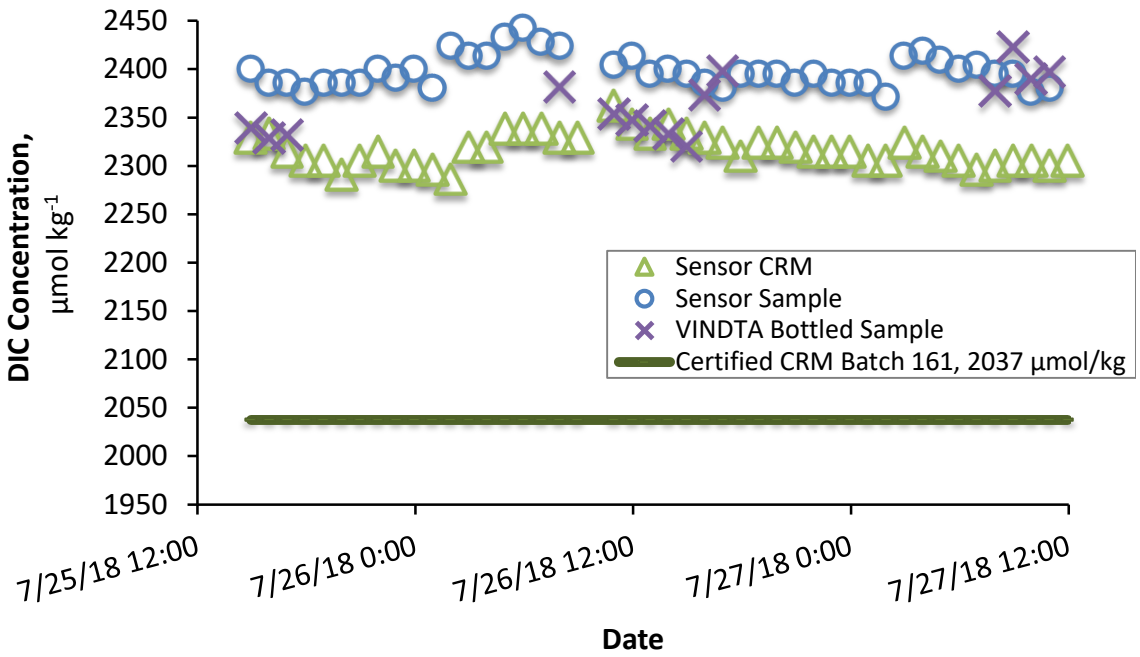

Figure 5.10 Sensor data from the dock deployment processed with the chamber calibration.

In summary, the initial field-testing in the dock demonstrated that smoothing and temperature normalisation of the data improved the precision of the measurements by 10 µmol kg^{-1}. The comparison of the three calibration techniques demonstrated that the methods achieved a similar performance; so all three were tested again using the lander data.

5.3.4 STEMM-CCS 2018 Lander Deployment

The DIC LOC Version One was deployed on a lander as part of a cruise establishing the baseline biogeochemical characteristics of a site in the North Sea in 2018. The RV *Poseidon* sailed to the North Sea to conduct a range of water column measurements and also to deploy a trial seabed lander carrying a suite of sensors, on cruise number POS527. The DIC LOC sensor was mounted to

the lander, shown in Figure 5.11. The sensor recorded data over the course of two deployments, each time recording for ~24 hours before its batteries were depleted. Bottled samples were collected throughout the water column and processed according to SOP 01 before being returned to Kiel for analysis using an Apollo instrument. These data are available on the Pangea database (Esposito, Martinez-Cabanas and Achterberg, 2019).

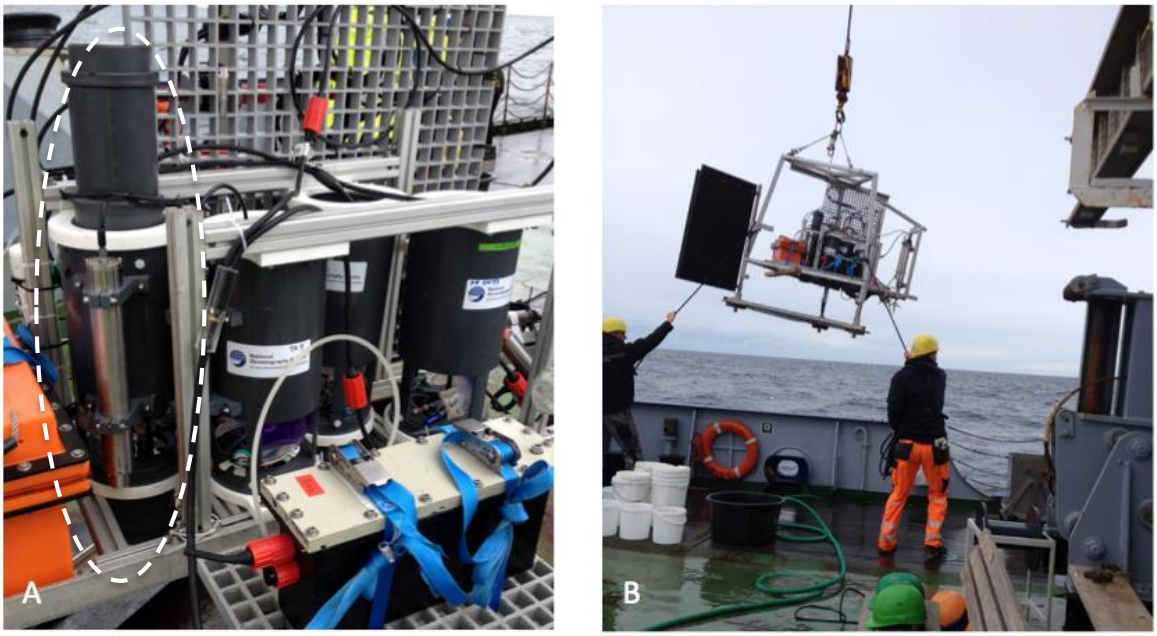

Figure 5.11 Photograph showing the lander. Panel A shows the suite of LOC sensors, with the DIC LOC sensor denoted by the white dashed line. Panel B shows the lander being deployed. Photograph credits to M. Arundell.

The DIC sensor operated following the same measurement cycle as in the dock testing, detailed in Table 5.1. The DIC data were processed and analysed using the same three calibration methods as described in section 5.3.3. During the two deployments, 47 pairs of seawater and CRM measurements were recorded and the accuracy and precision results are shown in Table 5.3. Due to the timings of the sample collection and the battery life of the DIC sensor, there were only two bottled samples with a corresponding sensor measurement.

Table 5.3 Comparison of the accuracy and precision of the three calibration methods for the lander deployments.

		On-board CRM Batch 161 2037 µmol kg^{-1} n = 47		**Bottled Sample** n = 2		**Range** µmol kg^{-1}
		Accuracy µmol kg^{-1}	**Precision** µmol kg^{-1}	**Accuracy** µmol kg^{-1}	**Precision** µmol kg^{-1}	
Laboratory Calibration	**Chamber Calibration**	3	± 83	27	± 8	208
***In situ* Calibrations**	**All CRMs Averaged**	0	± 10	-54	± 11	64
	Paired CRM and Sample	-	-	-52	± 9	52

During the lander deployments, the chamber calibration achieved an accuracy and precision of 3 ± 83 µmol kg^{-1} compared to the on-board CRMs. It also recorded the largest range in measured concentrations of 208 µmol kg^{-1} which was more than triple the range from the *in situ* calibrations. The reason for the poor precision is clear when the data are plotted, in Figure 5.12, which shows that, for the first deployment, the chamber calibration was consistently underestimating the CRM DIC concentration by ~70 µmol kg^{-1} and also underestimating the sample DIC concentration by ~140 µmol kg^{-1} relative to the bottled samples taken during the second deployment. The fact that both the CRM and the sample measurements were underestimated suggests this was a systemic error. Investigating this revealed that the blank voltages were stable across both days, with a blank voltage of 1.158 ± 0.006 V, and it was the magnitude of the peak which had altered between the two deployments. The cause of this is not apparent but a suggested mechanism for this could be a reduced gas exchange efficiency caused by a temporary blockage in the GEU, which was cleared by flushing the sensor before the second deployment. When the accuracy based on the CRMs is assessed for the second deployment alone, this calibration was overestimating the DIC concentration by 87 ± 8 µmol kg^{-1}.

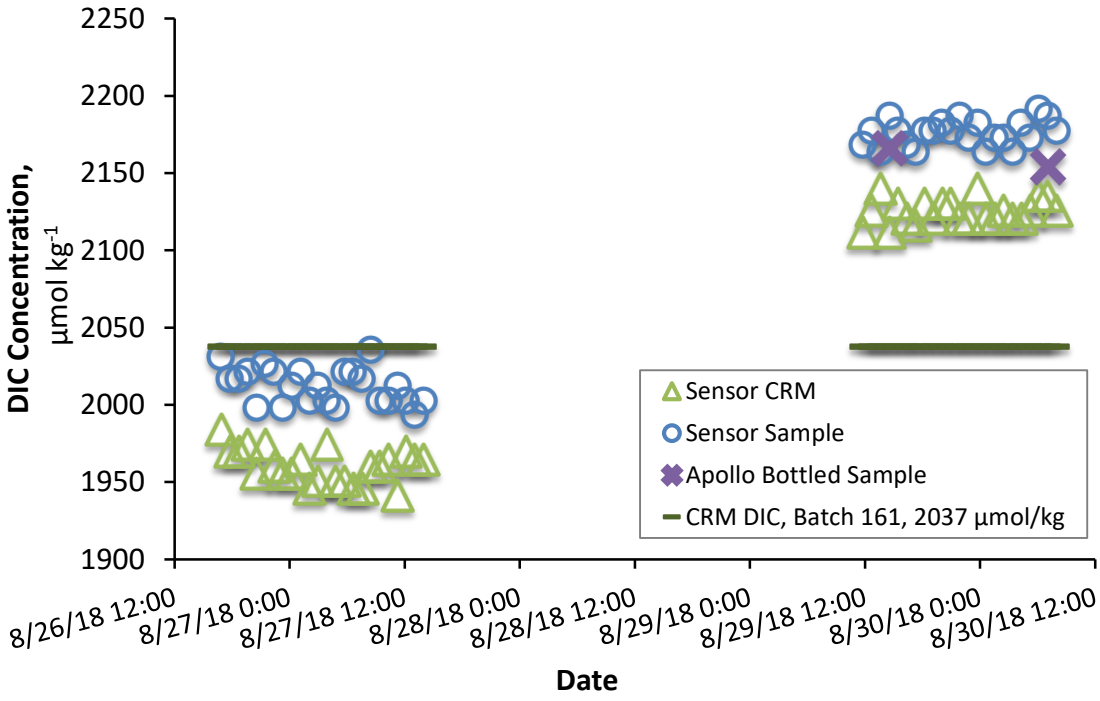

Figure 5.12 Sensor data from the lander deployment processed with the chamber calibration.

The two calibration methods based on the *in situ* CRMs accounted for the reduced peak that affected the chamber calibration on the first deployment so performed better than the chamber calibration over the two lander deployments. Both *in situ* calibration methods achieved a precision of approximately ± 10 µmol kg^{-1}. Neither of the calibrations presented evidence of drift in the CRM. The comparison of the calibration methods based on the two bottle data points is of limited use due to the low number of samples. However, when all the data from the 72 bottled samples collected from greater than 100 m depth over the course of the cruise are plotted versus time, it shows the range of DIC concentrations near the seafloor was 65 µmol kg^{-1} during the cruise, as shown in Figure 5.13. This range matches closest to the ranges of the calibration methods based on the *in situ* CRM measurements.

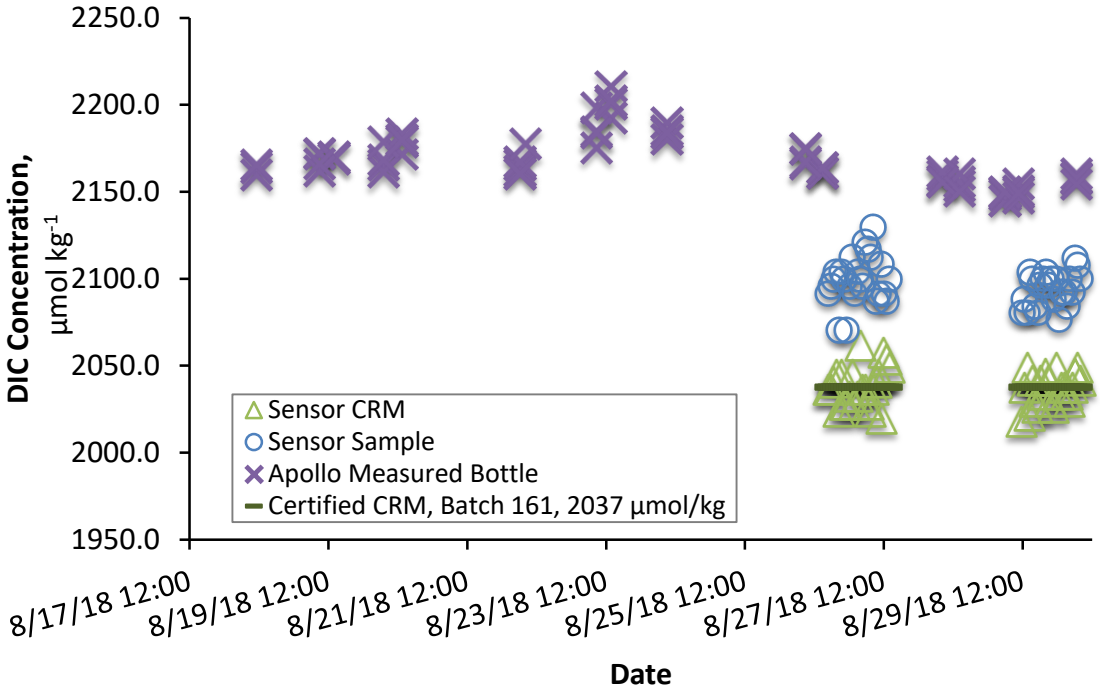

Figure 5.13 Sensor data from the lander deployment processed with the average CRM calibration alongside the Apollo measured bottled sample data from depths greater than 100 m, from POS527, Esposito, Martinez-Cabanas and Achterberg (2019).

Further analysis of the bottle data deeper than 100 m from the cruise revealed a relationship between the DIC and nitrate concentrations ($R^2 = 0.7$, $p < 0.001$, $n = 68$). The lowest DIC concentration was recorded at 0600 on 29th August 2018, which corresponds to a low nitrate concentration, shown in Figure 5.14 Panel A. The temperature and salinity data shows that for this time the water mass was the warmest and most saline recorded during the cruise, Figure 5.14 Panel B. Previous work has stated that warmer saline water found north of 55°N are likely to be the result of North Atlantic water entering the North Sea (Omar *et al.*, 2019) suggesting the source for this water mass with lower DIC and nitrate concentrations could be the North Atlantic.

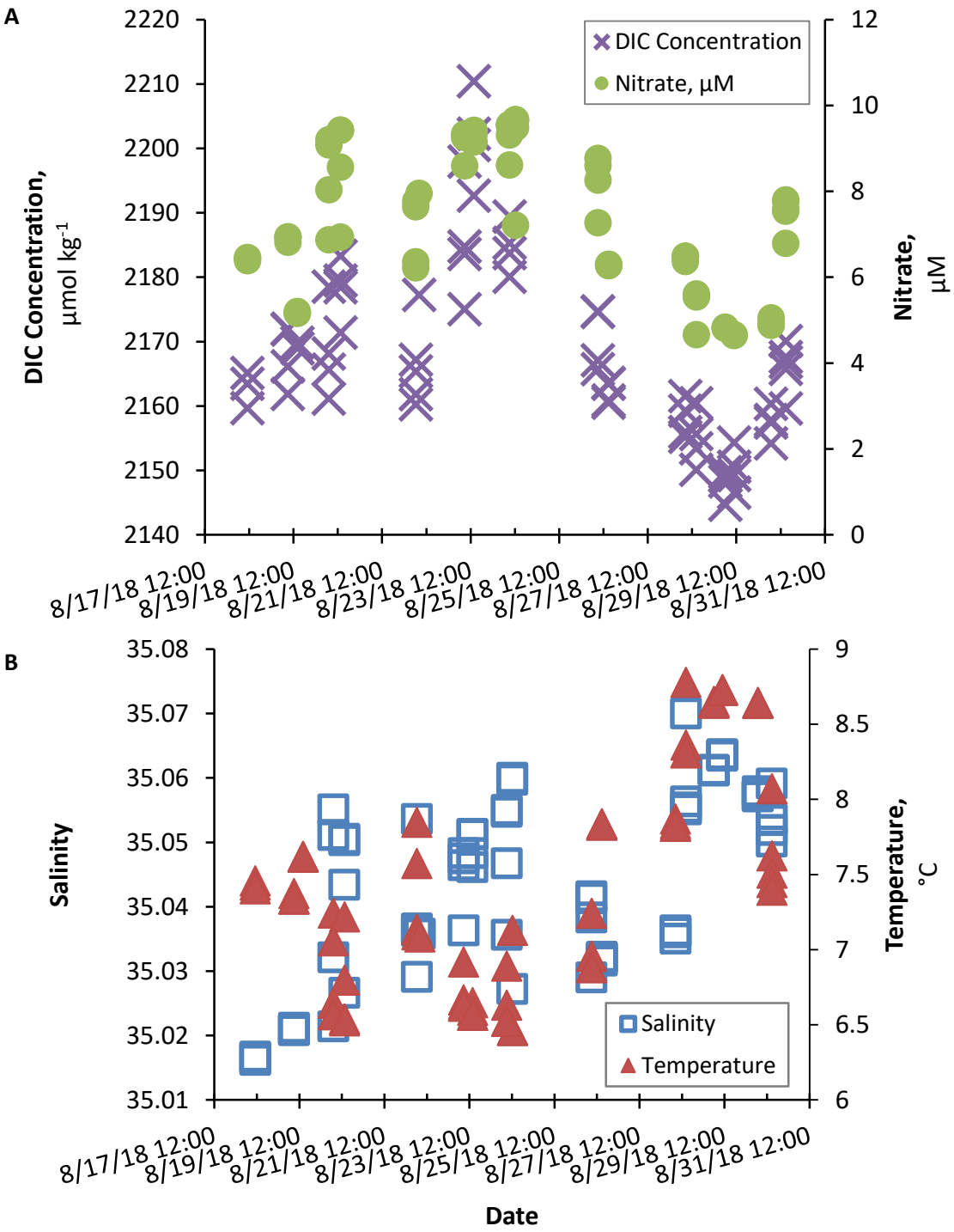

Figure 5.14 Bottle sample data from below 100 m depth, from the cruise POS527. Panel A shows the DIC and nitrate concentrations. Panel B shows the temperature and salinity data. All data from Esposito, Martinez-Cabanas and Achterberg (2019).

In summary, the lander data demonstrated that the chamber DIC calibration method had worse performance due to an issue in the first deployment, which the calibrations based on the *in situ* CRM measurements adjusted for. The calibrations based on the *in situ* CRM measurements had better performance, reaching a precision of approximately ± 10 µmol kg^{-1} over the 47 CRM

measurements. Based on these data the sensor was performing at a level required to measure DIC at the weather quality level as defined by GOA-ON (Newton *et al.*, 2014). This level of performance would provide useful data in areas with large DIC fluxes over short time periods. One area this could be useful would be in enclosed water bodies with calcifying organisms, where diurnal fluxes of ~300 µmol kg^{-1} have been reported (McMahon *et al.*, 2013).

5.3.5 Summary of Version One Testing and Modification for Version Two

The testing of the initial prototype demonstrated that the sensor had the potential to make weather quality measurements. The objective for the final sensor was to make climate quality measurements, requiring a precision of ± 2 µmol kg^{-1}. To achieve this, the C4D board was returned to eDAQ for further fine-tuning, to improve the signal to noise ratio by lowering the noise in the measurement.

The deployments also highlighted that the power consumption was a limiting factor. The C4D−EPU359 was found to require a high power when recording data. In the DIC LOC Version One the C4D board was constantly powered, resulting in a current draw of 480 mA. To reduce this, a custom electronic board was designed within OTEG to enable the C4D to be turned off when not recording data. This resulted in a saving of 100 mA and was an addition incorporated into the sensor Version Two.

The sensor Version One had a sample measurement cycle that took 48 minutes. A target application for the Version Two sensors was to integrate the sensor on to an ROV, which would require a faster sampling-measurement cycle. This was achieved by altering the measurement cycle. Integrating the sensor on the ROV also required an additional communications port to be added to the DIC LOC Version Two, which was the only physical change made to the design.

5.4 DIC LOC Version Two

A total of five DIC LOC Version Two sensors, incorporating the changes outlined in the previous section, were fabricated for deployment during the STEMM−CCS gas release experiment. One sensor was set up to measure seawater pumped by the underway system on the ship. Another sensor was mounted on the ROV *Isis* and two sensors were mounted on the seabed landers to be deployed close to the gas plume site, the final sensor remained as a spare. This section will focus on data from the underway and ROV systems.

5.4.1 LOC Version Two Overview

The Version Two sensor had the same microfluidic channel layout as the Version One design. The only physical difference was the addition of a third IE-55 communications port, to allow the sensor to interface with the ROV, sending real-time data through the ROV tether back to the ship. The C4D detector was modified by eDAQ Pty Ltd with components altered to reduce the measurement noise and to fine-tune the range of conductivities the C4D board was optimised to measure. The GEU remained the same as in Version One.

The testing of Version One demonstrated that the paired CRM calibration (equation 5.6) did not offer improved accuracy or precision compared to the calibration based on the average of all the CRMs (calculated using equation 5.7 and 5.8). For this reason, combined with the need to reduce the length of time taken for each measurement cycle, the paired CRM was dropped in the measurement cycle of the sensor Version Two. Instead, two CRMs were mounted on the sensor, one with a low DIC concentration and the other with a high DIC concentration. The CRMs were selected to give a range of ~200 µmol kg^{-1} covering the range of concentrations measured close to the seabed on the preliminary cruise in 2018, shown in Figure 5.13, allowing two point calibrations to be made *in situ*.

Replicate measurements of the high and low CRMs were made alternately, with a set of samples measured between them, as illustrated in Figure 5.15 Panel A. Two *in situ* calibration methods were trialled using the CRM data. In the first calibration method, the average of all the high DIC CRM and the average of all the low DIC CRM were used to generate a single two-point calibration, which is illustrated in Figure 5.15 Panel B, with the orange ellipse highlighting the average of the high DIC CRM and the blue ellipse highlighting the average of the low DIC CRM. This calibration equation was then applied to all the sample measurements. The second *in situ* calibration method involved generating a rolling calibration based on the high DIC and low DIC CRM that bookended each set of sample measurements. This rolling calibration gave a different two-point calibration for each sample set, illustrated by the colour-changing ellipse in Figure 5.15 Panel C. Post deployment calibrations were also developed based on the bottled sample data from the underway system and ROV deployments, and are further described in the following sections.

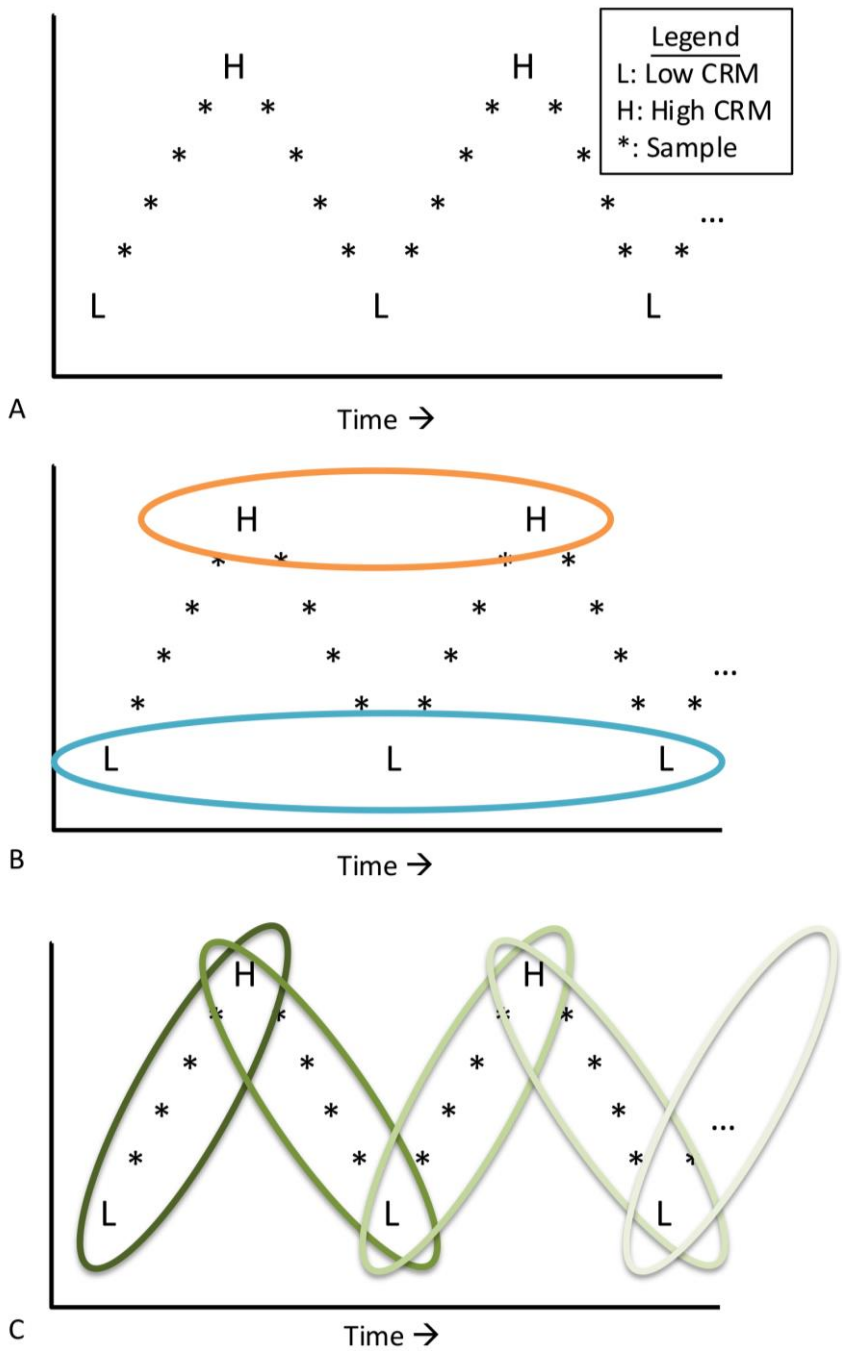

Figure 5.15 On-board calibrations for the DIC LOC Version Two. Panel A illustrates the cycle of low CRM, followed by a set of samples, then high CRM measurements. Each CRM was measured in duplicate. The ellipses in Panel B show the CRMs averaged to create the single calibration for all the samples. The colour-changing ellipses in Panel C show the rolling CRM calibration applied to all the samples bookended by the CRMs.

The altered measurement cycle for sensor Version Two is shown in Table 5.4. The cycle was altered such that the blank measurement came after the sample measurement, instead of before. The modified cycle dropped the paired CRM which removed a step from the Version One measurement cycle and reduced the time taken for each measurement to ~16 minutes, equivalent to 3 samples per hour.

Table 5.4 The DIC LOC Version Two sensor measurement cycle.

Step	**Process**	**Action**	**Flow Rate** ($\mu L\ min^{-1}$)	**Time** (min)
1	Load low CRM	Load Large Barrel 1 (LB1) low CRM, Small Barrel (SB) acid and Large Barrel 2 (LB2) NaOH	850	1
2	Inject to measure low CRM and acidify with small barrel	Inject LB1 low CRM to mixer, SB acid to mixer, LB2 to GEU	100	7
3	Load acid for flush and blank measurement	Load LB1 acid, SB acid and LB2 NaOH	850	1
4	Inject for acid flush and blank measurement	Inject LB1 acid to mixer, SB acid to mixer, LB2 to GEU	100	7
Repeat 1 to 4 for second low CRM measurement, after the second CRM measurement move to step 5 and start measuring seawater samples				
5	Load sample for measurement	Load LB1 sample, SB acid and LB2 NaOH	850	1
6	Inject sample and acidify with small barrel	Inject LB1 sample to mixer, SB acid to mixer, LB2 to GEU	100	7
7	Load sample for flush and sample measurement	Load LB1 acid, SB acid and LB2 NaOH	850	1
8	Inject for acid flush and sample measurement	Inject LB1 acid to mixer, SB acid to mixer, LB2 to GEU	100	7
Repeat 5 to 8 for five seawater samples, then proceed to step 9 to measure two high CRM				
9	Load high CRM	Load LB1 high CRM, SB acid and LB2 NaOH	850	1
10	Inject to measure high CRM and acidify with small barrel	Inject LB1 high CRM to mixer, SB acid to mixer, LB2 to GEU	100	7
11	Load acid for flush and blank measurement	Load LB1 acid, SB acid and LB2 NaOH	850	1
12	Inject for acid flush and blank measurement	Inject LB1 acid to mixer, SB acid to mixer, LB2 to GEU	100	7
Repeat 9 to 13 for second high CRM, then measure 5 samples before looping back to step 1 for a low CRM				

5.4.2 Laboratory Characterisation

Prior to the deployments, the measurement cycle was tested in the environmental chamber set to 10 °C (Discovery My, ACS, Italy). For this test three CRM batches were run at least 5 times and the standard deviation of the signal step for these measurements was found to be ≤ 0.0004 V (Table 5.5). This value was then used with the calibrations described in the following section to establish the laboratory precision.

Table 5.5 Laboratory precision testing of the Version Two sensor.

Batch Number	Certified Concentration µmol kg^{-1}	Standard Deviation of Signal Step V	Replicates
172	2038.99	0.0003	6
162	2177.27	0.0004	6
164	2238.89	0.0004	5

5.4.3 STEMM-CCS Gas Release Experiment 2019

The STEMM-CCS project culminated in a six-week cruise in the North Sea in spring 2019 to carry out a controlled gas release, simulating a sub seabed CO_2 leak. The experiment consisted of three phases. During phase one gas tanks were deployed and positioned on the seafloor, and a release pipe was drilled into the sediment, 100 m from the tank. In phase two, the gas flow was started and a plume was generated. During this phase, the gas flow rate was increased from 2 L_{STP} min^{-1} to 50 L_{STP} min^{-1}. The ROV *Isis* was deployed as a work horse to manoeuvre various sensor platforms into the plume site, as well as being a platform for a suite of LOC sensors. The third phase dealt with the removal of the tank system. The experiment involved the coordination of two international research vessels; further details of this experiment are currently being prepared for publication.

5.4.3.1 Underway System

Over the course of the experiment, a suite of OTEG designed LOC sensors were set up on board the RRS *James Cook* to measure the sea surface water autonomously. This suite of sensors consisted of a DIC, pH, TA, nitrate and phosphate sensor. The RRS *James Cook* has an underway system which pumped water from a depth of 5.5 m through a SBE45 Thermosalinograph. The seawater flowed out of a tap into a 1 L bottle, passing through Tygon® tubing via two inverted Y connectors that functioned to remove bubbles from the water. The water flowed at a rate of

~2 L min^{-1}. The sensors took samples from the overflowing bottle, shown in Figure 5.16. Of the carbonate sensors, the DIC and TA sensors were programmed to sample every 20 minutes and the pH sensor every 10 minutes. During the two-day transit from Aberdeen to Southampton 31 bottled samples were collected for sensor evaluation and calibration. Bottled samples were preserved with saturated mercuric chloride solution following SOP 01 in (Dickson, Sabine and Christian, 2007). The bottled samples were analysed using a VINDTA 3C (Marianda, Germany) at the Bermuda Institute of Ocean Sciences, within one month of the cruise.

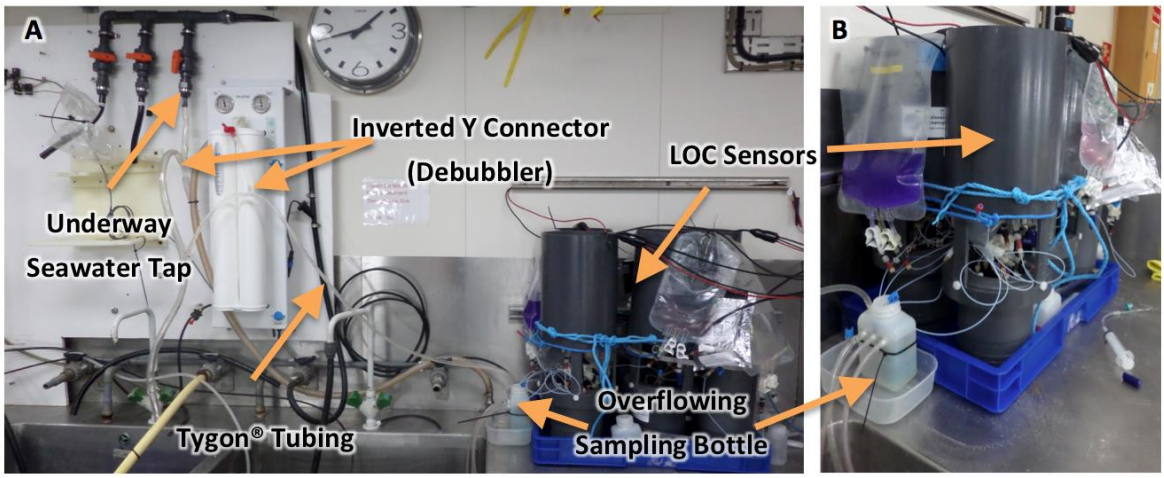

Figure 5.16 Photograph showing the set-up of the sensors taking measurements from the underway system. Panel A shows the full set up, and Panel B focuses on the overflowing sample bottle the sensors sampled from.

Alongside the two *in situ* calibrations described in section 5.4.1, post deployment calibrations were developed for the DIC LOC Version Two. The post deployment calibrations were based on the bottled samples. The first post deployment calibration was based on all 31 of the bottled samples. As this calibration was based on all of the bottled data the calculated accuracy and precision (equations 5.7 and 5.8) were effectively self referential, and therefore of potentially limited value. To solve this issue, two further post deployment calibrations were developed, which used half and quarter of the bottled samples, respectively. The bottled data not used to generate these further calibrations were then used to assess the accuracy and precision of the sensors, using equations 5.9 and 5.10. These calibrations, and their precision based on the chamber characterisation described in section 5.4.2, are detailed in Table 5.6. All three of the post deployment calibrations had a laboratory precision of < 0.2 µmol kg^{-1}, which demonstrated that the sensor was capable of making precise measurements, of the level required to monitor to climate precision as defined by GOA-ON, detailed in section 1.2.3 (Newton *et al.*, 2014).

Table 5.6 Post deployment calibrations and precisions from chamber characterisation.

		Calibration Equation	Laboratory Precision µmol kg^{-1}
Post Deployment Calibrations	**All Bottled Data**	$DIC\ (\mu mol\ kg^{-1}) = Signal\ Step\ (V) \times 402.1 + 1710.3$	0.2
	Half Bottled Data	$DIC\ (\mu mol\ kg^{-1}) = Signal\ Step\ (V) \times 341.8 + 1769.9$	0.1
	Quarter Bottled Data	$DIC\ (\mu mol\ kg^{-1}) = Signal\ Step\ (V) \times 408.0 + 1713.2$	0.2

The field-based accuracy and precision of the two *in situ* and three post deployment calibration methods were assessed using the same metrics as the Version One sensor (described with equations 5.7, 5.8, 5.9 and 5.10) and the results are shown in Table 5.7. During the deployment 27 measurements of the low CRM were taken along with 18 measurements of the high CRM. The difference in the number of measurements taken was due to the low CRM being measured first in the measurement cycle, so when the run was interrupted and restarted it resulted in more low CRM measurements being made.

Table 5.7 Comparison of the precision and accuracy of the calibration techniques trialled using the underway data. The grey numbers highlight the accuracy and precision calculated based on data used to generate that calibration.

		On-board Low CRM 2022 µmol kg^{-1} Batch 180 n = 27		**On-board High CRM** 2238 µmol kg^{-1} Batch 164 n = 18		**Bottled Samples**			**Range** µmol kg^{-1}
		Accuracy µmol kg^{-1}	**Precision** µmol kg^{-1}	**Accuracy** µmol kg^{-1}	**Precision** µmol kg^{-1}	**Accuracy** µmol kg^{-1}	**Precision** µmol kg^{-1}	**n**	
***In situ* Calibrations**	**All CRM**	-30	±63	-39	±54	-106	±69	31	425
	Rolling CRM	3	±11	0	±27	-66	±43	18	345
Post Deployment Calibrations	**All Bottled Data**	78	±9	-102	±10	0	±11	31	69
	Half Bottled Data	79	±7	-106	±9	1	±11	16	62
	Quarter Bottled Data	87	±9	-93	±10	-10	±10	24	74

The *in situ* two-point calibration based on all CRM measurements had poorer precision than the rolling two-point CRM calibration, approximately by a factor of 2. This shows that there was drift in the on-board CRM, which was accounted for by the rolling calibration. Because of the observed CRM drift, both the *in situ* calibrations can be discounted in this deployment. As noted in section 5.3.3, previous sensor development work found that foil-lined bags had drifted, possibly as the result of the foil reacting with the CRM (Wang *et al.*, 2015). Further investigation of the drift using the post deployment calibration is required before conclusions can be drawn.

As all three post deployment calibrations performed similarly, the calibration based on all the bottled data was selected to plot the data. In this calibration, the low CRM was overestimated by 78 ± 9 µmol kg^{-1} and the high CRM was underestimated by 102 ± 10 µmol kg^{-1}. Figure 5.17 shows the underway data plotted with the post deployment calibration based on all the bottled data, and in this plot the CRM drift is visible. The data show both the CRMs drifting over the duration of

the deployment and that the drift matched the trend of the sensor measured sample. This suggests that there was carry-over between the samples and CRMs as a result of incomplete flushing of the sensor between measurements. This is most apparent in the pairs of high CRM measurements following a seawater sample run, with the first measurement consistently lower than the second. This sub-optimal flushing of the system between measurements is possibly caused by the shortened measurement cycle and is likely the reason for the drop in precision performance between the laboratory characterisation in section 5.4.2 and the field-based sensor assessment.

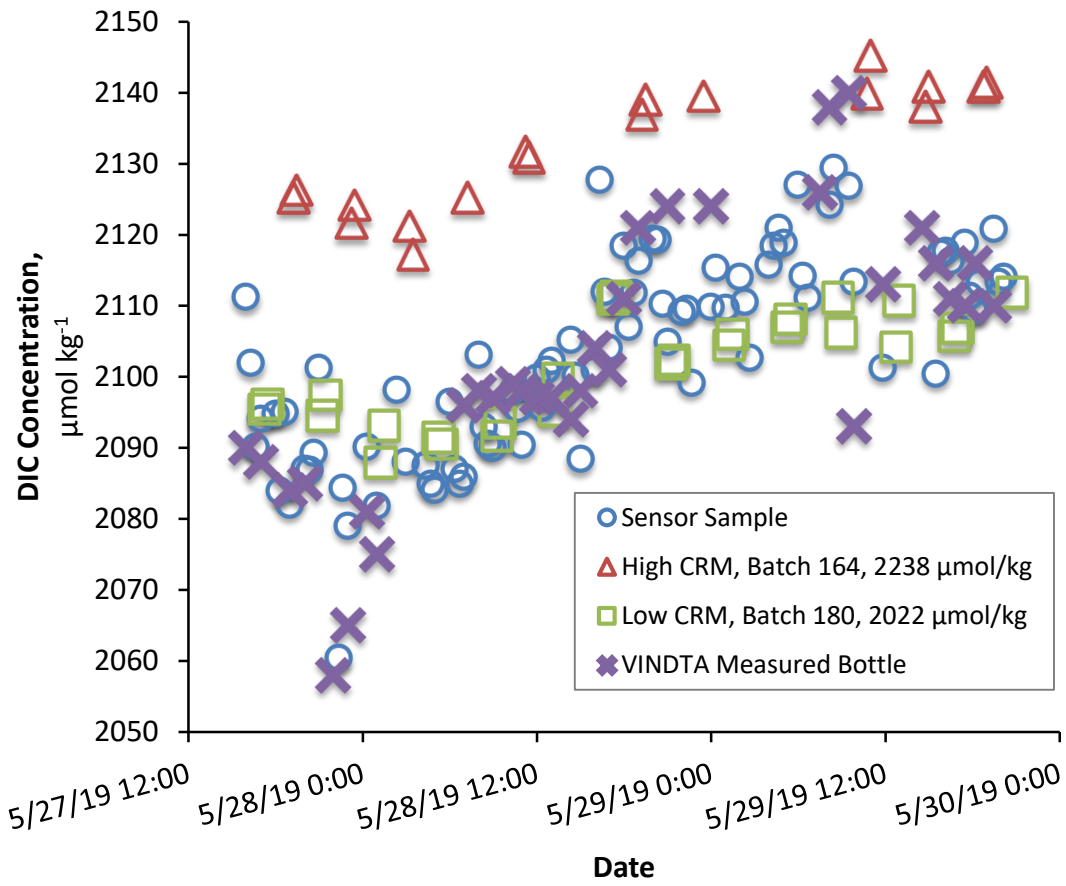

Figure 5.17 Underway data, showing the sensor measured sample concentrations and both sensor measured CRM values using the bottled sample calibration. The CRM concentrations are not shown because they are out of scale.

Despite the evidence of carry-over, the calibrations show a precision of ± 11 µmol kg^{-1} when comparing the sensor measured values to the bottled sample, using equation 5.10. By the end of the deployment there was not enough volume of CRM in the bags to measure these using a benchtop instrument but a separate bag, filled prior to the cruise and taken on the deployment, was analysed using a VINDTA 3C (Marianda, Germany) along with the bottled samples. This bagged batch of CRM batch 172 was shown to have drifted during the two months between

bagging and measurement from its certified value of 2038 µmol kg^{-1} to 2078 µmol kg^{-1}. This drift occurred despite the bags having the lowest possible gas diffusion coefficient. Future long term bag stability testing will be carried out to establish whether the drift occurred during the bag-filling process or during storage and transit.

The underway data are plotted in Figure 5.18. The underway system was temporarily shut down as the ship crossed the River Thames outflow, which is shown in the lack of data in that region. The regular gaps in the data correspond to sensor measurements of the on-board CRM. There is a general trend in the underway data of increasing DIC concentrations from the experiment site in the north towards the south of the North Sea. This trend, and its magnitude of ~30 µmol kg^{-1}, is in agreement with various previous studies (Bozec *et al.*, 2006; Clargo *et al.*, 2015; Burt *et al.*, 2016; Omar *et al.*, 2019). These previous works have identified that the northern North Sea is seasonally stratified, with this region being characterised by water depths greater than 50 m, found generally north of 55°N. In spring and summer in the northern region, photosynthesis in the surface layer reduces the DIC concentration (Clargo *et al.*, 2015). This is in contrast to the well-mixed southern North Sea, which is characterised by shallower water, less than 50 m deep.

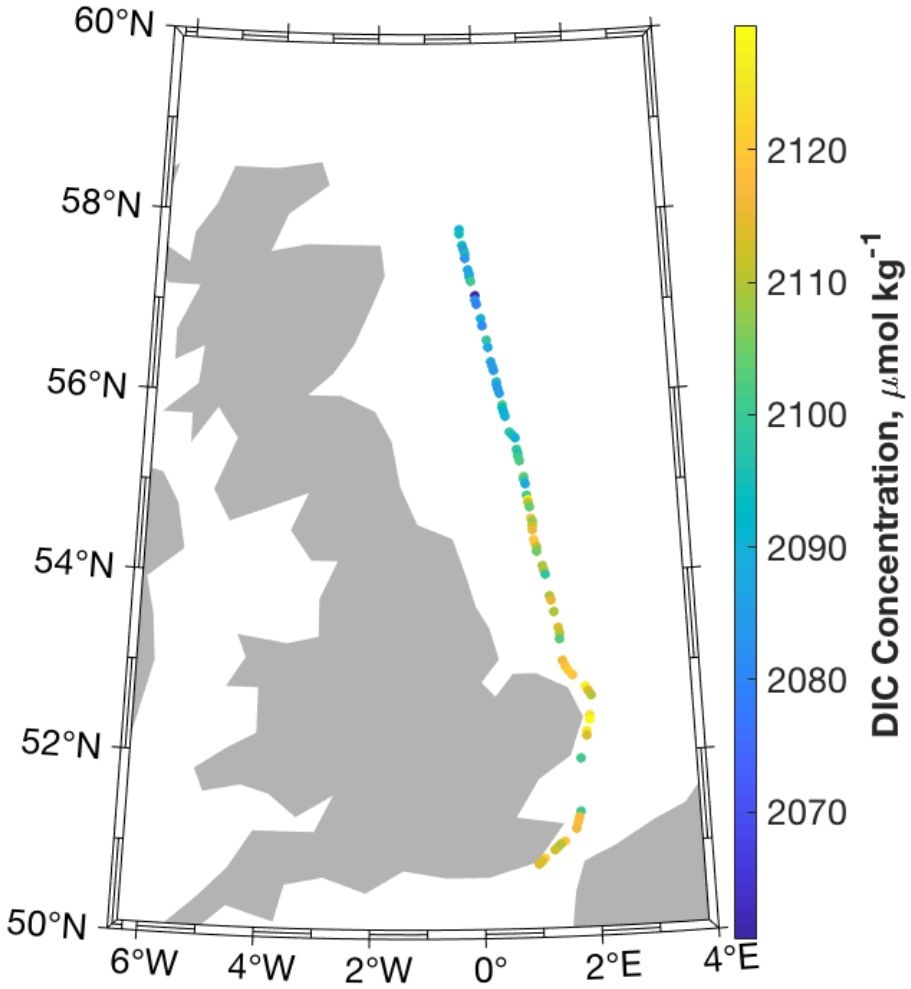

Figure 5.18 Map of the surface measurements made on the transit from off Aberdeen to Southampton on cruise JC180.

Plotting the underway DIC concentrations on a temperature-salinity diagram, in Figure 5.19 Panel A, shows that highest DIC concentrations are recorded at the lowest salinities, a result in line with a study which has shown that in the southern North Sea DIC concentrations are increased due to riverine inputs (Burt *et al.*, 2016). Plotting the DIC data north of 55°N as crosses in Figure 5.19 Panel B confirms the lower concentrations were found to the north of the transect and had a limited range in temperature and salinity. The data south of 55°N were plotted as squares and confirms that the highest DIC concentrations were in the lower salinity water to the south of the transect.

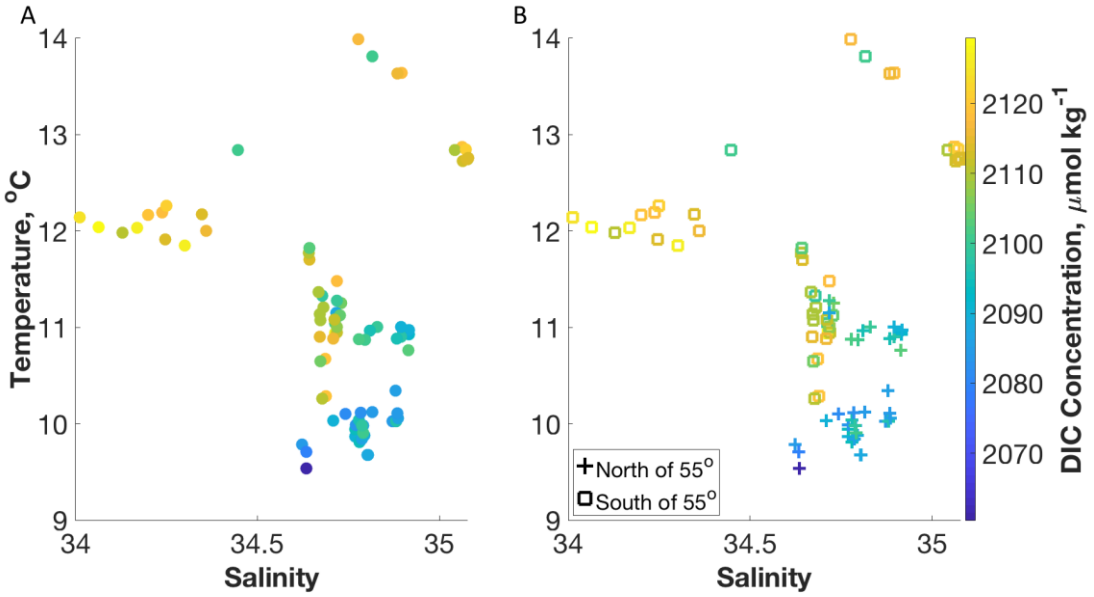

Figure 5.19 Temperature - Salinity plots of the underway surface data. Panel A shows the DIC concentration overlaid on the plot. Panel B illustrates the location of the data north or south of 55°N.

In summary, the underway data demonstrated that the post-deployment calibration based on the bottled samples was the most reliable calibration method. This calibration technique had a precision based on laboratory testing of ± 0.2 µmol kg^{-1}. The field-testing demonstrated poorer precision, approximately ± 10 µmol kg^{-1}, regardless of whether the precision was calculated from the residuals from the certified CRM data or the bottled samples. The difference in precision appears to be the result of insufficient flushing between samples, resulting in carry-over. Future work will be carried out to improve the flushing with the goal of improving the field precision.

5.4.4 ROV Data

The main focus of the STEMM-CCS cruise JC180 in 2019 was to assess the ability of a range of different techniques to detect a generated CO_2 plume. The addition of CO_2 from a bubble plume to the seawater will increase the DIC concentration through increasing the $CO_{2(aq)}$ in the seawater. In addition, the bubble plume will also lead the formation of carbonic acid, which will dissociate to produce bicarbonate and carbonate ions. This will produce protons, lowering the pH. To measure the extent of these impacts a suite of OTEG LOC sensors were mounted on the ROV *Isis*. This was the same suite of sensors as used on the underway system, described in section 5.4.3.1, consisting of DIC, pH, TA, nitrate and phosphate LOC sensors. The sensors were mounted in the rear right quadrant of the vehicle, as shown in Figure 5.20. To ensure the sensors were measuring as close to the plume as possible, a sample inlet tube was run from the front of the ROV back to the sensors, with sample pumped continuously through this tube by a SBE-5M pump (Sea-Bird

Scientific, USA). This section will focus on data from four of the ROV dives during the time of the highest gas flow of 50 L_{STP} min^{-1}.

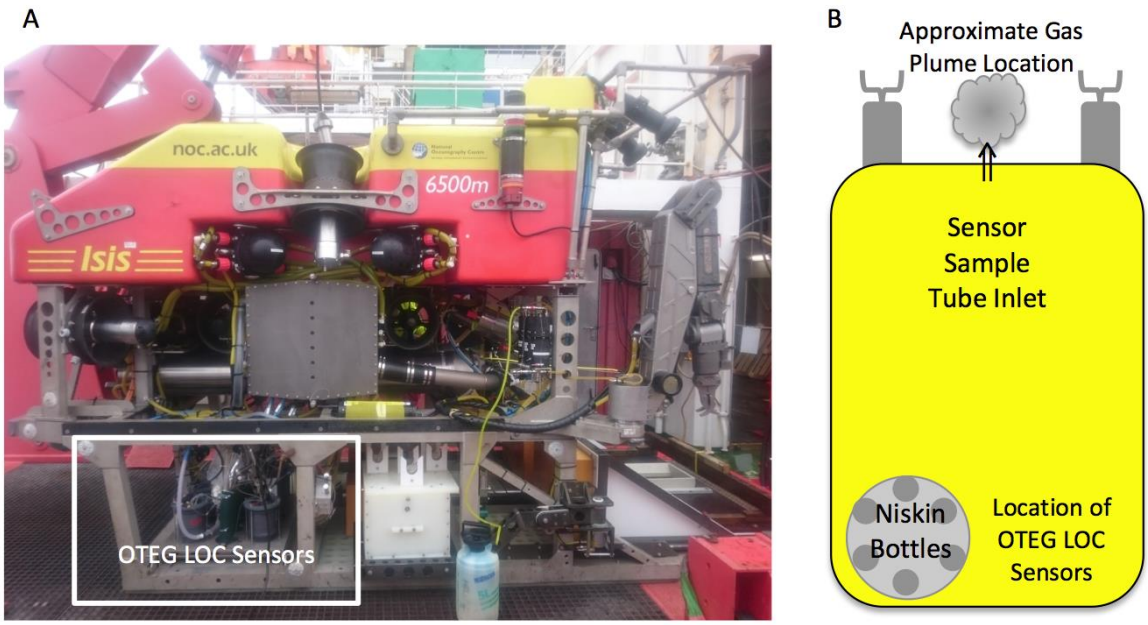

Figure 5.20 Panel A shows the location of the OTEG LOC sensors on the ROV *Isis*, with the sample tube visible in the centre of the white box. Panel B shows a plan view of the vehicle and illustrates the location of the sensors and Niskin bottles, relative to the front of the ROV.

The DIC sensor on the ROV was programmed to operate following the same measurement cycle as the underway system, described previously in Table 5.4, running replicate measurements of a low DIC CRM followed by a set of five sample measurements, then two replicate measurements of the high DIC CRM. As in the underway data, the CRM measurements were used to create two *in situ* two-point calibrations, one based on the average of all the CRM data and the second on the rolling CRM calibration. Two post deployment calibrations were generated based on the bottled data collected using samples taken from the Niskin bottles mounted on the ROV.

The ROV had six Niskin bottles mounted on the rear left quadrant of the vehicle, shown in Figure 5.20 Panel B. On each of the four dives, bottled DIC samples were collected and preserved following the SOP 01 (Dickson, Sabine and Christian, 2007). The Niskin bottle samples were always taken towards the end of the ROV dive to reduce the potential for biological processes to alter the DIC concentrations. The DIC concentrations in the bottled samples were measured on an Apollo DIC analyser and the data are presented in Table 5.8. Samples were taken at the gas plume site and away from the plume by the gas tank, indicated in Table 5.8. Replicate bottle samples were taken at the gas plume site ($n \geq 3$). The set of replicate measurements taken by the plume at 07:05 on the 19th May showed a high standard deviation of over 200 µmol kg^{-1}. This may have

been the result of the spatial heterogeneity of the plume being captured by the Niskin bottles. It may also have been the result of poor flushing of the Niskin bottles, because the bottles were located inside the ROV frame, and prior to the collection of these samples the ROV had been stationary on the seabed taking sediment push cores. Regardless of the cause, these data were excluded from the evaluation of the sensor performance and were not used in the post deployment calibrations.

Table 5.8 DIC concentration of Niskin bottle samples taken from bottles mounted on ROV.

Date Time	**Dive Number**	**Average** µmol kg^{-1}	**Standard Deviation** µmol kg^{-1}	**Rep 1** µmol kg^{-1}	**Rep 2** µmol kg^{-1}	**Rep 3** µmol kg^{-1}	**Rep 4** µmol kg^{-1}	**Plume or Tank**
17/5/19 1616	369	2163	3	2159.2	2163.8	2164.8	-	Plume
17/5/19 1631	369	2159	-	2158.5	-	-	-	Tank
18/5/19 0909	370	2200	34	2238.6	2172.6	2188.6	-	Plume
18/5/19 0923	370	2157	-	2156.8	-	-	-	Tank
19/5/19 0705	372	2494	203	2595.7	2725.3	2371.4	2282.5	Plume
19/5/19 0720	372	2152	-	2152.2	-	-	-	Tank
19/5/19 1515	373	2259	14	2265.2	2273.7	2255.1	2240.4	Plume
19/5/19 1528	373	2155	-	2155.5	-	-	-	Tank

The bottled data were used to generate two post deployment calibrations. The first was a single point calibration based on an average of the bottled samples collected at the plume from each dive, which produced a different calibration for each dive. This reduced the number of bottled sample data available to assess sensors the accuracy and precision using equations 5.9 and 5.10.

The second post deployment calibration was a two-point calibration generated from bottled sample data. This calibration gave a single equation that was then utilised for all of the dives; it also used fewer bottled samples, and so there were five remaining sampled bottles that could be used to assess the accuracy of the sensor and precision of its performance using equations 5.9 and 5.10. The assessment data for all calibrations are presented in Table 5.9.

Table 5.9 Comparison of the precision and accuracy of the calibration techniques trialled using the underway data. The grey numbers highlight the accuracy and precision, calculated based on data used to generate that calibration.

		On-board Low CRM 2039 µmol kg^{-1} Batch 172 n = 19		**On-board High CRM** 2239 µmol kg^{-1} Batch 164 n = 19		**Bottled Samples**			**Range** µmol kg^{-1}
		Accuracy µmol kg^{-1}	**Precision** µmol kg^{-1}	**Accuracy** µmol kg^{-1}	**Precision** µmol kg^{-1}	**Accuracy** µmol kg^{-1}	**Precision** µmol kg^{-1}	**n**	
***In situ* Calibrations**	**All CRM**	4	±22	5	±24	-28	±41	7	212
	Rolling CRM	5	±17	0	±10	-23	±49	7	153
Post Deployment Calibrations	**Single Bottled Sample per Dive**	30	±20	-11	±23	-9	±54	3	158
	Two Bottled Samples for all Dives	90	±25	66	±28	43	±42	5	297

The *in situ CRM* calibrations both showed evidence of less drift than the *in situ* calibrations for the underway data, but this would be expected because the ROV data were derived from a shorter deployment. Because the ROV data were collected using the same measurement cycle as the underway data, the *in situ* CRM calibrations were not selected as the optimal processing method for the ROV data, due to the carry-over issue described in section 5.4.3.1.

The two post-processing calibrations both had similar precision, so the calibration based on the single bottled sample from each dive was selected for processing the data and as this had improved accuracy for the CRM and bottled measurements, this was used to plot the ROV data shown in Figure 5.21. This calibration method overestimated the low CRM by 30 ± 20 µmol kg^{-1}, and underestimated the high CRM by 11 ± 23 µmol kg^{-1}. For the ROV data, the selected processing method underestimated the high CRM by 11 µmol kg^{-1}, an order of magnitude better than the processing used for the underway data, which underestimated the high CRM by 102 µmol kg^{-1}. This difference is probably due to the fact that the average of the measured sample concentrations from the ROV was closer to the certified value for the high CRM. The average measured DIC concentration was 2158 µmol kg^{-1} over the ROV data but only 2103 µmol kg^{-1} for all the underway data. This meant that any carry-over of sample in the underway system would have a bigger impact on the high CRM data.

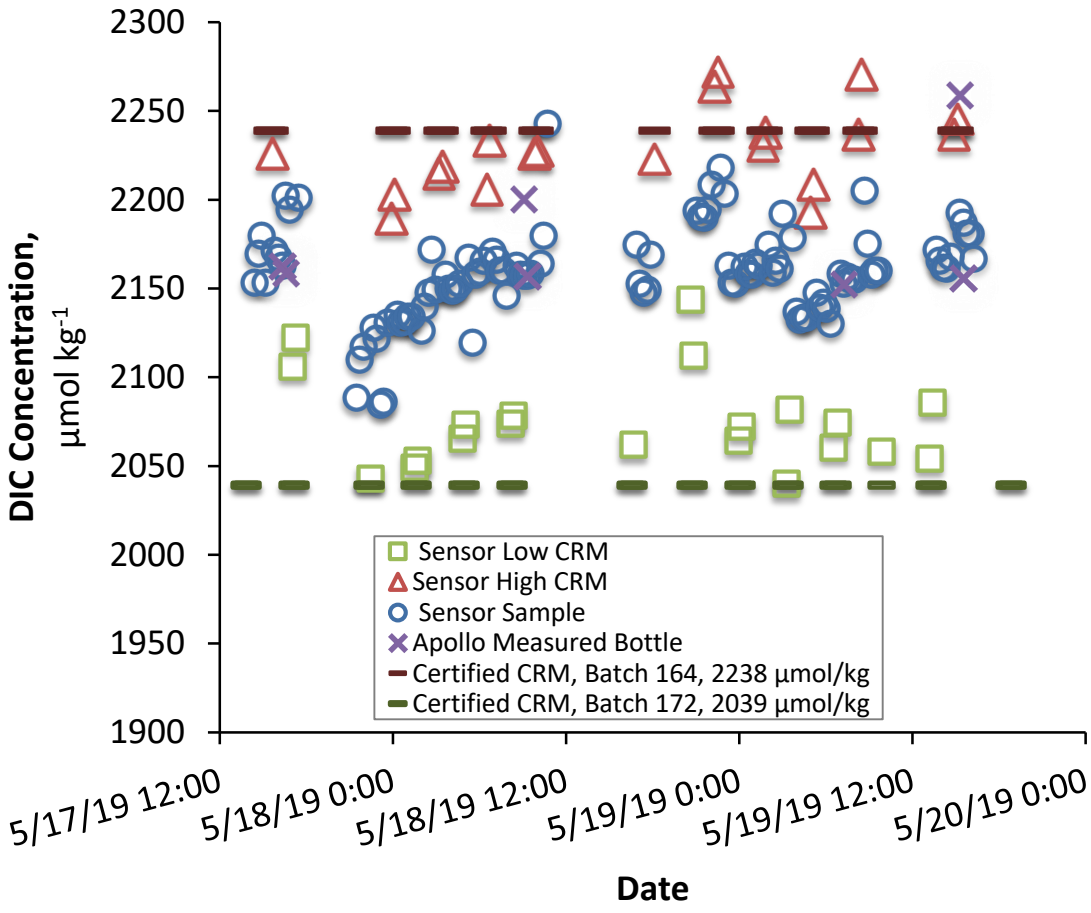

Figure 5.21 DIC concentration from the ROV data, calibrated using the single bottle post deployment calibration method.

The fact that the ROV sensor measured higher DIC concentrations than the underway sensor recorded for surface seawater corresponds well with the profiles collected in 2018, shown in

Figure 5.22. The plot of all the DIC profiles shows that the surface water had a concentration range of 2053 – 2095 µmol kg^{-1}, and at 120 m had a concentration range of 2150 – 2210 µmol kg^{-1}. This matches well with the data recorded by the DIC sensor mounted on the underway system and ROV, which had average values of 2103 µmol kg^{-1} and 2159 µmol kg^{-1} respectively. The magnitude of the difference between the surface and bottom water also compares well with those reported previously for previous cruises in the summers of 2001, 2005, 2008 and 2011 (Clargo *et al.*, 2015).

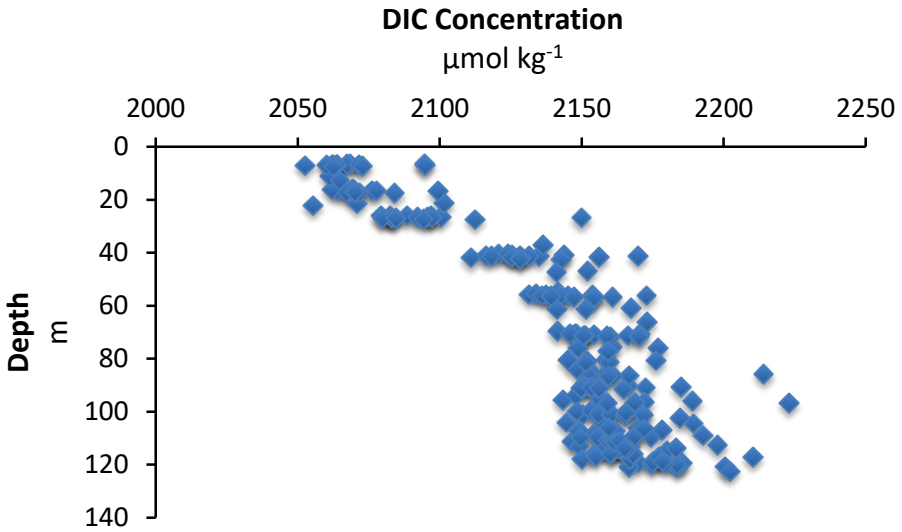

Figure 5.22 DIC concentration depth profiles from August 2018, using the data from POS527 Esposito, Martinez-Cabanas and Achterberg, (2019).

The ROV data are further examined in the following section by comparing the DIC LOC measured concentrations to the DIC derived from sensor-measured pH and TA data.

5.4.4.1 ROV DIC Derived from pH and TA

The suite of sensors mounted on the ROV also included pH and TA LOC sensors, and so the collected dataset is capable of over determining the carbonate system. The pH was measured spectrophotometrically using a LOC sensor developed from a benchtop instrument (Rérolle *et al.*, 2013). The LOC pH measurement was derived from the colour change of the purified pH sensitive dye *meta*-Cresol Purple (Liu, Patsavas and Byrne, 2011) when mixed with the seawater sample. The pH sensor recorded a measurement every 10 minutes. The TA LOC sensor determined TA from a single-point open system acid titration of seawater sample (sample CO_2 removal through a GEU), with spectrophotometric end-point pH determination using the indicator dye bromophenol blue. The TA sensor made a measurement every 7 minutes, with a calibration every 9 samples.

When both pH and TA are measured, DIC can be derived by solving the system of equations that describe the chemical equilibria of the oceanic carbonate system. Total alkalinity (TA) in oceanic water is the sum of the carbonate alkalinity (CA), borate alkalinity (BA), phosphate alkalinity (PA), silicate alkalinity (SiA), dissolved organic carbon alkalinity (DOCA), sulphide alkalinity (SA), and ammonia alkalinity (AA), such that:

$$TA = CA + BA + PA + SiA + DOCA + SA + AA + [OH^-] - [H^+] \quad (5.11)$$

In nutrient depleted oxic oceanic water, the two major components of TA are the carbonate alkalinity and borate alkalinity. The CA can be derived if TA is measured and BA is known, such that:

$$CA = TA - BA \quad (5.12)$$

The BA can be calculated from equilibrium dissociation reaction of boric acid:

$$BA = \frac{[B_{total}]_{Sample}}{1+\frac{H^+}{K_b}}, \quad (5.13)$$

where $[B_{total}]_{Sample}$ is determined as a function of salinity as:

$$[B_{total}]_{Sample} = \frac{[B_{total}]_{Ocean,S=35}}{35} \times Salinity_{Sample}, \quad (5.14)$$

The total boron concentration ($[B_{total}]_{Ocean,S=35}$) in seawater at salinity 35 is 0.000433 mol kg^{-1} (Lee *et al.*, 2010). The equilibrium dissociation constant of boric acid (K_b) is a function of salinity and temperature as described in (Dickson, 1990b). Equation 5.11 can be rearranged to give DIC in terms of CA and pH, such that:

$$DIC = CA \ \frac{[H^+]^2+[H^+]K_1+K_1K_2}{[H^+]K_1+2K_1K_2}, \quad (5.15)$$

where K_1 and K_2 are the equilibrium dissociation constants of dissolved CO_2 in oceanic water, which are functions of salinity and temperature (Dickson and Millero, 1987).

The DIC concentration was calculated using data from the ROV dive 370, using the CO2SYS code in Matlab® (van Heuven *et al.*, 2011). This dive, taking place over the 17th – 18th May 2019, was the longest ROV dive of the cruise, which was at the time of the highest CO_2 injection flow rate. The constants K_1 and K_2 were from (Mehrbach *et al.*, 1973) as refitted by (Dickson and Millero, 1987) and the $KHSO_4$ from (Dickson, 1990a). For the calculations the TA measurement closest temporally to each pH measurement was used. This data are presented in Figure 5.23.

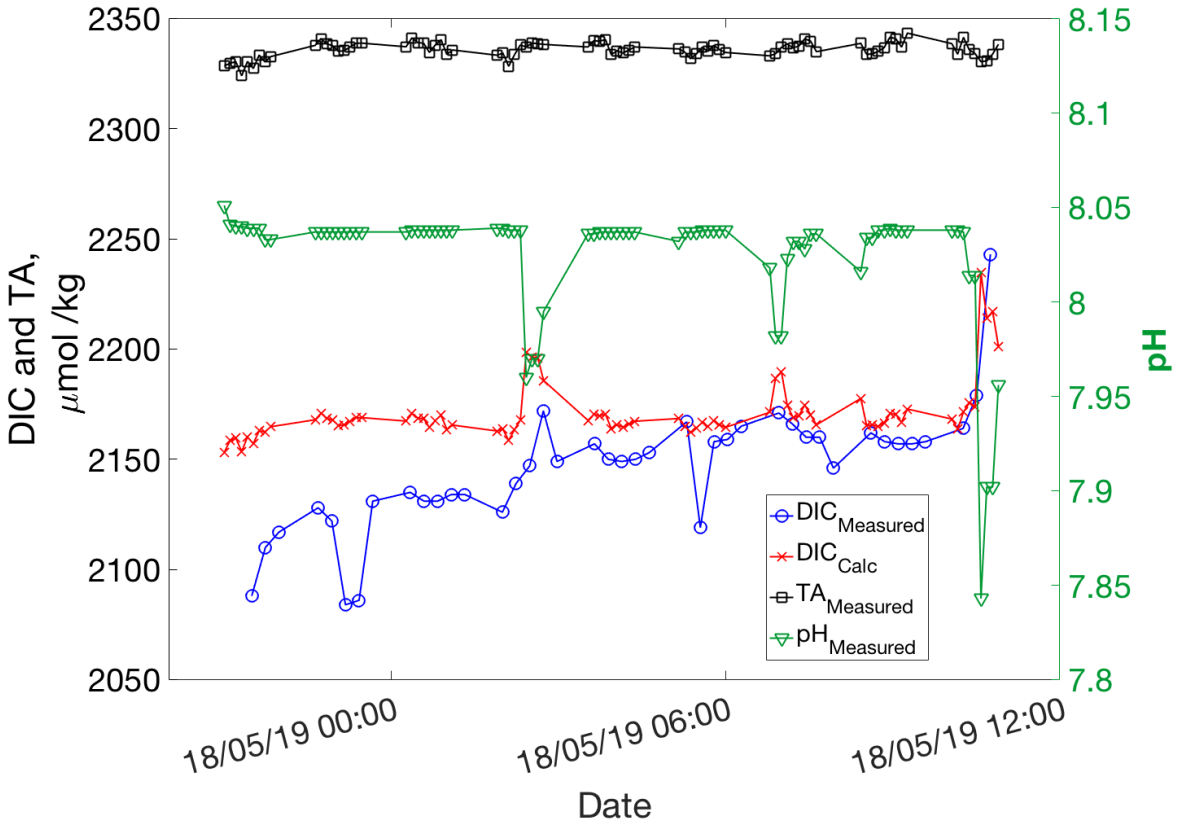

Figure 5.23 LOC sensor data from ROV dive 370, showing the DIC concentration derived from the pH and TA measurements.

There was very little variation measured by the TA sensor, with an average measured TA of 2336 µmol kg^{-1}, with a standard deviation of 4 µmol kg^{-1}. This is because the addition of $CO_{2(aq)}$ has no impact on the TA. The average pH for the duration of the dive was 8.023, and the pH sensor recorded three pH drops with magnitudes greater than 0.050 pH units during the deployment on 18th May 2019, as shown in the graph in Figure 5.23. The largest pH drop of 0.195 pH units occurred at 10:35. At this time the ROV was stationary on the seabed close to the plume collecting sediment push cores. The derived DIC_{calc} increased by 71 µmol kg^{-1}, which matches well with the sensor $DIC_{measured}$ increase of 79 µmol kg^{-1}. The next largest pH drop was of 0.078 pH units at 02:25. At this time the ROV was within a few meters of the plume, deploying other equipment. The derived DIC_{calc} increase had a magnitude of 35 µmol kg^{-1}. This corresponds well

with the $DIC_{measured}$ increase of 33 µmol kg^{-1}. The smallest third peak at 06:50 produced a pH drop of 0.056 pH unit, which yielded a DIC_{calc} increase of 21 µmol kg^{-1}, not captured in the $DIC_{measured}$, potentially as the sensor had just been running a CRM.

The derived DIC_{calc} concentrations were ~40 – 60 µmol kg^{-1} higher than the $DIC_{measured}$ for the first four hours of the deployment. This is possibly the result of the oil-filled housing coming into thermal equilibration with the seawater, after warming up during the time the ROV was on deck.

Over the course of the dive when the temperature in the oil-filled housing had stabilised, the accuracy and precision were assessed using the same metrics as used in the preceding sections. This assessment demonstrated that the $DIC_{measured}$ was on average 17 ± 15 µmol kg^{-1} less than the DIC_{calc}.

A potential limitation of using chemical equilibrium relationships to derive DIC from pH and TA, as used in CO2SYS, is that the relationships are only true for systems in equilibrium. In the gas release experiment CO_2 is being added to the system and in the region closest to the plume the system may not be in equilibrium. Modelling work has estimated the relaxation time for carbon to be 15 − 30 seconds (Zeebe, Wolf-Gladrow and Jansen, 1999), which could explain some of the differences seen when the ROV was closest to the plume.

5.4.5 Comparison of Underway and ROV data

Comparing the DIC measured in the bottled samples to the sensor estimated values for both the underway and ROV deployments shows generally good agreement, with the linear regression having an R^2 value of 0.75 and a standard error of 14 µmol kg^{-1}, as seen in Figure 5.24 Panel A. This plot shows that the DIC concentration recorded close to the seabed by the ROV was higher than the surface concentration recorded by the underway sensor. The ROV dataset contains only three bottled samples and, as detailed in Table 5.8, the replicate bottles collected by the ROV had high variation between replicate measurements, up to 203 µmol kg^{-1}. Excluding the ROV data for these reasons reduced standard error to 8 µmol kg^{-1}. The deviation of the regression from the linear line of y = x suggests the sensor was underestimating the DIC concentration at higher concentrations, however as there are limited bottle samples at the higher concentrations further testing of the system would be required to determine whether this was the case. A potential reason for this could be dilution of the sample by the low CRM if the flushing was insufficient. The plot of the residuals in Figure 5.24 Panel B show there is no trend with an $R^2 < 0.4$. The average of the residuals for both datasets is 2 ± 19 µmol kg^{-1}, excluding the ROV dataset that is reduced to 0 ± 11 µmol kg^{-1}.

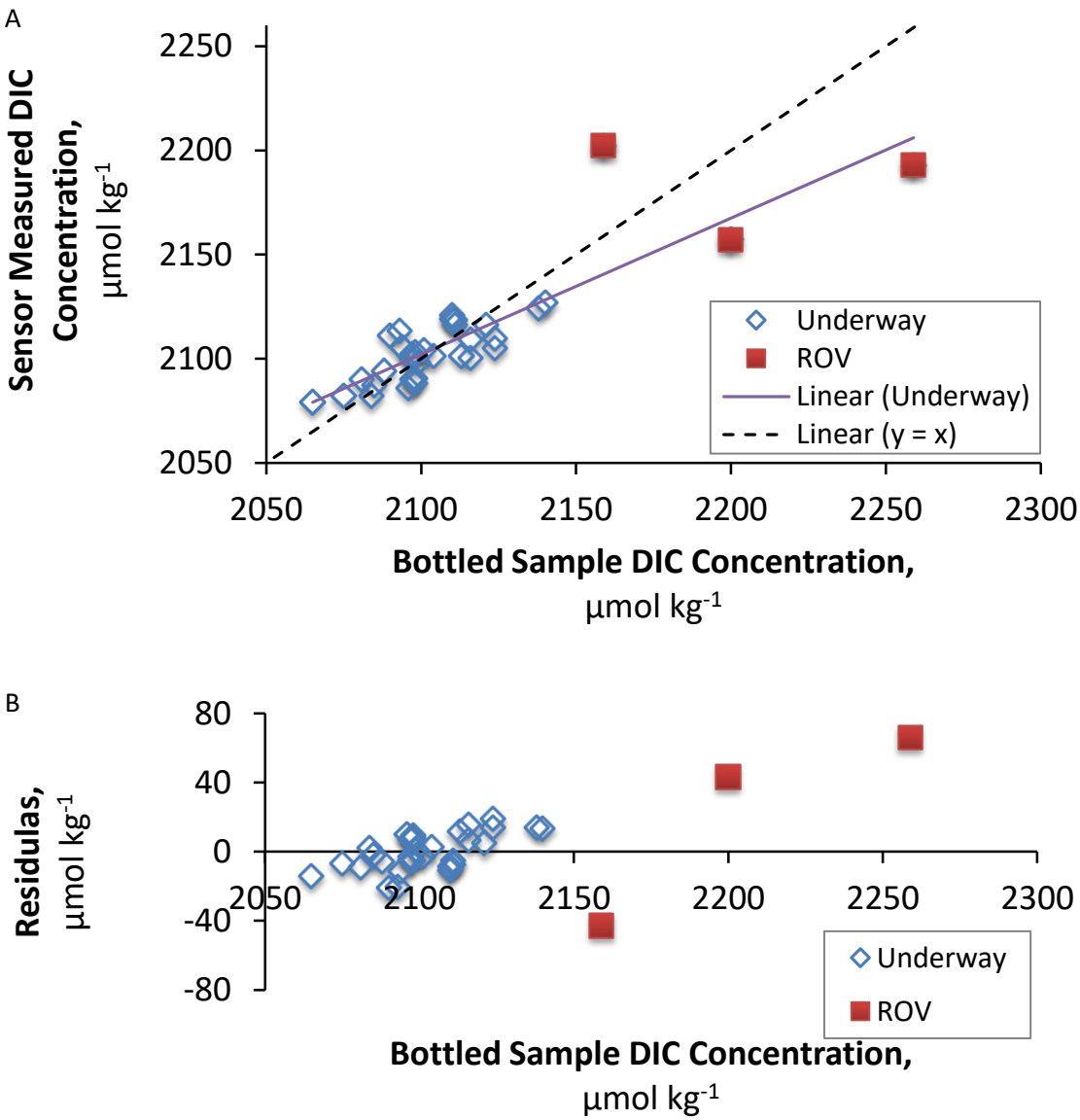

Figure 5.24 Comparison plots for the underway and ROV data. Panel A shows the bottled data compared to the sensor data. Panel B shows the residuals between the sensor and bottle measured samples.

5.4.6 Summary of Version Two Testing

The laboratory characterisation of the sensor Version Two gave a precision of ± 0.2 µmol kg^{-1}. This precision would be an order of magnitude better than the ± 2 µmol kg^{-1} required to give climate quality level measurements as defined by GOA-ON (Newton *et al.*, 2014). The results of the field-testing demonstrated precision closer to ± 10 µmol kg^{-1}, which is within the window of weather quality measurements as defined by GOA-ON. It is apparent in the data that there is carry-over between samples, which will be addressed in the next sensor version, details of which are presented in chapter 6. While the ROV measurements had fewer bottled samples available for

direct assessment of the performance of the sensor, it was possible to compare the measured concentrations to derived DIC concentrations from pH and TA measurements. This comparison confirmed that the sensor was performing close to the weather quality. The sensor mounted on the ROV detected the peaks in DIC caused by the plume, and these values matched well with the derived DIC, demonstrating that the sensor had good potential for mapping the plume.

The level of performance achieved by the sensor would provide useful data in areas with high DIC fluxes over short time periods, such as tropical lagoons where calcifying organisms have been found to generate diurnal fluxes of ~300 µmol kg^{-1} (McMahon *et al.*, 2013) or over spatial areas with a large range in DIC concentrations, such as marshy estuarine environments where DIC concentrations have been found to range by ~400 µmol kg^{-1} over 12 km (Wang *et al.*, 2018).

Chapter 6 Conclusions

6.1 DIC LOC Development Summary

This work presents the developmental process undertaken to design an autonomous DIC sensor for oceanic measurements, based on a microfluidic “Lab On Chip” (LOC) design. The DIC LOC sensor was developed following the Technology Readiness Level (TRL) roadmap. Starting from an idea based on theory, TRL 2, the system was developed into a benchtop instrument, TRL 4. The system was then miniaturised and automated to reach TRL 7 as the sensor was deployed multiple times.

The DIC LOC sensor operates by acidifying a water sample, converting the DIC to CO_2 which then crosses a membrane into an acceptor solution, which is monitored for a signal that is proportional to the DIC concentration. The sensor can be viewed as two key constituent components; the module responsible for facilitating the gas exchange, and the detector module. These were independently optimised and then integrated to produce benchtop instrument. The benchtop instrument was then miniaturised and automated to produce the DIC LOC sensor.

6.1.1 Gas Exchange Unit

To ensure the sensor operates effectively, a rapid and efficient CO_2 exchange is essential. The work described fully in Chapter 2 demonstrated that a Tube In A Tube (TIAT) was the optimal design for the Gas Exchange Unit (GEU) for the current version of the DIC LOC sensor. The TIAT was found to be mechanically robust and readily integrated into the sensor, while also providing a rapid gas exchange. The TIAT was also easily accessible, and serviceable, during the cases when it needed to be replaced. Testing demonstrated that the gas exchange occurred within one minute.

Further work investigated planar membranes and demonstrated the potential of a bonded planar GEU. Several of the bonded planar GEUs functioned well over many months, with work presented in Chapter 4 detailing a benchtop instrument, which utilised a bonded planar GEU. Ultimately, the bonded planar GEU was not selected for the current DIC LOC sensor, which is presented in this work, as the TIAT was more adaptable and offered the ability to repair the GEU in case of failure. The TIAT was also fabricated more easily, because the bonding method for the planar GEU took longer and had a higher failure rate. The failure rate of the planar GEU bonding process is being addressed in future work.

6.1.2 Detector

Conductometric detection was selected as the optimal method to measure the response in the acceptor solution, as this method had been demonstrated to show potential for making high quality measurements using readily available reagents. A Capacitively Coupled Contactless Conductivity Detector (C4D) design was selected for the current DIC LOC sensor. This was chosen as the electrodes were isolated from the acceptor measurement fluid, removing concerns over the electrode's long term stability. The C4D was optimised to measure the conductivity range of interest.

Contacting electrodes were also investigated as a potential design for the detector. Stability testing proved that the contacting electrodes were stable in 7 mM NaOH over multiple months. Further work then demonstrated that the four-electrode design offered improved performance over the two-electrode design. The contacting four-electrode design has been progressed further as detailed in section 6.1.4 and has demonstrated clear potential for use in future versions of the DIC LOC sensor.

6.1.3 DIC LOC Sensor

A total of seven sensors were fabricated and this work has detailed the data collected with a subset of these units over the course of the EU funded STEMM-CCS experiment. The fieldwork described Chapter 5 demonstrated that this sensor could be operated as both an underway instrument and an autonomous sensor. The final version of the sensor demonstrated a laboratory based precision of < 1 µmol kg^{-1} and field testing found the sensor had a precision of ~10 µmol kg^{-1}. The laboratory precision is an order of magnitude better than required to make climate quality measurements as defined by Global Ocean Acidification Observing Network (Newton *et al.*, 2014). The precision from field-testing was closer to the Global Ocean Acidification Observing Network definition of weather quality measurements, however with modification to the measurement cycle precision closer to the laboratory precision should be achievable. The deployments have demonstrated that the DIC LOC sensor is robust, flexible, and capable of making accurate measurements of the marine carbonate system.

A recent review of carbonate measurement technology found there is currently no commercially available sensors or underway instruments capable of measuring DIC (Martz *et al.*, 2015). The autonomous DIC LOC sensor developed in this work fills this current technological gap and enhances the ability to measure and monitor climate change. Since the conclusion of the fieldwork for the STEMM-CCS experiment, the sensor has been integrated on to the AUV *Autosub* and deployed in a Scottish loch, further highlighting the deployment potential for this sensor.

6.1.4 Future developments

The reduction in precision between the laboratory and field assessment has provided evidence of carry-over between samples, which will require addressing for future deployments. The flushing system could be improved with the current hardware by increasing the number of flushes between samples. There are several potential future modifications to the hardware, which could also improve the flushing, and therefore improve the performance of the sensor.

Following the work developing contacting tubular brass electrodes described in Chapter 3 further work has been started to develop planar platinum micro-electrodes. An in-house developed potentiostat has been tested with both tubular brass electrodes (from section 3.5) and planar platinum micro-electrodes, with both systems showing promising results. The planar electrodes have a greatly reduced volume compared to the detector used in the final version of the sensor, and also have the potential to be integrated with the main LOC module. This has two main impacts; the smaller volume will require a lower volume to flush the system, which will subsequently reduce the carry-over and potentially increase the sampling frequency. The micro-electrodes are manufactured in a more easily repeatable manner than the contacting tubular electrodes which will reduce the variation between units. As the new electrodes can be integrated directly into the LOC module it will dramatically reduce the overall physical dimensions of the sensor. This will increase the number of platforms the sensor could be deployed on.

The bonding technique developed in section 2.3.2 offers the potential to integrate a membrane directly within a detector based on planar electrodes. This would allow a reduction in the sample volume required, as well as offering improved flushing. This would increase the potential measurement frequency for future versions of the DIC LOC sensor.

Chapter 4 presented the results of simplex optimisation work carried out on a benchtop instrument. This demonstrated that independently adjusting the flow rate of the sample and acid increased the magnitude of the recorded signal. The optimisation work found that a sample to acid flow rate ratio of 1:2.5 produced the maximum signal. With the current sensor pump hardware, it is not possible to achieve this flow rate ratio. For future DIC LOC sensors, utilising pumps which could be set to pump at different flow rates would allow this ratio to be used to increase the signal, potentially reducing the signal to noise ratio in the measurement.

A TA LOC sensor is also in development. The TA LOC sensor operates based on a single-point open system acid titration of seawater, with the sample CO_2 extracted through a GEU. The waste acidified seawater from the DIC sensor could be taken as the sample for the TA LOC sensor. The reciprocal is also true, with the TA LOC waste from the GEU being equivalent to the DIC sample,

meaning that the two sensors could be combined into one unit. In the future an integrated TA-DIC sensor will be designed based on the sensor described in this work. This TA-DIC LOC sensor will be capable of completely resolving the carbonate system. This sensor system would have the potential to dramatically increase the coverage of carbonate data, as this unit would be of such a size that it could be integrated into the full range of sensor platforms currently available.

6.2 Future Outlook

Historically humans have benefited greatly from the world's oceans (Gee, 2019), viewing them as a limitless resource (Rock, Sima and Knapen, 2020). Now looking to the future as the world's population continues to grow, the number and complexities of human interactions with the oceans are set to increase (Halpern *et al.*, 2019). Temperature changes, rising sea levels and ocean acidification associated with global climate change (IPCC, 2014), in addition to increases in pollution are classic examples of marine stressors that require monitoring, but they are not the only ones. Marine ecosystems provide an essential source of nutrition; in 2015 fish provided 17% of the animal protein consumed by the global population (FAO, 2018) and aquaculture is the fastest growing sector producing food (FAO, 2018). Increasingly new fields are emerging which will impact the ocean, such as deep-sea mineral mining (Gollner *et al.*, 2017; Van Dover *et al.*, 2017), offshore energy production (Garel *et al.*, 2014) and carbon capture and storage (Turley *et al.*, 2009; Blackford *et al.*, 2014, 2015), and each of these processes will require sustained efforts to adequately monitor their impacts.

Traditional ship based monitoring is expensive and not always the most appropriate method to monitor the large scale oceanic process (Bushinsky, Takeshita and Williams, 2019). The limitations of traditional monitoring techniques have led to a recent drive in the development of *in situ* biogeochemical sensing systems. The key driver behind this development has been to improve spatiotemporal data coverage in the ocean (Delory and Pearlman, 2019). To continue to advance, sensor development has been focused on two main areas: miniaturisation and reducing the cost of sensors, whilst maintaining high quality measurements.

Through continued miniaturisation the range of platforms on which sensors can be mounted is increased, therefore improving coverage. A key example of this is the Argo program, which in 20 years has vastly improved global data coverage of physical parameters by recording over 2,000,000 profiles by 2018, all of which are openly accessible (Roemmich *et al.*, 2019). More recently the Argo program has started to improve the coverage of biogeochemical measurements by adding sensors capable of measuring parameters such as oxygen, nitrate and pH to floats (Johnson and Claustre, 2016; Roemmich *et al.*, 2019).

Moving forward, the price of miniaturised sensors will be leading factors in determining their long-term viability. Reducing the cost of sensors not only improves coverage by enabling more sensors to be deployed on a lower budget (Marcelli *et al.*, 2014) but can also facilitate improved community engagement and education (Wong *et al.*, 2018; Wang *et al.*, 2019; Brewin *et al.*, 2020). Recently in the field of air quality measurement there has been an increase in the number of low cost sensors, providing data over a larger area but with higher uncertainties in each measurement (Snyder *et al.*, 2013). Despite the higher uncertainties the data can be utilised alongside independent data to make reliable conclusions (Williams, 2019). In the future this approach could be applied to oceanic biogeochemical measurements in order to increase data coverage while maintaining a lower budget compared to traditional ship based monitoring.

With the UN ocean decade approaching, initial planning for the 2021-2030 project has focused on 6 objectives (Trakadas *et al.*, 2019):

1. A clean ocean
2. A healthy and resilient ocean
3. A predicted ocean
4. A safe ocean
5. A sustainably harvested and productive ocean
6. A transparent and accessible ocean

Each of these objectives will require a degree of monitoring which will be reliant on marine technology to effectively collect data. To meet the third objective of a predicted ocean, models will require access to data in as close to real time as possible (Partescano *et al.*, 2017), presenting another challenge for new observing methodologies. The final of the six objectives highlights transparency and accessibility, and points not only to open access data but also to the potential use of open source technology (Cressey, 2013; Valada *et al.*, 2014; Carlson *et al.*, 2019). As such, the UN ocean decade could facilitate the democratisation of access to ocean data, while utilising modern technologies such as miniaturised sensors.

A paper written in 1989 envisioning how ocean monitoring would look 25 years into the future imagined there would be a spread of vehicles operating across the globe, covering the traditional WOCE survey lines (Stommel, 1989). The Argo program has eclipsed the predicted 1,000 platforms, deploying more than 3,800 platforms to date, however these floats do not have the directional control outlined in that original paper. As the cost of purchasing, operating, and maintaining vehicles and sensors drops the envisioned reality of deploying swarms of vehicles gets closer (Gregory and Vardy, 2020). Swarms of vehicles offer the potential to improve the efficiency of data collection by using novel tracks, rather than traditional lawn mower survey

lines, to map features or survey more rapidly (Hwang, Bose and Fan, 2019). Swarms of vehicles also offer the potential to act as a distributed network allowing efficient transfer of data back to end users (Jaffe *et al.*, 2017). Increasing the density of platforms in the ocean also offers the opportunity to improve data quality by enabling inter calibration of sensors across vehicles (Allen *et al.*, 2020), which was also visualised in the 1989 paper.

It is apparent that there is a clear need for the continued development of ocean technology that can augment our understanding of global climate change, overcome the challenges presented by traditional data collection methods, and reliably monitor emerging fields. Innovative technology has the power to yield data on a diverse range of oceanic processes, supporting the sustainable management of marine resources that is essential for future generations.

List of References

Abdelrasoul, A., Doan, H., Lohi, A. and Cheng, C. H. (2015) 'Mass Transfer Mechanisms and Transport Resistances in Membrane Separation Process', in *Mass Transfer - Advancement in Process Modelling*, pp. 15–40. doi: 10.5772/60866.

Achterberg, E. P. and Esposito, M. (2018) *RV POSEIDON Fahrtbericht / Cruise Report POS527 - Baseline Study for the Environmental Monitoring of Subseafloor CO_2 Storage Operations*. Kiel, Germany. doi: 10.3289/geomar_rep_ns_45_2018.

Alam, K., Ray, T. and Anavatti, S. G. (2014) 'A brief taxonomy of autonomous underwater vehicle design literature', *Ocean Engineering*, 88, pp. 627–630. doi: 10.1016/j.oceaneng.2014.04.027.

Albright, R., Caldeira, L., Hosfelt, J., Kwiatkowski, L., Maclaren, J. K., Mason, B. M., Nebuchina, Y., Ninokawa, A., Pongratz, J., Ricke, K. L., Rivlin, T., Schneider, K., Sesboüé, M., Shamberger, K., Silverman, J., Wolfe, K., Zhu, K. and Caldeira, K. (2016) 'Reversal of ocean acidification enhances net coral reef calcification', *Nature*, 531(7594), pp. 362–365. doi: 10.1038/nature17155.

Allen, J. T., Munoz, C., Gardiner, J., Reeve, K. A., Alou-Font, E. and Zarokanellos, N. (2020) 'Near-Automatic Routine Field Calibration/Correction of Glider Salinity Data Using Whitespace Maximization Image Analysis of Theta/S Data', *Frontiers in Marine Science*, 7. doi: 10.3389/fmars.2020.00398.

Amornthammarong, N., Ortner, P. B., Hendee, J. and Woosley, R. (2014) 'A simplified coulometric method for multi-sample measurements of total dissolved inorganic carbon concentration in marine waters', *Analyst*, 139(20), pp. 5263–5270. doi: 10.1039/C4AN01049C.

Baker, R. W. (2012) 'Membrane Transport Theory', in Baker, R. W. (ed.) *Membrane Technology and Applications*, pp. 15–96. doi: 10.1002/9781118359686.ch2.

Bakker, D. C. E., Pfeil, B., Landa, C. S., Metzl, N., O'Brien, K. M., Olsen, A., Smith, K., Cosca, C., Harasawa, S., Jones, S. D., Nakaoka, S., Nojiri, Y., Schuster, U., Steinhoff, T., Sweeney, C., Takahashi, T., Tilbrook, B., Wada, C., Wanninkhof, R., Alin, S. R., Balestrini, C. F., Barbero, L., Bates, N. R., Bianchi, A. A., Bonou, F., Boutin, J., Bozec, Y., Burger, E. F., Cai, W.-J., Castle, R. D., Chen, L., Chierici, M., Currie, K., Evans, W., Featherstone, C., Feely, R. A., Fransson, A., Goyet, C., Greenwood, N., Gregor, L., Hankin, S., Hardman-Mountford, N. J., Harlay, J., Hauck, J., Hoppema, M., Humphreys, M. P., Hunt, C. W., Huss, B., Ibánhez, J. S. P., Johannessen, T., Keeling, R., Kitidis, V., Körtzinger, A., Kozyr, A., Krasakopoulou, E., Kuwata, A., Landschützer, P., Lauvset, S. K., Lefèvre, N., Lo Monaco, C., Manke, A., Mathis, J. T., Merlivat, L., Millero, F. J., Monteiro, P. M. S.,

Munro, D. R., Murata, A., Newberger, T., Omar, A. M., Ono, T., Paterson, K., Pearce, D., Pierrot, D., Robbins, L. L., Saito, S., Salisbury, J., Schlitzer, R., Schneider, B., Schweitzer, R., Sieger, R., Skjelvan, I., Sullivan, K. F., Sutherland, S. C., Sutton, A. J., Tadokoro, K., Telszewski, M., Tuma, M., van Heuven, S. M. A. C., Vandemark, D., Ward, B., Watson, A. J. and Xu, S. (2016) 'A multi-decade record of high-quality fCO_2 data in version 3 of the Surface Ocean CO_2 Atlas (SOCAT)', *Earth System Science Data*, 8(2), pp. 383–413. doi: 10.5194/essd-8-383-2016.

Baltussen, E., Guijt, R. M., Van Der Steen, G., Laugere, F., Baltussen, S. and Van Dedem, G. W. K. (2002) 'Considerations on contactless conductivity detection in capillary electrophoresis', *Electrophoresis*, 23(17), pp. 2888–2893.

Bates, N. R., Astor, Y. M., Church, M. J., Currie, K., Dore, J. E., González-Dávila, M., Lorenzoni, L., Muller-Karger, F., Olafsson, J. and Santana-Casiano, J. M. (2014) 'A time-series view of changing surface ocean chemistry due to ocean uptake of anthropogenic CO_2 and ocean acidification', *Oceanography*, 27(1), pp. 126–141. doi: 10.5670/oceanog.2014.16.

Beaton, A. D., Cardwell, C. L., Thomas, R. S., Sieben, V. J., Legiret, F. E., Waugh, E. M., Statham, P. J., Mowlem, M. C. and Morgan, H. (2012) 'Lab-on-chip measurement of nitrate and nitrite for in situ analysis of natural waters', *Environmental Science and Technology*, 46(17), pp. 9548–9556. doi: 10.1021/es300419u.

Bell, R. J., Short, R. T., Van Amerom, F. H. W. and Byrne, R. H. (2007) 'Calibration of an in situ membrane inlet mass spectrometer for measurements of dissolved gases and volatile organics in seawater', *Environmental Science and Technology*, 41(23), pp. 8123–8128. doi: 10.1021/es070905d.

Bell, R. J., Short, R. T. and Byrne, R. H. (2011) 'In situ determination of total dissolved inorganic carbon by underwater membrane introduction mass spectrometry', *Limnology and Oceanography: Methods*, 9, pp. 164–175. doi: 10.4319/lom.2011.9.164.

Betts, R. A., Jones, C. D., Knight, J. R., Keeling, R. F. and Kennedy, J. J. (2016) 'El Nino and a record CO_2 rise', *Nature Climate Change*, 6(9), pp. 806–810. doi: 10.1038/NCLIMATE3063.

Bezerra, M. A., dos Santos, Q. O., Santos, A. G., Novaes, C. G., Ferreira, S. L. C. and de Souza, V. S. (2016) 'Simplex optimization: A tutorial approach and recent applications in analytical chemistry', *Microchemical Journal*, 124, pp. 45–54. doi: 10.1016/j.microc.2015.07.023.

Birchill, A. J., Clinton-Bailey, G., Hanz, R., Mawji, E., Cariou, T., White, C., Ussher, S. J., Worsfold, P. J., Achterberg, E. P. and Mowlem, M. (2019) 'Realistic measurement uncertainties for marine macronutrient measurements conducted using gas segmented flow and Lab-on-Chip techniques',

Talanta, 200, pp. 228–235. doi: 10.1016/j.talanta.2019.03.032.

Blackford, J., Bull, J. M., Cevatoglu, M., Connelly, D., Hauton, C., James, R. H., Lichtschlag, A., Stahl, H., Widdicombe, S. and Wright, I. C. (2015) 'Marine base line and monitoring strategies for carbon dioxide capture and storage (CCS)', *International Journal of Greenhouse Gas Control*, 38, pp. 221–229. doi: 10.1016/j.ijggc.2014.10.004.

Blackford, J., Stahl, H., Bull, J. M., Bergès, B. J. P., Cevatoglu, M., Lichtschlag, A., Connelly, D., James, R. H., Kita, J., Long, D., Naylor, M., Shitashima, K., Smith, D., Taylor, P., Wright, I., Akhurst, M., Chen, B., Gernon, T. M., Hauton, C., Hayashi, M., Kaieda, H., Leighton, T. G., Sato, T., Sayer, M. D. J., Suzumura, M., Tait, K., Vardy, M. E., White, P. R. and Widdicombe, S. (2014) 'Detection and impacts of leakage from sub-seafloor deep geological carbon dioxide storage', *Nature Climate Change*, 4(11), pp. 1011–1016. doi: 10.1038/nclimate2381.

Bockmon, E. E. and Dickson, A. G. (2015) 'An inter-laboratory comparison assessing the quality of seawater carbon dioxide measurements', *Marine Chemistry*, 171, pp. 36–43. doi: 10.1016/j.marchem.2015.02.002.

Bozec, Y., Thomas, H., Schiettecatte, L. S., Borges, A. V., Elkalay, K. and De Baar, H. J. W. (2006) 'Assessment of the processes controlling seasonal variations of dissolved inorganic carbon in the North Sea', *Limnology and Oceanography*, 51(6), pp. 2746–2762. doi: 10.4319/lo.2006.51.6.2746.

Breitburg, D., Salisbury, J., Bernhard, J., Cai, W. J., Dupont, S., Doney, S., Levin, L., Long, C., Milke, L., Miller, S., Phelan, B., Passow, U., Seibel, B., Todgham, A. and Tarrant, A. (2015) 'And on top of all that… Coping with ocean acidification in the midst of many stressors', *Oceanography*, 28(2), pp. 48–61. doi: 10.5670/oceanog.2015.31.

Bresnahan, P. J. and Martz, T. R. (2018) 'Gas Diffusion Cell Geometry for a Microfluidic Dissolved Inorganic Carbon Analyzer', *IEEE Sensors Journal*, 18(6), pp. 2211–2217. doi: 10.1109/JSEN.2018.2794882.

Bresnahan, P. J., Martz, T. R., Takeshita, Y., Johnson, K. S. and LaShomb, M. (2014) 'Best practices for autonomous measurement of seawater pH with the Honeywell Durafet', *Methods in Oceanography*, 9, pp. 44–60. doi: 10.1016/j.mio.2014.08.003.

Brewin, R. J. W., Cyronak, T., Bresnahan, P. J., Andersson, A. J., Richard, J., Hammond, K., Billson, O., de Mora, L., Jackson, T., Smale, D. and Dall'Olmo, G. (2020) 'Comparison of Two Methods for Measuring Sea Surface Temperature When Surfing', *Oceans*, 1(1), pp. 6–26. doi: 10.3390/oceans1010002.

Brom-Verheijden, G. J. A. M., Goedbloed, M. H. and Zevenbergen, M. A. G. (2018) 'A Microfabricated 4-Electrode Conductivity Sensor with Enhanced Range', *Proceedings*, 2(13), p. 797. doi: 10.3390/proceedings2130797.

Burt, W. J., Thomas, H., Hagens, M., Pätsch, J., Clargo, N. M., Salt, L. A., Winde, V. and Böttcher, M. E. (2016) 'Carbon sources in the North Sea evaluated by means of radium and stable carbon isotope tracers', *Limnology and Oceanography*, 61(2), pp. 666–683. doi: 10.1002/lno.10243.

Bushinsky, S. M., Takeshita, Y. and Williams, N. L. (2019) 'Observing Changes in Ocean Carbonate Chemistry: Our Autonomous Future', *Current Climate Change Reports*, 5(3), pp. 207–220. doi: 10.1007/s40641-019-00129-8.

Butterworth, B. J. and Miller, S. D. (2016) 'Air-sea exchange of carbon dioxide in the Southern Ocean and Antarctic marginal ice zone', *Geophysical Research Letters*, 43(13), pp. 7223–7230. doi: 10.1002/2016GL069581.

Byrne, R. H. (2014) 'Measuring ocean acidification: New technology for a new era of ocean chemistry', *Environmental Science and Technology*, 48(10), pp. 5352–5360. doi: 10.1021/es405819p.

Byrne, R. H., Liu, X., Kaltenbacher, E. A. and Sell, K. (2002) 'Spectrophotometric measurement of total inorganic carbon in aqueous solutions using a liquid core waveguide', *Analytica Chimica Acta*, 451, pp. 221–229. doi: 10.1016/S0003-2670(01)01423-4.

Cardenas-Valencia, A. M., Adornato, L. R., Bell, R. J., Byrne, R. H. and Short, R. T. (2013) 'Evaluation of reagentless pH modification for in situ ocean analysis: Determination of dissolved inorganic carbon using mass spectrometry', *Rapid Communications in Mass Spectrometry*, 27(5), pp. 635–642. doi: 10.1002/rcm.6487.

Carella, G., Morris, A. K. R., Pascal, R. W., Yelland, M. J., Berry, D. I., Morak-Bozzo, S., Merchant, C. J. and Kent, E. C. (2017) 'Measurements and models of the temperature change of water samples in sea-surface temperature buckets', *Quarterly Journal of the Royal Meteorological Society*, 143(706), pp. 2198–2209. doi: 10.1002/qj.3078.

Di Carlo, D. (2009) 'Inertial microfluidics', *Lab on a Chip*, 9(21), pp. 3038–3046. doi: 10.1039/b912547g.

Carlson, D. F., Fürsterling, A., Vesterled, L., Skovby, M., Pedersen, S. S., Melvad, C. and Rysgaard, S. (2019) 'An affordable and portable autonomous surface vehicle with obstacle avoidance for coastal ocean monitoring', *HardwareX*, 5. doi: 10.1016/j.ohx.2019.e00059.

Ciais, P., Sabine, C., Bala, G., Bopp, L., Brovkin, V., Canadell, J., Chhabra, A., DeFries, R., Galloway, J., Heimann, M., Jones, C., Quéré, C. Le, Myneni, R. B., Piao, S. and Thornton, P. (2013) 'Carbon and other biogeochemical cycles', in Stocker, T. F., Qin, D., Plattner, G., Tignor, M., Allen, S. K., Boschung, J., Nauels, A., Xia, Y., Bex, V., and Midgley, P. M. (eds) *Climate Change 2013 the Physical Science Basis: Working Group I Contribution to the Fifth Assessment Report of the Intergovernmental Panel on Climate Change*, pp. 465–570. doi: 10.1017/CBO9781107415324.015.

Ciais, P., Tan, J., Wang, X., Roedenbeck, C., Chevallier, F., Piao, S. L., Moriarty, R., Broquet, G., Le Quéré, C., Canadell, J. G., Peng, S., Poulter, B., Liu, Z. and Tans, P. (2019) 'Five decades of northern land carbon uptake revealed by the interhemispheric CO_2 gradient', *Nature*, 568(7751), pp. 221–225. doi: 10.1038/s41586-019-1078-6.

Ciobotaru, I., Barbu, O., Rus, T. and Vaireanu, D. (2016) 'Conductivity cell constant revisited', *Bulletin of Romanian Chemical Engineering Society*, 3(1), pp. 34–46.

Clargo, N. M., Salt, L. A., Thomas, H. and de Baar, H. J. W. (2015) 'Rapid increase of observed DIC and pCO_2 in the surface waters of the North Sea in the 2001-2011 decade ascribed to climate change superimposed by biological processes', *Marine Chemistry*, 177, pp. 566–581. doi: 10.1016/j.marchem.2015.08.010.

Clinton-Bailey, G. S., Grand, M. M., Beaton, A. D., Nightingale, A. M., Owsianka, D. R., Slavik, G. J., Connelly, D. P., Cardwell, C. L. and Mowlem, M. C. (2017) 'A Lab-on-Chip Analyzer for in Situ Measurement of Soluble Reactive Phosphate: Improved Phosphate Blue Assay and Application to Fluvial Monitoring', *Environmental Science and Technology*, 51(17), pp. 9989–9995. doi: 10.1021/acs.est.7b01581.

Coltro, W. K. T., Lima, R. S., Segato, T. P., Carrilho, E., De Jesus, D. P., Do Lago, C. L. and Da Silva, J. A. F. (2012) 'Capacitively coupled contactless conductivity detection on microfluidic systems - Ten years of development', *Analytical Methods*, 4(1), pp. 25–33. doi: 10.1039/c1ay05364g.

Convery, N. and Gadegaard, N. (2019) '30 Years of Microfluidics', *Micro and Nano Engineering*, 2, pp. 76–91. doi: 10.1016/j.mne.2019.01.003.

Cressey, D. (2013) 'Crowdsourcing may open up ocean science', *Nature*. doi: 10.1038/nature.2013.13341.

Crutzen, P. J. (2006) 'The "Anthropocene"', in Ehlers, E. and Krafft, T. (eds) *Earth System Science in the Anthropocene*, pp. 13–18. doi: 10.1007/3-540-26590-2_3.

Csavina, J., Roberti, J. A., Taylor, J. R. and Loescher, H. W. (2017) 'Traceable measurements and

calibration: A primer on uncertainty analysis', *Ecosphere*, 8(2). doi: 10.1002/ecs2.1683.

DeGrandpre, M. D., Spaulding, R., Newton, J. O., Jaqueth, E. J., Hamblock, S. E., Umansky, A. A. and Harris, K. E. (2014) 'Considerations for the measurement of spectrophotometric pH for ocean acidification and other studies', *Limnology and Oceanography Methods*, 12, pp. 830–839. doi: 10.4319/lom.2014.12.830.

Delory, E. and Pearlman, J. (eds) (2019) 'Chapter 1 - Introduction', in *Challenges and Innovations in Ocean In Situ Sensors*, pp. 1–26. doi: https://doi.org/10.1016/B978-0-12-809886-8.00001-6.

Deming, S., Jr, L. and Denton, B. (2008) 'A Review of Simplex Optimization in Analytical Chemistry', *Critical Reviews in Analytical Chemistry*, 7, pp. 187–202. doi: 10.1080/10408347808542701.

Denuault, G. (2009) 'Electrochemical techniques and sensors for ocean research', *Ocean Science*, 5, pp. 697–710. doi: 10.5194/osd-6-1857-2009.

DeVries, T., Le Quéré, C., Andrews, O., Berthet, S., Hauck, J., Ilyina, T., Landschützer, P., Lenton, A., Lima, I. D., Nowicki, M., Schwinger, J. and Séférian, R. (2019) 'Decadal trends in the ocean carbon sink', *Proceedings of the National Academy of Sciences of the United States of America*, 116(24), pp. 11646–11651. doi: 10.1073/pnas.1900371116.

Dickson, A. G. (1990a) 'Standard potential of the reaction: $AgCl_{(s)} + 12H_{2(g)} = Ag_{(s)} + HCl_{(aq)}$, and the standard acidity constant of the ion HSO_4^- in synthetic sea water from 273.15 to 318.15 K', *The Journal of Chemical Thermodynamics*, 22(2), pp. 113–127. doi: 10.1016/0021-9614(90)90074-Z.

Dickson, A. G. (1990b) 'Thermodynamics of the Dissociation of Boric Acid in Potassium Chloride Solutions from 273.15 to 318.15 K', *Journal of Chemical and Engineering Data*, 35(3), pp. 253–257. doi: 10.1021/je00061a009.

Dickson, A. G. (2010) 'Standards for ocean measurements', *Oceanography*, 23(3), pp. 34–47. doi: 10.5670/oceanog.2010.22.

Dickson, A. G. and Goyet, C. (1994) 'Handbook of methods for the analysis of the various parameters of the carbon dioxide system in sea water, version 2'. doi: 10.2172/10107773.

Dickson, A. G. and Millero, F. J. (1987) 'A comparison of the equilibrium constants for the dissociation of carbonic acid in seawater media', *Deep Sea Research Part A, Oceanographic Research Papers*, 34(10), pp. 1733–1743. doi: 10.1016/0198-0149(87)90021-5.

Dickson, A. G., Sabine, C. L. and Christian, J. R. (2007) 'Guide to best practices for ocean CO_2

measurements', *PICES Special Publication*, 3, p. p191. doi: 10.1159/000331784.

Doney, S. C., Fabry, V. J., Feely, R. A. and Kleypas, J. A. (2009) 'Ocean Acidification: The Other CO_2 Problem', *Annual Review of Marine Science*, 1(1), pp. 169–192. doi: 10.1146/annurev.marine.010908.163834.

Van Dover, C. L., Ardron, J. A., Escobar, E., Gianni, M., Gjerde, K. M., Jaeckel, A., Jones, D. O. B., Levin, L. A., Niner, H. J., Pendleton, L., Smith, C. R., Thiele, T., Turner, P. J., Watling, L. and Weaver, P. P. E. (2017) 'Biodiversity loss from deep-sea mining', *Nature Geoscience*, 10(7), pp. 464–465. doi: 10.1038/ngeo2983.

Ellison, S. L. R. and Williams, A. (2012) *Eurachem/CITAC guide: Quantifying Uncertainty in Analytical Measurement,*. Third. Edited by S. L. R. Ellison and W. A. Available at: www.eurachem.org.

Emerson, S. and Hedges J (2008) 'Carbonate Chemistry', in Hedges, J. and Emerson, S. (eds) *Chemical Oceanography and the Marine Carbon Cycle*, pp. 101–133. doi: DOI: 10.1017/CBO9780511793202.005.

Esposito, M., Martinez-Cabanas, M. and Achterberg, E. P. (2019) 'Hydrochemistry and carbonate chemistry measured on water bottle samples during POSEIDON cruise POS527'. doi: 10.1594/PANGAEA.907809.

FAO (2016) *The State of World Fisheries and Aquaculture 2016*. Rome.

FAO (2018) *The State of World Fisheries and Aquaculture 2018 - Meeting the sustainable development goals*, *Fisheries Oceanography*. Rome.

Fassbender, A. J., Sabine, C. L., Lawrence-Slavas, N., De Carlo, E. H., Meinig, C. and Maenner Jones, S. (2015) 'Robust sensor for extended autonomous measurements of surface ocean dissolved inorganic carbon', *Environmental Science and Technology*, 49(6), pp. 3628–3635. doi: 10.1021/es5047183.

Fouletier, J. and Fabry, P. (2013) 'Impedancemetric Sensors', in Fouletier, J. and Fabry, P. (eds) *Chemical and Biological Microsensors*, pp. 307–330. doi: 10.1002/9781118603871.ch10.

Friedlingstein, P., Jones, M. W., O'Sullivan, M., Andrew, R. M., Hauck, J., Peters, G. P., Peters, W., Pongratz, J., Sitch, S., Le Quéré, C., Bakker, D. C. E., Canadell, J. G., Ciais, P., Jackson, R. B., Anthoni, P., Barbero, L., Bastos, A., Bastrikov, V., Becker, M., Bopp, L., Buitenhuis, E., Chandra, N., Chevallier, F., Chini, L. P., Currie, K. I., Feely, R. A., Gehlen, M., Gilfillan, D., Gkritzalis, T., Goll, D. S., Gruber, N., Gutekunst, S., Harris, I., Haverd, V., Houghton, R. A., Hurtt, G., Ilyina, T., Jain, A. K.,

Joetzjer, E., Kaplan, J. O., Kato, E., Klein Goldewijk, K., Korsbakken, J. I., Landschützer, P., Lauvset, S. K., Lefèvre, N., Lenton, A., Lienert, S., Lombardozzi, D., Marland, G., McGuire, P. C., Melton, J. R., Metzl, N., Munro, D. R., Nabel, J. E. M. S., Nakaoka, S.-I., Neill, C., Omar, A. M., Ono, T., Peregon, A., Pierrot, D., Poulter, B., Rehder, G., Resplandy, L., Robertson, E., Rödenbeck, C., Séférian, R., Schwinger, J., Smith, N., Tans, P. P., Tian, H., Tilbrook, B., Tubiello, F. N., van der Werf, G. R., Wiltshire, A. J. and Zaehle, S. (2019) 'Global Carbon Budget 2019', *Earth System Science Data*, 11(4), pp. 1783–1838. doi: 10.5194/essd-11-1783-2019.

Garel, E., Rey, C. C., Ferreira, Ó. and van Koningsveld, M. (2014) 'Applicability of the "Frame of Reference" approach for environmental monitoring of offshore renewable energy projects', *Journal of Environmental Management*, 141, pp. 16–28. doi: 10.1016/j.jenvman.2014.02.037.

Gaš, B., Demjanenko, M. and Vacík, J. (1980) 'High-frequency contactless conductivity detection in isotachophoresis', *Journal of Chromatography*, 192, pp. 253–257. doi: 10.1016/S0021-9673(80)80001-X.

Gattuso, J., Gao, K., Lee, K., Rost, B. and Schulz, K. G. (2010) 'Approaches and tools to manipulate the carbonate chemistry', in Riebesell, U., Fabry, V. J., Hansson, L., and Gattuso, J. (eds) *Guide for Best Practices in Ocean Acidification Research and Data Reporting*, pp. 41–52.

Gee, K. (2019) 'The Ocean Perspective', in Zaucha, J. and Gee, K. (eds) *Maritime Spatial Planning: past, present, future*, pp. 23–45. doi: 10.1007/978-3-319-98696-8_2.

Gollner, S., Kaiser, S., Menzel, L., Jones, D. O. B., Brown, A., Mestre, N. C., van Oevelen, D., Menot, L., Colaço, A., Canals, M., Cuvelier, D., Durden, J. M., Gebruk, A., Egho, G. A., Haeckel, M., Marcon, Y., Mevenkamp, L., Morato, T., Pham, C. K., Purser, A., Sanchez-Vidal, A., Vanreusel, A., Vink, A. and Martinez Arbizu, P. (2017) 'Resilience of benthic deep-sea fauna to mining activities', *Marine Environmental Research*, 129, pp. 76–101. doi: 10.1016/j.marenvres.2017.04.010.

Gong, W., Mowlem, M., Kraft, M. and Morgan, H. (2008) 'Oceanographic Sensor for in-situ temperature and conductivity monitoring', in *OCEANS 2008 - MTS/IEEE Kobe Techno-Ocean*, pp. 1–6. doi: 10.1109/OCEANSKOBE.2008.4530906.

Grand, M. M., Clinton-Bailey, G. S., Beaton, A. D., Schaap, A. M., Johengen, T. H., Tamburri, M. N., Connelly, D. P., Mowlem, M. C. and Achterberg, E. P. (2017) 'A Lab-On-Chip Phosphate Analyzer for Long-term In Situ Monitoring at Fixed Observatories: Optimization and Performance Evaluation in Estuarine and Oligotrophic Coastal Waters', *Frontiers in Marine Science*, 4, pp. 1–16. doi: 10.3389/fmars.2017.00255.

Gray, J. R. (2005) 'Conductivity Analyzers and Their Application', in Down, R. D. and Lehr, J. H.

(eds) *Environmental Instrumentation and Analysis Handbook*, pp. 491–510. doi: 10.1002/0471473332.ch23.

Gregory, C. and Vardy, A. (2020) 'microUSV: A low-cost platform for indoor marine swarm robotics research', *HardwareX*, 7, p. e00105. doi: 10.1016/j.ohx.2020.e00105.

Gruber, N., Clement, D., Carter, B. R., Feely, R. A., van Heuven, S., Hoppema, M., Ishii, M., Key, R. M., Kozyr, A., Lauvset, S. K., Monaco, C. Lo, Mathis, J. T., Murata, A., Olsen, A., Perez, F. F., Sabine, C. L., Tanhua, T. and Wanninkhof, R. (2019) 'The oceanic sink for anthropogenic CO_2 from 1994 to 2007', *Science*, 363(6432), pp. 1193–1199. doi: 10.1126/science.aau5153.

Guenther, P. R., Keeling, C. D. and Emanuele, G. (1994) 'Oceanic CO_2 Measurements for the WOCE Hydrographic Survey in the Pacific Ocean, 1990-1991: Shore Based Analyses', *SIO Reference Series Data Report*, pp. 123–129.

Hales, B., Chipman, D. W. and Takahashi, T. T. (2004) 'High-frequency measurement of partial pressure and total concentration of carbon dioxide in seawater using microporous hydrophobic membrane contactors', *Limnology and Oceanography: Methods*, 2, pp. 356–364. doi: 10.4319/lom.2004.2.356.

Hall, P. O. J. and Aller, R. C. (1992) 'Rapid, small volume, flow injection analysis for CO_2 and NH_4^+ in marine and freshwaters', *Limnology and Oceanography*, 37(5), pp. 1113–1119.

Halpern, B. S., Frazier, M., Afflerbach, J., Lowndes, J. S., Micheli, F., O'Hara, C., Scarborough, C. and Selkoe, K. A. (2019) 'Recent pace of change in human impact on the world's ocean', *Scientific Reports*, 9(1), pp. 1–8. doi: 10.1038/s41598-019-47201-9.

Heuer, R. M. and Grosell, M. (2014) 'Physiological impacts of elevated carbon dioxide and ocean acidification on fish', *Am J: Regulatory, Integrative and Comparative Physiology*, 307(9), pp. R1061–R1084. doi: 10.1152/ajpregu.00064.2014.

van Heuven, S., Pierrot, D., Rae, J. W. B., Lewis, E. and Wallace, D. W. R. (2011) 'MATLAB Program Developed for CO_2 System Calculations. ORNL/CDIAC-105b.', *ORNL/CDIAC-105b. Carbon Dioxide Information Analysis Center, Oak Ridge National Laboratory, U.S. Department of Energy, Oak Ridge, Tennessee*. doi: 10.3334/CDIAC/otg.CO2SYS_MATLAB_v1.1.

Hoherčáková, Z. and Opekar, F. (2005) 'A contactless conductivity detection cell for flow injection analysis: Determination of total inorganic carbon', *Analytica Chimica Acta*, 551, pp. 132–136. doi: 10.1016/j.aca.2005.07.029.

Hoherčáková, Z., Opekar, F. and Štulík, K. (2005) 'Thinly insulated wire cells - A new device for

sensitive contactless conductivity detection in flow analyses', *Electroanalysis*, 17(21), pp. 1924–1930. doi: 10.1002/elan.200503305.

Hoppe, C. J. M., Langer, G., Rokitta, S. D., Wolf-Gladrow, D. a. and Rost, B. (2012) 'Implications of observed inconsistencies in carbonate chemistry measurements for ocean acidification studies', *Biogeosciences*, 9(7), pp. 2401–2405. doi: 10.5194/bg-9-2401-2012.

Horton, R. (2019) 'Offline: Extinction or rebellion?', *The Lancet*, 394(10205), p. 1216. doi: 10.1016/S0140-6736(19)32260-3.

Huang, K., Cassar, N., Jonsson, B., Cai, W. J. and Bender, M. L. (2015) 'An Ultrahigh Precision, High-Frequency Dissolved Inorganic Carbon Analyzer Based on Dual Isotope Dilution and Cavity Ring-Down Spectroscopy', *Environmental Science and Technology*, 49(14), pp. 8602–8610. doi: 10.1021/acs.est.5b01036.

Huang, X., Pascal, R. W., Chamberlain, K., Banks, C. J., Mowlem, M. and Morgan, H. (2011) 'A miniature, high precision conductivity and temperature sensor system for ocean monitoring', *IEEE Sensors Journal*, 11(12), pp. 3246–3252. doi: 10.1109/JSEN.2011.2149516.

Hwang, J., Bose, N. and Fan, S. (2019) 'AUV adaptive sampling methods: A review', *Applied Sciences*, 9(15). doi: 10.3390/app9153145.

IPCC (2014) 'Summary for Policymakers', in Field, C. B., Barros, V. R., Dokken, D. J., Mach, K. J., Mastrandrea, M. D., Bilir, T. E., Chatterjee, M., Ebi, K. L., Estrada, Y. O., Genova, R. C., Girma, B., Kissel, E. S., Levy, A. N., MacCracken, S., Mastrandrea, P. R., and White, L. L. (eds) *Climate Change 2014: Impacts, Adaptation, and Vulnerability. Part A: Global and Sectoral Aspects. Contribution of Working Group II to the Fifth Assessment Report of the Intergovernmental Panel on Climate Change*, pp. 1–32.

Jaffe, J. S., Franks, P. J. S., Roberts, P. L. D., Mirza, D., Schurgers, C., Kastner, R. and Boch, A. (2017) 'A swarm of autonomous miniature underwater robot drifters for exploring submesoscale ocean dynamics', *Nature Communications*, 8. doi: 10.1038/ncomms14189.

Johnson, K. and Claustre, H. (2016) 'Bringing Biogeochemistry into the Argo Age', *Eos*. doi: 10.1029/2016eo062427.

Johnston, I. D., McDonnell, M. B., Tan, C. K. L., McCluskey, D. K., Davies, M. J. and Tracey, M. C. (2014) 'Dean flow focusing and separation of small microspheres within a narrow size range', *Microfluidics and Nanofluidics*, 17(3), pp. 509–518. doi: 10.1007/s10404-013-1322-6.

Jones, R. G. (2002) 'Measurements of the electrical conductivity of water', *IEE Proceedings* -

Science, Measurement and Technology, 149(6), pp. 320–322. doi: 10.1049/ip-smt:20020767.

de Jong, J., Lammertink, R. G. H. and Wessling, M. (2006) 'Membranes and microfluidics: a review.', *Lab on a chip*, 6(9), pp. 1125–1139. doi: 10.1039/b603275c.

Kaltin, S., Haraldsson, C. and Anderson, L. G. (2005) 'A rapid method for determination of total dissolved inorganic carbon in seawater with high accuracy and precision', *Marine Chemistry*, 96(1–2), pp. 53–60. doi: 10.1016/j.marchem.2004.10.005.

Kanehashi, S., Sato, T., Sato, S. and Nagai, K. (2014) 'Microstructure and Gas Diffusivity of Poly(dimethylsiloxane) Dense Membrane Using Molecular Dynamics (MD) Simulation', *Transactions of the Materials Research Society of Japan*, 37(3), pp. 439–442. doi: 10.14723/tmrsj.37.439.

Keeling, C. D., Bacastow, R. B. and Bainbridge, A. E. (1976) 'Atmospheric carbon dioxide variations at Mauna Loa Observatory, Hawaii', *Tellus*, 28(6), pp. 538–551. doi: 10.3402/tellusa.v28i6.11322.

Kelley, D. S., Delaney, J. R. and Juniper, S. K. (2014) 'Establishing a new era of submarine volcanic observatories: Cabling Axial Seamount and the Endeavour Segment of the Juan de Fuca Ridge', *Marine Geology*, 352, pp. 426–450. doi: 10.1016/j.margeo.2014.03.010.

Kim, K., Park, S. W. and Yang, S. S. (2010) 'The optimization of PDMS-PMMA bonding process using silane primer', *Biochip Journal*, 4(2), pp. 148–154. doi: 10.1007/s13206-010-4210-0.

Kleypas, J. A., Feely, R. A., Fabry, V. J., Langdon, C., Sabine, C. L. and Robbins, L. L. (2006) *Impacts of ocean acidification on coral reefs and other marine calcifiers. A guide for future research*.

Kubáň, P. and Hauser, P. C. (2004) 'Fundamental aspects of contactless conductivity detection for capillary electrophoresis. Part I: Frequency behavior and cell geometry', *Electrophoresis*, 25(20), pp. 3387–3397. doi: 10.1002/elps.200406059.

Kubáň, P. and Hauser, P. C. (2008) 'A review of the recent achievements in capacitively coupled contactless conductivity detection', *Analytica Chimica Acta*, 607, pp. 15–29. doi: 10.1016/j.aca.2007.11.045.

Kubáň, P. and Hauser, P. C. (2013) 'Contactless conductivity detection for analytical techniques: developments from 2010 to 2012.', *Electrophoresis*, 34(1), pp. 55–69. doi: 10.1002/elps.201200358.

Kubáň, V. and Dasgupta, P. K. (1993) 'Comparison of photometry and conductometry for the determination of total carbonate by gas permeation flow injection analysis', *Talanta*, pp. 831–

840. doi: 0039-9140/93.

Lamberti, A., Marasso, S. L. and Cocuzza, M. (2014) 'PDMS membranes with tunable gas permeability for microfluidic applications', *RSC Advances*, 4(106), pp. 61415–61419. doi: 10.1039/c4ra12934b.

Laugere, F., Guijt, R. M., Bastemeijer, J., Van der Steen, G., Berthold, A., Baltussen, E., Sarro, P., Van Dedem, G. W. K., Vellekoop, M. and Bossche, A. (2003) 'On-chip contactless four-electrode conductivity detection for capillary electrophoresis devices', *Analytical Chemistry*, 75(2), pp. 306–312. doi: 10.1021/ac0157371.

Lee, K., Kim, T. W., Byrne, R. H., Millero, F. J., Feely, R. A. and Liu, Y. M. (2010) 'The universal ratio of boron to chlorinity for the North Pacific and North Atlantic oceans', *Geochimica et Cosmochimica Acta*, 74(6), pp. 1801–1811. doi: 10.1016/j.gca.2009.12.027.

Liu, J., An, L., Xu, Z., Wang, N., Yan, X., Du, L., Liu, C. and Wang, L. (2013) 'Modeling of capacitively coupled contactless conductivity detection on microfluidic chips', *Microsystem Technologies*, 19(12), pp. 1991–1996. doi: 10.1007/s00542-013-1736-9.

Liu, X., Byrne, R. H., Adornato, L., Yates, K. K., Kaltenbacher, E., Ding, X. and Yang, B. (2013) 'In situ spectrophotometric measurement of dissolved inorganic carbon in seawater', *Environmental Science and Technology*, 47, pp. 11106–11114. doi: 10.1021/es4014807.

Liu, X., Patsavas, M. C. and Byrne, R. H. (2011) 'Purification and characterization of meta-cresol purple for spectrophotometric seawater ph measurements', *Environmental Science and Technology*, 45(11), pp. 4862–4868. doi: 10.1021/es200665d.

Ma, J., Shu, H., Yang, B., Byrne, R. H. and Yuan, D. (2019) 'Spectrophotometric determination of pH and carbonate ion concentrations in seawater: Choices, constraints and consequences', *Analytica Chimica Acta*. doi: 10.1016/j.aca.2019.06.024.

Magnusson, B., Naykki, T., Hovind, H. and Krysell, M. (2012) *Handbook for Calculation of Measurement Uncertainty in Environmental Laboratories*.

Mäki, A. J., Peltokangas, M., Kreutzer, J., Auvinen, S. and Kallio, P. (2015) 'Modeling carbon dioxide transport in PDMS-based microfluidic cell culture devices', *Chemical Engineering Science*, 137(2015), pp. 515–524. doi: 10.1016/j.ces.2015.06.065.

Mäntynen, M. (2001) *Temperature correction coefficients of electrical conductivity and of density measurements for saline groundwater*, *Working report 2001–15 Posiva, Finland*.

Marcelli, M., Piermattei, V., Madonia, A. and Mainardi, U. (2014) 'Design and application of new low-cost instruments for marine environmental research', *Sensors*, 14(12), pp. 23348–23364. doi: 10.3390/s141223348.

Martinotti, V., Balordi, M. and Ciceri, G. (2012) 'A flow injection analyser conductometric coupled system for the field analysis of free dissolved CO_2 and total dissolved inorganic carbon in natural waters.', *Analytical and bioanalytical chemistry*, 403(4), pp. 1083–1093. doi: 10.1007/s00216-012-5762-8.

Martz, T., Daly, K., Byrne, R., Stillman, J. and Turk, D. (2015) 'Technology for Ocean Acidification Research: Needs and Availability', *Oceanography*, 25(2), pp. 40–47. doi: 10.5670/oceanog.2015.30.

Marzouk, S. A. M. M., Al-Marzouqi, M. H., Abdullatif, N. and Ismail, Z. M. (2010) 'Removal of carbon dioxide from pressurized CO_2 – CH_4 gas mixture using hollow fiber membrane contactors', *Journal of Membrane Science*, 360, pp. 21–27. doi: 10.1016/j.memsci.2010.05.046.

McClanahan, T., Allison, E. H. and Cinner, J. E. (2015) 'Managing fisheries for human and food security', *Fish and Fisheries*, 16(1), pp. 78–103. doi: 10.1111/faf.12045.

McCleskey, R. B., Nordstrom, D. K., Ryan, J. N. and Ball, J. W. (2012) 'A new method of calculating electrical conductivity with applications to natural waters', *Geochimica et Cosmochimica Acta*, 77, pp. 369–382. doi: 10.1016/j.gca.2011.10.031.

McKee, C. B. (2009) 'An Accurate Equation for the Electrolytic Conductivity of Potassium Chloride Solutions', *Journal of Solution Chemistry*, 38(9), pp. 1155–1172. doi: 10.1007/s10953-009-9436-x.

McMahon, A., Santos, I. R., Cyronak, T. and Eyre, B. D. (2013) 'Hysteresis between coral reef calcification and the seawater aragonite saturation state', *Geophysical Research Letters*, 40(17), pp. 4675–4679. doi: 10.1002/grl.50802.

McNamara, C. J., Breuker, M., Helms, M., Perry, T. D. and Mitchell, R. (2004) 'Biodeterioration of Incralac used for the protection of bronze monuments', *Journal of Cultural Heritage*, 5(4), pp. 361–364. doi: 10.1016/j.culher.2004.06.002.

Mehrbach, C., Culberson, C. H., Hawley, J. E. and Pytkowicx, R. M. (1973) 'Measurement of the Apparent Dissociation Constants of Carbonic Acid in Seawater At Atmospheric Pressure', *Limnology and Oceanography*, 18(6), pp. 897–907. doi: 10.4319/lo.1973.18.6.0897.

Merkel, T. C., Bondar, V. I., Nagai, K., Freeman, B. D. and Pinnau, I. (2000) 'Gas sorption, diffusion, and permeation in poly(dimethylsiloxane).', *Journal of Polymer Science, Part B: Polymer Physics*,

38(3), pp. 415–434.

Mettler Toledo (2012) *Reducing Common Errors in Conductivity Measurements*, *Mettler Toledo*.

Míka, J., Opekar, F., Coufal, P. and Štulík, K. (2009) 'A thin-layer contactless conductivity cell for detection in flowing liquids', *Analytica Chimica Acta*, 650, pp. 189–194. doi: 10.1016/j.aca.2009.07.053.

Miller, C. A., Pocock, K., Evans, W. and Kelley, A. L. (2018) 'An evaluation of the performance of Sea-Bird Scientific's SeaFET^{tm} autonomous pH sensor: Considerations for the broader oceanographic community', *Ocean Science*, 14(4), pp. 751–768. doi: 10.5194/os-14-751-2018.

Millero, F. J. (2007) 'The marine inorganic carbon cycle.', *Chemical Review*, 107, pp. 308–341. doi: 10.1021/cr0503557.

Monser, L., Adhoum, N. and Sadok, S. (2004) 'Gas diffusion-flow injection determination of total inorganic carbon in water using tungsten oxide electrode', *Talanta*, 62(2), pp. 389–394. doi: 10.1016/j.talanta.2003.08.008.

Newton, J. A., Feely, R. A., Jewett, E. B., Williamson, P. and Mathis, J. (2014) 'Global Ocean Acidification Observing Network: Requirements and Governance Plan', *Global Ocean Acidification Observing Network*, p. 57.

Nguyen, D. T., Leho, Y. T. and Esser-Kahn, A. P. (2013) 'The effect of membrane thickness on a microvascular gas exchange unit', *Advanced Functional Materials*, 23(1), pp. 100–106. doi: 10.1002/adfm.201201334.

Nightingale, A. M., Beaton, A. D. and Mowlem, M. C. (2015) 'Trends in microfluidic systems for in situ chemical analysis of natural waters', *Sensors and Actuators, B: Chemical*, 221, pp. 1398–1405. doi: 10.1016/j.snb.2015.07.091.

Novotný, M., Opekar, F. and Štulík, K. (2005) 'The effects of the electrode system geometry on the properties of contactless conductivity detectors for capillary electrophoresis', *Electroanalysis*, 17, pp. 1181–1186. doi: 10.1002/elan.200403232.

Ogilvie, I. R. G., Sieben, V. J., Floquet, C. F. A., Zmijan, R., Mowlem, M. C. and Morgan, H. (2010) 'Reduction of surface roughness for optical quality microfluidic devices in PMMA and COC', *Journal of Micromechanics and Microengineering*, 20(6). doi: 10.1088/0960-1317/20/6/065016.

Ohno, K., Tachikawa, K. and Manz, A. (2008) 'Microfluidics:Applcations for analytical purposes in chemistry and biochemistry', *Electrophoresis*, 29, pp. 4443–4453. doi: 10.1002/elps. 200800121.

Okazaki, R. R., Sutton, A. J., Feely, R. A., Dickson, A. G., Alin, S. R., Sabine, C. L., Bunje, P. M. E. and Virmani, J. I. (2017) 'Evaluation of marine pH sensors under controlled and natural conditions for the Wendy Schmidt Ocean Health XPRIZE', *Limnology and Oceanography: Methods*, 15(6), pp. 586–600. doi: 10.1002/lom3.10189.

Omar, A. M., Thomas, H., Olsen, A., Becker, M., Skjelvan, I. and Reverdin, G. (2019) 'Trends of Ocean Acidification and pCO_2 in the Northern North Sea, 2003–2015', *Journal of Geophysical Research: Biogeosciences*, 124(10), pp. 3088–3103. doi: 10.1029/2018JG004992.

Partescano, E., Brosich, A., Lipizer, M., Cardin, V. and Giorgetti, A. (2017) 'From heterogeneous marine sensors to sensor web: (near) real-time open data access adopting OGC sensor web enablement standards', *Open Geospatial Data, Software and Standards*, 2(1). doi: 10.1186/s40965-017-0035-2.

Pawlowicz, R., Feistel, R., McDougall, T. J., Ridout, P., Seitz, S. and Wolf, H. (2015) 'Metrological challenges for measurements of key climatological observables Part 2: Oceanic salinity', *Metrologia*, 53(1), pp. R12–R25. doi: 10.1088/0026-1394/53/1/R12.

Pencharee, S., Faber, P. a., Ellis, P. S., Cook, P., Intaraprasert, J., Grudpan, K. and McKelvie, I. D. (2012) 'Underway determination of dissolved inorganic carbon in estuarine waters by gas-diffusion flow analysis with C4D detection', *Analytical Methods*, 4, pp. 1278–1283. doi: 10.1039/c2ay25113b.

Pongratz, J., Raddatz, T., Reick, C. H., Esch, M. and Claussen, M. (2009) 'Radiative forcing from anthropogenic land cover change since A.D. 800', *Geophysical Research Letters*, 36(2), pp. 2004–2008. doi: 10.1029/2008GL036394.

Press, W. H. and Teukolsky, S. A. (1990) 'Savitzky-Golay Smoothing Filters', *Computers in Physics*, 4(6), pp. 669–672. doi: 10.1063/1.4822961.

Pumera, M. (2007) 'Contactless conductivity detection for microfluidics: designs and applications.', *Talanta*, 74(3), pp. 358–364. doi: 10.1016/j.talanta.2007.05.058.

Ramos, P. M., Pereira, J. M. D., Member, S., Ramos, H. M. G., Member, S. and Ribeiro, A. L. (2008) 'A Four-Terminal Water-Quality-Monitoring Conductivity Sensor', *IEEE Transations om Instrumentation and Measurement*, 57(3), pp. 577–583.

Rérolle, V. M. C., Floquet, C. F. A., Harris, A. J. K., Mowlem, M. C., Bellerby, R. R. G. J. and Achterberg, E. P. (2013) 'Development of a colorimetric microfluidic pH sensor for autonomous seawater measurements', *Analytica Chimica Acta*, 786, pp. 124–131. doi:

10.1016/j.aca.2013.05.008.

Rérolle, V., Ruiz-Pino, D., Rafizadeh, M., Loucaides, S., Papadimitriou, S., Mowlem, M. and Chen, J. (2016) 'Measuring pH in the Arctic Ocean: Colorimetric method or SeaFET?', *Methods in Oceanography*, 17, pp. 32–49. doi: 10.1016/j.mio.2016.05.006.

Riser, S. C., Freeland, H. J., Roemmich, D., Wijffels, S., Troisi, A., Belbeoch, M., Gilbert, D., Xu, J., Pouliquen, S., Thresher, A., Le Traon, P., Maze, G., Klein, B., Ravichandran, M., Grant, F., Poulain, P., Suga, T., Lim, B., Sterl, A., Sutton, P., Mork, K., Velez-Belchi, P. J., Ansorge, I., King, B., Turton, J., Baringer, M. and Jayne, S. R. (2016) 'Fifteen years of ocean observations with the global Argo array', *Nature Climate Change*, 6(2), pp. 145–153. doi: 10.1038/nclimate2872.

Rock, J., Sima, E. and Knapen, M. (2020) 'What is the ocean: A sea-change in our perceptions and values?', *Aquatic Conservation: Marine and Freshwater Ecosystems*, 30(3), pp. 532–539. doi: 10.1002/aqc.3257.

Roemmich, D., Alford, M. H., Claustre, H., Johnson, K. S., King, B., Moum, J., Oke, P. R., Owens, W. B., Pouliquen, S., Purkey, S., Scanderbeg, M., Suga, T., Wijffels, S. E., Zilberman, N., Bakker, D., Baringer, M. O., Belbeoch, M., Bittig, H. C., Boss, E., Calil, P., Carse, F., Carval, T., Chai, F., Conchubhair, D. O., D'Ortenzio, F., Dall'Olmo, G., Desbruyères, D., Fennel, K., Fer, I., Ferrari, R., Forget, G., Freeland, H., Fujiki, T., Gehlen, M., Greenan, B., Hallberg, R., Hibiya, T., Hosoda, S., Jayne, S., Jochum, M., Johnson, G. C., Kang, K. R., Kolodziejczyk, N., Koertzinger, A., Le Traon, P. Y., Lenn, Y. D., Maze, G., Mork, K. A., Morris, T., Nagai, T., Nash, J., Garabato, A. N., Olsen, A., Pattabhi, R. R., Prakash, S., Riser, S., Schmechtig, C., Shroyer, E., Sterl, A., Sutton, P., Talley, L., Tanhua, T., Thierry, V., Thomalla, S., Toole, J., Troisi, A., Trull, T., Turton, J. D., Velez-Belchi, P. J., Walczowski, W., Wang, H., Wanninkhof, R., Waterhouse, A., Watson, A., Wilson, C., Wong, A. P., Xu, J. and Yasuda, I. (2019) 'On the future of Argo: A global, full-depth, multi-disciplinary array', *Frontiers in Marine Science*, 6, pp. 1–28. doi: 10.3389/fmars.2019.00439.

Rogelj, J., den Elzen, M., Höhne, N., Fransen, T., Fekete, H., Winkler, H., Schaeffer, R., Sha, F., Riahi, K. and Meinshausen, M. (2016) 'Paris Agreement climate proposals need a boost to keep warming well below 2 °C', *Nature*, 534(7609), pp. 631–639. doi: 10.1038/nature18307.

Rossby, T., Flagg, C. N., Donohue, K., Sanchez-Franks, A. and Lillibridge, J. (2014) 'On the long-term stability of Gulf Streamtransport based on 20 years of direct measurements', *Geophysical Research Letters*, 41, pp. 114–120. doi: 10.1002/2013GL058636.

Sabine, C. L., Feely, R. A., Gruber, N., Key, R. M., Lee, K., Bullister, J. L., Wanninkhof, R., Wong, C. S. S., Wallace, D. W. R., Tilbrook, B., Millero, F. J., Peng, T. H., Kozyr, A., Ono, T. and Rios, A. F. (2004)

'The Oceanic Sink for Anthropogenic CO_2', *Science*, 305, pp. 367–371.

Sastri, A. R., Christian, J. R., Achterberg, E. P., Atamanchuk, D., Buck, J. J. H., Bresnahan, P., Duke, P. J., Evans, W., Gonski, S. F., Johnson, B., Juniper, S. K., Mihaly, S., Miller, L. A., Morley, M., Murphy, D., Nakaoka, S. I., Ono, T., Parker, G., Simpson, K. and Tsunoda, T. (2019) 'Perspectives on in situ Sensors for Ocean Acidification Research', *Frontiers in Marine Science*, 6(653), pp. 1–6. doi: 10.3389/fmars.2019.00653.

Sayles, F. L. and Eck, C. (2009) 'An autonomous instrument for time series analysis of TCO_2 from oceanographic moorings', *Deep-Sea Research Part I: Oceanographic Research Papers*, 56, pp. 1590–1603. doi: 10.1016/j.dsr.2009.04.006.

Schneider, B., Gülzow, W., Sadkowiak, B. and Rehder, G. (2014) 'Detecting sinks and sources of CO_2 and CH_4 by ferrybox-based measurements in the Baltic Sea: Three case studies', *Journal of Marine Systems*, 140(PA), pp. 13–25. doi: 10.1016/j.jmarsys.2014.03.014.

Schuster, U., Hannides, A., Mintrop, L. and Körtzinger, A. (2009) 'Sensors and instruments for oceanic dissolved carbon measurements', *Ocean Science*, 5, pp. 547–558. doi: 10.5194/os-5-547-2009.

Singh R (2015) 'Introduction to Membrane Technology', in *Membrane Technology and Engineering for Water Purification, Application, Systems Design and Operation*. 2nd edn, pp. 1–78.

Smith, B. D. and Zeder, M. A. (2013) 'The onset of the Anthropocene', *Anthropocene*, 4, pp. 8–13. doi: 10.1016/j.ancene.2013.05.001.

Snyder, E. G., Watkins, T. H., Solomon, P. A., Thoma, E. D., Williams, R. W., Hagler, G. S. W., Shelow, D., Hindin, D. A., Kilaru, V. J. and Preuss, P. W. (2013) 'The changing paradigm of air pollution monitoring', *Environmental Science and Technology*, 47(20), pp. 11369–11377. doi: 10.1021/es4022602.

Spendley, W., Hext, G. R. and Himsworth, F. R. (1962) 'Sequential Application of Simplex Designs in Optimisation and Evolutionary Operation', *Technometrics*, 4(4), pp. 441–461. doi: 10.1080/00401706.1962.10490033.

Steffen, W., Crutzen, J. and McNeill, J. R. (2007) 'The Anthropocene: are humans now overwhelming the great forces of Nature?', *Ambio*, 36(8), pp. 614–621.

Stommel, H. (1989) 'The slocum mission', *Oceanography*, 2(1), pp. 22–25. doi: 10.5670/oceanog.1989.26.

Szulczewski, M. L., MacMinn, C. W., Herzog, H. J. and Juanes, R. (2012) 'Lifetime of carbon capture and storage as a climate-change mitigation technology.', *Proceedings of the National Academy of Sciences*, 109(14), pp. 5185–9. doi: 10.1073/pnas.1115347109.

Tang, L. and Lee, N. Y. (2010) 'A facile route for irreversible bonding of plastic-PDMS hybrid microdevices at room temperature', *Lab on a Chip*, 10(10), pp. 1274–1280. doi: 10.1039/B924753J.

Tans, P. and Keeling, R. F. (2020) *Tans, P., NOAA/ESRL (www. esrl. noaa.gov/gmd/ccgg/trends/) and Ralph Keeling, Scripps Institution of Oceanography (scrippsco2. ucsd. edu/)*.

Temiz, Y., Lovchik, R. D., Kaigala, G. V. and Delamarche, E. (2015) 'Lab-on-a-chip devices: How to close and plug the lab?', *Microelectronic Engineering*, 132, pp. 156–175. doi: 10.1016/j.mee.2014.10.013.

Tracey, D., Bostock, H., Currie, K., Mikaloff-Fletcher, S., Williams, M., Hadfield, M., Neil, H., Guy, C. and Cummings, V. (2013) *The potential impact of ocean acidification on deep-sea corals and fisheries habitat in New Zealand waters*, *New Zealand Aquatic Environment and Biodiversity Report*.

Trakadas, A., Firth, A., Gregory, D., Elkin, D., Guerin, U., Henderson, J., Kimura, J., Scott-Ireton, D., Shashoua, Y., Underwood, C. and Viduka, A. (2019) 'The Ocean Decade Heritage Network: Integrating Cultural Heritage Within the UN Decade of Ocean Science 2021–2030', *Journal of Maritime Archaeology*, 14(2), pp. 153–165. doi: 10.1007/s11457-019-09241-0.

Tue-Ngeun, O., Sandford, R. C., Jakmunee, J., Grudpan, K., McKelvie, I. D. and Worsfold, P. J. (2005) 'Determination of dissolved inorganic carbon (DIC) and dissolved organic carbon (DOC) in freshwaters by sequential injection spectrophotometry with on-line UV photo-oxidation', *Analytica Chimica Acta*, 554, pp. 17–24. doi: 10.1016/j.aca.2005.08.043.

Tůma, P., Opekar, F. and Štulik, K. (2002) 'A contactless conductivity detector for capillary electrophoresis: Effects of the detection cell geometry on the detector performance', *Electrophoresis*, 23, pp. 3718–3724. doi: 10.1002/1522-2683(200211)23:21<3718::AID-ELPS3718>3.0.CO;2-U.

Tůma, P., Samcová, E. and Štulík, K. (2009) 'The dependence of the sensitivity and reliability of contactless conductivity detection on the wall thickness of electrophoretic fused-silica capillaries', *Electroanalysis*, 21, pp. 590–594. doi: 10.1002/elan.200804398.

Turley, C. and Gattuso, J. P. (2012) 'Future biological and ecosystem impacts of ocean acidification

and their socioeconomic-policy implications', *Current Opinion in Environmental Sustainability*, 4(3), pp. 278–286. doi: 10.1016/j.cosust.2012.05.007.

Turley, C. M., Blackford, J. C., Hardman-Mountford, N. J., Litt, E. J., Llewellyn, C. A., Lowe, D. M., Miller, P. I., Nightingale, P. D., Rees, A. P., Smyth, T. J., Tilstone, G. H. and Widdicombe, S. (2009) 'Carbon Uptake Transport and Storage by Oceans and the Consequences of Change In Carbon Capture and Storage (CCS) Issues', *Environmental Science and Technology*, 29, pp. 240–284.

UNFCCC. Conference of the Parties (COP) (2015) 'Adoption of the Paris Agreement. Proposal by the President.', *Paris Climate Change Conference - November 2015, COP 21*, 21932, p. 32. doi: FCCC/CP/2015/L.9/Rev.1.

Valada, A., Velagapudi, P., Kannan, B., Tomaszewski, C., Kantor, G. and Scerri, P. (2014) 'Development of a Low Cost Multi-Robot Autonomous Marine Surface Platform', in Yoshida, K. and Tadokoro, S. (eds) *Field and Service Robotics: Results of the 8th International Conference*, pp. 643–658. doi: 10.1007/978-3-642-40686-7_43.

Vincent, A. G., Pascal, R. W., Beaton, A. D., Walk, J., Hopkins, J. E., Woodward, E. M. S., Mowlem, M. and Lohan, M. C. (2018) 'Nitrate drawdown during a shelf sea spring bloom revealed using a novel microfluidic in situ chemical sensor deployed within an autonomous underwater glider', *Marine Chemistry*, 205, pp. 29–36. doi: 10.1016/j.marchem.2018.07.005.

Volk, T. and Hoffert, M. I. (1985) 'Ocean Carbon Pumps: Analysis of relative strengths and efficiencies in ocean-driven atmospheric CO_2 changes', in Sundquist, E. and Broecker, W. (eds) *The Carbon Cycle and Atmospheric CO_2 Natural Variations Archean to Present*, pp. 99–110. doi: https://doi.org/10.1029/GM032p0099.

Waldmann, C., Tamburri, M., Prien, R. D. and Fietzek, P. (2010) 'Assessment of sensor performance', *Ocean Science Discussions*, 6(2), pp. 1687–1716. doi: 10.5194/osd-6-1687-2009.

Wallace, D. (2001) 'Chapter 6.3 Storage and transport of excess CO_2 in the oceans: The JGOFS/WOCE global CO_2 survey', in Siedler, G., Church, J., and Gould, J. (eds) *Ocean Circulation and Climate*, pp. 489–523. doi: https://doi.org/10.1016/S0074-6142(01)80136-4.

Wallmann, K., Haeckel, M., Linke, P., Haffert, L., Schmidt, M., Buenz, S., James, R., Hauton, C., Tsimplis, M., Widdicombe, S., Blackford, J., Queiros, A. M., Connelly, D., Lichtschlag, A., Dewar, M., Chen, B., Baumberger, T., Beaubin, S., Vercelli, S., Proelss, A., Wildenborg, T., Mikunda, T., Nepveu, M., Maynard, C., Finnerty, S., Flach, T., Ahmed, N., Ulfsnes, A., Brooks, L., Moskeland, T. and Purcell, M. (2015) *Best Practice Guidance for Environmental Risk Assessment for offshore CO_2 geological storage*. doi: 10.3289/ECO2_D14.1.

Walters, F. H., Parker, Lloyd R., J., Morgan, S. L. and Deming, S. N. (1991) 'Systems Theoy and Response Surfaces', in *Sequential simplex optimization: a technique for improving quality and productivity in research, development, and manufacturing*, pp. 30–64.

Wang, S. R., Di Iorio, D., Cai, W. J. and Hopkinson, C. S. (2018) 'Inorganic carbon and oxygen dynamics in a marsh-dominated estuary', *Limnology and Oceanography*, 63(1), pp. 47–71. doi: 10.1002/lno.10614.

Wang, Z. A., Chu, S. N. and Hoering, K. A. (2013) 'High-frequency spectrophotometric measurements of total dissolved inorganic carbon in seawater', *Environmental Science and Technology*, 47, pp. 7840–7847. doi: 10.1021/es400567k.

Wang, Z. A., Liu, X., Byrne, R. H., Wanninkhof, R., Bernstein, R. E., Kaltenbacher, E. A. and Patten, J. (2007) 'Simultaneous spectrophotometric flow-through measurements of pH, carbon dioxide fugacity, and total inorganic carbon in seawater', *Analytica Chimica Acta*, 596(1), pp. 23–36. doi: 10.1016/j.aca.2007.05.048.

Wang, Z. A., Moustahfid, H., Mueller, A. V., Michel, A. P. M., Mowlem, M., Glazer, B. T., Mooney, T. A., Michaels, W., McQuillan, J. S., Robidart, J. C., Churchill, J., Sourisseau, M., Daniel, A., Schaap, A., Monk, S., Friedman, K. and Brehmer, P. (2019) 'Advancing Observation of Ocean Biogeochemistry, Biology, and Ecosystems With Cost-Effective in situ Sensing Technologies', *Frontiers in Marine Science*, 6, pp. 1–22. doi: 10.3389/fmars.2019.00519.

Wang, Z. A., Sonnichsen, F. N., Bradley, A. M., Hoering, K. A., Lanagan, T. M., Chu, S. N., Hammar, T. R. and Camilli, R. (2015) 'In situ sensor technology for simultaneous spectrophotometric measurements of seawater total dissolved inorganic carbon and pH', *Environmental Science and Technology*, 49(7), pp. 4441–4449. doi: 10.1021/es504893n.

Weller, R., Toole, J., McCartney, M. and Hogg, N. (2000) 'Outposts in the Ocean', *Oceanus Magazine*, 42(1), pp. 20–23.

Wijmans, J. G. and Baker, R. W. (1995) 'The solution-diffusion model: A review', *Journal of Membrane Science*, 107(1–2), pp. 1–21. doi: 10.1016/0376-7388(95)00102-I.

Williams, D. E. (2019) 'Low Cost Sensor Networks: How Do We Know the Data Are Reliable?', *ACS Sensors*, 4(10), pp. 2558–2565. doi: 10.1021/acssensors.9b01455.

Williams, R. G. and Follows, M. J. (2011) *Ocean Dynamics and the Carbon Cycle*. 1st edn.

Wolf-Gladrow, D. A., Zeebe, R. E., Klaas, C., Körtzinger, A. and Dickson, A. G. (2007) 'Total alkalinity: The explicit conservative expression and its application to biogeochemical processes',

Marine Chemistry, 106(1-2 SPEC. ISS.), pp. 287–300. doi: 10.1016/j.marchem.2007.01.006.

Wong, M., Bejarano, E., Carvlin, G., Fellows, K., King, G., Lugo, H., Jerrett, M., Meltzer, D., Northcross, A., Olmedo, L., Seto, E., Wilkie, A. and English, P. (2018) 'Combining community engagement and scientific approaches in next-generation monitor siting: The case of the imperial county community air network', *International Journal of Environmental Research and Public Health*, 15(3). doi: 10.3390/ijerph15030523.

Worsfold, P. J., Achterberg, E. P., Birchill, A. J., Clough, R., Leito, I., Lohan, M. C., Milne, A. and Ussher, S. J. (2019) 'Estimating uncertainties in oceanographic trace element measurements', *Frontiers in Marine Science*, 6. doi: 10.3389/fmars.2018.00515.

Wynn, R. B., Huvenne, V. A. I., Le Bas, T. P., Murton, B. J., Connelly, D. P., Bett, B. J., Ruhl, H. A., Morris, K. J., Peakall, J., Parsons, D. R., Sumner, E. J., Darby, S. E., Dorrell, R. M. and Hunt, J. E. (2014) 'Autonomous Underwater Vehicles (AUVs): Their past, present and future contributions to the advancement of marine geoscience', *Marine Geology*, 352, pp. 451–468. doi: 10.1016/j.margeo.2014.03.012.

Yampolskii, Y. and Finkelshtein, E. (2017) *Membrane Materials for Gas and Vapor Separation: Synthesis and application of silicon-containing polymers*. 1st edn.

Yeom, C. K., Lee, S. H. and Lee, J. M. (2000) 'Study of Transport of Pure and Mixed CO_2 / N_2 Gases through Polymeric Membranes', *Journal of Applied Physics*, 78, pp. 179–189.

Yoerger, D., Bradley, A., Jakuba, M., German, C., Shank, T. and Tivey, M. (2007) 'Autonomous and Remotely Operated Vehicle Technology for Hydrothermal Vent Discovery, Exploration, and Sampling', *Oceanography*, 20(1), pp. 152–161. doi: 10.5670/oceanog.2007.89.

Zeebe, R. E. and Wolf-Gladrow, D. A. (2001) *CO_2 in seawater: equilibrium, kinetics, isotopes*.

Zeebe, R. E., Wolf-Gladrow, D. A. and Jansen, H. (1999) 'On the time required to establish chemical and isotopic equilibrium in the carbon dioxide system in seawater', *Marine Chemistry*, 65(3–4), pp. 135–153. doi: 10.1016/S0304-4203(98)00092-9.